Preparation of Pt-based Bimetallic Catalysts for the Oxygen Reduction Reaction in PEM Fuel Cells

Thesis

Preparation of Pt-based Bimetallic Catalysts for the Oxygen Reduction Reaction in PEM Fuel Cells

Yangdong Qian

January 2004

A thesis submitted for the degree of Doctor of Philosophy
to
The Open University

Department of Chemistry
The Open University
Walton Hall
Milton Keynes MK7 6AA
United Kingdom

Submission date: 22 January 20..
Award date: 18 June 2004

ProQuest LLC.
789 East Eisenhower Parkway
P.O. Box 1346
Ann Arbor, MI 48106 – 1346

ABSTRACT

This work includes the preparation and characterization of carbon supported Pt-based bimetallic electrocatalysts and their subsequent electrochemical evaluation for the oxygen-reduction reaction (ORR) in polymer electrolyte membrane (PEM) fuel cells. Monometallic Pt/C was modified using a surface organometallic chemistry (SOMC) route to prepare a series of PtFe/C, PtCr/C, PtNi/C and PtCo/C bimetallic electrocatalysts. The catalysts were studied as prepared, and after a range of different heat treatments.

Physical characterization of unmodified Pt/C and the PtM/C bimetallic electrocatalysts was performed using a range of techniques. UV-visible spectroscopy, ICP, TGA and DSC were used to analyse the composition of the electrocatalysts and to postulate a reaction mechanism for the SOMC reaction during the electrocatalyst preparation. TEM/EDX, BET, chemisorption and X-ray diffraction examined particle size, showing that electrocatalysts prepared using the SOMC method sinter less readily than those prepared by conventional methods, and also provided evidence that a selective reaction had occurred between the reduced surface Pt of the Pt/C catalyst and the organometallic precursor of the second metal. XRD and EXAFS indicated that an alloy was formed between the surface Pt and the second metal in many of the heat-treated samples. EXAFS, TPR and XPS were used to examine the metal oxidation states in the PtM/C bimetallic electrocatalysts.

The PtM/C electrocatalysts were evaluated for the oxygen-reduction reaction (ORR) in PEM fuel cells. The optimum electrocatalyst, was found to be 0.67 PtCr/C after heat treatment at 750 °C; this had high catalytic activity compared with the commercial electrocatalyst, PtCr/C(JM), provided by Johnson Matthey Technology Centre.

STATEMENT

I declare that the work included in this thesis was carried out by the author during the period of March 2000 to October 2003 at the Chemistry Department of the Open University under the supervision of Dr E. M. Crabb and Dr L. E. Smart.

The work in this thesis is the result of my own investigation apart from the following which are fully acknowledged:

- Element analysis carried out by Johnson Matthey Technology Centre
- EXAFS data analysis carried out jointly with Dr Andrea Russell and Ms Abbe Rose, Chemistry Department of University of Southampton

The publications and presentations during my PhD work so far, are listed below:

- E. M. Crabb, M. K. Ravikumar, Y. Qian, A. E. Russell, S. Maniguet, J. Yao, D. Thompsett, M. Hurford and S. C. Ball, Electrochemical and Solid-State Letters 5 (1), 5-9 (2000)
- 8th CSCST & SCICS Joint Conference, Oxford, UK, October 2001 (poster)
- 4th International Conference, ELECTROCATALYSIS, From Theory to Industrial Applications, Como, Italy, September 2002 (poster)
- 10th CSCST & SCICS Joint Conference, London, UK, September 2003 (oral presentation)

Yangdong Qian, January, 2004

ACKNOWLEDGEMENTS

I would like to express my sincere gratitude to my two supervisors, Dr Eleanor M. Crabb and Dr Lesley E. Smart, for their patient help, guidance and continued enthusiasm and encouragement throughout the duration of my work.

I would wish to acknowledge the very substantial help and advice from Dr Dave Thompsett (Johnson Matthey Technology Centre) and Dr M.K. Ravikumar for this work.

Many thanks to the following people who have supported me at various stages of this work: Dr Andrea E. Russell and Ms Abbe Rose (University of Southampton) for their instruction with EXAFS experiment; Dr Brian Theobald (Johnson Matthey Technology Centre) for his assistance with Half Cell experiment; the research staff and technical staff of the Department of Chemistry --- Mr Graham Jeffs, Mr Brandon Cook and Mr Gordon Oates for their technical expertise of GC, TGA and XRD; Ms Naomi Williams and Dr Xianwei Liu for their help with the electron microscopy work; Dr Ruth T. Williams, Dr Michael Mortimer and Professor Frank Berry for their help with the annual year reports and my talks at the Solid State Chemistry Research Group.

Thanks to The Open University and Johnson Matthey Technology Centre for the studentship and funding.

Finally, I would like to thank my parents, family and friends, who have been behind me all the way. I would especially like to thank my wife, Li, and my son, Jiji, who have given and helped more than they could.

Contents

CHAPTER 1 INTRODUCTION **1**

1.1 AIMS 1
1.2 POLYMER ELECTROLYTE MEMBRANE (PEM) FUEL CELLS 2
1.2.1 Fuel cells *2*
1.2.2 History of fuel cells *3*
1.2.3 Polymer electrolyte membrane (PEM) fuel cells *5*
1.2.4 The performance of PEM fuel cells *8*
1.2.5 The applications of PEM fuel cells *14*
1.2.6 Obstacles to using PEM fuel cells *15*
1.3 THE OXYGEN REDUCTION ELECTROCATALYSTS OF H_2/O_2 PEMFC 16
1.4 SURFACE ORGANOMETALLIC CHEMISTRY (SOMC) 18
1.5 REFERENCES 22

CHAPTER 2 EXPERIMENTAL TECHNIQUES **25**

2.1 REAGENTS 25
2.2 PREPARATION OF PTM/C BIMETALLIC CATALYSTS USING SOMC 26
2.2.1 Apparatus *26*
2.2.2 Preparation procedures for PtM/C bimetallic catalysts *27*
2.3 TECHNIQUES FOR SURFACE CHARACTERISATION 30
2.3.1 Ultraviolet and visible spectroscopy (UV-Vis) *30*
2.3.2 Total surface area and Pt metal dispersion of bimetallic catalysts *33*
2.3.3 Transmission electron microscopy (TEM) and energy dispersive X-ray analysis (EDX) *41*
2.3.4 X-ray photoelectron spectroscopy (XPS) *44*
2.3.5 Powder X-ray diffraction (XRD) *47*
2.3.6 Temperature-programmed reduction (TPR) *50*
2.3.7 Thermogravimetic analysis and differential scanning calorimetry (TGA/DSC) *52*
2.3.8 Extended X-ray absorption fine structure (EXAFS) *56*
2.3.9 Inductively Coupled Plasma - Atomic Emission Spectroscopy *62*
2.4 ELECTROCHEMICAL EVALUATION 63
2.4.1 Electrode Preparation *63*
2.4.2 Cyclic Voltammetry *65*
2.4.3 Steady State Galvanostatic Polarization *72*
2.5 REFERENCES 76

CHAPTER 3 PREPARATION AND CHARACTERIZATION OF CARBON SUPPORTED PT-BASED BIMETALLIC ELECTROCATALYSTS 80

3.1 INTRODUCTION 80
3.2 PREPARATION OF PTM/C BIMETALLIC CATALYSTS (M = FE, NI, CR OR CO) USING SOMC METHOD 81
3.2.1 The Preparative Procedure 81
3.2.2 Analysis of catalyst composition 84
3.2.3 The mechanism of PtM/C catalysts preparation using SOMC 91
3.3 CHARACTERIZATION OF CARBON SUPPORTED PT-BASED BIMETALLIC CATALYSTS 95
3.3.1 Transmission electron microscopy (TEM) and energy dispersive X-ray analysis (EDX) 95
3.3.2 Total surface area and Pt metal dispersion of bimetallic catalysts 111
3.3.3 Powder X-ray diffraction (XRD) 116
3.3.4 Extended X-ray adsorption fine structure (EXAFS) 127
3.3.5 X-ray photoelectron spectra (XPS) 138
3.3.6 Temperature-programmed reduction (TPR) 143
3.4 CONCLUSIONS 152
3.5 REFERENCES 153

CHAPTER 4 CATALYTIC EVALUATION OF THE CARBON SUPPORTED PT-BASED BIMETALLIC ELECTROCATALYSTS 157

4.1 CYCLIC VOLTAMMETRY 157
4.2 CO CYCLIC VOLTAMMETRY 164
4.3 OXYGEN-REDUCTION REACTION AT THE CATHODE IN PEM FUEL CELLS 169
4.4 CONCLUSION 176
4.5 REFERENCES 177

CHAPTER 5 PREPARATION AND CHARACTERIZATION OF HEAT-TREATED CARBON SUPPORTED PT-BASED BIMETALLIC CATALYSTS. 179

5.1 PREPARATION OF HEAT-TREATED PT-BASED BIMETALLIC CATALYSTS 179
5.2 PHYSICAL CHARACTERIZATION OF HEAT-TREATED PT-BASED BIMETALLIC CATALYSTS 180
5.2.1 Powder X-ray diffraction 180
5.2.2 Transmission electron microscopy and Energy Dispersive X-ray 187
5.2.3 Extended X-ray adsorption fine structure (EXAFS) 201
5.3 CONCLUSIONS 222
5.4 REFERENCES 223

CHAPTER 6 CATALYTIC EVALUATION OF THE CARBON SUPPORTED PT-BASED BIMETALLIC PTM/C(T) CATALYSTS AFTER HEAT TREATMENT, AND OPTIMIZATION OF THE CATALYSTS 226

6.1 CO STRIPPING VOLTAMMETRY 226
6.2 THE OXYGEN-REDUCTION REACTION 234
6.2.1 Tafel plots 235
6.2.2 Specific activity 238
6.2.3 Mass activity 241
6.2.4 Discussion and further experiments 246
6.3 OPTIMIZATION OF ELECTROCATALYSTS FOR OXYGEN REDUCTION REACTION 249
6.3.1 Comparison of mass activity for different composition PtCr/C electrocatalysts 249
6.4 CONCLUSION 255
6.4 REFERENCES 256

Chapter 1 Introduction

1.1 Aims

The aims of this thesis are to report the study of carbon supported Pt-based bimetallic electrocatalysts and their application for the oxygen reduction reaction (ORR) at the cathode, in polymer electrolyte membrane (PEM) fuel cells.

Chapter 1 introduces the PEM fuel cells, oxygen-reduction electrocatalysts and the new electrocatalyst preparation method used here --- surface organometallic chemistry (SOMC). The main focus in Chapter 2 is experimental techniques. The theories, experimental procedures and apparatus for all techniques used in this work are described in this chapter. Chapters 3 to 6 are central to this thesis; they contain detailed results and discussion of this work. Chapter 3 is concerned with the preparation and physical characterisation of a series of Pt-based bimetallic electrocatalysts using surface organometallic chemistry (SOMC). Chapter 4 describes the catalyst evaluation of these carbon supported Pt and Pt-based bimetallic catalysts using electrochemical methods. Chapter 5 describes the physical characterisation of Pt-based bimetallic electrocatalysts after heat treatment. The evaluation of catalytic activity of carbon supported Pt-based bimetallic electrocatalysts after heat treatment, is discussed in Chapter 6. Chapter 6 also discusses the optimization of electrocatalysts for the oxygen-reduction reaction.

After Section 1.1 the remainder of this chapter includes three sections. Section 1.2 describes the principles underlying PEM fuel cells. A short review is given of the historical developments which led up to the modern work in this field. An introduction to oxygen reduction electrocatalysts is given in Section 1.3. Section 1.4 describes the surface organometallic chemistry (SOMC) technique, used for preparing the electrocatalysts.

1.2 Polymer electrolyte membrane (PEM) fuel cells

1.2.1 Fuel cells

Fuel cells are electrochemical devices that continuously convert the chemical energy of a reaction directly into electrical energy. Unlike a battery, a fuel cell does not run down or require recharging. It will continuously produce energy in the form of electricity and heat as long as the fuels (usually hydrogen) are supplied [1]. The basic physical structure of a fuel cell consists of an electrolyte layer, catalyst layers in contact with a porous anode and cathode on either side and gas diffusion layers. A schematic representation of a H_2/O_2 fuel cell is shown in Figure 1.1.

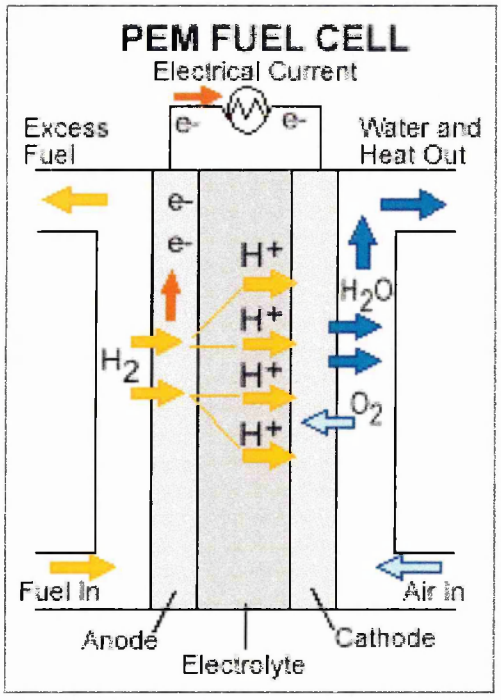

Figure 1.1 Schematic diagram of a H_2/O_2 fuel cell

As Figure 1.1 depicts, hydrogen (fuel) is fed into the anode of the fuel cell and oxygen (or air) enters the fuel cell through the cathode. At the anode the H_2 molecule is dissociated into two hydrogen atoms (H) and oxidized to produce two hydrogen ions (H^+) and two electrons (e^-). The hydrogen ions migrate through the electrolyte to the cathode.

The electrons create an electric current that can be utilized to provide power before returning to the cathode by the external circuit. At the cathode, oxygen combines with the electrons and hydrogen ions to produce water. These reactions in the fuel cells are as follows:

Anode (Oxidation half reaction): $2H_2 \rightarrow 4H^+ + 4e^-$ (1.1)

Cathode (Reduction half reaction): $O_2 + 4H^+ + 4e^- \rightarrow 2H_2O$ (1.2)

Overall (Fuel cell reaction): $2H_2 + O_2 \rightarrow 2H_2O$ + energy (1.3)

The most common classification of fuel cells is by the type of electrolyte used in the cell because the electrolyte defines the key properties, particularly the operating temperature, of the fuel cells. Types of fuel cell include (1) polymer electrolyte membrane (PEM) fuel cells, (2) alkaline fuel cell (AFC), (3) phosphoric acid fuel cell (PAFC), (4) molten carbonate fuel cell (MCFC), and (5) solid oxide fuel cell (SOFC). These fuel cells are listed in the order of approximate operating temperature, ranging from ~80 °C for PEM, ~100 °C for AFC, ~200 °C for PAFC, ~650 °C for MCFC, and 800 - 1000 °C for SOFC.

1.2.2 History of fuel cells

Sir William Grove (1811-1896) developed the first fuel cell in 1839. The principle was discovered by accident during an electrolysis experiment [2]. When Sir William Grove disconnected the battery from the electrolyzer and connected the two electrodes together, he observed a current flowing in the opposite direction, consuming the gases of hydrogen and oxygen (Figure 1.2). However, due to problems of corrosion of the electrodes and instability of the materials, Grove's fuel cell was not practical.

In the 1950s Francis (Tom) Bacon, a chemical engineer at Cambridge University, successfully produced the first practical fuel cell, which was an alkaline fuel cell. It used an alkaline electrolyte (molten KOH) instead of dilute sulphuric acid.

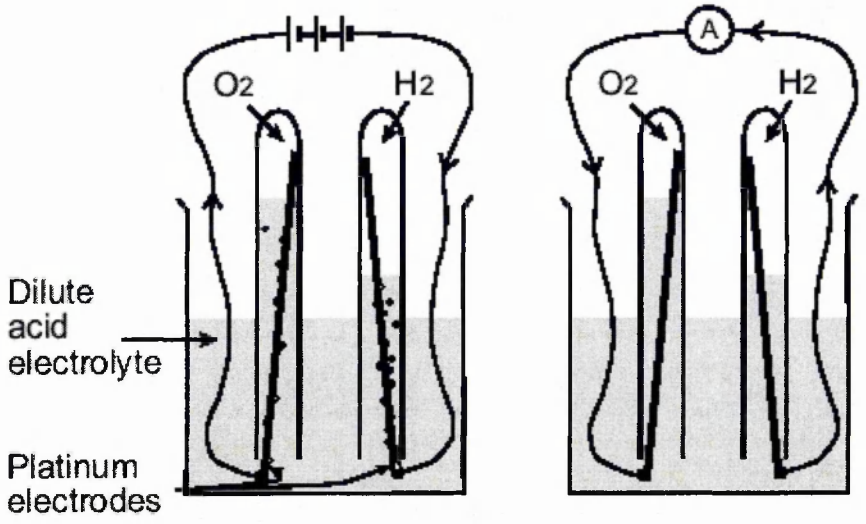

Figure 1.2 The principle of an electrolyzer, shown left; and of a fuel cell, shown right [3].

The PEM fuel cell was invented by General Electric (GE) in the early 1960s. This was a significant breakthrough in fuel cell technology. It was initially developed under a program with the US Navy's Bureau of Ships and U.S. Army Signal Corps to supply portable power for personnel in the field. After the successful space application using GE´s PEM fuel cell on the Apollo missions in the 1960s, industry began to recognize the commercial potential of PEM fuel cells. Since environmental impacts, due to emissions produced from conventional power supplies, such as global climate change, ozone depletion and acid rain, became of concern in the 1980s, the Department of Energy in the US has been supporting research and development of fuel cell technology [4, 5] as an alternative 'cleaner' source of power. As a result, hundreds of companies and universities around the world are now working towards making commercially viable, operational fuel cells. Up to now most car manufacturers have their prototypes of fuel cells. However, there are still some obstacles before the commercial application of PEM fuel cells, which are discussed in Section1.2.6.

Finally, let us introduce President George W Bush's State of the Union address on January 28, 2003 to end this brief review of history of fuel cells:

"……

A single chemical reaction between hydrogen and oxygen generates energy, which can be used to power a car - producing only water, not exhaust fumes. Our scientists and engineers will overcome obstacles to taking these cars from laboratory to showroom, so that the first car driven by a child born today could be powered by hydrogen, and pollution-free.

……"

1.2.3 Polymer electrolyte membrane (PEM) fuel cells

As discussed in section 1.2.1, fuel cells are normally classified into five types according to the electrolyte used in the cells. Because our work is concerned specifically with the study of carbon supported Pt-based bimetallic electrocatalysts and its application in polymer electrolyte membrane (PEM) fuel cells, only an account of PEM fuel cells is given below.

1.2.3.1 Polymer electrolyte membrane

The electrolyte in PEM fuel cells is a thin polymer membrane. The most prevalent membrane, Nafion™, produced by DuPont, resembles the plastic wrap used for sealing foods. Nafion consists of polytetrafluoroethylene (PTFE) chains, commonly known as Teflon™, forming the backbone of the membrane. Attached to the Teflon chains, are side chains ending with sulphonic acid (HSO_3) groups (Figure 1.3). Because their structure is based on a teflon backbone, PEM is a very strong and stable substances. It is an effective gas separator. It can separate H_2 gas from O_2 gas, a feature essential to the efficient operation of a fuel cell. Only the positive ions contained within the PEM are

mobile and are free to carry positive charge (hydrogen ions) through the membrane. In PEM fuel cells movement of the hydrogen ions through the membrane from anode to cathode is essential to fuel cell operation. Although PEM is ionic conductor, it does not conduct electrons. The organic nature of the PEM structure makes them electronic insulators, another feature essential to fuel cell operation.

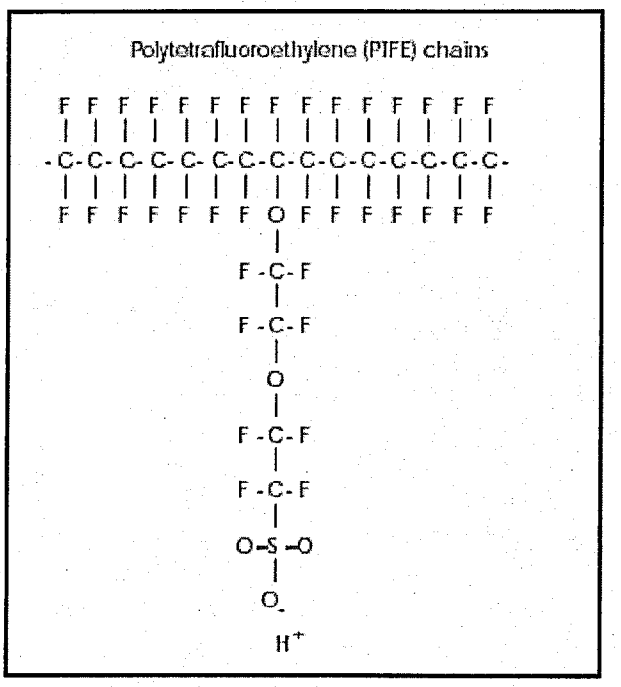

Figure 1.3 Chemical structure of the PEM fuel cell membrane.

1.2.3.2 The catalysts in PEM fuel cells

In a PEM fuel cell, two half-cell reactions take place simultaneously, an oxidation half-reaction (loss of electrons) at the anode and a reduction half-reaction (gain of electrons) at the cathode. These two reactions make up the total oxidation-reduction (redox) reaction of the fuel cell, the formation of water from hydrogen and oxygen gases (see equations 1.1 – 1.3).

These two half-reactions would normally occur very slowly at the low operating temperature, typically 80°C, of the PEM fuel cells. Thus, catalysts are used on both the

anode and cathode to increase the rates of each half-reaction. Expensive Pt based catalysts seem to be the best catalysts for the two half-reactions in PEM fuel cells.

At the anode, the hydrogen molecules first come into contact with a platinum catalyst on the electrode surface. The hydrogen molecules break apart, bonding to the platinum surface forming weak H-Pt bonds (equation 1.4). Then the H atoms are released as H^+ and e^- (equation 1.5). The hydrogen ion (H^+) travels through the membrane material to the cathode. The electron (e^-) travels around the external circuit to the cathode.

$$H_2 + 2Pt \rightarrow 2Pt\text{-}H \quad (1.4)$$

$$2Pt\text{-}H \rightarrow 2Pt + 2H^+ + 2e^- \quad (1.5)$$

At the cathode, oxygen molecules come into contact with a platinum catalyst on the electrode surface. The oxygen molecules break apart bonding to the platinum surface forming weak Pt-O bonds (equation 1.6). Each oxygen atom then leaves the platinum catalyst site, combining with two electrons and two hydrogen ions (from the anode) to form a molecule of water (equation 1.7).

$$O_2 + 2Pt \rightarrow 2Pt\text{-}O \quad (1.6)$$

$$2Pt\text{-}O + 4H^+ + 4e^- \rightarrow 2Pt + 2H_2O \quad (1.7)$$

After the redox reaction is completed, the platinum catalysts on the anode and cathode are again free for the next reaction. Pt based catalysts are the best catalysts for these reactions because Pt is sufficiently reactive in binding H and O intermediates, and also capable of effectively releasing the intermediate to form the final products.

1.2.3.3 Membrane electrode assembly (MEA)

The combination of anode, membrane and cathode is referred to as the membrane electrode assembly (MEA) shown in Figure 1.4. PEM fuel cells are made from a number of MEAs arranged in series, known as a stack. The platinum catalysts are coated on to teflon carbon paper, the catalysts facing the polymer membrane. Gases (oxygen and hydrogen) in the field flow plates pass through the teflon carbon paper to the Pt catalysts where the two reactions take place at the anode and cathode. A MEA can produce about 1 volt of electric energy.

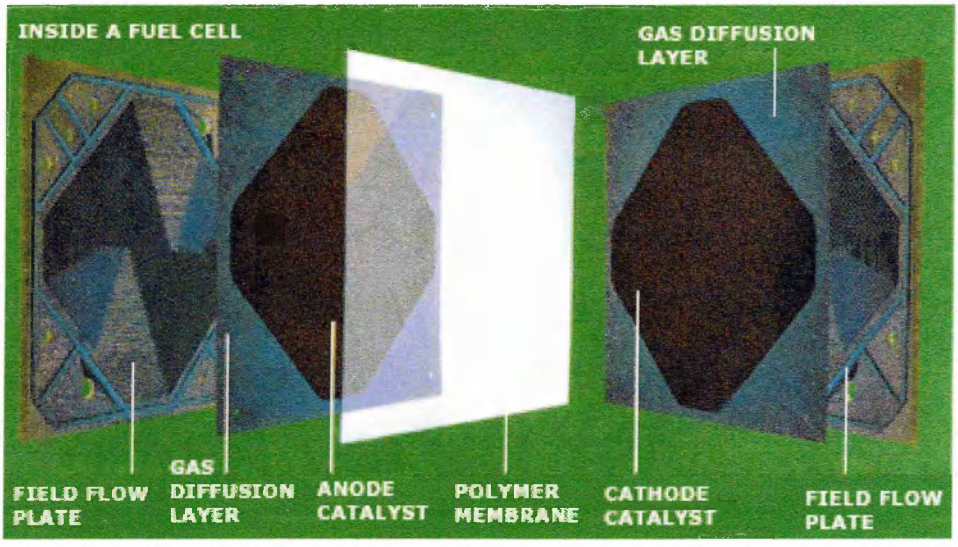

Figure 1.4 Membrane electrode assembly (MEA) in PEM fuel cells (courtesy: JMTC)

1.2.4 The performance of PEM fuel cells

The aim of this section is to provide the thermodynamic and kinetic analyses of PEM fuel cells to understand the maximum available and practical voltage of PEM fuel cells. Such an understanding is helpful for the design of PEM fuel cells.

1.2.4.1 Thermodynamics of PEM fuel cells

The overall cell reaction of PEM fuel cells using hydrogen/oxygen is:

$$H_2(g) + \tfrac{1}{2} O_2(g) \rightarrow H_2O(l) \quad (1.8)$$

The maximum cell voltage at a specific temperature and pressure can be obtained by the change in Gibbs free energy (ΔG°) of the electrochemical reaction (equation 1.9),

$$\Delta G^\circ = -nE^\circ F \quad (1.9)$$

where F is the value of the faraday, 96,487 coulombs, and n is the number of electrons transferred in the course of the reaction to which ΔG° relates. E° is the ideal potential of the cell.

At a constant pressure of 1 atmosphere, the Gibbs free energy change in the fuel cell process (per mole of H_2) is calculated from the reaction temperature (T), and from changes in the reaction enthalpy (ΔH) and entropy (ΔS)

$$\Delta G = \Delta H - T\Delta S \quad (1.10)$$

For standard state conditions (25 °C or 298 K and 1 atm),

$$\Delta G^\circ = \Delta H^\circ - T\Delta S^\circ = -285{,}800 - (298) \times (-163.2)$$

$$= -237\,200 \text{ J}$$

$$E^\circ = -\frac{\Delta G}{nF} = -\frac{-237200}{2 \times 96487}$$

$$= 1.23 \text{ V}$$

As temperature rises from room temperature to that of an operating PEM fuel cell (80°C or 353 K), the values of ΔH and ΔS change only slightly, but T changes by 55 K.

$$\Delta G = -285\,800 - (353) \times (-163.2)$$

$$= -228\,200 \text{ J mol}^{-1}$$

$$E = -\frac{\Delta G}{nF} = -\frac{-228200}{2 \times 96487}$$

$$= 1.18 \text{ V}$$

The thermal efficiency of an energy conversion device is defined as the amount of useful energy produced relative to the change in stored chemical energy (commonly referred to as thermal energy) that occurs when a fuel is reacted with an oxidant. According to the second law of thermodynamics, the maximum work, W_{max}, obtainable from an ideally reversible heat engine, working by the natural flow of heat from a higher temperature T_1 to a lower temperature T_2, depends on the temperatures between which heat is transferred:

$$W_{max} = \frac{T_1 - T_2}{T_1} \times q_1 = \eta_c \times q_1 \tag{1.11}$$

$$\eta_c = \frac{T_1 - T_2}{T_1} = \frac{W_{max}}{q_1} \tag{1.12}$$

where q_1 is the heat absorbed at the higher temperature, and η_c is the so-called Carnot factor. If the heat supplied to the engine at the higher temperature comes from a chemical reaction (for example, the combustion of a fuel), q_1 can be identified with the heat liberated by the reaction proceeding at constant pressure ($-\Delta H$). In practice, the optimum efficiency of steam turbine is 45%; less for diesel (30%) and petrol (20%) driven generators[6, 7].

The theoretical efficiencies of PEM fuel cells and heat engines are different. Because PEM fuel cells convert chemical energy directly to electrical energy, this process does not involve conversion of heat to mechanical energy. The PEM fuel cell is not limited by temperature as is the heat engine [8]. Therefore, PEM fuel cell efficiencies can exceed the Carnot limit.

In the ideal case of PEM fuel cell, the change in Gibbs free energy (ΔG) of the electrochemical reaction is available as useful electric energy at the temperature of the conversion. The ideal efficiency of PEM fuel cell is

$$\eta_c = \frac{W_{max}}{q_1} = \frac{\Delta G}{\Delta H} \tag{1.13}$$

For standard state conditions (25 °C or 298 K and 1 atm),

$$\eta_c = \frac{W_{max}}{q_1} = \frac{\Delta G°}{\Delta H°} = 237\ 200/285\ 800 = 0.83$$

For an operating PEM fuel cell condition (80 °C or 353 K),

$$\eta_c = \frac{W_{max}}{q_1} = \frac{\Delta G}{\Delta H} = 228\ 200/285\ 800 = 0.80$$

The efficiency of an actual PEM fuel cell can be expressed in terms of the ratio of the operating cell voltage to the ideal cell voltage. The actual cell voltage is less than the ideal cell voltage because of the losses associated with cell polarizations and the internal resistance loss. PEM fuel cells should, from the thermodynamic point of view, be operated at the lowest possible temperature. On the other hand, however, reaction velocity, and hence the current density available at a given terminal voltage, increases exponentially with temperature. The influence of kinetics on the efficiency of PEM fuel cells is discussed in section 1.2.4.2.

1.2.4.2 Kinetics of PEM fuel cells

If the PEM fuel cell was perfect at transferring chemical energy into electrical energy, the ideal cell voltage (thermodynamic reversible cell potential, $E°$ of H_2/O_2 PEM fuel cell could be, at 25 °C and 1 atmosphere, 1.23 V. As the PEM fuel cell heats up to operating temperature, around 80 °C the ideal cell voltage (rest-potential, E) drops to about 1.18 V. However there are many limiting factors that reduce the fuel cell voltage further. Figure 1.5 shows various potential vs current (or current density) of PEM fuel cell. The voltage out of the cell is a good measure of electrical efficiency; the lower the voltage, the lower the electrical efficiency and the more chemical energy is released in the formation of water and transferred into heat.

The primary losses that contribute to a reduction in cell voltage are[1, 9]:

(1) *Ohmic polarization:*

Ohmic losses (η_Ω) are a result of the internal resistances (R) of the various components of the fuel cell. This includes the resistance of the electrode materials, the resistance of the electrolyte membrane and the resistance of the various interconnections. The potential drop in PEM fuel cell increases proportionally to the current (I),

$$\eta_\Omega = I \times R \tag{1.14}$$

where I is the current flowing through the cell, and R is the total internal resistance.

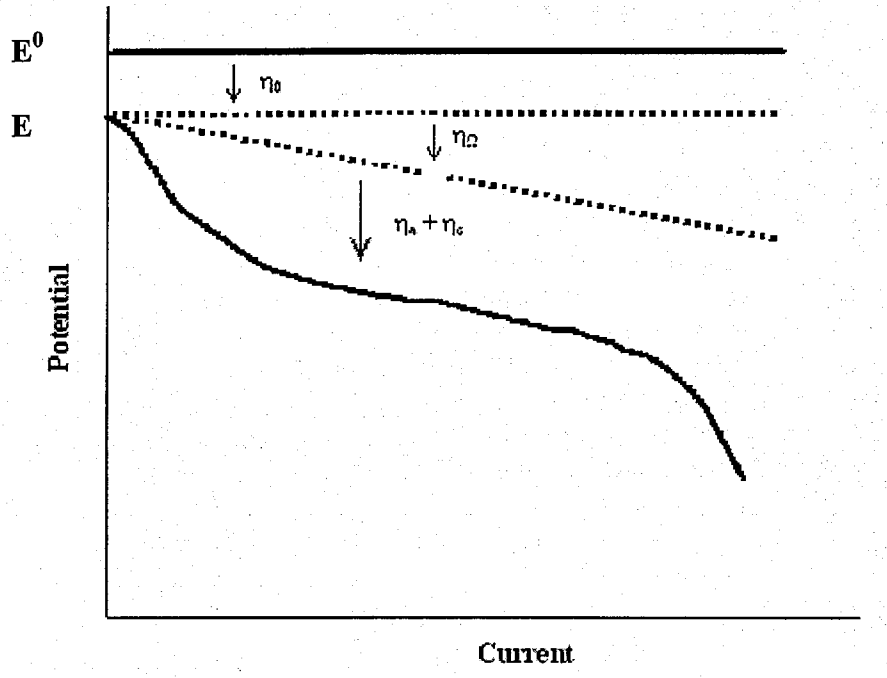

Figure 1.5 Current–voltage curves for a fuel cell

(2) *Concentration Polarization:*

Concentration Polarization is due to the concentration change at the electrode by rate-limiting mass transfer or hindrance to preliminary reaction. As a reactant is consumed at the electrode by electrochemical reaction, there is a loss of potential due to the inability of the surrounding material to maintain the initial concentration of the bulk fluid. At

practical current densities, slow transport of reactants/products to/from the electrochemical reaction site is a major contributor to concentration polarization:

$$\eta_c = \frac{RT}{nF} \ln\left(1 - \frac{I}{I_L}\right) \tag{1.15}$$

where I_L is the limiting current. The limiting current is a measure of the maximum rate at which a reactant can be supplied to an electrode, and surface concentration is zero.

(3) *Activation Polarization:*

Activation polarization (η_a) arises from charge-transfer and is present when the rate of an electrochemical reaction at an electrode surface is controlled by sluggish electrode kinetics. In other words, activation polarization is directly related to the rates of electrochemical reactions. It is customary to express the voltage drop due to activation polarization by a semi-empirical equation, called the Tafel equation [7]. The equation for activation polarization is shown by equation (1.16):

$$\eta_a = \frac{RT}{\alpha nF} \ln\left(\frac{i}{i_0}\right) \tag{1.16}$$

where α is the electron transfer coefficient of the reaction at the electrode being addressed, n is the number of electrons transferred in the course of the reaction, and i_0 is the exchange current density. Tafel plots provide a visual understanding of the activation polarization of a PEM fuel cell. They are used to measure the exchange current density (given by the extrapolated intercept at $\eta_a = 0$ which is a measure of the maximum current that can be extracted at negligible polarization [8]) and the transfer coefficient (from the slope).The usual form of the Tafel equation that can be easily expressed by a Tafel Plot is

$$\eta_a = a + b \log i \tag{1.17}$$

where $a = (-2.3RT/\alpha nF)\log i_0$ and $b = 2.3RT/\alpha nF$. The term b is called the Tafel slope, and is obtained from the slope of a plot of η_a as a function of log$i$. The Tafel slope for an electrochemical reaction is about 100 mV (log current density) at room temperature. Thus, a ten-fold increase in current density causes a 100 mV increase in the activation

polarization. Conversely, if the Tafel slope is only 50 mV/decade, then the same increase in current density produces a 50 mV increase in activation polarization. Clearly, there exists a strong incentive to develop electrocatalysts that yield a lower Tafel slope for electrochemical reactions.

1.2.5 The applications of PEM fuel cells

The characteristics summarized in Section 1.2.1 of the five fuel cell types respond to a variety of application needs. The major applications for fuel cells are as stationary electric power plants; as motive power for vehicles; and as on-board electric power for space vehicles, portable power system or other closed environments.

The major application of PEM fuel cells is in transportation. A major drive for this application is the need for clean, efficient vehicles that can operate on conventional fuels (gasoline, diesel), as well as renewable and alternative fuels (hydrogen, methanol, ethanol, natural gas, and other hydrocarbons).

All of the cars driven on the road are currently powered by internal combustion engine (ICE). These engines run on noisy, high temperature explosions resulting from the release of chemical energy by burning fuel with oxygen. Internal combustion engines are less efficient because they include the conversion of thermal to mechanical energy, which is limited by the Carnot Cycle.

If cars are powered by PEM fuel cells, under consideration by vehicle manufacturers around the world as an alternative to the internal combustion engine, there will be no combustion involved. PEM fuel cells can operate at relatively low temperatures (~ 80 °C), have high power density, and vary their output quickly to meet shifts in power demand, such as in automobiles, where quick start-up is required. According to US Department of Energy, PEM fuel cells are the primary candidates for

light-duty vehicles. In PEM fuel cells, hydrogen and oxygen undergo a relatively cool, electrochemical reaction that directly produces electrical energy and water. So, these cars powered by PEM fuel cells have virtually no pollutant emissions of sulphur dioxide, oxides of nitrogen, carbon monoxide or particulates, the primary pollutants of the internal combustion engine. The efficiency of a PEM fuel cell engine is about a factor of two higher than that of an internal combustion engine.

1.2.6 Obstacles to using PEM fuel cells

There are many benefits to using cars powered by PEM fuel cells. For example, they are efficient (double that of internal combustion engine); they are clean (if hydrogen is the fuel, there are no pollutant emissions from a PEM fuel cell itself, only the production of pure water); and they are quiet (no moving parts, so no engine noise). However, there are three main obstacles to the success of PEM fuel cells and its application:

- Both the membranes and the Pt catalysts are expensive,
- Pt catalysts have too high a sensitivity to H_2 fuel impurities (CO),
- low performance of the oxygen reduction reaction at the cathode.

To overcome these obstacles research is ongoing to:

- to develop new and cheaper polymer electrolyte membranes,
- decrease the loading of Pt catalyst, by increasing the performance of the electrocatalysts,
- to improve the tolerance of the Pt catalysts to the presence of CO at the anode
- to develop catalysts which help "clean-up" the fuel stream before the H_2 is provided to PEM fuel cells,
- to increase performance of the oxygen reduction reaction by improving the Pt catalyst.

It is this final area which is the subject of the research presented in this thesis. One method of improving the properties of the Pt electrocatalyst is to modify it with a second (or more) metal or metal oxide.

1.3 The oxygen reduction electrocatalysts of H_2/O_2 PEMFC

The oxygen reduction reaction (ORR) in H_2/O_2 PEM fuel cells has been widely studied because of the application of oxygen cathodes in electrochemical energy conversion systems [10]. The oxygen reduction reaction takes place at the cathode:

$$O_2 + 4H^+ + 4e^- \rightarrow 2H_2O \qquad (1.2)$$

This reaction rate is very slow, so a catalyst is used to increase the rate of the oxygen reduction reaction. Noble metals such as Pt, Pd, and Ru and their alloys have been found to be the catalysts of choice for oxygen reduction [11-20]. However, even the best of these catalysts, Pt, is at least 10^6 times less active for oxygen reduction than for H_2 oxidation at the anode. This leads to high overpotentials and is the major catalytic limitation to PEM fuel cell efficiency [16].

Recently there have been various reports on the development of the Pt catalyst for oxygen reduction reaction [11-21]. To obtain the optimum utilization of Pt, it is generally dispersed as small particles on a conductive support such as high-surface-area carbon powders [22, 23]. Carbon supported Pt has proven to be the most active and durable catalyst for oxygen reduction. However, at reasonable current densities, Pt still shows overpotentials of 400 mV from the equilibrium reversible potentials (1.2 V at 80 °C). Therefore, great efforts have been made to identify and develop superior Pt catalysts for oxygen reduction. Many studies have reported that noble metal alloys, in particular, platinum alloy catalysts have been found to display increased catalytic activity for oxygen reduction [24-26]. These nano-dispersed particles of Pt alloys were found to show improved intrinsic activity and stability over pure Pt.

The metals used to modify the Pt/C include Fe, Ga, Ti, Cr, Mn, V, Ni, Co, Ru, and Ni [27-34]. Hwang *et al.* prepared a PtFe/C catalyst using impregnation, and showed that the mass activity of oxygen reduction became a maximum at particle sizes around 3.5 nm [32]. Various carbon-supported platinum-based binary and ternary alloy catalysts were synthesized using impregnation techniques with the metal salts ($Co(NO_3)_2$, $Ni(NO_3)_2$, or $Cr(NO_3)_2$), and a Pt/C catalyst [27]. These binary and ternary alloy catalysts, after heat-treatment at 900 °C, exhibited superior activity for the oxygen-reduction reaction, relative to the Pt/C catalyst [27]. Paulus *et al.* used an arc melting method to prepare bulk PtNi or PtCo alloy electrocatalysts [35]. These bulk alloy electrocatalysts also have an enhanced activity for the oxygen-reduction reaction by about a factor of two compared with the identically prepared Pt electrocatalyst.

The techniques reported for the preparation of carbon supported Pt-based bimetallic or alloy catalysts include the traditional methods, such as impregnation [19, 32], precipitation[32], and more novel methods, such as ball milling [30, 36] and surface organometallic chemistry (SOMC) [37, 38].

The simplest method of preparing a carbon supported Pt-based bimetallic or alloy catalysts is impregnation. In the method of successive impregnation, a solution of a second metal salt is prepared and mixed with a carbon supported Pt catalyst. Alternatively, a co-impregnation technique can be used where solutions of the two metal salts are mixed simultaneously with the support. In both cases, the resulting slurry is dried to remove the solvent and then usually heat-treated and/or reduced to decompose the salt(s). Formation of the alloy can be induced by high-temperature heat treatment under either inert or reducing gas streams. This impregnation method has the disadvantage of particle sintering due to the high temperature required to form the alloy, resulting in a lower catalyst active area [39]. Another disadvantage of this method is that

the two metals may deposit at separate sites on the carbon, rather than in close association.

The main method used for the preparation of Pt-based bimetallic or alloy catalysts is co-precipitation. Two solutions of Pt and second metal salts are prepared and mixed with the carbon support. The co-deposition of the Pt and second metal salts out of solution is carried out using changes in pH or the addition of reducing agents. This method has the advantage of forming bimetallic structures at low temperature and hence, at high dispersion. However, this approach is generally restricted to components with similar precipitation chemistry and/or ease of reduction to metals [39]. Again the two metals may also not be deposited together but at separate sites on the support. This method rarely leads to homogeneous compositions due to the differences in solubility of the components. Hence, the traditional methods for preparing bimetallic catalysts are not always successful in creating bimetallic particles, instead randomly distributed particles of both metals are found on the surface of the support.

An alternative method of depositing a second metal on carbon supported Pt catalyst is the use of the surface organometallic chemistry (SOMC) method. This method utilizes a selective reaction between hydrogen adsorbed on the Pt surface and a solution of an organometallic precursor of the second metal [37, 40-42].

1.4 Surface organometallic chemistry (SOMC)

Surface organometallic chemistry (SOMC) is a relatively new field of chemistry that deals with the reactivity of organometallic compounds with the surface of a monometallic catalyst [38, 43-46]. There has been increasing interest in the application of SOMC to the preparation of bimetallic catalysts [47, 48]. Surface science has been very successful in identifying some of the concepts relevant to the bimetallic catalysts,

for example, formation of surface alloys, phase segregation at the surface, decoration of crystallographic sites by adatoms, site sensitive chemisorption and changes in electronic properties. However, careful studies of the reactivity of organometallic complexes towards metallic surfaces have revealed new aspects of the chemistry of bimetallic catalysts.

Unlike conventional catalyst preparation techniques, SOMC techniques can control the relative location of the two components by utilizing a selective surface reaction between an organometallic compound of the second metal and the surface of the first metal. In this approach, an organometallic precursor is reacted in a solvent with carbon supported Pt catalyst that has a layer of adsorbed H_2. This approach has the advantage that the precursor only reacts with adsorbed hydride on the Pt surface and therefore is only deposited on to the active catalyst sites. The role of the two metals in bimetallic catalysts can be attributed to either a geometric effect or an electronic effect of the second metal on the first one. Bimetallic catalysts have to be perfectly homogeneous and precise in composition on an atomic scale. SOMC is one possible way to achieve such homogeneity, because high temperature treatments can usually be avoided. The strategy of SOMC is to utilize the "controlled" surface reaction, in which the transformation of monometallic materials into homogeneous bimetallic ones is understood in terms of molecular processes. Due to the above advantages, SOMC has been used to prepare bimetallic catalysts for fuel cells [40, 41].

Reactions between the organometallic compounds MR_n (M is the second metal, R_n is CH_3, C_4H_9, C_5H_5) and the surfaces of reduced, supported metals M' (M' is the first metal) may occur in one of several ways:

(a) The organometallic complex can react under an inert atmosphere with the surface of a metal on which hydrogen has been preadsorbed. This approach was used originally by Margitfalvi [49].

(b) The organometallic complex can react with the metallic surface in the presence of a partial pressure of hydrogen under either static or dynamic conditions. This is the approach used in this work.

It is believed that reducing the monometallic catalyst (Pt) produces hydrogen sites adsorbed on the parent metal (Pt-H) [50]. Reaction of the organometallic species (MR_n) is believed to proceed preferentially with the hydrogen preadsorbed on the first metal to produce an organometallic (Pt_x-$MR_{(n-x)}$) species physisorbed on the surface:

$$x\text{Pt—H} + MR_n \rightarrow Pt_x\text{—}MR_{(n-x)} + x\text{RH} \qquad (1.18)$$

This may possibly cover a number of surface metal atoms [51]. Further reaction, in the presence of hydrogen, results in the stepwise hydrogenolysis of the remaining alkyl groups of the second metal, yielding a metallic particle with the two metals (Pt_x–M) in intimate contact (Equation 1.19), and the alkane. The PtM species is thought to exist as naked M 'ad-atoms' localized on specific crystal faces on the metallic particle [45, 52-54].

$$Pt_x\text{—}MR_{(n-x)} + \tfrac{1}{2}(n-x)H_2 \rightarrow Pt_x\text{—}M + (n-x)\text{RH} \qquad (1.19)$$

These can then be incorporated into the surface of the particle by heating, to form a surface alloy [44, 54].

In principle, by controlling the amount of the second metal introduced in the form of the organometallic species, it is possible to deposit a known amount of the second metal onto the surface of the first metal, Pt. Assuming that all of the second metal introduced is deposited on Pt and that the surface dispersion of Pt is known, it is therefore possible to control the coverage of the surface sites of the Pt catalyst by the

second metal. This predicted coverage of Pt by the second metal can be described in terms of monolayer coverage of the second metal. Theoretical maximum coverage would occur when all the surface sites of Pt are covered by the second metal; that is, when a complete monolayer of the second metal is present on the surface of the first metal.

In our work a metallocene, $M(C_5H_5)_2$, (where M is Fe, Ni, Cr or Co) as the organometallic precursor, is reacted with the monometallic Pt/C catalyst.

1.5 References

1. W. Vielstich and D.J.G. Ives, Fuel Cell, Wiley-Interscience, 1965.
2. W.R. Grove, Philos. Mag., 1839. **14**: p. 127.
3. B. Cook, An Introduction To Fuel Cells and Hydrogen Technology, Heliocentris, 2001.
4. W. Hafele, Energy in a Finite World: A Global Systems Analysis, Ballinger, Toronto, 1981.
5. J. Goldemberg, T.B. Johansson, A.K.N. Reddy and R.H. Williams, Energy for a Sustainable World, Wiley, New York, 1988.
6. G.M. Barrow, Physical Chemistry, New York: McGraw-Hill, 1979.
7. H.A. Liebhafsky and E.J. Cairns Jr., Fuel Cells and Batteries, 1965.
8. A.J. Appleby and F.R. Foulkes, Fuel Cell Handbook, Van Nostrand Reinhold, New York, 1989.
9. A.J. Bard and L.R. Faulkner, Electrochemical Methods, John Wiley, 1980.
10. K. Kinoshita, Electrochemical Oxygen Technology, Wiley, New York, 1992.
11. V. Jalan and E.J. Taylor, J. Electrochem. Soc., 1983. **130**: p. 2299.
12. J.T. Glass, G.L. Cathen and G.E. Stoner, J. Electrochem. Soc., 1987. **134**: p. 58.
13. M.T. Paffet, G.J. Beery and S. Gottesfeld, J. Electrochem. Soc., 1998. **135**: p. 1431.
14. B.C. Beard and P.N. Ross Jr., J. Electrochem. Soc., 1990. **137**: p. 3368.
15. A.J. Appleby, Energy, 1986. **11**: p. 13.
16. D. Thompsett, *Catalysts for the Proton Exchange Membrane Fuel Cell.* Fuel Cell Technology Handbook, CRC Press, 2003.
17. V. M. Jalan, US Patent 4192907, 1980.
18. T. Itoh, US Patent 5024905, 1991.
19. T. Itoh, US Patent 5096866, 1992.

20. R. Tsurumi, US Patent 4985386, 1991.

21. P. Stonehart, US Patent 5593934, 1997.

22. L. Bregoli, Electrochim. Acta, 1978. **23**: p. 23.

23. J. Bett and J. Lundquist, Electrochim. Acta, 1973. **18**: p. 343.

24. D.A.Landsman and F.J.Luczak, U.S. Patent 4,316,944, 1982.

25. F.J. Luczak and D.A. Landsman, US Patent 4, 880 711, 1989.

26. S. Mukerjee and S. Srinivasan, J. Electroanal. Chem., 1993. **201**: p. 357.

27. M. Neergat, A.K. Shukla and K.S. Gandhi, J. Appl. Electrochem., 2001. **31**: p. 373.

28. A.S. Arico, P.Creti, E.Modica, G.Monforte, V.Baglio and V.Antonucci, Electrochim. Acta, 2000. **45**: p. 4319.

29. M.K. Min, J. Cho, K. Cho and H. Kim, Electrochimica Acta, 2000. **45**: p. 4211.

30. M.C. Denis and G. Lalande, J. Appl. Electrochemistry, 1999. **29**: p. 951.

31. Y. Takasu, Y. Fujii, K. Yasuda, Y. Iwanaga and Y. Matsuda, Electrochim. Acta, 1989. **34**: p. 452.

32. J.T. Hwang and J.S. Chung, Electrochim. Acta, 1993. **38**: p. 18.

33. T. Toda, H. Igarashi, H. Uchida and M. Watanabe, J. Electrochem. Soc., 1999. **146**: p. 3750.

34. E. Antolini, R.R. Passos and E.A.Ticianelli, Electrochim. Acta, 2002. **48**: p. 263.

35. U.A.Paulus, A. Wokaun, G.G. Scherer, T.J. Schmidt, V. Stamenkovic, N.M. Markovic and P.N. Ross, Electrochim. Acta, 2002. **47**: p. 3787.

36. T. Benameur and B. Rezgui, Materials Science Forum, 1997. **235**: p. 917.

37. E. M. Crabb and M.K. Ravikumar, Electrochim. Acta, 2001. **46**: p. 1033.

38. S. T. Srinivas and P. K. Rao, J. Catal., 1998. **179**: p. 1.

39. David Thompsett, *Catalysts for the Proton Exchange Membrane Fuel Cell.* Fuel Cell Technology Handbook, CRC Press, 2003.

40. E. M. Crabb, R. Marshall and D. Thompsett, J. Electrochem. Soc., 2000. **147**: p. 4440.

41. E.M. Crabb, M.K. Ravikumar, Y.Qian, A.E. Russell, S. Maniguet, J. Yao, D. Thompsett, M. Hurford and S.C. Ball, Electrochemical and Solid-State Letters, 2002. **5**: p. 5.

42. E.M. Crabb and Robert Marshall, Appl. Catal. A: Gen., 2001. **217**: p. 41.

43. B. Didillon, C. Houtman and T. Shay, J. Am. Chem. Soc., 1993. **115**: p. 9380.

44. F. Humblot, J.P.Candy, F. Le Peltier and B. Didillon, J. Catal., 1998. **179**: p. 459.

45. J. P. Candy, B. Didillon and E.L. Smith, J. Mol. Catal., 1994. **86**: p. 79.

46. B. Coq, A. Bittar and R. Dutartre, J. Catal, 1991. **128**: p. 275.

47. J. Margitfalvi and S. Szabo, Catalytic Dehydrogenation, Elsevier, Amsterdam, 1986. **27**: p. 373.

48. Y.A. Ryndin and Y. I. Yermakov, Surface Organometallic Chemistry: Molecular Approaches to Surface Catalysis, 1988: p. 127.

49. J. Margitfalvi, 8th International Congress on Catalysts vol. IV (Berlin, 1984): p. 903.

50. J. Margitfalvi, H.P. Jalett, E. Talas, A.Baiker and H.U.Blaser, Catal. Lett., 1991. **10**: p. 325.

51. O.A. Ferretti, C. Lucas, J.P. Candy, J.M. Basset and F. Le Peltier, J. Mol. Cat. A: Chem, 1995. **103**: p. 125.

52. F.Lefebvre, J. P. Candy, C. C. Santini and J.M. Basset, Topics in Catalysis, 1997. **4**: p. 211.

53. B. Coq, A. Goursot, T. Tazi, F. Figueras and D.R. Salahub, J. Am. Chem. Soc., 1991. **113**: p. 1485.

54. F. Humblot, J.P. Candy, F. Le Peltier, J. Corker, O. Clause, F. Bayard and J.M. Basset, J. Am. Chem. Soc., 1998. **120**: p. 137.

Chapter 2 Experimental techniques

This chapter gives information on the theory and experimental procedures of the experimental techniques used in this work. This will include the chemical reagents and materials used (section 2.1), the Surface Organometallic Chemistry (SOMC) preparation method (section 2.2), the techniques to characterise the catalyst surface properties (section 2.3) and the electrochemical methods of testing the catalysts (section 2.4).

2.1 Reagents

Table 2.1 lists the chemicals and materials used in this work with their suppliers.

Table 2.1 Chemical reagents and materials

Chemical reagents /materials	Supplier
Black Carbon	Johnson Matthey Technology Centre
20 % Pt/C (XC72R)	Johnson Matthey Technology Centre
Ferrocene	Aldrich
Bis(cyclopentadienyl)nickel	Aldrich
Bis(cyclopentadienyl)cobalt	Aldrich
Bis(cyclopentadienyl)chromium	Aldrich
Carbon Paper	Stackpole
Sulphuric acid	BDH AnalaR
Nitric Acid	Prolabo
Hydrochloric acid	BDH AnalaR
Nickel nitrate	BDH AnalaR
Cobalt(II) chloride	Aldrich
H_2	Air Products
N_2	Air Products
O_2	Air Products
Nafion solution	Johnson Matthey Technology Centre
Teflon suspension	Johnson Matthey Technology Centre
Heptane	Aldrich
2-propanol	Aldrich

2.2 Preparation of PtM/C bimetallic catalysts using SOMC

PtM/C bimetallic catalysts have been typically prepared by either impregnation or by precipitation reactions. However, these traditional methods often lead to a multicomponent system including Pt-M bimetallic particles and two kinds of monometallic particles (Pt and M) on the carbon support. Surface organometallic chemistry is one of the best methods to prepare PtM/C bimetallic catalysts [1-3]. The technique involves the modification of a monometallic catalyst (Pt/C) by addition of a second metal (M), which is introduced in the form of an organometallic species. This species is believed to react preferentially with hydrogen preadsorbed on the surface of the first metal, thus forming particles, which contain the two metals (Pt-M) in intimate contact. In our work $M(C_5H_5)_2$ (M = Fe, Ni, Co and Cr) has been used to deposit a second metal M on the Pt/C catalyst. In principle the SOMC technique allows greater control of the two metals on PtM/C bimetallic catalysts than the traditional techniques of bimetallic catalyst preparation.

2.2.1 Apparatus

An apparatus was constructed in the laboratory for the preparation of the bimetallic catalysts using SOMC (Figure 2.1). It was made from a series of interconnected lengths of polytetrafluoroethylene (PTFE) tubing (od $1/8^{th}$ inch). A specially made pyrex reactor and saturator vessel were used in the apparatus. The reactor was fitted with a condenser to minimize loss of the solvent by vaporization. Three way valves (Hoke) and two taps were included in the apparatus to allow the system to be purged of air. The apparatus was designed to allow the reduction of the Pt/C monometallic catalyst with H_2, the transfer of a solution of the precursor from the saturator vessel into the reactor vessel, and the reaction of the precursor with the reduced monometallic catalyst to prepare PtM/C bimetallic catalysts without exposure to air.

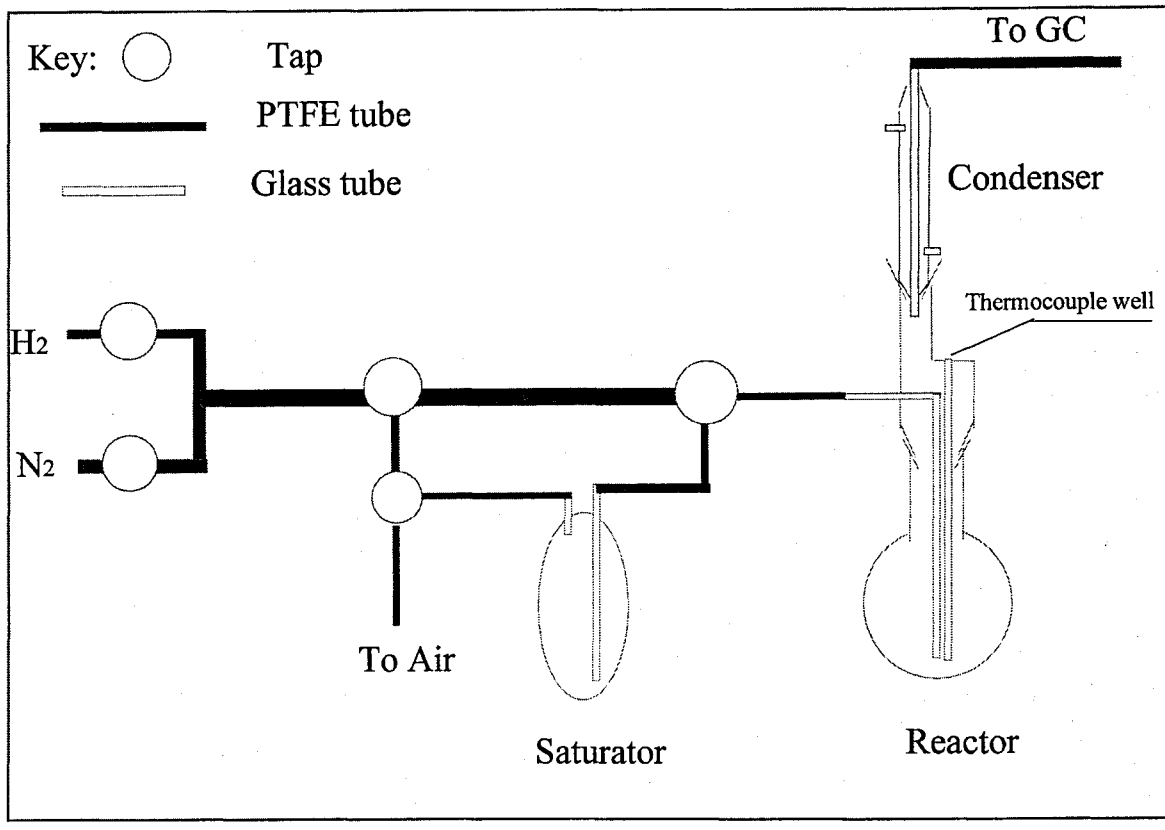

Figure 2.1 SOMC apparatus for the preparation of bimetallic catalyst

The reactor was heated using a heating mantle. Sampling of the effluent gases from the reactor was achieved by feeding a length of PTFE tubing from the exit of the reactor into a gas chromatograph fitted with a Porapak T on chrompac 80/100 mesh column (od $1/8^{th}$ inch, 8m). The GC used was a Perkin-Elmer 8410 Gas chromatograph fitted with a flame ionization detector (FID). The column was operated at 100°C.

2.2.2 Preparation procedures for PtM/C bimetallic catalysts

2.2.2.1 Preparation of the standard catalysts (xPtM/C)

The carbon support (Vulcan XC72R) and the carbon-supported platinum (20% Pt/C) (XC72R/JMTC 96/12) were supplied by Johnson Matthey Technology Centre (JMTC) and details of the preparation of the Pt/C catalyst are given elsewhere [4]. In brief, the preparation of the Pt/C catalyst involved the hydrolysis of the platinum salt, chloroplatinic acid (H_2PtCl_6) by sodium hydrogen carbonate in the presence of the

carbon support at 100 °C in demineralised water. The resulting catalyst was reduced in-situ by aqueous formaldehyde at 90 °C, filtered, washed free of sodium and chloride ions and dried at 100 °C in air.

A known mass of the 20 wt% Pt/C catalyst was loaded into the reactor vessel. The reactor was attached to the apparatus and mounted in a heating mantle, then purged with nitrogen for approximately 1 hour to remove air from the system. The Pt/C catalyst was then reduced in the reactor under flowing hydrogen (flow 60-100 ml min^{-1}) heating to a temperature of 200 °C (heating rate of 1 °C min^{-1}). This temperature was maintained for 3 hours and then the catalyst was cooled to room temperature under H_2. The required amount of organometallic precursor ($M(C_5H_5)_2$) (Table 2.2) was calculated using the platinum metal surface area obtained experimentally by chemisorption of hydrogen on Pt/C. The organometallics were dissolved in *n*-heptane (ratio 15 ml solvent to 1 g catalyst), and added to the saturator vessel. After purging the saturator with nitrogen gas for 10-15 minutes to remove air from the system, the contents of the saturator were transferred into the reactor containing the reduced Pt/C catalyst by reversing the direction of the gas-flow. Hydrogen gas was then passed through the reactor. The reaction was monitored by analyzing for cyclopentane in the gas stream leaving the reactor using GC and GC-MS. After 12 hours at room temperature, the reaction was continued, heating at 90 °C for a further 8-12 hours. During the reaction further *n*-heptane was added to the reactor vessel by adding *n*-heptane to the saturator vessel and purging the system in the same manner as described above and then pumping the *n*-heptane into the reactor.

After the reaction, the system was flushed with nitrogen for 20-30 minutes. The contents of the reactor were discharged, filtered, washed with *n*-heptane to remove any unreacted organometallics ($M(C_5H_5)_2$), and filtered again. The filtrates were transferred into a small volumetric flask, and any unreacted organometallics were determined using

UV-visible spectrometry. The catalyst was then placed on a watch glass, and dried in a fume cupboard in air.

To prepare the reduced catalyst, the dried catalyst was transferred into the reactor and nitrogen gas was passed for 30 minutes to remove air from the system. The contents of the reactor were then reduced in flowing hydrogen at 200 °C for 3 hours as in the pre-reduction step, and finally flushed with nitrogen for 20-30 minutes to prevent combustion before opening to the atmosphere. The catalyst samples were stored in a sample bottle.

A series of bimetallic catalysts *x*PtM/C were prepared, where M = Fe, Ni, Cr and Co and x is 0.25 – 1.0; the number (x) represents the *theoretical* surface coverage of surface Pt sites by M expressed in monolayer equivalents. Four blank reactions between the carbon support and $Fe(C_5H_5)_2$, $Ni(C_5H_5)_2$, $Cr(C_5H_5)_2$ and $Co(C_5H_5)_2$ were also performed using the same procedure and will be given the notation (Fe/C, Ni/C, Cr/C and Co/C).

Table 2.2 List of PtM/C bimetallic catalysts prepared using SOMC

Catalysts *	**Support - Pt/C or Carbon**	**$M(C_5H_5)_2$**
*x*PtFe/C	20% Pt/C	$Fe(C_5H_5)_2$
*x*PtNi/C	20% Pt/C	$Ni(C_5H_5)_2$
*x*PtCo/C	20% Pt/C	$Co(C_5H_5)_2$
*x*PtCr/C	20% Pt/C	$Cr(C_5H_5)_2$
*x*PtFe/C(*T*)	20% Pt/C	$Fe(C_5H_5)_2$
*x*PtNi/C(*T*)	20% Pt/C	$Ni(C_5H_5)_2$
*x*PtCo/C(*T*)	20% Pt/C	$Co(C_5H_5)_2$
*x*PtCr/C(*T*)	20% Pt/C	$Cr(C_5H_5)_2$
Fe/C	Carbon support	$Fe(C_5H_5)_2$
Ni/C	Carbon support	$Ni(C_5H_5)_2$
Co/C	Carbon support	$Co(C_5H_5)_2$
Cr/C	Carbon support	$Cr(C_5H_5)_2$

*: x = 0.25, 0.5, 0.67, 0.75 and 1.0; T = 400 - 950 °C

2.2.2.2 *Preparation of a heat treated series of catalysts (xPtM/C(T))*

Each catalyst (Pt/C, *x*PtFe/C, *x*PtNi/C, *x*PtCo/C and *x*PtCr/C bimetallic catalysts) was loaded into a silica tube, and heated in 10% hydrogen and 90% nitrogen gas at a ramp rate of 5 °C min^{-1} to the desired temperature (*T*, 400 °C – 950 °C) and held at this temperature for 1 hour. These catalysts are denoted as *x*PtFe/C(*T*), *x*PtNi/C(*T*), *x*PtCo/C(*T*) and *x*PtCr/C(*T*), respectively (Table 2.2).

2.3 Techniques for surface characterisation

The physical and chemical properties of the Pt/C, *x*PtM/C and *x*PtM/C(T) catalysts were characterised using a series of physical techniques. Each technique used in this work is described in this section by an introduction, theory, apparatus (instrumentation) and experimental procedure [5-11] .

2.3.1 Ultraviolet and visible spectroscopy (UV-Vis)

2.3.1.1 *Introduction*

PtM/C bimetallic catalysts were prepared from the Pt/C catalyst using an appropriate metallocene $M(C_5H_5)_2$. Ultraviolet and visible (UV-Visible) absorption spectroscopy was used to determine any unreacted metallocene in the filtrates after the SOMC reaction. UV-Visible absorption spectroscopy is a useful technique to analyse the concentration of unreacted metallocene as these organometallics all have strong absorbances in the ultraviolet and visible region of the electromagnetic spectrum.

2.3.1.2 *Theory*

UV-visible spectroscopy involves the absorption of ultraviolet/visible light by a molecule causing the promotion of an electron from a ground electronic state to an

excited electronic state. Figure 2.2 shows the various kinds of electronic excitation that may occur in organic molecules.

The visible region of the spectrum comprises photon energies of 8.6 - 17.2 kJ mol^{-1}, and the near ultraviolet region, out to 200 nm, extends this energy range to 34.2 kJ mol^{-1}. The energies noted above are sufficient to promote or excite a molecular electron to a higher energy orbital. Of the six transitions shown in Figure 2.2, only the two lowest energy ones ($n \rightarrow \pi^*$ and $\pi \rightarrow \pi^*$) are achieved by the energies available in the 200 to 800 nm spectrum (typical UV-Visible spectra range).

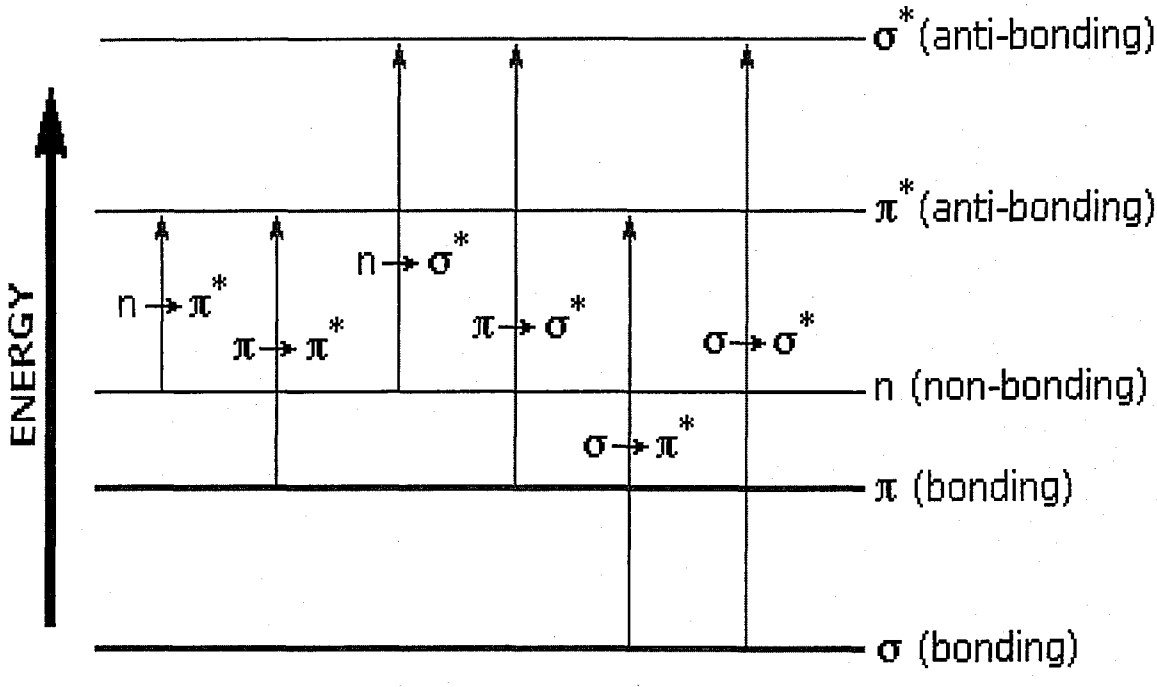

Figure 2.2 Electronic transitions of π, σ, and n electrons

Many molecules absorb ultraviolet or visible light. The absorbance of a solution increases as attenuation of the beam increases. Absorbance is directly proportional to the path length, *b*, and the concentration, *c*, of the absorbing species. A more precise way of reporting intensity of absorption is by use of the Beer-Lambert law:

$$A = \log\left(\frac{I_o}{I}\right) = abc \qquad (2.1)$$

where A is absorbance, a is a constant of proportionality called the absorptivity, I_0 is the intensity of the incident light and I is the intensity of the transmitted light.

2.3.1.3 Apparatus

The diagram of the components of a typical UV-Visible spectrometer is shown in Figure 2.3 [12]. A beam of light from a visible and/or UV light source is separated into its component wavelengths by a prism or diffraction grating. Each monochromatic (single wavelength) beam in turn is split into two equal intensity beams by a half-mirrored device. One beam, the sample beam, passes through a small transparent container (cuvette) containing a solution of the compound being studied in a transparent solvent. The other beam, the reference, passes through an identical cuvette containing only the solvent. The intensities of these light beams are then measured by electronic detectors and compared. The intensity of the reference beam, which should have suffered little or no light absorption, is defined as I_0. The intensity of the sample beam is defined as I. By moving the grating over a short period of time, the spectrometer automatically scans all the component wavelengths in the manner described. The ultraviolet (UV) region scanned is normally from 200 to 400 nm, and the visible portion is from 400 to 800 nm. The intensities of the transmitted light are then compared over the whole wavelength range of the instrument. The spectrum is plotted automatically as a $\log(I_0/I)$ ordinate and x abscissa. The x unit is plotted in nanometers (nm).

2.3.1.4 Experimental procedure

After the preparation of PtM/C bimetallic catalysts, 10 – 50 ml of the filtrates were pipetted into a 50 ml volumetric flask and diluted quantitatively using *n*-heptane if the concentration of the filtrates was too strong. A series of standard solutions of $M(C_5H_5)_2$) (M = Fe. Ni, Cr and Co) were made with 10 - 100 mg in 100 ml of *n*-heptane. The absorbance of these solutions was measured using UV-Vis to give a set of

calibration curves with which to compare the concentrations of the experimental filtrates. The relative peak heights of the standard solution, and of each filtrate were used to determine the amount of $M(C_5H_5)_2$ in the filtrate.

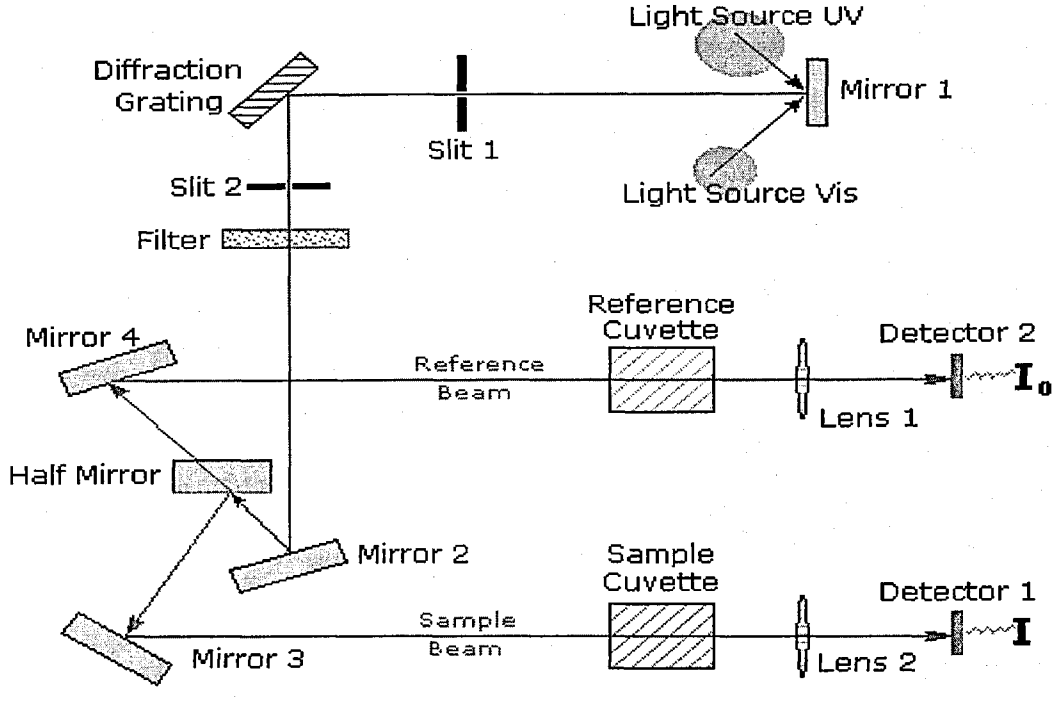

Figure 2.3 Schematic diagram of UV-visible spectrometer

2.3.2 Total surface area and Pt metal dispersion of bimetallic catalysts

2.3.2.1 Introduction

The total surface area of the Pt/C and various PtM/C catalysts was obtained by the BET method using nitrogen gas physical adsorption. The Pt metal dispersion (defined as the ratio of the number of Pt atoms on the surface to the total number of Pt atoms) of the Pt/C and various PtM/C catalysts was determined using the chemical adsorption (often referred to as chemisorption) of hydrogen gas on the surface Pt atoms. The theory of physical adsorption and chemisorption and their applications will be given below.

2.3.2.2 *Theory*

Adsorption

Adsorption describes the process by which atoms or molecules are attached to a solid surface: it is purely a surface effect. Detailed accounts of physical adsorption and chemisorption are given in the literature [13-15]. When a solid is exposed in a closed space to a gas or vapour at some definite pressure, the solid begins to adsorb the gas. The adsorption is brought about by the forces acting between the solid (adsorbent) and the molecules of the gas (adsorbate). These forces are of two main kinds — physical and chemical — and they give rise to physical adsorption and chemisorption, respectively.

Physical adsorption is due to the attraction that exists between a molecule and a surface resulting from weak intermolecular (van der Waals) forces. The strength of the adsorption relates to the physical properties of the adsorbate and depends very little on the chemical nature of the solid. This adsorption is normally not specific and can be used to determine the total surface area of a solid. Tens of thousand of adsorption isotherms have been reported in the literature [14] for a wide variety of solids. An adsorption isotherm is the relationship between the amount of gas adsorbed and the pressure at constant temperature. The five types I to V of the classification of these adsorption isotherms, originally proposed by Brunauer, Deming, Deming and Teller (BET)[14], result from physical adsorption.

Chemisorption between the solid (adsorbent) and the molecules of the gas (adsorbate) is a very specific interaction and occurs as a result of a molecule's interaction with an active site on the surface of the solid. This may be regarded as a chemical reaction because there is a molecular rearrangement. The simplest case to consider is that of the hydrogen molecule, which in order to chemisorb must dissociate into hydrogen atoms. This is represented as

$$H_2 + 2Pt_{(s)} \rightarrow 2Pt_{(s)}H \qquad (2.2)$$

where $Pt_{(s)}$ signifies a surface Pt metal atom. By choosing an adsorbate which adsorbs on the surface metal atoms and not the support, chemical adsorption can be used to estimate the degree of dispersion of supported metal catalysts [16].

Total surface area measurement

The method of determining the total surface area can be derived from the Type II isotherm which results in the m*onolayer coverage* of the solid. If the conditions under which a complete adsorbed layer of gas, averaging one molecule thick, can be established and the area per molecule of the gas (a_m) is known, then the number of moles of gas adsorbed (n_m), determined from the adsorption isotherm, gives the surface area (A). The total surface area of 1 g of the solid can be given:

$$A = (\text{number of adsorbate molecules}) \times (\text{area per molecule}) = n_m a_m L \qquad (2.3)$$

where a_m is the average area occupied by a molecule of adsorbate in the completed monolayer, L is the Avogadro constant (6.023×10^{23}), and n_m is the number of moles of adsorbate per gram of adsorbent.

The most useful method for determining the value for the monolayer capacity, and hence the total surface area was proposed by BET [17]. This is based on the kinetic model of the process of chemical adsorption proposed by Langmuir [18] which can be extended to cover physical adsorption.

The monolayer volume can be calculated from BET equation derived from their theoretical model [17]:

$$\frac{p}{V(p^o - p)} = \frac{1}{V_m c} + \frac{c-1}{V_m c}\left(\frac{p}{p^o}\right) \qquad (2.4)$$

where V is the volume of gas adsorbed for a given mass of adsorbent at the equilibrium pressure p; p^o is the saturated vapour pressure of the adsorbing gas at the temperature

used (1 atm. for N_2 at 77 K); V_m is the monolayer capacity and parameter c is a constant related to the entropy.

Plotting $\frac{p}{V(p^o - p)}$ against $\left(\frac{p}{p^o}\right)$ gives a straight line with intercept, $a = \frac{1}{V_m c}$ and gradient, $b = \left(\frac{c-1}{V_m c}\right)$. Solving these two equations simultaneously gives V_m and c.

The number of adsorbed molecules in the monolayer, n_m, can be also obtained from the following equation:

$$n_m = V_m / V_s \qquad (2.5)$$

where V_s is the molar volume of an ideal gas. So the total surface area can be calculated according to equation (2.3).

Nitrogen is usually used to determine the BET total surface area because the molecules of nitrogen are small with small quadrupole moment and roughly spherical, so that all the interior surface area of a porous solid is contacted. The physical adsorption of nitrogen will be fairly weak and detectable only at low temperature, thus the surface area is measured at 77 K. It is assumed that a_m, the average area occupied by one nitrogen molecule in the completed monolayer, is 0.162 nm^2 [14].

Pt metal dispersion measurement

The adsorption isotherm obtained from selective H_2 chemisorption on the Pt metal surface can be used to calculate the ratio of the chemisorbed hydrogen atoms to the total Pt metal atoms, by plotting the quantity (Q_3) of gas adsorbed onto the catalyst versus p:

$$\text{H/Pt} = \frac{2Q^o}{Mass\left(\frac{\%M}{RMM}\right)} \qquad (2.6)$$

where Q^o is moles of hydrogen atoms adsorbed on the surface Pt of the catalysts, *Mass* is the mass of the catalyst sample (~0.1 g), $\%M$ is the percentage Pt metal in the sample (20 wt%), and *RMM* is the relative molar mass of the Pt metal, 195. Q^o can be obtained by extrapolating the isotherm to the region of zero pressure; the volume of gas adsorbed at this point is Q^o. If it is assumed that only one hydrogen atom is chemisorbed per surface Pt metal atom, then H/Pt can be taken as the Pt metal dispersion (defined as the ratio of the number of Pt atoms on the surface to the total number of Pt atoms) of the Pt/C and various PtM/C catalysts. The factor of 2 in the numerator derives from the assumption that hydrogen is dissociatively adsorbed on the catalyst surface.

2.3.2.3 Apparatus

The total surface area and Pt metal dispersion of the Pt/C and the various PtM/C catalysts was carried out in a conventional static glass volumetric apparatus (Figure 2.4). A detailed description of the apparatus set up in our laboratory can be found in the literature[19].

The sample was placed into a pyrex sample chamber which was clipped to the line using a ball and socket joint (J. Young) with a silicone 'O' ring. A sinter was placed above the sample chamber to prevent catalyst particles being sucked up into the system. The samples were heated using a home-made vertical heating column controlled by a Zenith variable transformer. The system was evacuated by an Edward Air Cooled Diffusion pump [A] backed up by a Edwards two-way rotary pump [B]; together these allowed a vacuum of $10^{-5}/10^{-6}$ mbar to be achieved. A trap containing liquid nitrogen was situated on the line leading to the pumps to prevent any unwanted products from contaminating the pumps. The pressure in the vacuum line was measured by means of

two pressure gauges attached to the line (C, D); an Edward Active Pirani Gauge [C] reads the pressure in the range 100 to 10^{-3} to 10^{-8} mbar range. Regular heating of the vacuum line by means of a hot air blower was necessary to keep the system dry.

High purity hydrogen gas, helium gas and nitrogen gas cylinders were attached to the line via taps 1, 2 and 3 respectively. These were prevented from over pressuring the line by means of mini-pressure regulators. The pressure of the gases in the dosing volume was measured by two Edward Barocel Capacitance Barometers positioned as shown, [E, F]. [E] measured the pressures in the range 0 to 1,000 mbar and [F] in the range 0 to 10 mbar. All pressures measured by the pressure gauges were displayed by an Edward Active Controller [G].

The apparatus was calibrated by expansion of nitrogen from the dosing volume into two bulbs of known volume. A method of calibration has been given in the literature [19].

2.3.2.4 Experimental procedure

The experimental procedures for the determination of total surface area and Pt metal dispersion using the apparatus set up in our laboratory, is well described in the literature[19] and the following section gives a brief description for our catalyst samples.

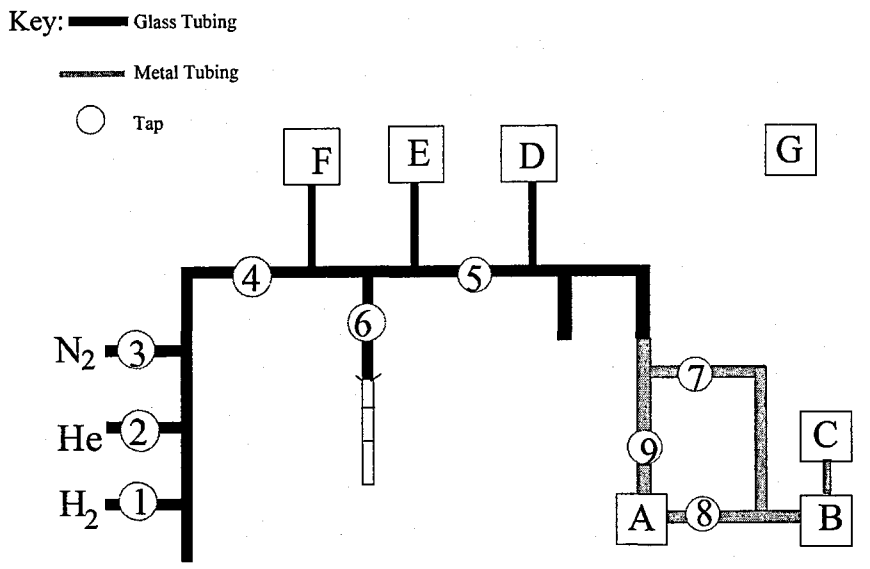

Figure 2.4 Schematic diagram of a static glass volumetric apparatus used for the determination of catalyst surface area and the Pt metal dispersion. Definition of the boxes is given in the text.

Total surface area measurement

The catalyst sample (~0.1 g) was loaded into the dry, clean quartz glass sample holder and attached, with the sinter in place, to the vacuum system. The sample was outgassed at room temperature for about 17 hours followed by heating to 250 °C for 1 hour. Outgassing was essential to ensure that any water or other gases present had desorbed from the catalyst surface. After removing the furnace, outgassing was continued as the sample was allowed to return to room temperature. The vacuum attained was in the region of $10^{-4} - 10^{-5}$ mbar.

With taps 4, 5, and 6 closed, the sample holder was immersed in a Dewar containing liquid nitrogen up to a pre-etched mark on the sample holder. This level was kept constant by continually topping up the Dewar. Nitrogen gas was then admitted into the dosing volume by opening taps 3 and 4 and the dosing pressure recorded (P_d^1). The

temperature of the dosing volume was also recorded (T_1) using a thermocouple attached to the vacuum line for this purpose. Tap 6 was then opened, a pre-determined amount and the nitrogen allowed to expand into the sample volume, and adsorb onto the sample. On reaching equilibrium (indicated by constant pressure) tap 6 was closed and the equilibrium pressure recorded (P_e^1). Successive expansions were performed with increasing dosing pressure until sufficient adsorption points had been acquired. Typically seven points were taken with dosing pressures 50, 75, 100, 150, 200, 250, and 300 mbar.

The data points obtained from the BET experiment were processed using a personal computer program to solve the BET equation giving the total surface area in m^2g^{-1}.

To validate the calibration of the apparatus and the procedure used, a standard sample of graphitized carbon black with a known total surface area (71.3 m^2g^{-1} ± 2.7 m^2g^{-1}) was used (obtained from the National Physical Laboratory, UK). The total surface area, 72.7 $m^2 g^{-1}$, for this standard sample was obtained with a correlation coefficient of 0.9999 using our apparatus.

Pt metal dispersion measurement

The catalyst sample (~0.1 g) was loaded into the dry, clean sample holder and attached to the vacuum system. The sample was outgassed at 250 °C for 1 hour before cooling to room temperature. The sample was then reduced under a static pressure (750 mbar) of hydrogen for 30 min at 200 °C. Tap 5 was then opened to remove the hydrogen from the sampleholder and dosing volume and the sample was outgassed for a further 30 min at this temperature. Outgassing was continued once the furnace was removed while the sample cooled down. Once cool, taps 4, 5 and 6 were closed and hydrogen was admitted to the line (opening tap 1). The data for the isotherm were obtained by

successive expansion of hydrogen onto the sample at room temperature. Typically 7 or 8 data points were collected in each experiment with values of P_d^n between 1 and 750 mbar. Again the data points obtained were processed by a personal computer program which generated Q^o and the Pt metal dispersion was obtained from equation (2.6).

2.3.3 Transmission electron microscopy (TEM) and energy dispersive X-ray analysis (EDX)

2.3.3.1 Introduction

Information on the local microstructure of a catalyst concerning the phase, size, shape and chemical components can be obtained by means of TEM and EDX. TEM is a useful physical technique to help us determine the particle size of the catalysts, and in particular whether there is any sintering of the bimetallic catalysts by using SOMC, and the proximity of the two metals. The metals and their support are imaged by TEM under high magnification, and the size and shape of metal particles can easily be obtained. EDX was used in conjunction with electron diffraction and the imaging techniques of TEM to obtain complementary information on the composition of the catalysts.

2.3.3.2 Theory

The basic construction of a modern transmission electron microscope is shown schematically in Figure 2.5 [20]. It consists of an electron gun and an assembly of electromagnetic lenses, all within a column which is evacuated to about 1×10^{-5} mbar. The beam of electrons produced by the electron gun is accelerated by a high voltage and then focused onto the thin specimen by two condenser lenses. This beam is allowed to strike the surface of the specimen, at which point the electrons are decelerated and scattered by collision with atoms in the specimen materials. In TEM an image of the specimen is formed by electrons which penetrate and pass through the specimen. The different

detectors are connected to the column together with the facility for taking photographic images.

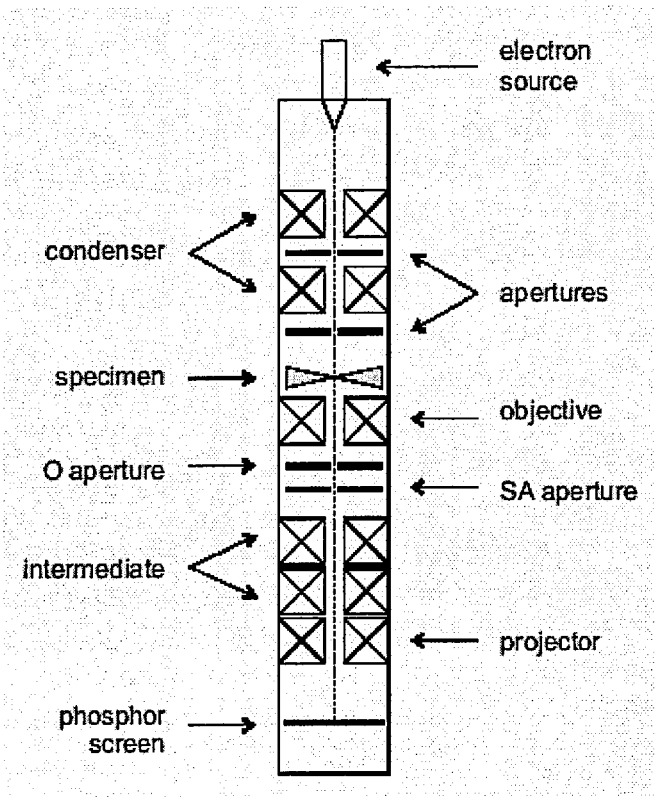

Figure 2.5 Schematic representation of a transmission electron microscope (O = objective, SA = selected area).

The interaction between a high energy electron and an atom of metal on the catalyst may involve the transfer of energy to a core electron which can then be displaced from its shell. The energy of this X-ray is equal to the energy difference between the excited and final atomic states, and is characteristic of the emitting element. Therefore, it is possible, by measuring the intensity of emitted X-rays and their respective wavelengths, to perform in most cases qualitative elemental microanalysis. This is known as Energy Dispersive X-ray analysis (EDX).

Transmission electron microscopes fitted with an EDX spectrometer are now relatively common. A major advantage of EDX spectrometers is that they accept all the incoming X-rays simultaneously and then sort them electronically according to their energies so that the complete spectrum can be displayed on a computer monitor. When a

sufficient number of "counts" have been recorded, the spectrum is stored in the associated computer, after which subtraction of background and calculation of the chemical composition of the sample can be carried out.

2.3.3.3 Apparatus

A JEOL 2000fx Transmission Electron Microscope fitted with a side entry port was used for TEM/EDX analysis [20]. The microscope was fitted with a lanthanum hexaboride (LaB_6) crystal filament and was equipped with the necessary detector for detecting X-ray and could therefore be used for energy dispersive X-rays microanalysis (EDX) using the commercially available Quantum Kevex Instrument. Electron micrographs of the catalysts were obtained using a camera fitted beneath the image screen. The negatives used for the electron micrographs were obtained from Agfa Scienta EM file and were printed on Ilford photograph paper. The EDX spectrum was plotted using software to plot X-ray intensity versus energy.

2.3.3.4 Experimental Procedure

The samples were prepared according to a method described in the literature [21, 22]. A small amount of catalyst sample was added to a glass ampoule containing acetone and placed in an ultrasonic bath for approximately 10 minutes. A drop of the suspension was pipetted on a carbon coated copper grid (3 mm, 200 mesh) and the solvent was allowed to evaporate from the grid. The grid was then placed into the microscope.

Transmission electron micrographs were recorded using a JEOL 2000fx Transmission Electron Microscope under an accelerating voltage of 200 kV. The elemental distribution of EDX spectrum was carried out using a computer program. The size of metal particles was measured by NIH image software.

2.3.4 X-ray photoelectron spectroscopy (XPS)

2.3.4.1 Introduction

Photoelectron spectroscopy is used to study the composition and electronic state of the surface region of a sample by using photo-ionization and energy-dispersive analysis of the emitted photoelectrons. Photoelectron spectroscopy has been subdivided, according to the source of exciting radiation, into X-ray photoelectron spectroscopy (XPS) and ultraviolet photoelectron spectroscopy (UPS). XPS uses soft (200 – 2000 eV) X-ray excitation to examine the electrons in core levels; UPS uses vacuum UV (10 - 45 eV) radiation to examine only valence electrons.

The aims of XPS analysis in this project are (i) the identification of the elements in the catalyst sample from the kinetic energies of these ejected photoelectrons and (ii) the determination of relative concentrations of elements from the photoelectron intensities.

Ultraviolet photoelectron spectroscopy (UPS) was not used in this project so only a description of X-ray photoelectron spectroscopy (XPS) technique is given below.

2.3.4.2 Theory

X-ray Photoelectron Spectroscopy (XPS), also known as Electron Spectroscopy for Chemical Analysis (ESCA), is the most widely used surface analysis technique because of its relative simplicity in use and data interpretation [23, 24] . The sample is irradiated with monochromatic X-rays causing photoelectrons to be emitted from the sample surface. An electron energy analyzer determines the binding energy of the photoelectrons. From the binding energy and intensity of a photoelectron peak, the elemental identity, chemical state, and quantity of an element can be determined.

In XPS the energy of a photoelectron is given by the Einstein equation:

$$E = h\nu \tag{2.7}$$

where h is Planck's constant (6.62×10^{-34} J s); ν is the frequency (Hz) of the radiation.

If a photoelectron in XPS is absorbed by an atom or molecule of the sample, it may lead to ionization and the emission of a core electron (Figure 2.6). The kinetic energy of a photoelectron, E_k , is related to E_B, the binding energy (or ionization energy) of that electron in an atom or molecule of the sample, according to the Einstein equation:

$$h\nu = E_k + E_B \tag{2.8}$$

where $h\nu$ = photoelectron energy of the incident radiation. As $h\nu$ is known, and E_k is measured, E_B can be calculated. The relationship between $h\nu$, E_k and E_B is illustrated schematically in Figure 2.6.

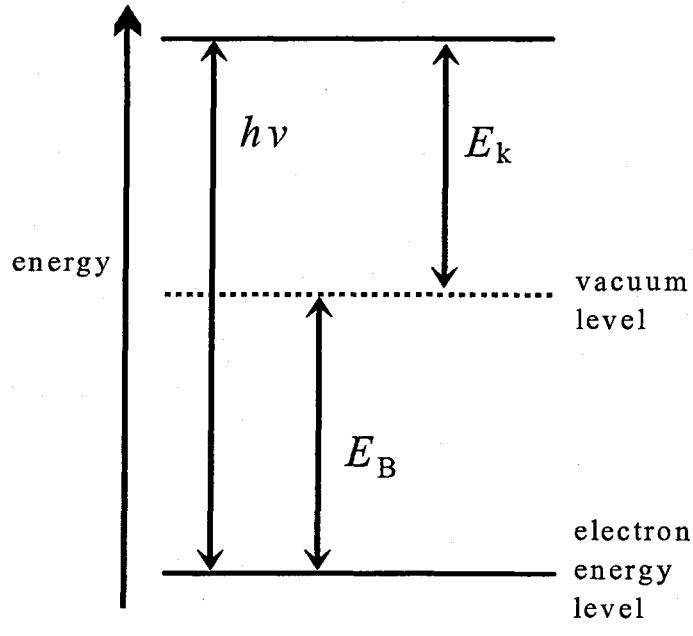

Figure 2.6 The relationship between the photoelectron energy, hν, the binding energy, E_B, and the electron kinetic energy, E_K.

2.3.4.3 Instrumentation

A modern XPS instrument consists of six main parts: source of radiation, sample chamber, lens system, energy analyzer, detector and computer. The typical components

of an XPS instrument are shown in Figure 2.7 [25]. The most usual source of X-rays in XPS is by electron bombardment of a magnesium or aluminium target anode. X-rays illuminate an area of a sample, causing electrons to be ejected with a range of energies and directions. The kinetic energies of these ejected electrons are analyzed using a hemispherical analyzer, which permits only electrons of particular energy to traverse the space between the two charged hemispheres. By changing the electric potential between the two hemispheres, electrons of various kinetic energies pass through the analyzer, and so a spectrum of kinetic energies can be recorded. For every element there will be a characteristic binding energy associated with each core atomic orbital. Each element will thus give rise to a characteristic set of peaks in the photoelectron spectrum at kinetic energies determined by the photon energy and the respective binding energies.

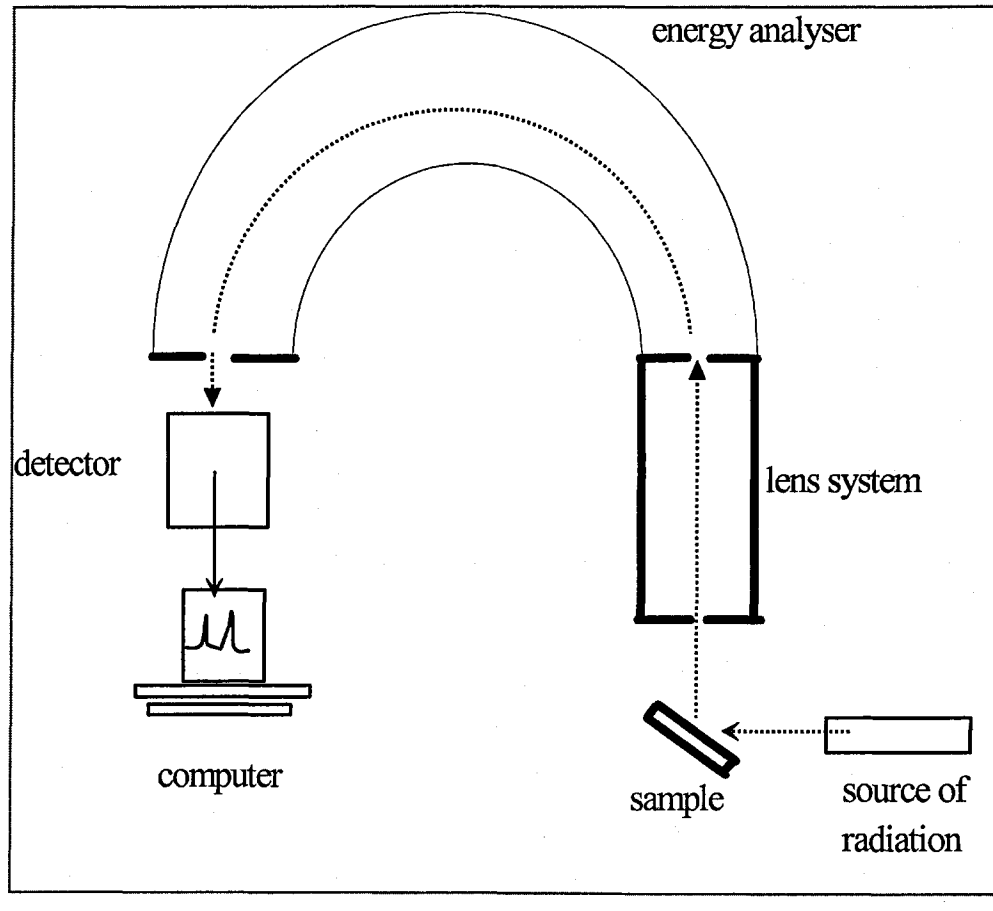

Figure 2.7 Schematic diagram of an XPS instrument

2.3.4.4 *Experimental procedure*

XPS analyses of the samples were carried out at the Johnson Matthey Technology Centre, using a Kratos XSAM 800. The catalyst samples were mounted on specimen stubs using double-sided adhesive tape and analysed using MgK_{α} radiation at 195 W with 7.5 mm slit and 80/40/10 eV pass energies. The carbon 1s spectra were recorded and the binding energy 284.8 eV was used as the reference. The data were analysed using a Shirley background subtraction procedure [3].

2.3.5 Powder X-ray diffraction (XRD)

2.3.5.1 *Introduction*

The application of X-ray powder diffraction technique in the catalysis field has been restricted due to the limited crystallinity of most supported metal catalyst systems. In addition the loading of the active metal phase in a typical metal catalyst is usually below the threshold of sensitivity of the technique. A further limitation is that only relatively large particles can be examined due to the severe X-ray line broadening in the case of small particles so, therefore, a well dispersed catalytic phase will not be observed. Nevertheless in favourable circumstances, where the catalyst displays a degree of crystallinity and where the phases under investigation are present in sufficient quantities, it is possible to extract structural information, such as phase composition and crystallite size, from an XRD pattern [19, 26].

The primary use of powder X-ray diffraction in this work is in identification of metal compounds in the catalysts by comparison of their diffraction patterns with known standards. It includes (i) identification of single-phase and multiple-phases in microcrystalline mixtures (ii) determination of the crystal structure of identified metals (iii) determination of the average size of metal particles. Powder X-ray diffraction is well

described in the literature [9, 27, 28] and only a brief description of the theory, instrumentation and experimental procedure is given below.

2.3.5.2 Theory

X-rays were discovered by W.C. Röentgen in 1895 [9]. X-rays are electromagnetic radiation of wavelength ~1 Å. They occur in that part of the electromagnetic spectrum between γ-rays and the ultraviolet. X-rays are produced when high-energy charged particles (for example, electrons accelerated through 30,000 V) collide with matter. When the beam of X-rays strikes the catalyst sample, interaction of the X-rays with the sample creates secondary "diffracted" beams of X-rays related to interplanar spacings in the crystalline powder according to the Bragg equation [9]:

$$n\lambda = 2d\sin\theta \tag{2.8}$$

where n is an integer, λ is the wavelength of the incident X-ray beam, d is the interplanar spacing and θ is the diffraction angle. The powder X-ray diffraction method is very important and useful in qualitative phase analysis because every crystalline material has its own characteristic powder pattern which may be used as a "fingerprint" for its identification. All powder X-ray patterns that have been determined and peer reviewed, are available for comparison on a database from the Joint Committee on Powder Diffraction Standards (known as JCPDS files).

The average size of sample crystallite may be estimated by the Debye-Scherrer equation [9]:

$$T = \frac{C\lambda}{B\cos\theta} = \frac{C\lambda}{(U^2 - S^2)^{\frac{1}{2}}}\cos\theta \tag{2.9}$$

where T is the crystallite size (the diameter of a crystal particle in Å), λ is the X-ray wavelength (Å) (1.5406 Å for CuK_α), θ = Bragg angle, C = a factor (typically from 0.9 to 1.0) depending on crystallite shape, B is the full width at half maximum, FWHM, of the

peak (radians) corrected for instrumental broadening, and U and S are the FWHMs of the unknown and standard peaks respectively. For our experiment, $C = 1.0$; $\lambda = 1.5406$ Å; $S = 0.136$ (standard SiO_2); $B = \frac{(U^2 - S^2)^{1/2}}{57.2727}$ (radians).

2.3.5.3 Instrumentation

A powder X-ray diffractometer consists of five main parts: X-ray tube, a series of slits to collimate the X-rays, sample holder, detector and computer. Figure 2.8 shows the conformation of the Siemens D5000 diffractometer used in our experiments [29].

2.3.5.4 Experimental procedure

Powder X-ray diffraction patterns were collected using a Siemens D5000 diffractometer. The catalyst samples were held on a single crystal of Si using a very small amount of grease. An incident beam of X-rays of wavelength 1.5418 Å (CuK_α) filtered by a nickel filter was used. The samples were scanned from $10° < 2\theta < 90°$. The recorded patterns were matched against existing powder patterns using the JCPDS files.

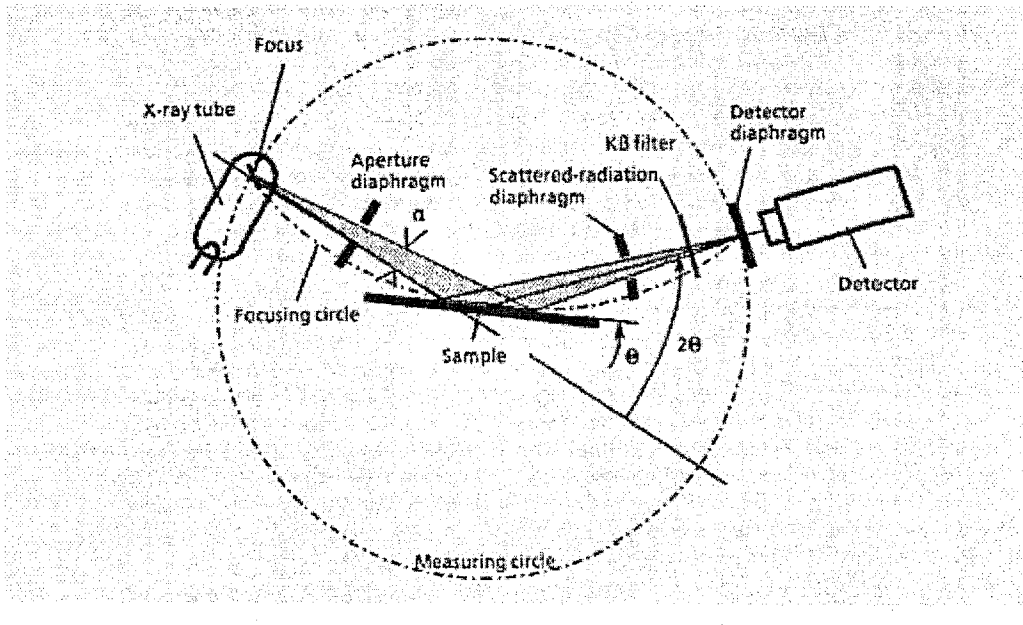

Figure 2.8 Schematic diagram of a powder X-ray diffractometer

2.3.6 Temperature-programmed reduction (TPR)

2.3.6.1 Introduction

Temperature-programmed reduction (TPR) is a technique developed from temperature-programmed desorption (TPD)[10]. It is a relatively simple technique used commonly in catalyst characterization. The first review on the subject of TPR appeared in Catalysis Reviews [11] in 1982. TPR has been extensively applied to the characterization of supported catalysts, and valuable information has been obtained that has led to a greater understanding of the role of the catalyst. The general TPR technique has been found to be useful for supported metallic catalyst studies by characterising phases present in a catalytic system and providing information on the reducibility of the metal components.

TPR is a thermal-analytical technique in which the composition of a gas stream, usually a dilute hydrogen mixture, is monitored as it passes over a sample as the temperature of the sample is raised linearly. A typical TPR profile consists of a series of peaks. Each peak represents a distinct reduction process involving a particular chemical component of the heterogeneous catalyst. The position of a peak in the profile is determined by the chemical nature and environment of the chemical component, and the area of the peak reflects the hydrogen consumption and concentration of that component present in the heterogeneous catalyst. The shapes of curves for reduction are also obtained. The temperatures at which each of the reduction products form are measured; these values can provide information about the reaction mechanism. The reduction profile gained from supported bimetallic catalysts, when compared with the TPR profiles of the respective monometallic catalysts, can reveal the two metal are in close contact [30, 31]

2.3.6.2 *Theory*

The reduction of a metal oxide (MO_x) involves the dissociative adsorption of hydrogen on to the metal oxide surface and can be represented by the general equations:

$$MO_n(s) + nH_2\,(g) \rightarrow M(s) + nH_2O\,(g) \qquad (2.10)$$

$$2M(s) + H_2(g) \rightarrow 2M\text{-}H \qquad (2.11)$$

Hence, a typical TPR profile will record the total amount of hydrogen gas consumed by the sample as a function of temperature.

2.3.6.3 *Apparatus*

A schematic diagram of the TPR apparatus is shown in Figure 2.9. The experiment involved flowing a 10% H_2 in N_2 gas mixture through the reference arm of a katharometer detector of a gas chromatograph (Varian Model 3700 GAS) operating at 59 °C and then through the sample under investigation. The sample was placed in a quartz reactor tube attached via Chemcon PTFE fittings. The sample was heated using a Carbolite furnace controlled by a Eurotherm model 818 temperature programmer. The gas mixture was returned to the other arm of the katharometer. Consumption of hydrogen was detected as a voltage imbalance between the two arms of the katharometer. The gas flow was measured as it left the detection system using a bubble flow meter. The current from the detector was collected, processed and analysed using Pico Data Logger software (Pico Technology Ltd.)

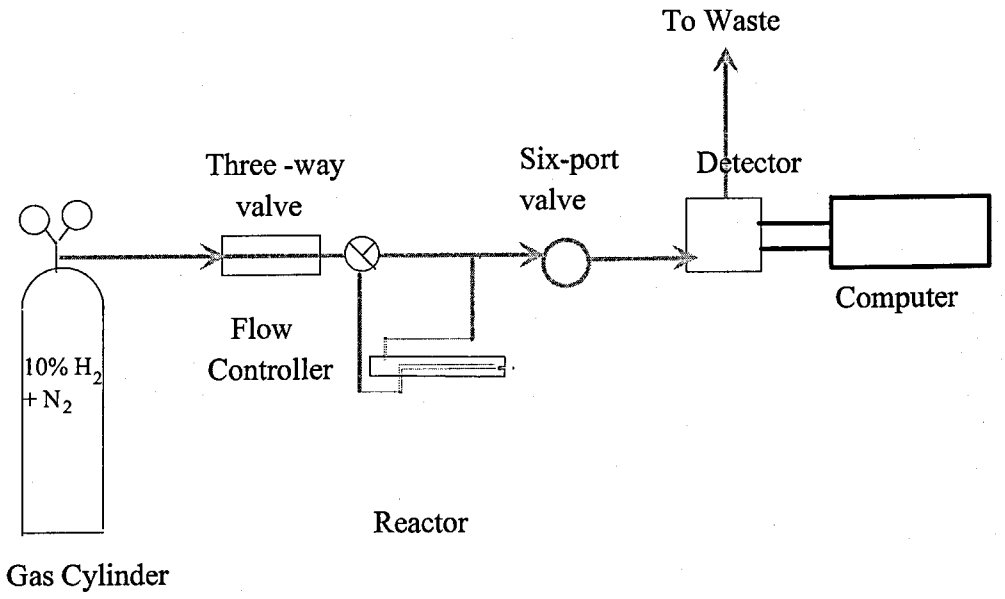

Figure 2.9 Schematic diagram of the TPR apparatus

2.3.6.4 Experimental procedure

In the TPR experiment a small amount of sample (150 mg) was placed in a special quartz glass reactor. The reactor was attached to the apparatus and placed in a Dewar filled with solid CO_2 and acetone. After 20 minutes the reactor was removed from the Dewar and then placed in the centre of a programmable furnace. The 10% H_2 in N_2 gas mixture was started at a flow rate of 20 ml min^{-1}. The detector was switched on and data were collected at the same time. Once the sample had warmed to room temperature the sample was heated to 950 °C at 5 °C min^{-1}. A plot of hydrogen consumption versus temperature was obtained.

2.3.7 Thermogravimetic analysis and differential scanning calorimetry (TGA/DSC)

2.3.7.1 Introduction

Thermal Analysis is a generic term for methods by which the physical and chemical properties of a substance, mixture and/or reaction mixtures are determined as a function of temperature or time, while the sample is subject to a controlled temperature

programme. The programme may involve heating or cooling (dynamic), or holding the temperature constant (isothermal), or any sequence of these. The graphical result is called a *thermal analysis curve.*

Three widely used thermal analysis techniques are thermogravimetric analysis (TGA), differential scanning calorimetry (DSC) and differential thermal analysis (DTA). TGA quantifies the change in mass with respect to temperature. DSC examines heat flow as a function of temperature when compared to a temperature reference. DTA measures the difference in temperature between a sample and a thermally inert reference as the temperature is raised. DTA was not used in this project so only a description of TGA and DSC is given below.

2.3.7.2 Theory

Thermogravimetric Analysis (TGA) measures changes in mass of a material as a function of temperature under a controlled atmosphere. Its principal uses include measurement of a material's thermal stability. For example, TGA can directly record the loss in mass with time or temperature due to dehydration or decomposition. Changes in mass are a result of the rupture and/or formation of various physical and chemical bonds at elevated temperatures that lead to the evolution of volatile products or the formation of heavier reaction products. Data are obtained from TGA curves concerning the thermodynamics and kinetics of the various chemical reactions, reaction mechanism, and the intermediate and final reaction products.

Differential scanning Calorimetry (DSC) measures temperatures and heat flows associated with thermal transitions in a material as a function of time and temperature. It determines transition temperatures, such as melting and crystallization, and heat capacity.

For TGA the sample is continuously weighed as it is heated to elevated temperatures. Samples are placed in a crucible or shallow dish that is attached to an automatic-recording balance.

DSC measurements are carried out by precise heating of the heat-flux plate, creating a temperature differential between the sample and the reference. This temperature difference, produced by the differential heat flow, causes the thermocouples to generate a voltage that is proportional to the heat flow. By measuring the heat absorbed or given off by a sample as it is heated or cooled under a controlled temperature and atmosphere, DSC is able to record changes in specific heat capacity and latent heat that indicate changes in amorphous and crystalline structures.

2.3.7.3 Apparatus

TGA and DSC experiments were performed on a Rheometric Scientific Simultaneous Thermal Analyzer (STA). Figure 2.10 shows the schematic diagram of the STA main module. STA permits simultaneous TGA and DSC experiments by combining a sensitive balance with a TG-DSC hangdown. TG-DSC hangdown is shown in Figure 2.11. The TG-DSC hangdown carries the sample and reference crucibles, and is enclosed in the furnace for experiments and non-ambient temperatures. To perform differential scanning calorimetry experiments, the hangdown is equipped with a heat-flux plate. DSC measurements are carried out by precise heating of the heat-flux plate, creating a temperature differential between the sample and the reference. This temperature difference, produced by the differential heat flow, causes the thermocouples to generate a voltage that is proportional to the heat flow.

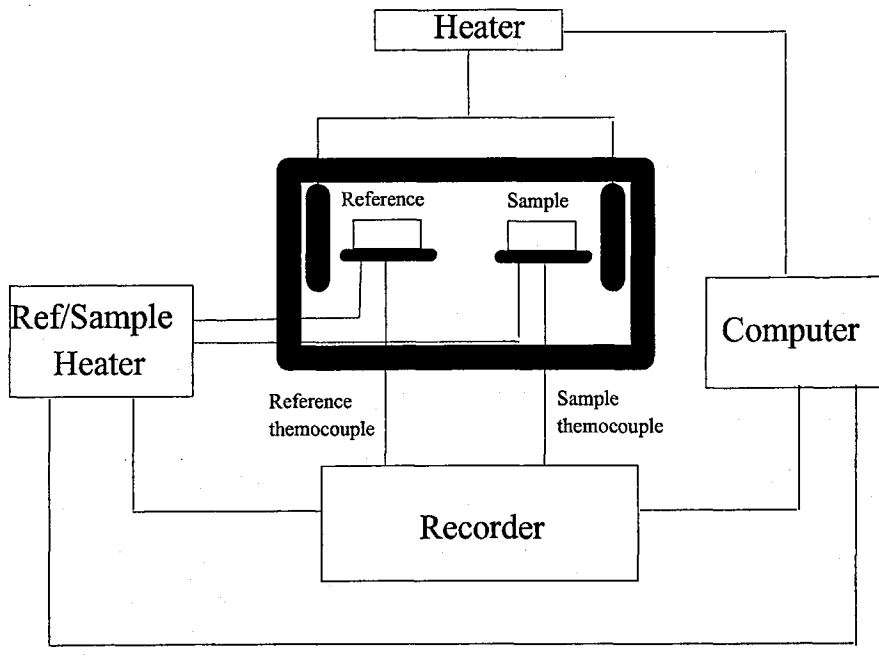

Figure 2.10 Schematic diagram of the STA main module

The advantages for simultaneous TGA and DSC are obvious. Both analyses are carried out at the same time, assuring identical conditions. This completely eliminates any correlation problems between TGA and DSC that exist when experiments are carried out on separate test instruments. In addition, the STA utilizes the highly accurate and internationally accepted DSC temperature calibration standards for both TGA and DSC, thus avoiding the troublesome temperature calibrations associated with standalone TGA instruments.

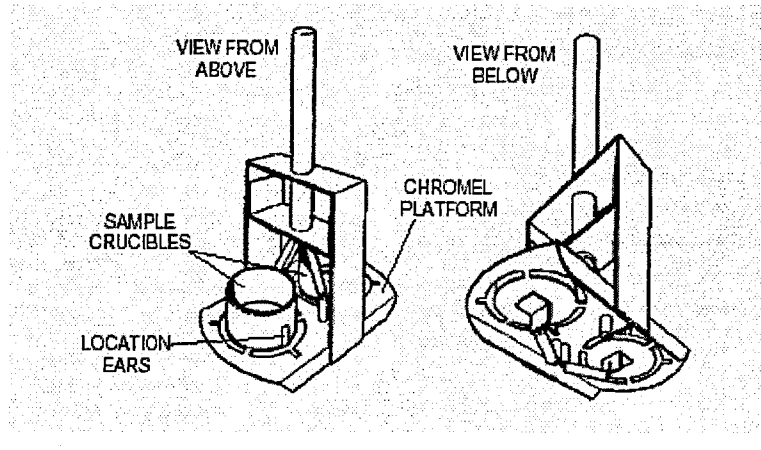

Figure 2.11 The heat-flux TG-DSC hangdown [32]

2.3.7.4 *Experimental procedure*

2-5 mg sample was loaded in the main module of the STA. A 10% H_2 in N_2 gas mixture was flowed through the sample at 50 ml min^{-1} and the sample heated at a rate of 5 °C min^{-1} to the desired temperature (900 °C). Experimental conditions were entered using the IBM-compatible host computer and corresponding instrument software. The data was analysed using Origin software.

2.3.8 Extended X-ray absorption fine structure (EXAFS)

2.3.8.1 *Introduction*

EXAFS, or extended X-ray absorption fine structure, has become a popular technique in the research of electrocatalysts where small particles of chemically active elements are dispersed on a suitable support [33-36]. EXAFS can be used to obtain structural and electronic information about the atoms of one specific element, such as the type and number of neighbours, and the distance to the neighbours. It should be noted that EXAFS gives an average picture of the environment around the atom of a particular element, so therefore, unlike other techniques such as XRD, it is not necessary for the sample to have an ordered structure. A brief account of EXAFS technique used in this project is given below but detailed description of EXAFS theory and the mathematical modelling are available in the literature [37-39].

2.3.8.2 *Theory*

In high energy accelerators, electrons are injected into an electron storage ring, captured, and accelerated around this circular path by a series of magnets. When the electrons are accelerated to kinetic energies above the MeV range, they are travelling close to the speed of light and they emit synchrotron radiation. The synchrotron at

Daresbury, UK operates at 2 GeV, and the peak power is radiated at about 10^{18} Hz (approximately 10 keV and 1 Å) in the X-ray region of the electromagnetic spectrum.

In an EXAFS experiment the X-radiation is absorbed by a bound electron in a core shell (usually the K shell) and ejected as a photoelectron. If you measure the absorption coefficient of the sample as a function of the X-ray frequency, a sharp rise, or absorption edge is observed at the K shell threshold energy (Figure 2.12a). Each element has its own characteristic K shell energy, and this makes it possible to study one type of atom in the presence of many others, by tuning the X-ray energy to its absorption edge: the appropriate frequency X-radiation from the continuous synchrotron radiation is selected by using the Bragg reflection from a single plane of a crystal such as Si (220) or Si (111). By changing the Bragg angle of reflection, the frequency of the X-rays selected may be changed, and thus the absorption edges of a wide range of elements can be studied.

The waves of the ejected photoelectron from the K shell can be thought of as a spherical wave emanating from the nucleus of the absorbing atom; this encounters neighbouring atoms and is partially scattered by them producing a phase shift (Figure 2.12b). Depending on the phase shift experienced by the electron, the reflected waves can then interfere constructively or destructively with the outgoing wave, producing a net interference pattern at the nucleus of the original atom. Absorption by the original atom is now modified, and the effect is seen as sinusoidal oscillations or fine structure superimposed on the absorption edge (Figure 2.12a) extending out to several hundred eV after the edge. The intensity of the reflected wave, is partly dependent on the atomic number of that atom. The interference pattern making up the EXAFS thus depends on the *number*, and the *type* of neighbouring atoms, and their *distance* from the absorbing atom.

The EXAFS function is obtained from the X-ray absorption spectrum by subtracting the absorption due to the free atom. A Fourier transform of the EXAFS data gives a radial distribution function which shows the distribution of the neighbouring atoms as a function of internuclear distance from the absorbing atom.

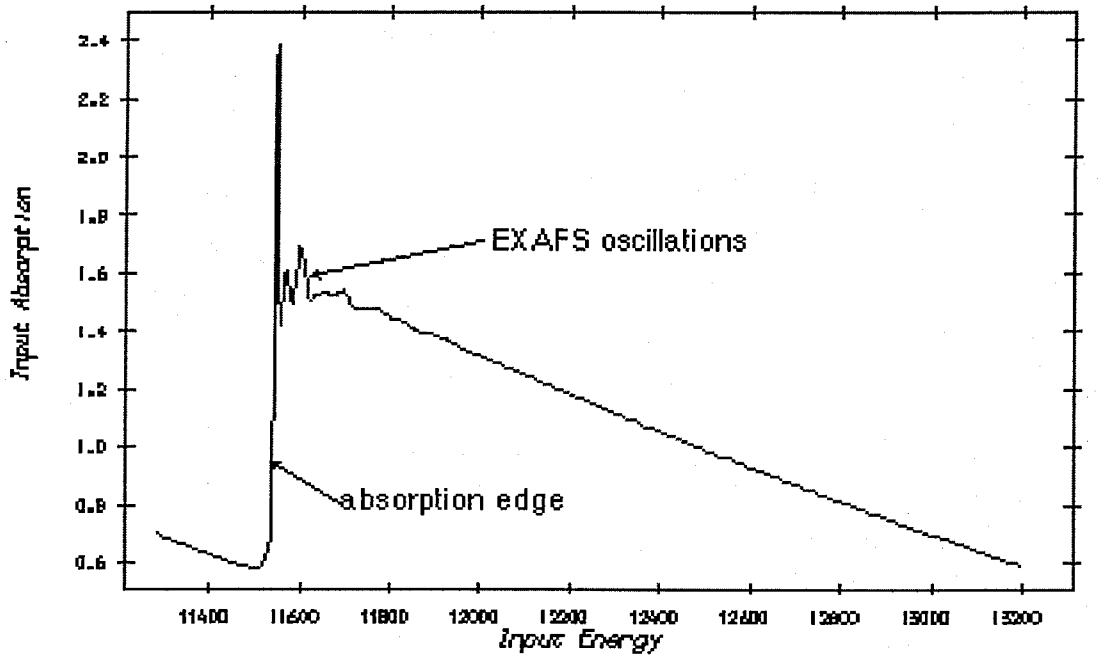

Figure 2.12 (a) A typical absorption edge showing EXAFS, (b) the EXAFS process (i) the photoelectron is ejected by X-ray absorption (ii) the outgoing photoelectron wave (solid line) is backscattered constructively by the surrounding atoms (dashed line) (iii) destructive interference between the outgoing and the backscattered wave[24].

The absorbing atom is surrounded by shells of neighbours, known as coordination shells. Finally the radial distribution function is fitted to a series of trial structural models until a structure which best fits the data is obtained, and the data is refined as a series of coordination shells surrounding the absorbing atom. The final structure will refine the

number and types of atoms, and their distance from the absorbing atom. It is difficult to differentiate atoms of similar atomic number, and important to note that EXAFS only gives data on distance - there is no angular information. Depending on the quality of the data obtained, distances can be refined to about 1 pm, and in favourable cases several coordination shells out to about 600 pm can be refined.

2.3.8.3 Apparatus

EXAFS experiments at the Fe K-edge, the Ni K-edge and the Cr K-edge were carried out using synchrotron radiation sources (SRS) at the double crystal Si(111) harmonic monochromator on Station 7.1 at Daresbury Laboratory, UK. The storage ring was operated at 2.0 GeV energy with an average current of about 125 mA. Figure 2.13 shows the experimental setup at Daresbury for collecting the EXAFS data.

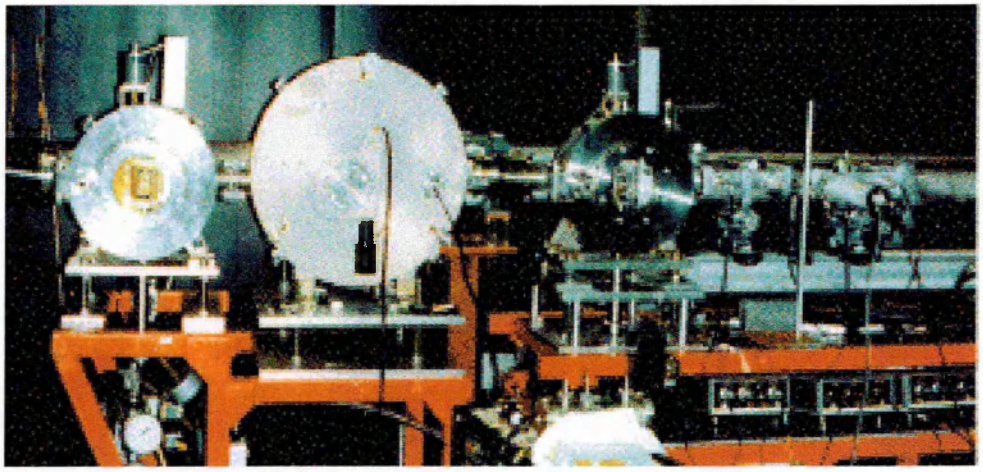

Figure 2.13 Our EXAFS set-up at Station 7.1, Daresbury.

In Figure 2.13, the X-ray beam enters from the left, passes through a pre-slit to adjust its size, through the monochromator which is used for energy variation, and finally emerges from the exit slit, which allows for a further adjustment in beam shape. The amount of X-rays before and after the sample are measured by ionisation counters, which can just be seen in the right of Figure 2.13.

The sample holder and a gas treatment cell, designed and made by Dr Andrea E. Russell's research group in University of Southampton, were made from stainless steel (Figure 2.14). The sample holder was mounted in the gas treatment cell in order to reduce the samples in hydrogen gas and seal the samples during EXAFS experiments.

The gas treatment cell was designed so that both transmission and fluorescence data could be collected without the configuration of the cell requiring considerable change. The top half of the cell with the gas outlet valve can be orientated to two positions; this moves the powder sample holder. It can be positioned at either 90° for transmission data collection or to 45° for fluorescence data collection (Figure 2.15). The cell can be mounted directly on the beamline via a cell holder, which is a metal plate with two pins, which fit directly into two holes in the bottom of the cell.

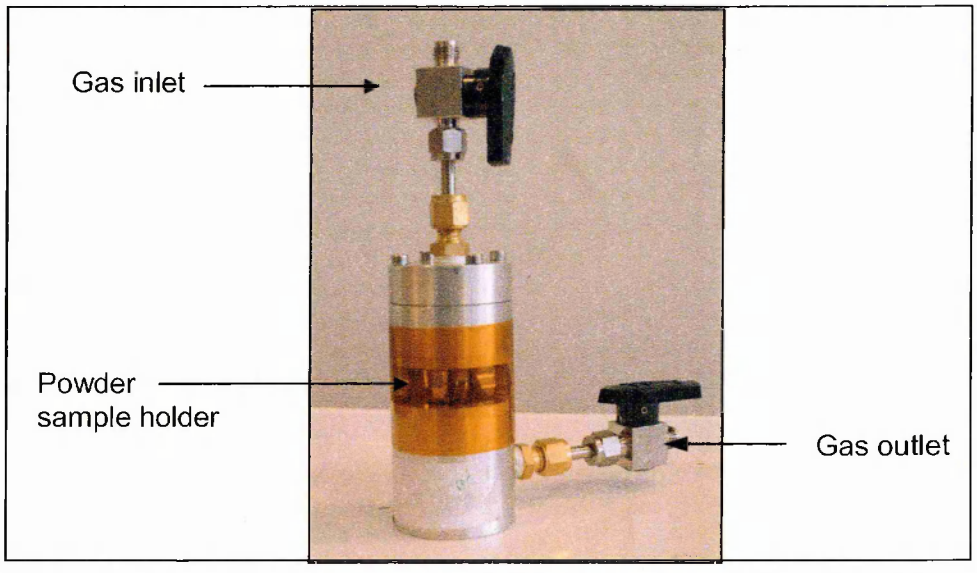

Figure 2.14 Annotated photograph of the sample holder and gas treatment cell.

The window of the cell is covered with Kapton film, which will hold an atmosphere of gas pressure. For safety reasons, gas is not flowed through the cell during the experiment but is purged through the cell for at least one hour prior to an experiment.

The taps are then closed leaving the sample in a defined gaseous environment – in our case hydrogen - during the measurement.

The powder sample is prepared by mixing the 30 mg of sample with 30 mg polyethylene (used as a binder) and pressing in a die press.

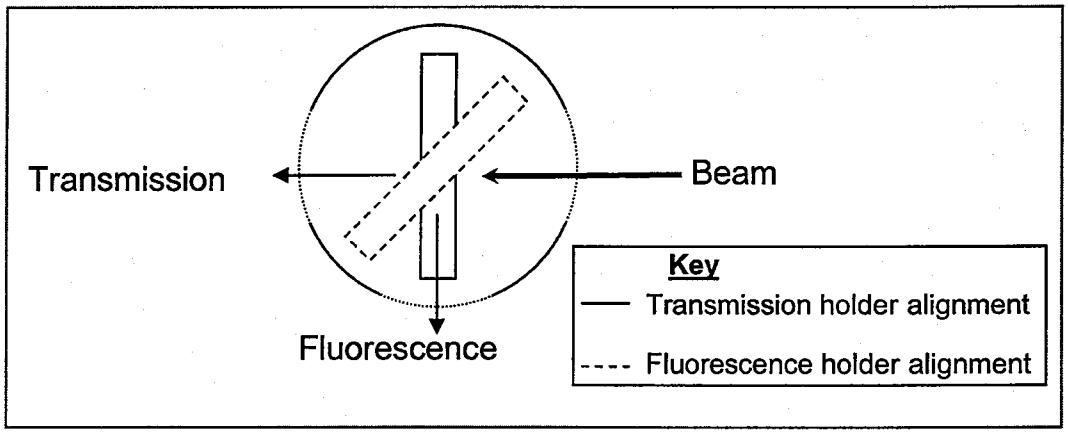

Figure 2.15 Schematic diagram of gas treatment cell and sample holder

2.3.8.4 Experimental procedure

The samples were loaded on the sample holder and mounted in the gas treatment cell and reduced at room temperature in a steady stream of hydrogen for 1 h. The position of the beam was recorded by burning a spot on a piece of photographic paper. A laser was then lined up with the position of the beam and the sample position corrected using the laser beam. The EXAFS experiments were carried out at room temperature in the fluorescence mode. The spectra were obtained using standard ion chambers filled with Ar as detector (20% absorbing I_0, and 80% absorbing I_t, backfilled to 1000 mbar with He). The relative energy scale was calibrated against Fe, Ni or Cr pure metal foils. Four individual fluorescence spectra were taken for each sample and added together to improve the signal levels in the data.

The analysis of EXAFS data was very complex and was performed in collaboration with Ms Abbe Rose and Dr Andrea E. Russell, University of Southampton, using the Daresbury suite of analysis programs. Overall the averaged and calibrated raw absorption spectra were processed using EXBROOK to achieve the background subtraction. A theoretical model was made using EXCURV 98 program to match the observed interference pattern as closely as possible. The parameters of the model including the type, number and distance of atoms in the sample were obtained according to the best fit figure [40].

2.3.9 Inductively Coupled Plasma - Atomic Emission Spectroscopy

Inductively Coupled Plasma - Atomic Emission Spectroscopy (ICP-AES) is a multi-element analysis technique that will dissociate a sample into its constituent atoms and ions and cause them to emit light at a characteristic wavelength by exciting them to a higher energy level. This is accomplished by the use of an inductively coupled plasma source, usually argon. A monochromator can separate specific wavelengths of interest, and a detector is used to measures the intensity of the emitted light. This information can be used to calculate the concentration of that particular element in the sample.

The assay of each catalyst obtained by element was performed by the Johnson Matthey Technology Centre, using Inductively Coupled Plasma - Atomic Emission Spectroscopy.

2.4 Electrochemical Evaluation

This section describes the electrochemical evaluation used in this project. This includes electrode preparation, cyclic voltammetry, electrode Pt surface area measurement and the oxygen-reduction reaction. More detailed information can be obtained from the literature [41-47].

2.4.1 Electrode Preparation

In the following sections the electrode preparation of Pt/C and PtM/C bimetallic electrocatalysts will be given. Electrodes with two different Pt loadings were prepared – 1 mg Pt cm^{-2}, and 0.35 mg cm^{-2}. Three-layer (substrate/diffusive layer/catalyst layer) electrodes were prepared using either a filter transfer technique for electrodes with the higher Pt loading, or brushing technique for electrodes with the lower Pt loading [48-50]. The substrate in both cases was carbon paper (Stackpole PC 206). The platinum-based electrocatalyst layers are located between the membrane and the substrate, and can be deposited either on the gas diffusion substrate or on the proton conducting membrane electrolyte. The catalyst layer was prepared by mixing appropriate amounts of the electrocatalyst, Teflon suspension (for the higher Pt loading) or Nafion suspension (for the lower Pt loading) respectively. The ratio of electrocatalyst : Teflon and electrocatalyst : Nafion were 1:9 and 3:7 respectively. The higher Pt loading electrode (1 mg Pt/cm^2) was used to measure adsorption properties of the catalysts in order to be able to observe the change of the peaks of hydrogen adsorption and oxidation between Pt/C and PtM/C. The lower Pt loading electrode (0.35 mg Pt/cm^2) was used to determine the electrochemical surface area by CO oxidation or evaluate the activity of the electrocatalyst for the oxygen-reduction at the cathode in PEM fuel cells. This would show if improved performance can be achieved at the lower electrode Pt loadings.

2.4.1.1 *Preparation of electrodes with the higher Pt loading*

The electrodes were fabricated using a filter transfer technique onto wet proofed carbon paper (Stackpole PC 206). A weighed amount (~0.05 g) of the Pt/C or PtM/C catalyst was dispersed in de-ionised water and placed into a 50 ml beaker. The catalyst was then agitated ultrasonically at 60 °C for 15 minutes. 10 wt% of Teflon suspension (Fluon GP1, 66 wt% solid) was added to the dispersion. A required amount of isopropanol (about 5 drops) was added to the contents which were allowed to soak for 1 hour (agitated once every 15 minutes with addition of further isopropanol). The resulting slurry was spread on a 9 cm^2 Teflon carbon paper using a scalpel and pressed at a pressure of 50 kg cm^{-2} for 5 minutes. The electrodes obtained were dried at 140 °C for 15 minutes and subsequently sintered at 350 °C for 30 minutes in a muffle furnace. Buttons of 1 cm diameter were cut from these electrodes. The nominal platinum loading in all the electrodes was 1mg.

2.4.1.2 *Preparation of electrodes with the lower Pt loading*

A weighed amount of the Pt/C or PtM/C catalyst was dispersed in de-ionised water and mixed with a required amount of 10 wt% aqueous Nafion solution to make a catalyst ink (70% catalyst and 30% solid Nafion). The ink was agitated ultrasonically at room temperature for 30 minutes. The electrodes were made by brushing this ink onto a Teflon carbon paper at 100 °C and were dried at 180 °C. The nominal platinum loading in all the electrodes was 0.35 mg/cm^2. Buttons of 16 mm diameter were cut from these electrodes.

2.4.2 Cyclic Voltammetry

2.4.2.1 Introduction

Voltammetry is an electrochemical measuring technique used for electrochemical analysis or for the determination of the kinetics and mechanism of electrode reactions. "Voltammetry" is a family of techniques with the common characteristics that the potential of the working electrode is controlled (typically with a potentiostat) and the current flowing through the electrode is measured. In one of the most common applications of the technique, the potential is scanned linearly in time; this is called the "linear-sweep voltammetry", "LSV", or "LV". "Cyclic Voltammetry (CV)" is a linear-sweep voltammetry with the scan continued in the reverse direction at the end of the first scan, this cycle can be repeated a number of times.

2.4.2.2 Theory

Before introducing cyclic voltammetry, we will first discuss linear-sweep voltammetry (LSV) techniques. In linear-sweep voltammetry the voltage is scanned from a lower limit to an upper limit as shown below (Figure 2.16).

The voltage scan rate (v) is calculated from the slope of the line. Clearly by changing the time taken to sweep the range, we alter the scan rate. The characteristics of the linear-sweep voltammogram recorded depend on a number of factors including:

- The rate of the electron transfer reaction(s)
- The chemical reactivity of the electroactive species
- The voltage scan rate

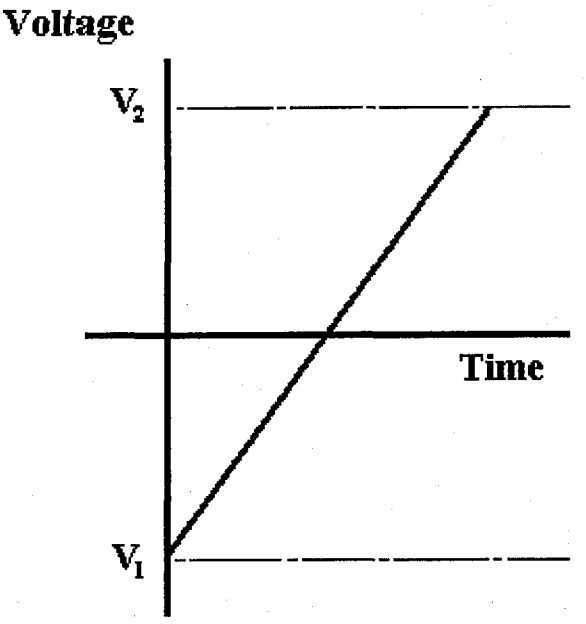

Figure 2.16 Potential wave form for linear-sweep voltammetry

Cyclic voltammetry is very similar to linear-sweep voltammetry. In this case the voltage is swept between two values (Figure 2.17) at a fixed rate, however, when the voltage reaches V_2 the scan is reversed and the voltage is swept back to V_1. This process, in turn cycles any redox reaction that occurs within the range studied. Multiple cycles can take place. A plot of potential versus current is then produced.

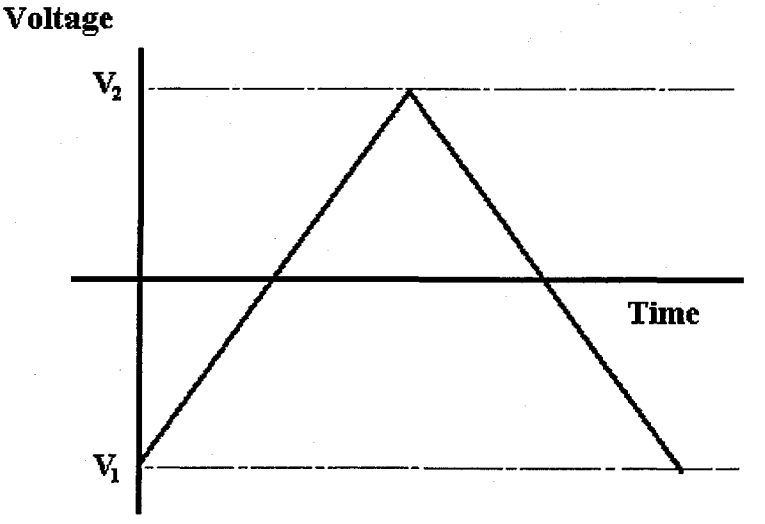

Figure 2.17 Potential wave form for cyclic voltammetry

A typical cyclic voltammogram for a metallic Pt (Pt/black) electrode is shown in Figure 2.18 [51]. This cyclic voltammogram is characteristic of the nature of the metal and any adsorbed species (hydrogen or oxygen). Generally peaks are seen for oxidative processes in the anode sweep (0-1.5 V) and reductions in the cathodic sweep (1.5-0 V). A detailed discussion of this CV for Pt will be given in Chapter 4.

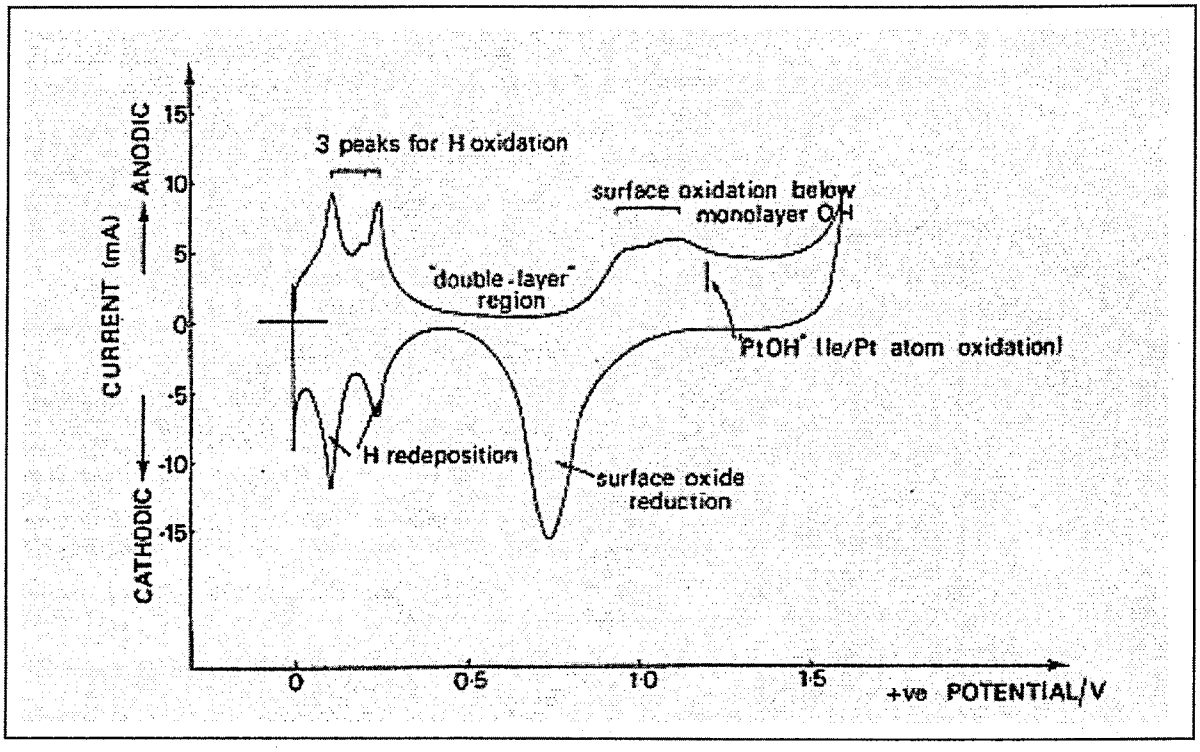

Figure 2.18 A typical cyclic voltammogram for a metallic Pt (Pt/black) electrode, in 3M H_2SO_4 at 20 °C with sweep rate of 50 mV s^{-1}

Cyclic voltammetry has become a very popular technique for initial electrochemical studies of new systems and has proved very useful in obtaining information about fairly complicated electrode reactions. Cyclic voltammetry is also a very versatile electroanalytical technique. It can be used to quickly determine oxidation and reduction behaviour of electroactive species in solution. More specifically, the voltage at a working electrode is scanned in a linear fashion, resulting in a current-voltage plot (voltammogram) for the solution.

Another useful application of CV is that it can be used to quantify the electrode Pt surface area (EPSA). EPSA is a measure of the maximum Pt surface area available for reaction. Traditionally, the electrode Pt surface area (EPSA) is determined by cyclic voltammetry in an aqueous acidic medium. As each surface platinum atom has the capacity to adsorb close to one hydrogen atom, the charge associated with hydrogen adsorption and desorption (equation 2.12) indicates the number of surface platinum atoms and hence the surface area [52-54].

$$Pt + H^+ + e^- \rightarrow Pt\text{-}H \qquad 210\ \mu C\ cm^{-2} \qquad (2.12)$$

Hydrogen adsorption and stripping may be an unreliable method for measuring the electrode Pt surface area of bimetallic Pt catalysts and its measured value can be larger than the true value because of uptake of hydrogen by the oxidised second metal [54, 55].

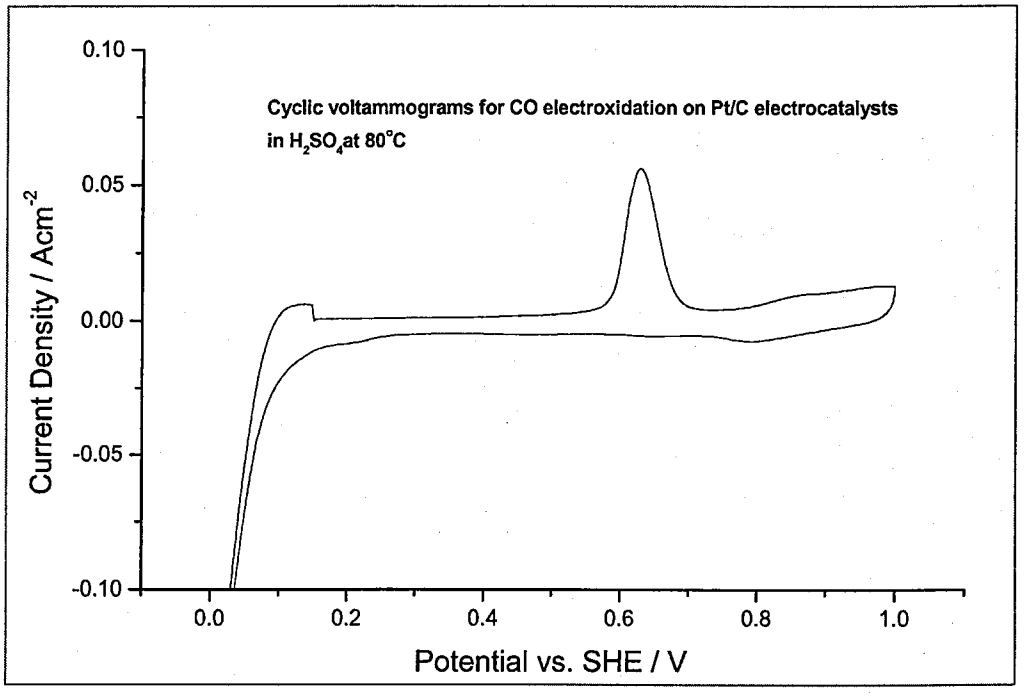

Figure 2.19 CO cyclic voltammogram of Pt/C catalysts in 1 M H_2SO_4 at 80 °C

CO stripping voltammetry is currently the favoured method for measuring the electrode Pt surface area of bimetallic Pt catalysts [53, 56, 57]. The electrode Pt surface

area (EPSA) can be determined from *in situ* cyclic voltammetry, by measuring the charge for the electrooxidation of CO to CO_2. In this procedure CO is adsorbed on the catalyst surface and the electrode potential increased until the CO is oxidised, indicated by an increase in the current. The activity of the catalysts can be compared by comparing the potential at which the reaction starts (known as the *onset potential*) and the potential at which the reaction is at a maximum (the *peak potential*). Figure 2.19 shows a typical CO cyclic voltammogram for a Pt/C catalyst. The determination of EPSA is based on the determination of the CO electrooxidation peak area. This involves measuring the charge for the electrooxidation of CO to CO_2 from the cyclic voltammogram and calculating the EPSA based on the established ratio of charge to Pt surface area for the catalyst [50, 58].

Usually the ratio 420 $\mu C\ cm^{-2}$ Pt is used to calculate the electrode Pt surface area [50, 58, 59] assuming that there are 1.305×10^{15} Pt atoms/cm^2 and that two surface atoms accommodate one CO molecule [59]. To get what we call the electrochemical surface area (ECA), EPSA is divided by the mass of Pt. The ECA allows us to compare the area per unit mass of Pt of electrodes with different Pt loadings.

2.4.2.3 Apparatus and experimental procedure

Cyclic voltammetry experiment

The electrochemical catalytic activity of the Pt/C and the various M-Pt/C electrocatalysts was characterized using cyclic voltammetry. The three-electrode compartment cell used in the cyclic voltammetry experiments is shown in Figure 2.20. The electrode was placed in a 100 ml beaker, wetted with de-ionised water and isopropanol, 20 ml de-ionised water was added, and boiled for 10 minutes. The 1 mg Pt cm^{-2} electrode was mounted into the three-electrode compartment cell using a gold clip. A Standard Hydrogen Electrode (SHE) was used as the reference electrode, platinum foil

as the counter electrode and 1M sulfuric acid as the electrolyte. The electrochemical cell was maintained at 25 °C by immersion in a thermostated water bath. The cyclic voltammograms were recorded using an EG & G Princeton Applied Research Potentiostat /Galvanostate Model 273A. A creative electrochemistry software (Headsaart version 1.4) was used to record the cyclic voltammograms. All the cyclic voltammograms were recorded at a scan rate of 10 mV s^{-1} in the potential range 0 to 1.2 V *vs*. SHE.

CO cyclic voltammetry experiment

The electrode Pt surface area (EPSA) was carried out by the electrooxidation CO to CO_2 from the cyclic voltammetry in a Half-Cell apparatus (Figure 2.21). The 0.35 mg Pt cm^{-2} electrode was mounted into the three-electrode compartment cell of the Half-Cell apparatus. A Standard Hydrogen Electrode (SHE) was used as the reference electrode, platinum foil as the counter electrode and 1 M sulfuric acid as the electrolyte. The electrochemical cell was maintained at 80 °C by immersion in a thermostatic water bath. The CO was bubbled into the cell for 5 minutes followed by a 10 minute purge with N_2. The CO cyclic voltammograms were recorded using an EG & G Princeton Applied Research Potentiostat /Galvanostate Model 273A. A creative electrochemistry software (Headsaart version 1.4) was used to record the cyclic voltammograms. All the cyclic voltammograms were recorded at a scan rate of 10 mV s^{-1} in the potential range 0 to 1.2 V *vs*. SHE.

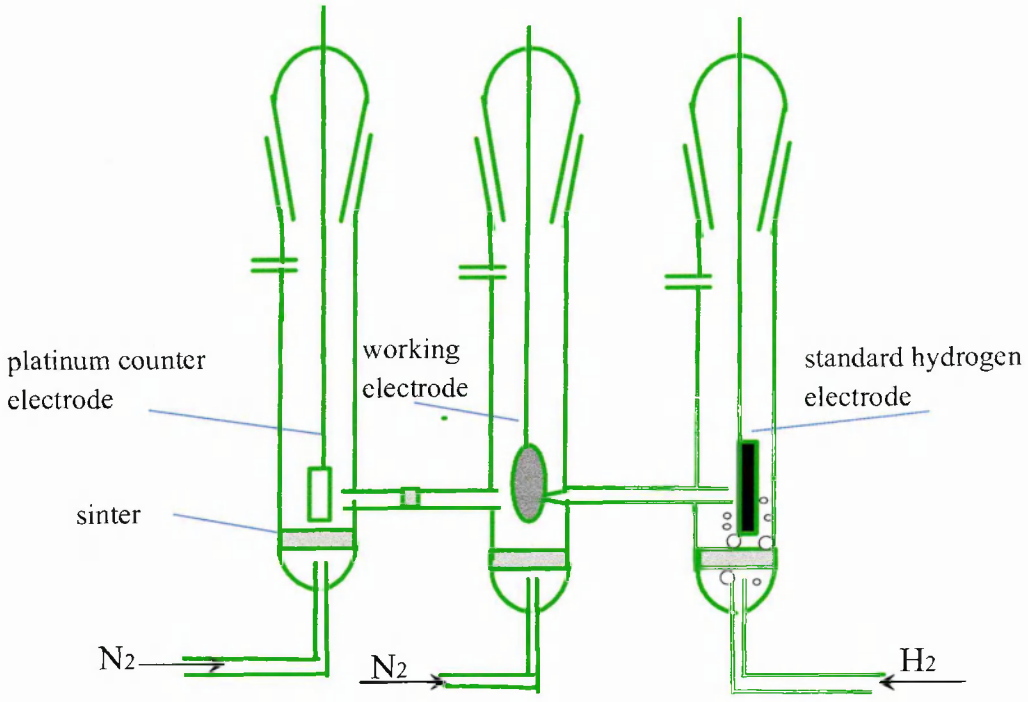

Figure 2.20 Three-electrode cell used in cyclic voltammetry experiments

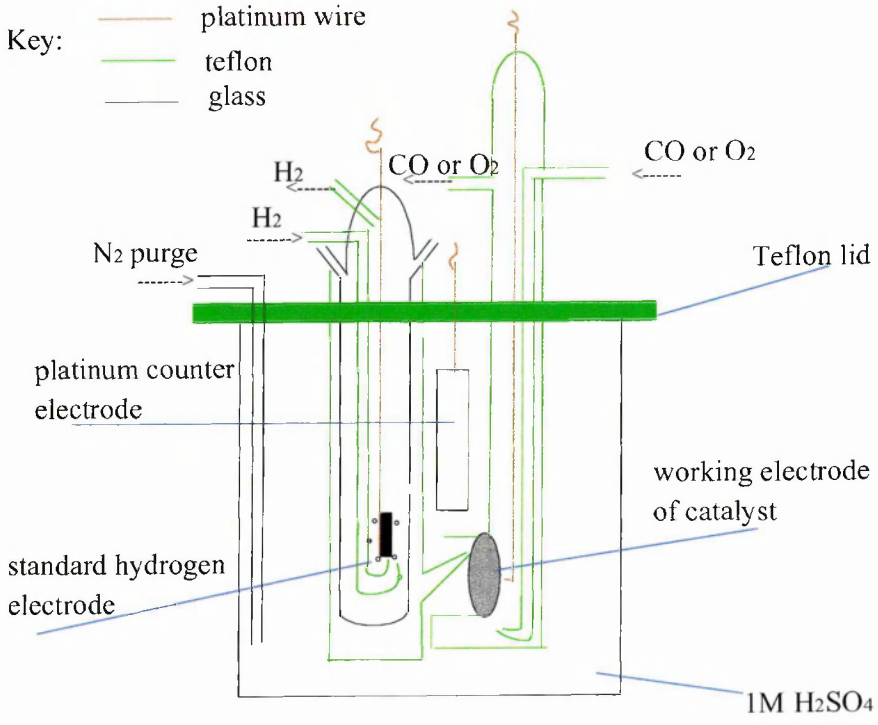

Figure 2.21 Half-cell used in the electrode Pt surface area and steady state galvanostatic/potentiostat experiments

2.4.3 Steady State Galvanostatic Polarization

2.4.3.1 Introduction

Steady state galvanostatic polarisation is carried out by applying a controlled current between the working electrode (electrode under study) and the counter (auxiliary) electrode with a current source (called a galvanostat) and determining the potential between the working electrode and a reference electrode (Figure 2.22). These measurements were used for the assessment of the activity of catalysts towards the oxygen-reduction reaction (ORR) at the cathode.

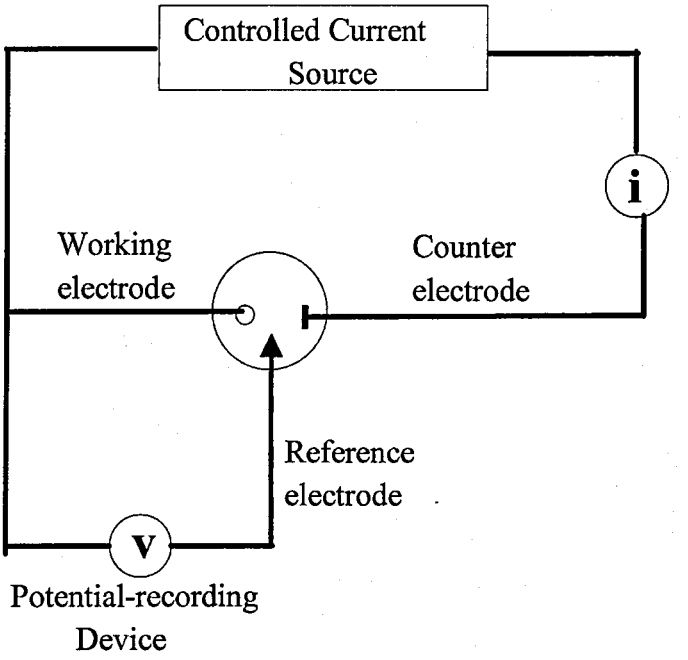

Figure 2.22 Diagram for Steady State Galvanostatic Polarization

2.4.3.2 Theory

The Butler-Volmer equation is a general representation of the polarization of an electrode supporting one redox system

$$i = i_0(\exp(\frac{\alpha nF\eta}{RT}) - \exp(\frac{(1-\alpha)nF\eta}{RT})) \qquad (2.13)$$

where, i is the anodic or cathodic current density; α the symmetry coefficient (values are typically close to 0.5); $\eta = E_{applied} - E_{eq}$, i.e. positive for anodic polarization and negative for cathodic polarization; n = number of participating electrons; and i_0 is the exchange current density.

For the cathode:

$$i = i_0\left(\exp\frac{-\alpha nF\eta}{RT}\right) \tag{2.14}$$

$$\eta = b_c \log\left(\frac{i_c}{i_o}\right) \tag{2.15}$$

$$b_c = 2.303\left(\frac{RT}{\alpha nF}\right) \tag{2.16}$$

So, $$\eta = E_{applied} - E_{eq} = b_c \log\left(\frac{i_c}{i_o}\right) = a + b\log i \tag{2.17}$$

The current-potential, *i-E*, curves of an electrode reaction are often gained by determining the current as a function of potential.

2.4.3.3 Apparatus and experimental procedure

These galvanostatic polarisation measurements in the half-cell (Figure 2.21) were used for the assessment of catalysts towards the oxygen reduction reaction (ORR). The 0.35 mg Pt cm^{-2} electrode was mounted into a three-electrode compartment cell of the Half-Cell apparatus. A Standard Hydrogen Electrode (SHE) was used as the reference electrode, platinum foil as the counter electrode and 1M sulfuric acid as the electrolyte. The electrochemical cell was maintained at 80 °C by immersion in a thermostatic water bath. The assessment of catalysts towards the oxygen reduction reaction (ORR) at cathode was carried by using the galvanostatic polarization measurement. After the CV experiment, oxygen gas was bubbled through the working electrode compartment.

Autolab's Potentistat/Galvanostat model PGSTAT interfaced with a computer, was used to do the steady state galvanostatic polarisation measurements. All galvanostatic polarisation curves were internal resistance (IR) compensated by measuring the uncompensated ohmic resistance through current-interrupter method using the GPES software supplied with the instrument.

Internal resistance correction of electrodes:

The internal resistance was measured for all half-cell electrodes using the interrupt technique [60]. This technique involved measuring the instantaneous change in the potential of the electrode when the circuit was suddenly broken. This was made possible with a dedicated function on the GS2020 potentiostat. Measurements were made at three different current values and the resistance values averaged to enable a more accurate value of the internal resistance to be determined.

2.4.3.4 Data analyses

Three different analyses of the steady state galvanostatic polarization data were made:

(1) Current-potential curves

The *current-potential curves* are a plot of the PEM fuel cell potential (corrected for cell resistance) *vs* the current density. The current density is the current divided by the geometrical flow area (2.01 cm^2).

(2) Tafel plot

Tafel plots were obtained by the following equation:

$$\eta = a + b\log i \tag{2.18}$$

$\eta = E_{cell} - E_0$, so we can get the new Tafel plot:

$$E_{cell} = a_0 + b\log i \quad (2.19)$$

where E_{cell} is the cell potential, a_0 is a constant which is dependent on the cell operating conditions and the cathode electrocatalyst, b is the Tafel slope for oxygen reduction reaction and i is the current density.

(3) Specific activity plot.

The *specific activity plot* is the PEM fuel cell potential (corrected for cell resistance) *vs* specific activity. Specific activities were calculated from the current density, i, and the electrode Pt surface area (EPSA):

$$\text{Specific activity} = i/\text{EPSA (mA cm}^{-2}\text{Pt)} \quad (2.20)$$

The specific activity compares the intrinsic activity of the Pt present in different catalysts in terms of current per unit area of electrochemically available Pt.

(3) Mass activity plot.

The Mass Activity plot is the PEM fuel cell potential E, (corrected for cell resistance) *vs.* mass activity. Mass activities were calculated from the current density, i, and the electrode Pt loading:

$$\text{Mass activity} = i/\text{Pt loading (A/g Pt)} \quad (2.21)$$

2.5 References

1. B. Didillon, C. Houtman and T. Shay, J. Am. Chem. Soc., 1993. **115**: p. 9380.
2. E. M. Crabb, R. Marshall and D. Thompsett, J. Electrochem. Soc., 2000. **147**: p. 4440.
3. E. M. Crabb and M.K. Ravikumar, Electrochim. Acta, 2001. **46**: p. 1033.
4. L. Keck, US Patent 5068161, 1991.
5. G.W. Ewing, Instrumental methods of chemical analysis, McGraw-Hill Book Company, 1975.
6. A. Putnis and R.C. Liebermann, Transmission electron microscopy of minerals and rocks, Cambridge University, 1991.
7. H.H. Willard, J. L.L. Merritt and J.A. Dean, Instrumental methods of analysis, D. Van Nostrand Company, 1974.
8. T.A. Carlson, Photoelectron and Auger Spectroscopy, Plenum Press, 1975.
9. B. D. Cullity, Elements of X-ray diffraction, Second Edition, Addision-Wesley Publishing Company, 1978.
10. J.L. Falconer and J.A. Schwarz, Catal. Rev. -Sci. Eng., 1983. **25**: p. 141.
11. N. W. Hurst, S. J. Gentry and A. Jones, Catal. Rev.-Sci. Eng., 1982. **24**: p. 233.
12. *http://www.chemistry.ccsu.edu (02/20/2003 12:58:32).*
13. G.G. Bond, Heterogeneous Catalysis --- Principles and Applications, Second Edition, Oxford Science Publications, 1987.
14. S. J. Gregg and K.S.W. Sing, Adsorption, Surface Area and Porosity, Second Edition, Academic Press Inc., 1982.
15. Physical Chemistry --- Principles of chemical change (S342 Block 5), The Open University, 2002.
16. J.R. Anderson, Structure of Metallic Catalysts, Acadmic Press, 1975.
17. S. Brunauer, P.H. Emmett and E. Teller, J. Am. Chem. Soc., 1938. **60**: p. 309.

18. I. Langmuir, J. Am. Chem. Soc., 1916. **38**: p. 2221.

19. R. Marshall, PhD Thesis, The Open University, 1998.

20. *http://materials.open.ac.uk/ (03/22/2003 16:38:39).*

21. C.R. Adams, H.A. Benesi, R.M. Curtis and R.J. Meisenheimer, J. Catal., 1962. **1**: p. 336.

22. W. Zou and R.D. Gonzalez, J. Catal., 1992. **133**: p. 202.

23. Thomas A. Carlson, Photoelectron and Auger Spectroscopy, Plenum Press, 1975.

24. Physical Chemistry --- Principles of chemical change (S342 Block 6), The Open University, 1996.

25. *http://www.casaxps.com/help_manual/XPSInformation/XPSInstr.htm (11/28/2003 10:33:11).*

26. R.D. Gonzalez and H. Miura, Catal. Rev. -Sci. Eng., 1994. **36**: p. 145.

27. L.E. Smart and E.A. Moore, Solid State Chemistry, An Introduction, Second Edition, Stanley Thornes, 1998.

28. A.R. West, Basic Solid State Chemistry, John Wiley & Sons Ltd., 1998.

29. H&M Analytical Services Inc, Siemens manual for the D5000 diffractometer., 1999.

30. W. Juszczyk, J. Pielaszek, Z. Karpinski and F. Pinna, Appl.Cat. A: Gen., 1996. **144**: p. 281.

31. F. Pinna, M. Selva, M. Signoretto, G. Strukul, F. Boccuzzi, A. Benedetti, P. Canton and G. Fagherazzi, J. Catal., 1994. **150**: p. 356.

32. STA Hardware Manual, Rheometric Scientific, 1996.

33. R. A. Lampitt, L. P.L. Carrette, M. P. Hogarth and A. E. Russell, J. Electroanal. Chem., 1999. **460**: p. 80.

34. E.M. Crabb, M.K. Ravikumar, Y.Qian, A.E. Russell, S. Maniguet, J. Yao, D. Thompsett, M. Hurford and S.C. Ball, Electrochemical and Solid-State Letters, 2002. **5**: p. 5.

35. S. Maniguet, R.J. Mathew and A.E. Russell, J. Phys. Chem. B, 2000. **104**: p. 1998.

36. M.C.S. Sierra, J.G. Ruiz, M.G. Proietti and J. Blasco, J. Mol. Catal. A; Chemical, 1996. **108**: p. 95.

37. H.D. Abruna, Electrochemical Interfaces, New York, 1991.

38. B.K.Teo, EXAFS: Basic Principles and Data Analysis, Springer Verlag, Berlin-Heidelberg, 1986.

39. P.A. Lee and J.B. Pendry, Phys. Rev. B, 1975. **11**: p. 2795.

40. N. Binstead, EXCURV98: CCLRC Daresbury Laboratory computer program, 1998.

41. C.H. Hamann, A. Hammnett and W. Vielstich, Electrochemistry, Wiley-Vch, 1998.

42. A.J. Bard and L.R. Faulkner, Electrochemical Methods, John Wiley, 1980.

43. The Southhampton Electrochemistry Group, Instrumental Methods in Electrochemistry, Ellis Horwood, 1985.

44. A.J. Appleby and F.R. Foulkes, Fuel Cell Handbook, Van Nostrand Reinhold, 1989.

45. D.T. Sawyer, A. Sobkowiak and J.L. Roberts. Jr. , Electrochemistry For Chemists, Wiley-Interscience, 1995.

46. W. Vielstich and D.J.G. Ives, Fuel Cell, Wiley-Interscience, 1965.

47. H.A. Liebhafsky and E.J. Cairns Jr., Fuel Cells and Batteries, 1965.

48. L. Giorgi, E. Antolini, A. Pozio and E. Passalacqua, Electrochim. Acta, 1998. **43**: p. 3675.

49. E. Antolini, L. Giorgi, A. Pozio and E. Passalacqua, J. Power Source, 1999. **77**: p. 136.

50. T.R. Ralph and M.P. Hogarth, Platinum Metal Review, 2002. **46**: p. 3.

51. D. R. Lowde and J.O. Williams, Appl. Surf. Sci., 1978. **1**: p. 215.

52. A. Essalik, K. Amouzegar and O. Savagogo, J. Appl. Electrochem., 1995. **25**: p. 404.

53. C. L. Green and A. Kucernak, J. Phys. Chem. B, 2002. **106**: p. 1036.

54. K. Kinoshita and P.N. Ross, J. Electroanal. Chem., 1977. **78**: p. 313.

55. J. Jiang and A. Kucernak, J. Electroanaly Chemistry, 2003. **543**: p. 187.

56. H. A. Gasteiger, N. Markovic, P.N. Ross and E.J. Cairns Jr, J. Phys. Chem., 1994. **98**: p. 617.

57. T. Schmidt, M. Noeske, H. Gasteiger, R.J. Behm, P. Britz, W. Brijoux and L. H. Bonnemann, Langmuir, 1997. **13**: p. 2591.

58. T.R. Ralph, G.A. Hards, J.E. Keating, S.A. Campbell, D.P. Wilkinson, M. Davis, J. St-Pierre and M. C. Johnson, J .Electrochem. Soc., 1997. **144**: p. 3845.

59. J. Bett, K.Kinoshita, K. Routsis and J.C. P. Stonehart, J. Catal., 1973. **29**: p. 160.

60. M. Hayes and A.T.Kuhn, J. Power Sources, 1977. **2**: p. 121.

Chapter 3 Preparation and characterization of carbon supported Pt-based bimetallic electrocatalysts

3.1 Introduction

This chapter discusses the preparation and characterization of carbon supported Pt-based bimetallic catalysts. A series of PtFe/C, PtNi/C, PtCo/C and PtCr/C bimetallic catalysts prepared using surface organometallic chemistry (SOMC) will be described in Section 3.2. UV-visible spectroscopy, ICP, TGA and DSC were used to analyse the composition of the catalysts and to postulate a reaction mechanism for the SOMC reaction during the catalyst preparation. The physical characterization of pure Pt/C and the PtM/C bimetallic catalysts was performed using TEM/EDX, BET, chemisorption, X-ray diffraction, XPS, TPR, and EXAFS methods (Section 3.3). The main aims of the characterization were:

- to determine whether a selective reaction had occurred between the reduced surface Pt of the Pt/C catalyst and the organometallic precursor of the second metal (TEM/EDX, BET, chemisorption and X-ray diffraction);
- to determine whether an alloy was formed between surface Pt and the second metal (XRD, EXAFS);
- to determine the metal oxidation state of the pure Pt/C and the PtM/C bimetallic catalysts (EXAFS, TPR and XPS);
- to determine the metal particle size of the pure Pt/C and the PtM/C bimetallic catalysts (TEM/EDX, BET and chemisorption, X-ray diffraction).

3.2 Preparation of PtM/C bimetallic catalysts (M = Fe, Ni, Cr or Co) using SOMC method

3.2.1 The Preparative Procedure

A series of PtM/C bimetallic catalysts namely, *x*PtFe/C, *x*PtNi/C, *x*PtCr/C and *x*PtCo/C (x = 0.25 – 1.0) were prepared from the Pt/C catalyst using the appropriate metallocene $M(C_5H_5)_2$ (where M is Fe, Ni, Cr or Co). The number (x) represents the theoretical surface coverage of surface Pt sites by M. The detailed preparation procedure for the PtM/C bimetallic catalysts using SOMC, and subsequent heat treatment, were described in Chapter 2. Typical results for the PtM/C bimetallic catalysts prepared using SOMC are listed in the first column in Table 3.1, which also gives the mass of precursor used (column 3). Column 2 shows the mass of Pt/C taken. The mass of precursor was calculated using the weight of 20% Pt/C taken, the dispersion of 20% Pt/C measured using H_2 chemisorption, and the theoretical surface coverage of surface Pt sites by M required expressed in monolayer equivalents. Thus the mass of precursor can be calculated according to the equation (3.1):

$$W = \frac{20\% \times W_{Pt}}{195} \times H/Pt \times RMM \times x \qquad (3.1)$$

where W_{Pt} is the mass of 20% Pt/C; H/Pt is the dispersion of 20% Pt/C (H/M = 0.40 for PtFe and 0.48 for the other systems); 195 is the relative molar mass of Pt; RMM is the relative molar mass of $M(C_5H_5)_2$ and x is the theoretical surface coverage of surface Pt sites by M expressed in monolayer equivalents.

Four blank reactions between the carbon black support and metallocene $M(C_5H_5)_2$ were also performed for each metal using the same procedure and are given as Fe/C, Ni/C, Cr/C, and Co/C.

For each catalyst the required amount of the organometallic precursor, the metallocene $M(C_5H_5)_2$, was dissolved in *n*-heptane and added under nitrogen to the reactor containing the reduced Pt/C catalyst. Hydrogen gas was then passed through the reactor. The reaction was allowed to continue at room temperature for 12 hours and then at 90 - 95 °C for a further 8 - 12 hours.

Table 3.1 Preparation of PtM/C bimetallic catalysts

Sample	**20%Pt/C /g**	**Required $M(C_5H_5)_2$ /g ***	**$M(C_5H_5)_2$ in filtrate /g ****	**$M(C_5H_5)_2$ (reacted or decomposed) / %**
0.25 PtFe/C	1.50	0.028	0	100
0.50 PtFe/C	2.00	0.075	0	100
0.75 PtFe/C	1.10	0.062	0.003	95.2
1.0 PtFe/C	2.00	0.149	0.008	94.6
Fe/C	1.0 g carbon	0.075	0.069	8.0
0.25 PtNi/C	2.00	0.045	0	100
0.50 PtNi/C	2.00	0.091	0	100
0.75 PtNi/C	1.50	0.102	0	100
1.0 PtNi/C	1.50	0.136	0	100
Ni/C	1.5 g carbon	0.136	0.128	5.9
0.25 PtCr/C	2.00	0.043	0	100
0.50 PtCr/C	2.00	0.087	0	100
0.75 PtCr/C	2.00	0.130	0.012	90.8
1.0 PtCr/C	2.00	0.173	0.028	83.8
Cr/C	1.5 g carbon	0.087	0.080	8.1
0.25 PtCo/C	2.51	0.057	0	100
0.50 PtCo/C	3.09	0.140	0	100
0.75 PtCo/C	2.51	0.171	0	100
1.0 PtCo/C	2.50	0.228	0	100
Co/C	1.5 g carbon	0.137	0.129	5.8

Note:* The dispersion of Pt/C, H/M, is 0.40 for PtFe/C preparation; and 0.48 for other PtM/C preparations
**Determined using UV-visible analysis of the filtrate after reaction

The reaction was continuously monitored by analyzing the exit gas using gas chromatography. GC-MS was used to identify the products for the PtM/C catalysts. Cyclopentane was the only product observed. The retention time of the product was the same for all the systems. For the PtFe/C and PtNi/C bimetallic catalysts cyclopentane attained a maximum after 2 hours at room temperature before decreasing until almost no cyclopentane was detected after 12 hours. On heating the reaction to 90 – 95 °C, further cyclopentane evolution occurred until after 8 – 12 hours no cyclopentane was detected. For one of the PtCo/C catalysts, cyclopentane was only observed at room temperature, suggesting that $Co(C_5H_5)_2$ easily reacted with Pt/C or had decomposed. For the PtCr/C catalyst, cyclopentane was detected at room temperature, and also during the 3 hour reaction at 90 - 95 °C. In addition for all systems, the colour intensity of the metallocene solution changed considerably during the reaction. Table 3.2 shows the colours of different metallocenes [1, 2]. The intensity of the colour of the metallocene in heptane solution decreased to an observable extent during the reaction at room temperature, and decreased to a light colour, or disappeared completely during the reaction at 90 – 95 °C, depending on the metal.

Table 3.2 The physical description of $M(C_5H_5)_2$

$M(C_5H_5)_2$	**Colour**	**Stability in ethanol / mg ml^{-1}**	**Sensitivity**	
			Air	**Light**
$Fe(C_5H_5)_2$	orange-yellow	stable for at least 24 hours	stable after prolonged exposure	stable after prolonged exposure
$Ni(C_5H_5)_2$	deep purple	decompose	sensitive	No available data
$Cr(C_5H_5)_2$	reddish-purple	stable	very sensitive	sensitive
$Co(C_5H_5)_2$	dark-blue	decompose after 2 hours	very sensitive	sensitive

After the reaction the contents of the reactor were discharged, filtered, and washed with *n*-heptane to remove unreacted organometallics. The concentration of

unreacted organometallics in the filtrates was determined using UV-visible spectrometry and the results are shown in column 4 of Table 3.1.

3.2.2 Analysis of catalyst composition

The UV-visible spectra of the filtrate of PtM/C catalysts are shown in Figures 3.1 – 3.4, and spectra data summarized in Table 3.1. In UV-visible spectra the absorbance peak at 200 – 400 nm (UV range) result from $-(C_5H_5)_2$ group. The exact peak position and shape varies with different metals, M. The peak at 400 – 700 nm (visible spectrum range) in the UV-visible spectra results from the color of the solution tested. The results showed that there was no unreacted metallocene observed for the 0.25PtFe/C, 0.50PtFe/C and 0.25PtCr/C, 0.50PtCr/C catalysts. Unreacted $Fe(C_5H_5)_2$ or $Cr(C_5H_5)_2$ were detected, however, for the catalysts with the higher iron or chromium loadings, 0.75PtFe/C, 1.0PtFe/C and 0.75PtCr/C, 1.0PtCr/C, suggesting that there is a limitation for the deposition of Fe or Cr on surface Pt. There was no unreacted $Ni(C_5H_5)_2$ and $Co(C_5H_5)_2$ detected in the filtrate for PtNi/C and PtCo/C catalysts from UV-visible spectra analysis, suggesting that either all the $Ni(C_5H_5)_2$ and $Co(C_5H_5)_2$ had reacted, or had decomposed.

Four blank reactions between the carbon black support and $M(C_5H_5)_2$ were also performed using the same preparation procedure. The aim of blank reactions was to determine whether the second metal had been deposited on the carbon support. The colour of $M(C_5H_5)_2$ solution did not change during the reaction. The concentration of unreacted $M(C_5H_5)_2$ in the filtrate, given in Table 3.1, indicated that no significant reaction took place between the support and the precursor for any system. The slight loss of $M(C_5H_5)_2$ seen may be due to limited reaction of some of the $M(C_5H_5)_2$ with the support or loss after the filtration. Thus these experimental results suggest that the second

metals did not deposit to any significant extent on to the carbon support during the SOMC reaction.

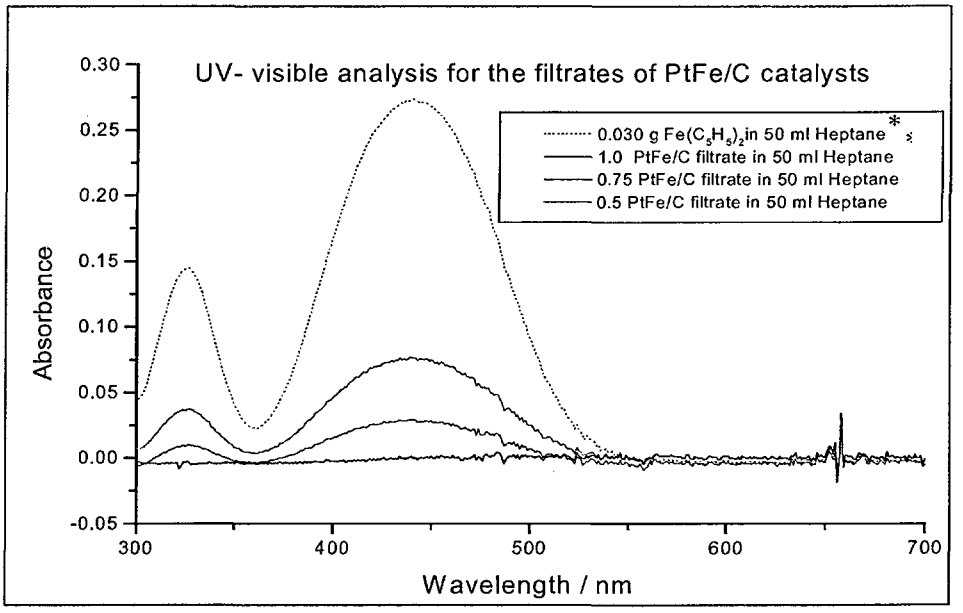

*

Figure 3.1 UV-visible analysis for the filtrates of PtFe/C catalysts

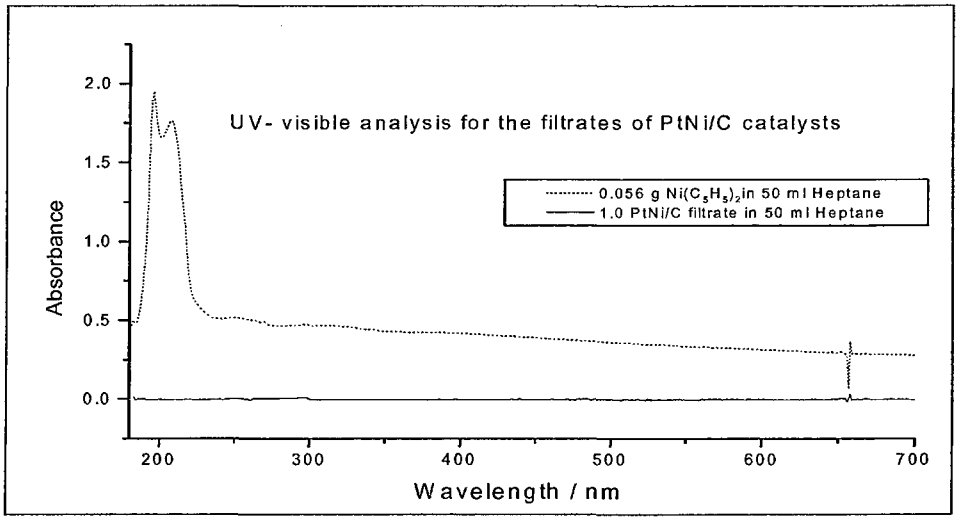

Figure 3.2 UV-visible analysis for the filtrates of PtNi/C catalysts

*The catalyst was washed using 50 ml of heptane to give the filtrate for analysis

The assay of the PtM/C catalysts determined using Inductively Coupled Plasma Atomic Emission Spectroscopy (ICP-AES) is given in Table 3.3. The second and third columns in Table 3.3 show that the platinum experimental data and theoretical calculation data are the same within experimental error, meaning that almost no platinum from the Pt/C catalyst was lost during SOMC.

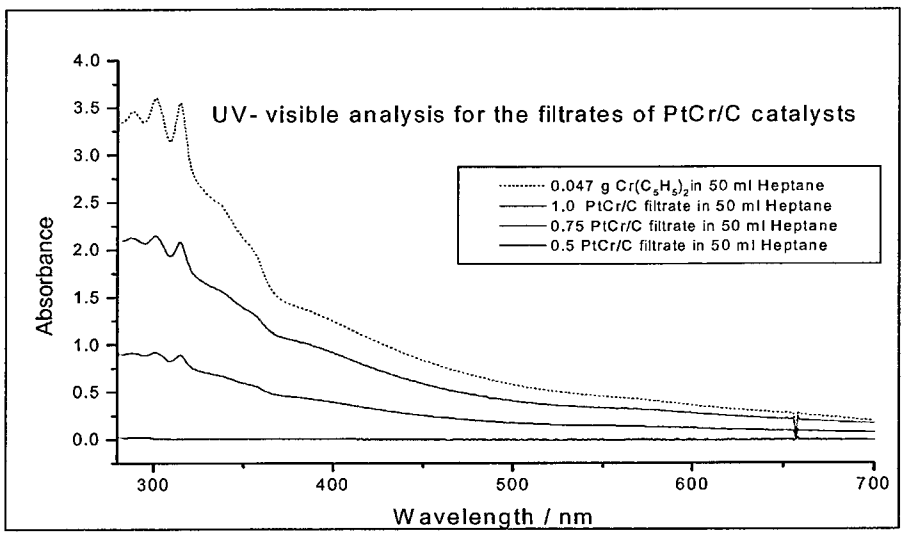

Figure 3.3 UV-visible analysis for the filtrates of PtCr/C catalysts

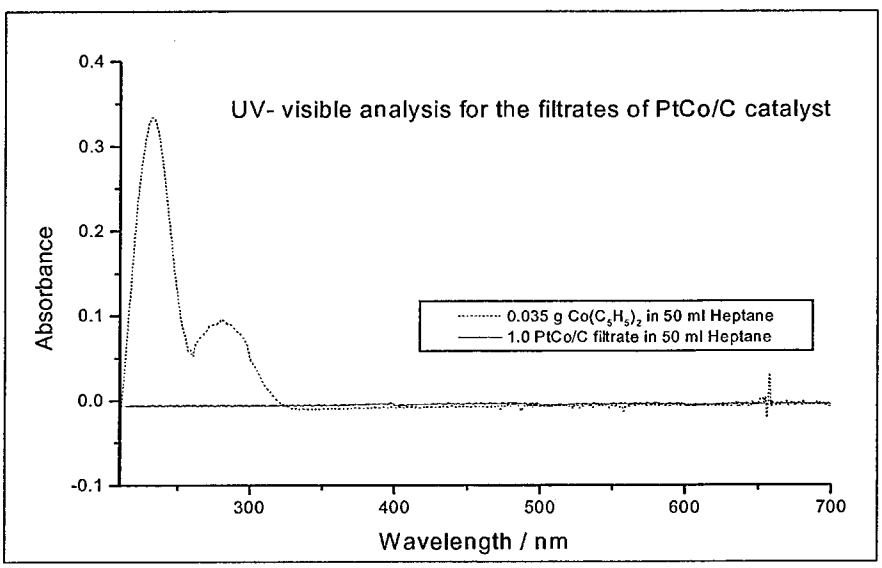

Figure 3.4 UV-visible analysis for the filtrates of PtCo/C catalysts

A comparison of the theoretical and experimental wt% of the second metal (fourth and fifth columns in Table 3.3) indicates, within experimental error, that almost all of the Fe and Cr were deposited on the Pt/C catalyst for the 0.25PtFe/C, 0.25PtCr/C, 0.5PtFe/C and 0.5PtCr/C catalysts, However, the iron or chromium content is slightly lower than predicted for the 0.75PtFe/C, 0.75PtCr/C, 1.0PtFe/C and 1.0PtCr/C catalysts, in agreement with UV-visible results, suggesting again that there is a limit for the deposition of Fe or Cr on surface Pt under the reaction conditions used. Similar results were found for the PtCo/C catalysts with similar metal content for the 0.75 and 1.0PtCo/C catalysts, however, unreacted $Co(C_2H_5)_2$ was not picked up in the UV-visible results.

For all the PtNi/C and most PtCo/C catalysts, there is a significant difference between the experimental data and theoretical metal content data (the fourth and fifth columns in Table 3.3), suggesting in each case, that some of the second metal did not deposit on Pt/C catalyst after the SOMC reaction. However, no $Ni(C_5H_5)_2$ or $Co(C_5H_5)_2$ from the filtrate was found in the UV-visible results. The discrepancies between UV-visible and ICP-AES is likely to be due to decomposition of the starting materials during the preparation process, so that no unreacted metallocene starting material is detected in the UV-visible in these cases. Table 3.2 shows some physical properties of $M(C_5H_5)_2$ [2]. $Ni(C_5H_5)_2$ and $Co(C_5H_5)_2$ easily decompose in some organic solvents, for example, ethanol, thus these may decompose in the heptane solution during the reaction and hence are not observed in analysis of the filtrate.

The fact that no $Ni(C_5H_5)_2$ or $Co(C_5H_5)_2$ was detected by UV-visible in the filtrate, and that ICP-AES analysis shows lower than expected Ni and Co concentrations, suggests that, for the PtNi/C and PtCo/C catalysts, $Ni(C_5H_5)_2$ or $Co(C_5H_5)_2$ partially decomposed during SOMC reaction. The decomposition of $Ni(C_5H_5)_2$ and $Co(C_5H_5)_2$ in

the filtrate would expect to produce metal ion formation. To verify this suggestion, we tested $Ni(NO_3)_2$ and $CoCl_2.6H_2O$ solutions (50 mg in 50 ml), and no absorption peaks in the UV range studied were observed at these concentrations (Figure 3.5), similar to that of the filtrate of all PtNi/C and 1.0PtCo/C catalysts.

Table 3.3 ICP Analysis of PtM/C catalyst samples

Catalyst	Pt Assay Wt%	Theoretical Pt Wt% (*)	M Assay Wt%	Theoretical M Wt% (*)	M:Pt_s ratio (ICP)
0.25PtFe/C	18.5 ±1.5	19.9	0.6 ±0.2	0.7	0.24
0.5PtFe/C	18.6 ±1.5	19.7	1.1±0.2	1.3	0.43
0.75PtFe/C	18.5 ±1.5	19.6	1.6 ±0.3	2.0	0.63
1.0PtFe/C	18.1 ±1.5	19.5	2.0 ±0.3	2.7	0.80
0.25PtNi/C	18.5 ±1.5	19.9	0.3 ±0.2	0.7	0.11
0.5PtNi/C	18.7 ±1.5	19.7	0.5 ±0.2	1.4	0.18
0.75PtNi/C	19.0 ±1.5	19.6	0.8 ±0.2	2.1	0.29
1.0PtNi/C	18.5 ±1.5	19.4	1.1 ±0.2	2.8	0.41
0.25PtCr/C	19.5 ±1.5	19.9	0.5 ±0.2	0.6	0.20
0.5PtCr/C	18.7 ±1.5	19.7	1.2 ±0.3	1.3	0.50
0.75PtCr/C	19.1 ±1.5	19.6	1.3 ±0.3	1.9	0.53
1.0PtCr/C	19.3 ±1.5	19.5	1.5 ±0.3	2.5	0.61
0.25PtCo/C	19.4 ±1.5	19.9	0.7 ±0.2	0.7	0.25
0.5PtCo/C	19.1 ±1.5	19.7	1.0 ±0.2	1.4	0.37
0.75PtCo/C	19.3 ±1.5	19.6	2.2 ±0.3	2.1	0.77
1.0PtCo/C	19.0 ±1.5	19.4	2.1 ±0.3	2.8	0.77

Note: * Calculated by amounts of 20% Pt/C and the Pt/C dispersion of 0.48.

According to the results of UV-visible and ICP (Table 3.3), the main conclusions about the preparation of PtM/C bimetallic catalysts are summarized as follows:

i) For the PtFe/C and PtCr/C bimetallic catalysts, the amount of Fe or Cr deposited on the surface Pt of Pt/C catalyst increases as $Fe(C_5H_5)_2$ or $Cr(C_5H_5)_2$ increases. Good agreement between the theoretical and experimental compositions is found for x = 0.25 or 0.5 (x is the theoretical surface coverage of surface Pt sites by M expressed in monolayer equivalents). Thus the reaction between Pt/C and iron (or chromium) appears to be complete in these two cases. However, there seem to be saturation when x exceeds 0.5. The assays for the 0.75PtFe/C, 0.75PtCr/C, 1.0PtFe/C and 1.0PtCr/C are lower than the theoretical values and suggest that the reaction between Pt/C and iron or chromium is incomplete. Indeed, this is consistent with UV-Visible spectra of the filtrates of these four samples at the end of the preparation procedure, which showed the presence of unreacted iron or chromium in solution.

ii) According to the ICP results, the amount of Ni deposited on the surface Pt of Pt/C catalyst was considerably less than expected. For the PtCo/C, the saturation of Co deposited on the surface Pt of Pt/C catalyst appear at x = 0.75. However, UV-Visible spectra of the filtrates of PtCo/C and PtNi/C catalysts at the end of the preparation procedure did not show the presence of unreacted nickel or cobalt in solution. This suggests that $Ni(C_5H_5)_2$ or $Co(C_5H_5)_2$ are more easily decomposed under the conditions of bimetallic catalyst preparation.

iii) It appears that the reaction is saturated at approximately half-monolayer level for PtFe/C or PtCr/C catalysts and three quarter monolayer level for PtCo/C

catalyst under the experimental conditions used. Crabb et al [3] reported that this saturation of the Pt surface was observed at different coverage for different metals and suggested that the size of the organometallic fragments adsorbed on the platinum surface blocking access of more second metal to the surface could be a contributing factor.

iv) For simplification of reference, the catalysts will be referred to throughout by the *theoretical* M:Pt surface mole ratio, and *not* the ICP determined value.

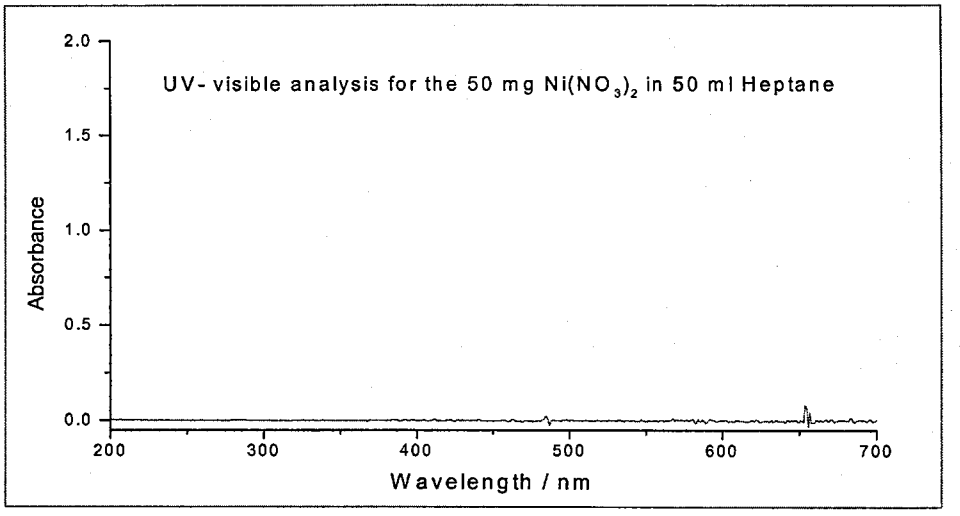

(a)

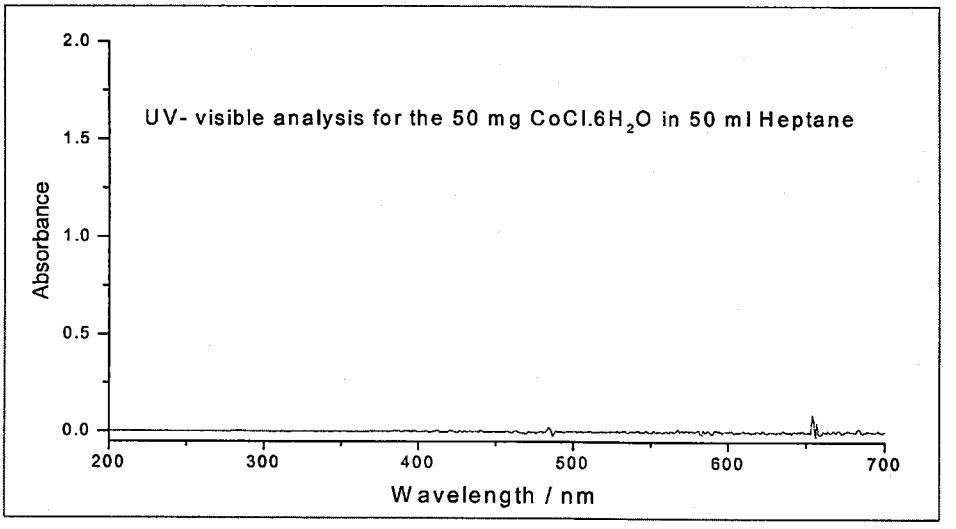

(b)

Figure 3.5 UV-visible analysis for (a) $Ni(NO_3)_2$ and (b) $CoCl_2.6H_2O$

3.2.3 The mechanism of PtM/C catalysts preparation using SOMC

The TGA thermograms of 20% Pt/C and 0.25PtFe/C catalyst (before 200 °C reduction) are shown in Figure 3.6 and Figure 3.7. Any weight loss up to 120 °C is due to loss of adsorbed moisture and the evaporation of heptane deposited on catalysts during the preparation procedure. The TGA indicates that the 20% Pt/C and 0.25PtFe/C catalysts only lose 1% weight up to 300 °C, and 3% weight up to 600 °C, respectively. This means that 20 wt% Pt/C and 0.25PtFe/C catalysts are stable to heat treatment up to this temperature. This stability of the catalyst is enough for PEM fuel cells to operate at 80 °C.

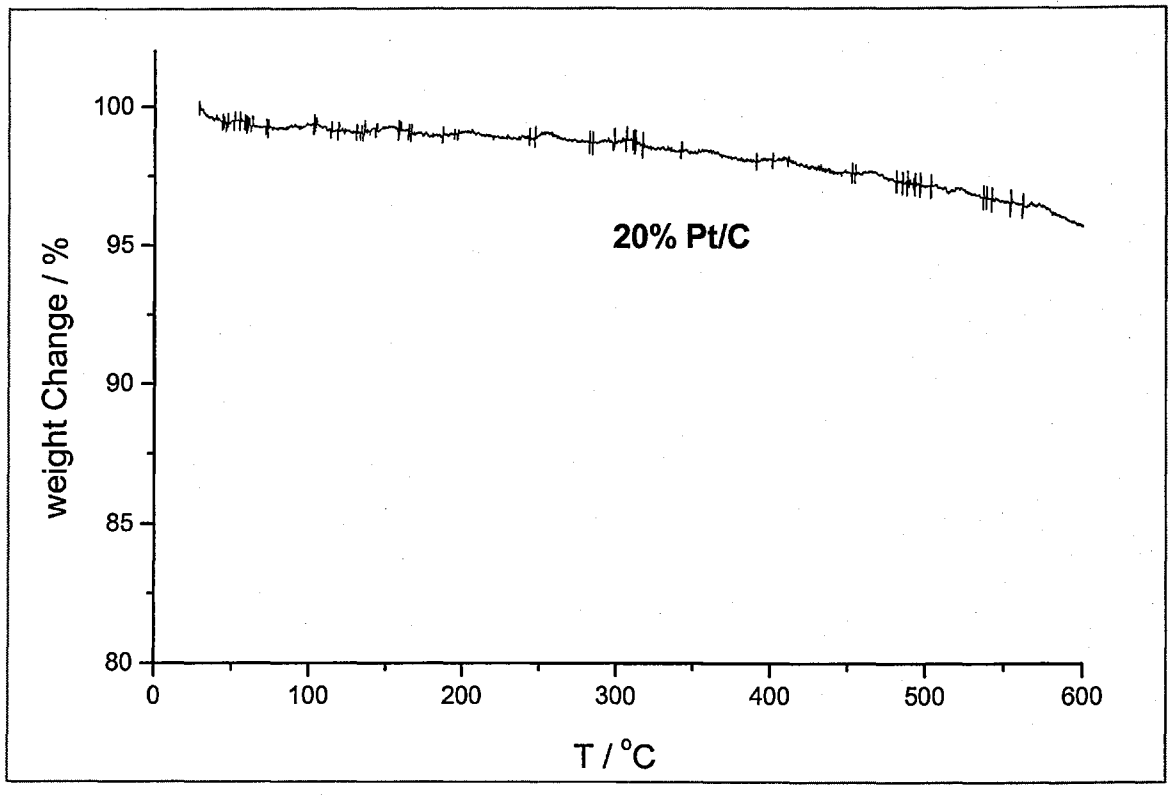

Figure 3.6 TGA thermogram of 20% Pt/C catalyst

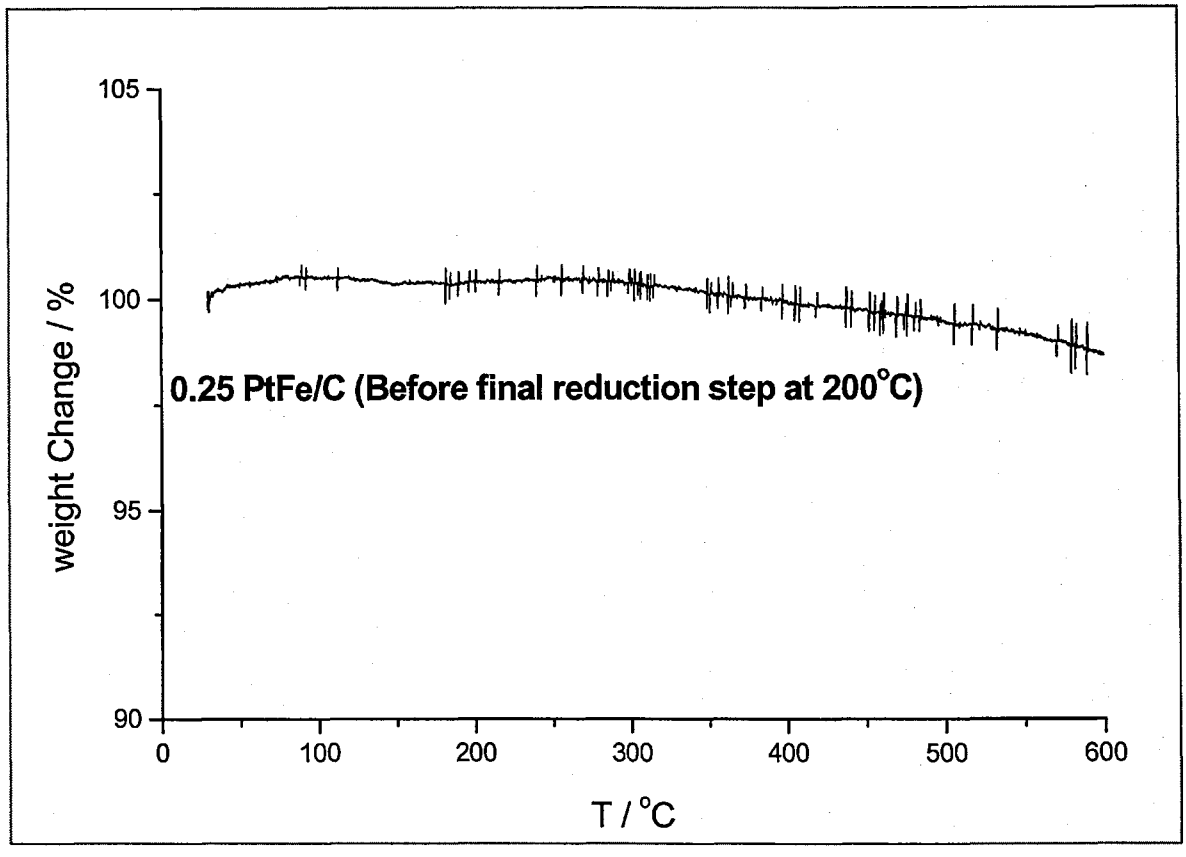

Figure 3.7 TGA thermogram of 0.25PtFe/C catalyst

Figure 3.8 shows the DSC thermograms of the 20% Pt/C and 0.25PtFe/C catalysts (before reduction at 200 °C). In the curve of 20% Pt/C obtained in 10% H_2 and 90% N_2, a downward exothermic drift was observed as a result of hydrogen adsorption on the Pt/C catalyst because hydrogen continued to pass during the DSC experiment. The gradient above 100 °C is higher than below 100 °C because there was the evaporation of moisture, an endothermic process below 100 °C. In the curve of the 0.25PtFe/C catalyst, the first, broad, strong endothermic peak, corresponding to the evaporation of moisture and heptane, had its maximum at about 82 °C, beginning at ~25 °C and ending at ~108 °C. The second, sharper, strong endothermic peak had a maximum at 150 °C, starting at ~110 °C and ending at ~185 °C. This was attributed to decomposition of an intermediate

organometallic surface species (C_5H_5-M-Pt/C) adsorbed on the catalyst surface. This is consistent with the enthalpy calculation using bond energies. [4, 5]:

$$C_5H_5\text{-M-Pt/C} + 5/2H_2 \rightarrow \text{M-Pt/C} + C_5H_{10} \quad \Delta H^{\circ} = 5.23 \text{ KJ/mol} \tag{3.2}$$

There were no further peaks in the thermogram.

The DSC results suggest that reduction at 200 °C is sufficient to reduce the dried PtFe/C catalyst and remove all ligands after SOMC reaction for the PtFe system.

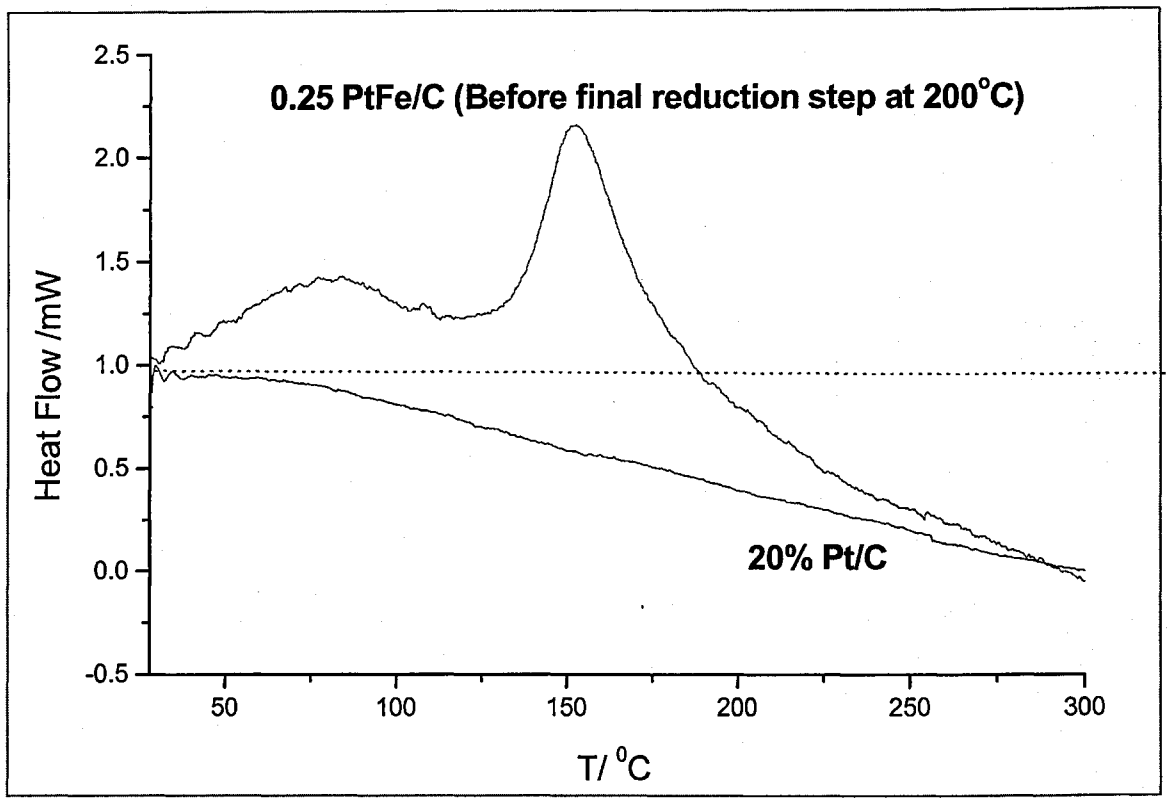

Figure 3.8 DSC thermogram of 20%Pt/C and 0.25PtFe/C catalysts

The SOMC reaction between a metallocene and the reduced Pt/C catalyst has been proposed by a number of authors [6]. Faudon et al prepared silica-supported Pd-Ni catalysts using a monometallic Pd catalyst and nickelocene [3]. This was performed in two steps. A monometallic Pd catalyst (silica-supported Pd catalyst) was first prepared by the cationic coexchange method and nickelocene was decomposed on the surface Pd

catalyst in the isoamylacetate and presence of hydrogen. The simplest written expression of the decomposition reaction is

$$(C_5H_5)_2Ni + 2H_{ads} \rightarrow Ni + 2C_5H_6 \quad (3.3)$$

though other organic products are formed [6, 7].

As our reaction was carried out under hydrogen, we might expect that the hydrogenation of cyclopentadiene could also take place. The progress of the reaction between the reduced Pt/C catalyst and metallocene in our experiments was continuously monitored by analyzing the exit gas using gas chromatography and MS-GC, and cyclopentane was the only product observed, rather than the cyclopentadiene observed by Faudon. Thus the following reaction mechanism is postulated:

- Reduction of Pt/C with H_2 at 200 °C:

$$Pt/C + \tfrac{1}{2}H_2 \rightarrow H\text{-}Pt/C \quad (3.4)$$

- Reaction between metallocene $M(C_5H_5)_2$ and H-Pt/C to form a surface organometallic species, for example such as C_5H_5 -M-Pt/C, followed by reduction with hydrogen during the reaction, and reduction treatment at 200 °C:

$$H\text{-}Pt/C + 2H_2 + M(C_5H_5)_2 \rightarrow C_5H_5\text{-}M\text{-}Pt/C + C_5H_{10} \quad (3.5)$$

- Reduction reaction of C_5H_5 -M-Pt/C with H_2 at 200 °C:

$$C_5H_5\text{-}M\text{-}Pt/C + 5/2H_2 \rightarrow M\text{-}Pt/C + C_5H_{10} \quad (3.6)$$

The overall reaction:

$$Pt/C + 5H_2 + M(C_5H_5)_2 \rightarrow M\text{-}Pt/C + 2C_5H_{10} \quad (3.7)$$

The mechanism postulated above is in agreement with the result of Crabb and Marshall's research on the reaction mechanism of ferrocene with palladium or platinum metal surfaces [8]:

$$Fe(C_5H_5)_2 + 5H_2 \rightarrow Fe + 2C_5H_{10} \quad (3.8)$$

3.3 Characterization of carbon supported Pt-based bimetallic catalysts

In the following sections the physical and surface characterisation of carbon supported Pt and Pt-based bimetallic electrocatalysts will be given.

3.3.1 Transmission electron microscopy (TEM) and energy dispersive X-ray analysis (EDX)

The transmission electron micrograph images for the XC72R carbon and 20% Pt/C samples are shown in Figure 3.9. The larger spheres correspond to individual particles of XC72R carbon-black. The small dense black spheres are Pt particles, which can clearly be seen on the outer surfaces of the carbon-black particles.

The particle size (diameter) was measured directly from TEM micrographs. In order to obtain metal particle size distribution, over three hundred particles visible on the micrographs were measured for each Pt/C or bimetallic PtM/C catalyst using NIH image software. The average metal particle size for each catalyst was calculated using the following equation (3.9):

$$d = \frac{\sum n_i d_i}{\sum n_i} \tag{3.9}$$

where n_i is the number of particles with diameter d_i and d is the average diameter of particles, and is presented in Table 3.4.

The 20% Pt/C catalyst appeared to be well dispersed, with almost no agglomeration of the particles, with an average particle diameter of 2.7 nm. Figure 3.9

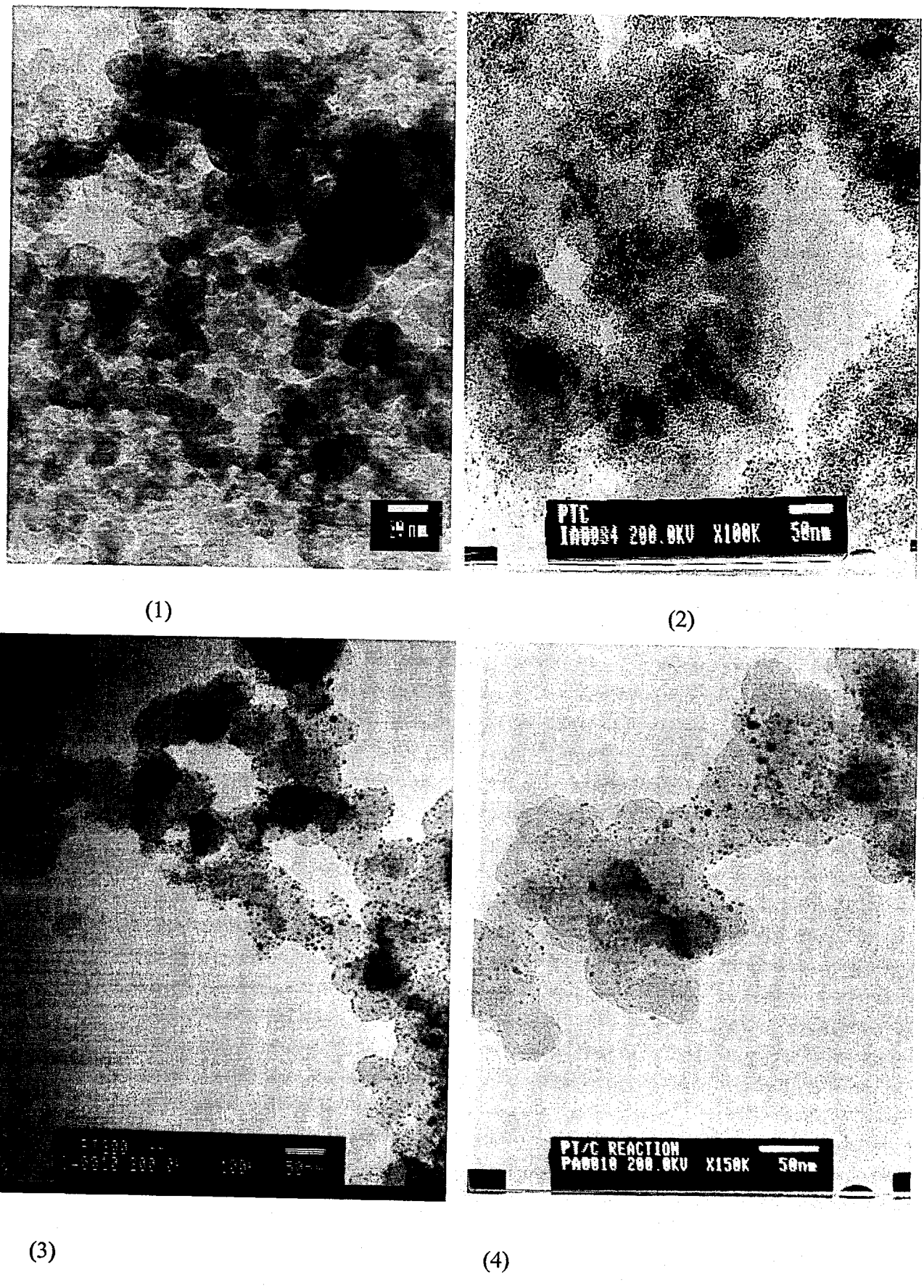

(1) (2)

(3) (4)

Figure 3.9 TEM images of (1) XC72R carbon, (2) 20% Pt/C, (3) 20% Pt/C (200°C), and (4) 20% Pt/C (Reaction). A 50 nm bar scale is shown on each micrograph.

also shows TEM images of 20% Pt/C after reduction in H_2 at 200 °C and after the SOMC reaction procedure (without a precursor). The particles were still uniform, however the average particle size increased to 3.2 and 3.5 nm respectively. Figure 3.10 shows the histograms of particle size distributions of 20% Pt/C and 20% Pt/C (reaction) catalysts, indicating a relatively narrow particle size distribution.

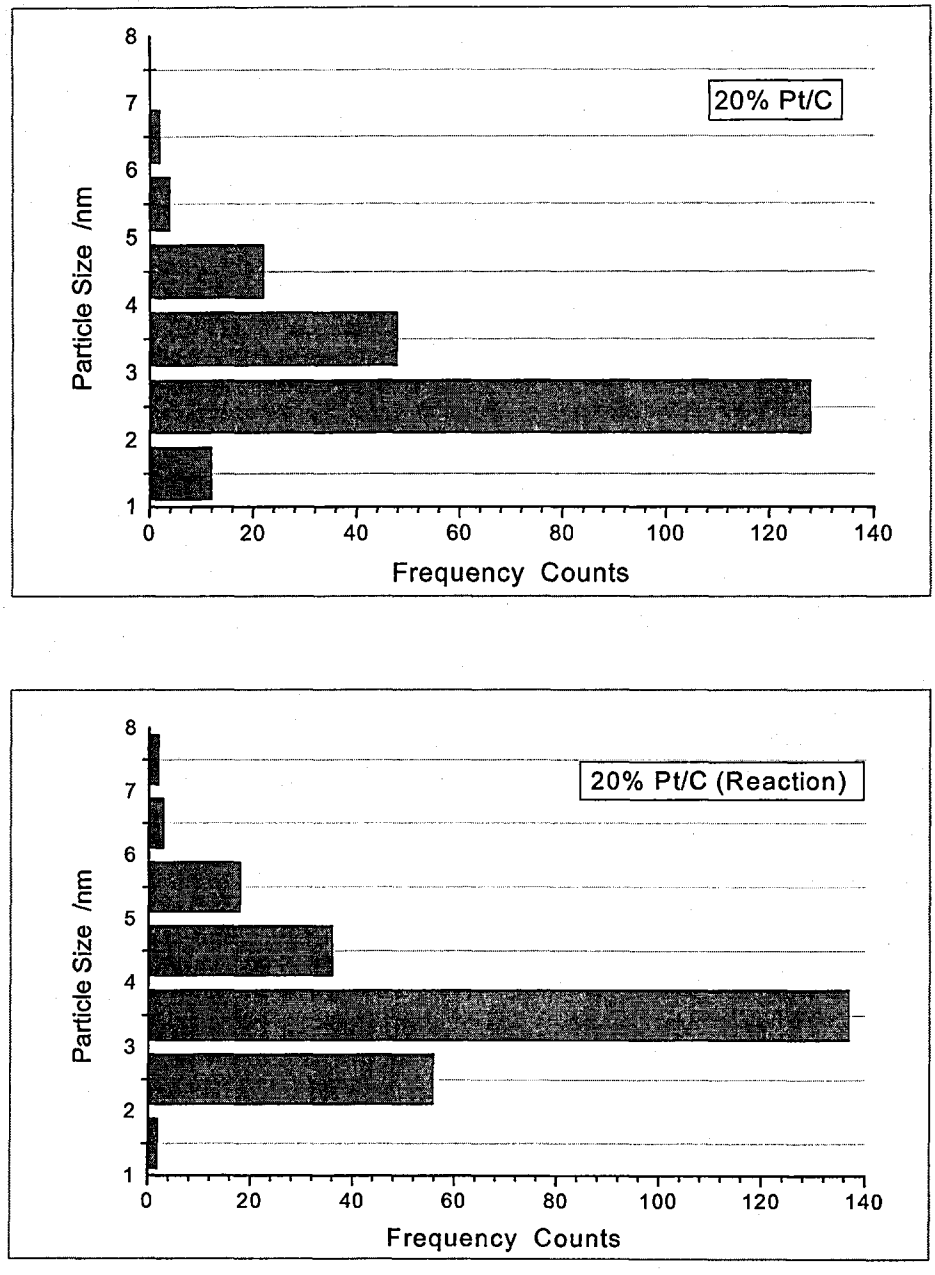

Figure 3.10 Histogram of particle size distribution for20% Pt/C and 20% Pt/C(Reaction) catalyst

The TEM images of the four blank reaction samples (M/C) are shown in Figure 3.11. There was no evidence for any metal particles on the blank samples (M/C). This is further evidence, with the UV-visible results, that the second metal did not deposit on the carbon support during the SOMC reaction.

Figures 3.12 – 3.15 show the TEM images of PtM/C bimetallic catalysts prepared by SOMC. The average metal particle sizes for Pt/C and the various PtM/C catalysts prepared using SOMC are listed in Table 3.4, estimated from image analyses of the TEMs. The average metal particle sizes (Table 3.4) are likely to be slightly higher than the true mean as we were unable to resolve particle size below 1 nm. Indeed, these values are higher than the values estimated from the XRD data (section 3.3.3) using the Scherrer equation [9]. A clear trend is seen on increasing the second metal content of the catalyst. The average particle size for the Pt/C (after SOMC reaction) catalyst sample was 3.5 nm and it was found to increase further as the second metal was introduced. The size of PtM/C catalyst particles was seen to increase with the proportion of second metal. This further suggests that the second metal was deposited on the surface of the Pt/C catalyst.

Figures 3.16 – 3.19 show the typical particle size distributions of bimetallic PtM/C catalysts. The PtM/C catalyst particles varied generally between 3.5 – 5.5 nm, indicating a narrow particle size distribution. The results of TEM image analysis showed the majority of metal particles to be between 4 - 5 nm, with little evidence of particle agglomeration. This meant that SOMC reaction was a successful method for preparing highly dispersed bimetallic PtM/C catalysts with little evidence of sintering.

It is evident (Table 3.4) that the average metal particle size for each bimetallic PtM/C catalyst increased slightly with increasing coverage of the second metal. Crabb [10] and Coq [11] reported a similar increase in particle size with increasing tin content for PtSn/C and $PdSn/SiO_2$ catalysts prepared using SOMC which they attributed to

addition of an atomic monolayer of the second metal to the platinum or palladium particles. They found for example that the average particle size of 1.0PtSn/C increased to 4.1 nm from 3.2 nm of Pt/C [10]. Halttunen and Didillon [12, 13] similarly reported that the increase in metal particle size observed for their catalysts arose from the fact that the second metal was deposited on the parent metal. Neri studied the relation between average size (d) and surface mean diameter (d_s) of metal particles on bimetallic PtSn/C catalysts, where $d_s = \sum n_i d_i^3 / \sum n_i d_i^2$. As the tin loading increased, the difference between d and d_s became larger. This was attributed to a progressive broadening of the particle size distribution as tin was added [14]. Crabb et al have similarly reported a narrow particle size distribution for $PtFe/Al_2O_3$ and $PdFe/Al_2O_3$ catalysts prepared using SOMC method [8, 10]. In our experiments the average particle size for the Pt/C (after SOMC procedure) catalyst sample was 3.5 nm and it was found to increase to 4.2-4.6 nm for the various bimetallic PtM/C catalysts. Our results of TEM particle size analysis support Halttunen, Didillon, Neri and Crabb's work.

(1) (2)

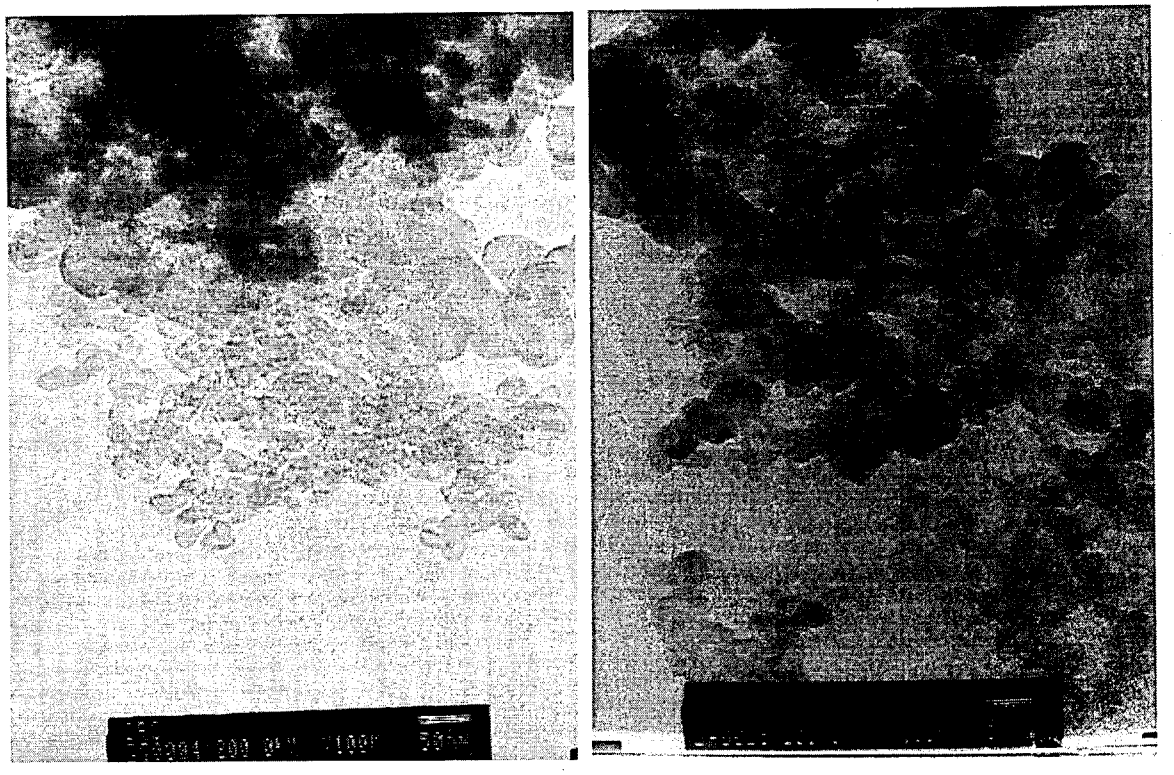

(3) (4)

Figure 3.11 TEM images of (1) Fe/C, (2) Ni/C, (3) Cr/C and (4) Co/C.

0.25PtFe/C

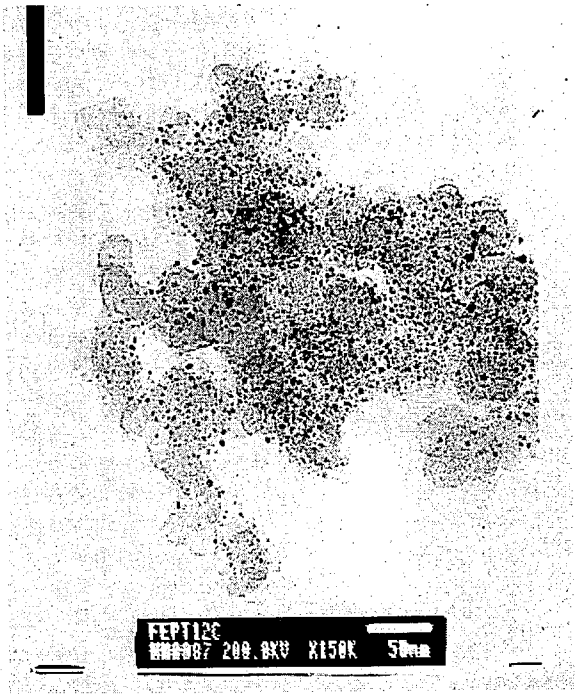

0.50PtFe/C

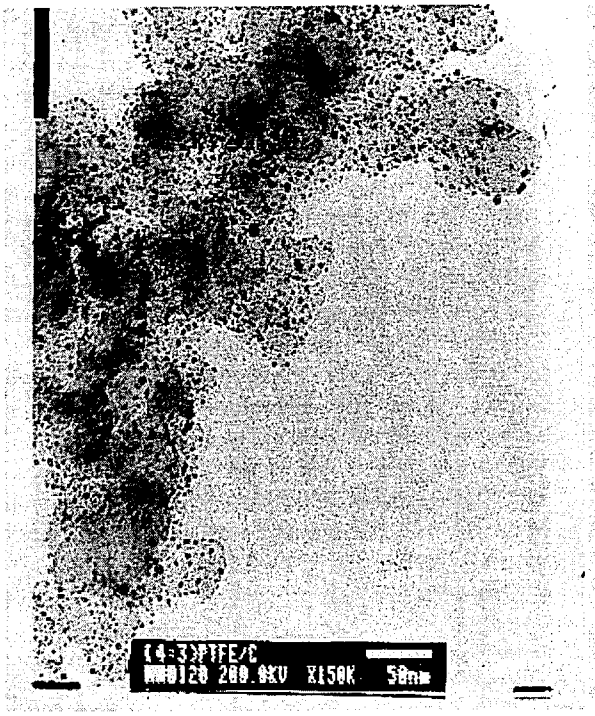

0.75PtFe/C

1.0PtFe/C

Figure 3.12 TEM image of various PtFe/C catalysts.

0.25PtNi/C

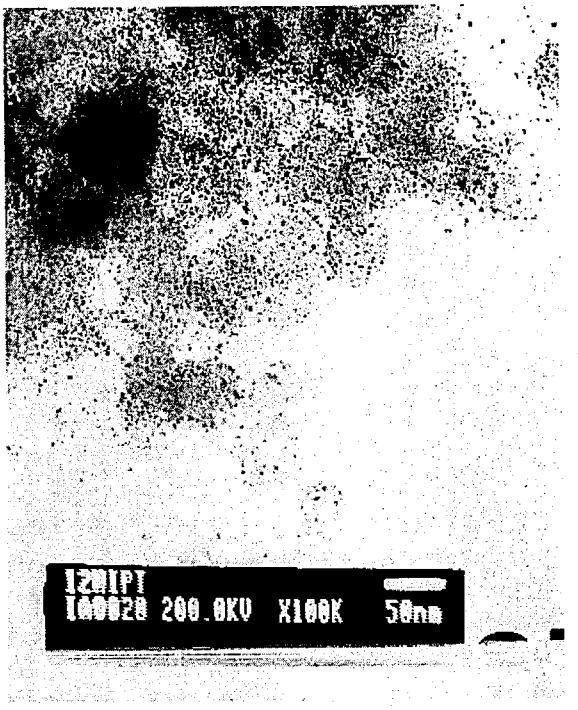

0.50PtNi/C

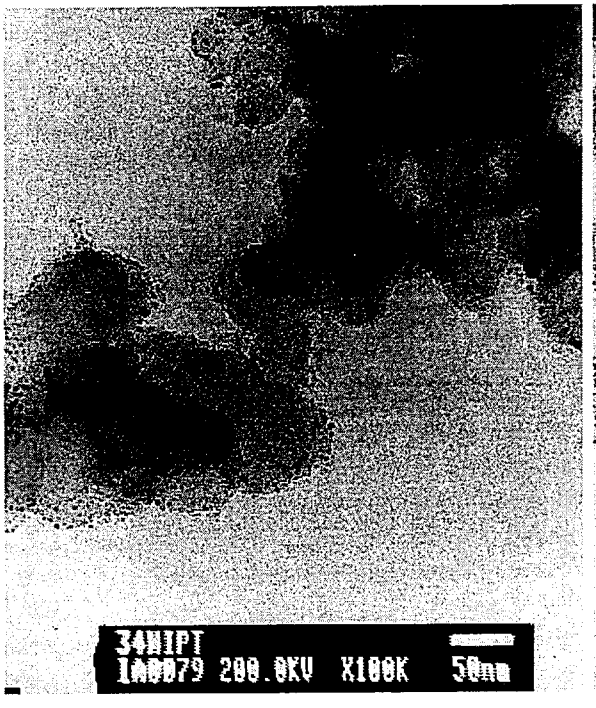

0.75PtNi/C

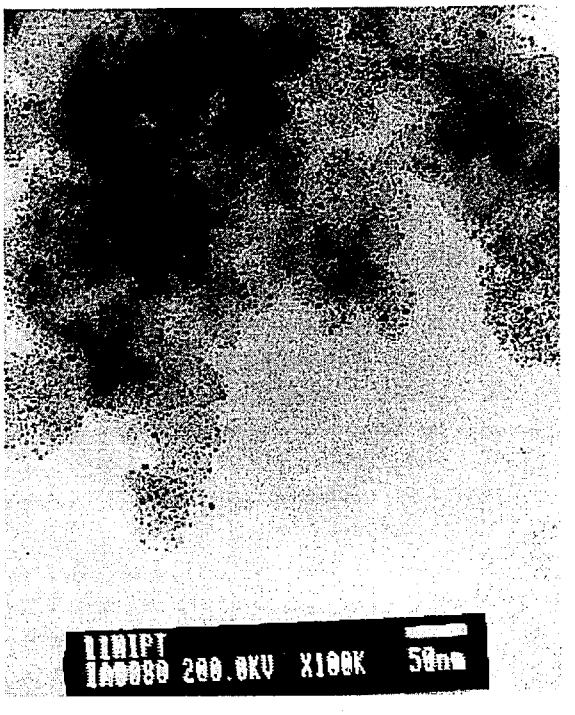

1.0PtNi/C

Figure 3.13 TEM image of various PtNi/C catalysts

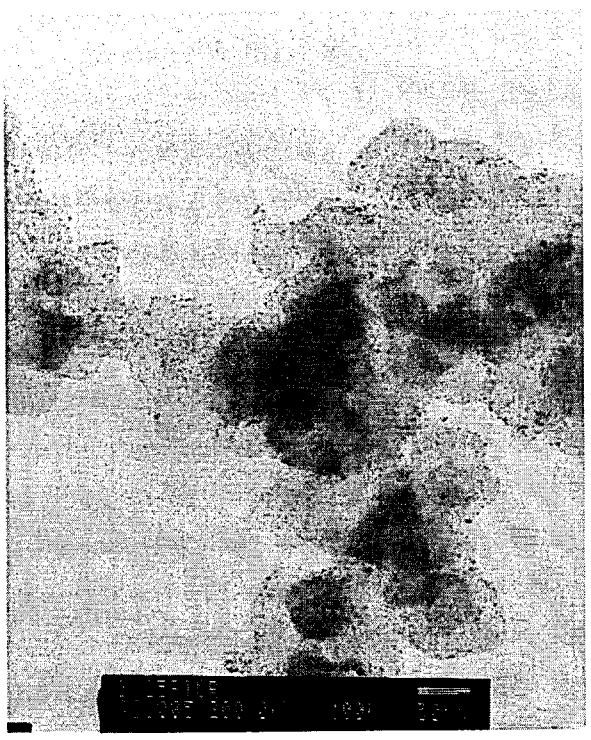

0.25CrPt/C

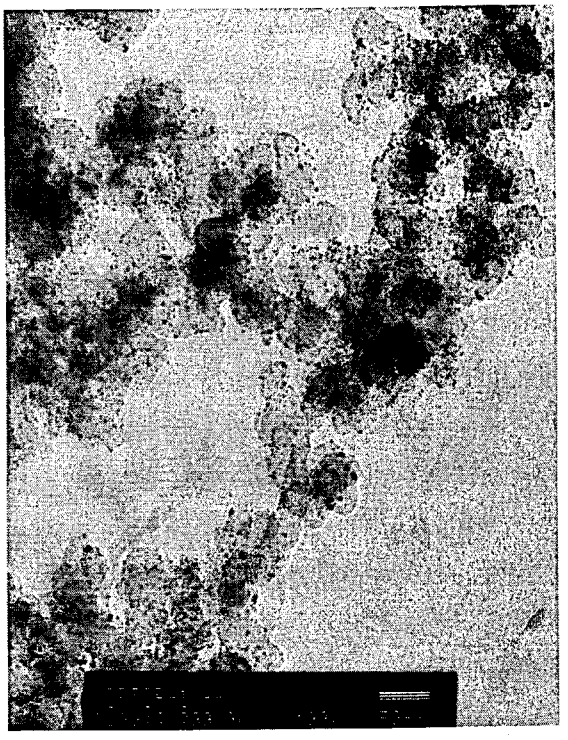

0.5PtCr/C

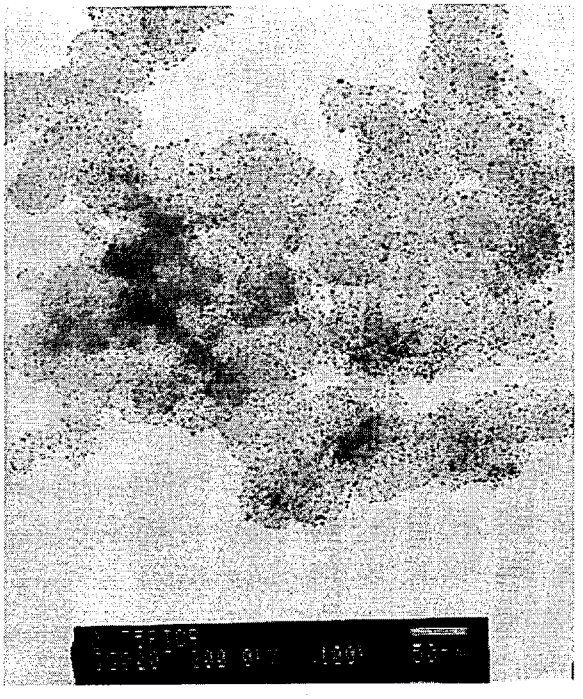

0.75PtCr/C

1.0PtCr/C

Figure 3.14 TEM image of various PtCr/C catalysts

0.25 PtCo/C

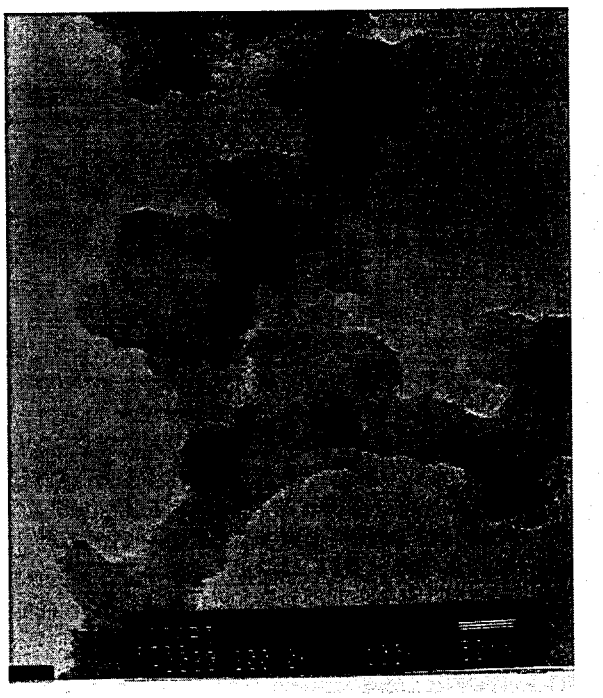

0.5 PtCo/C

0.75 PtCo/C

1.0 PtCo/C

Figure 3.15 TEM images of PtCo/C bimetallic catalysts

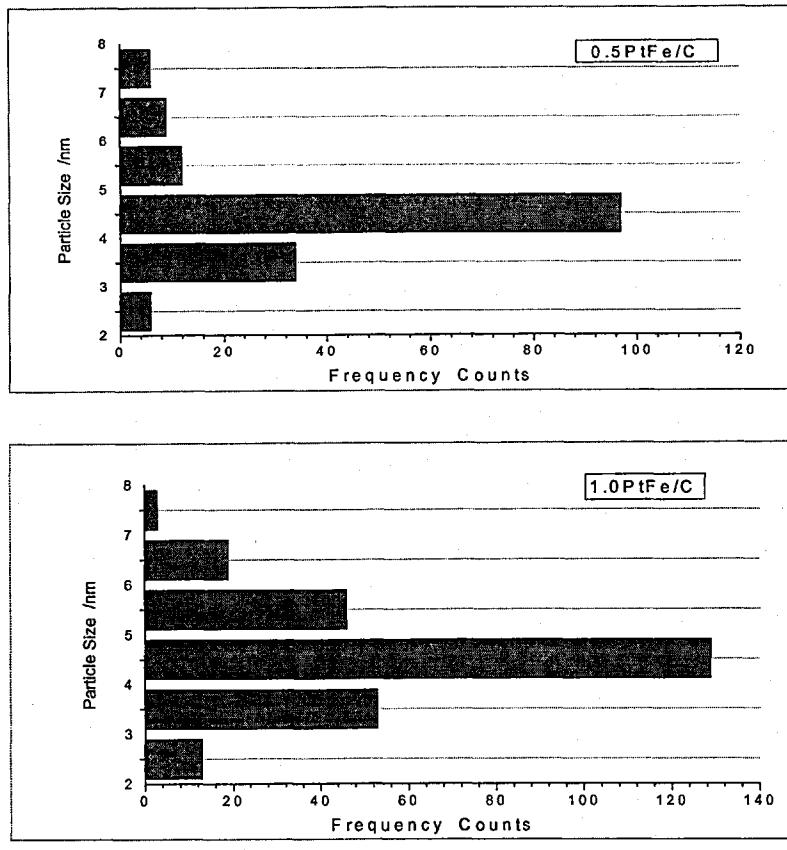

Figure 3.16 Histograms of particle size distribution for 0.5PtFe/C and 1.0PtFe/C catalysts.

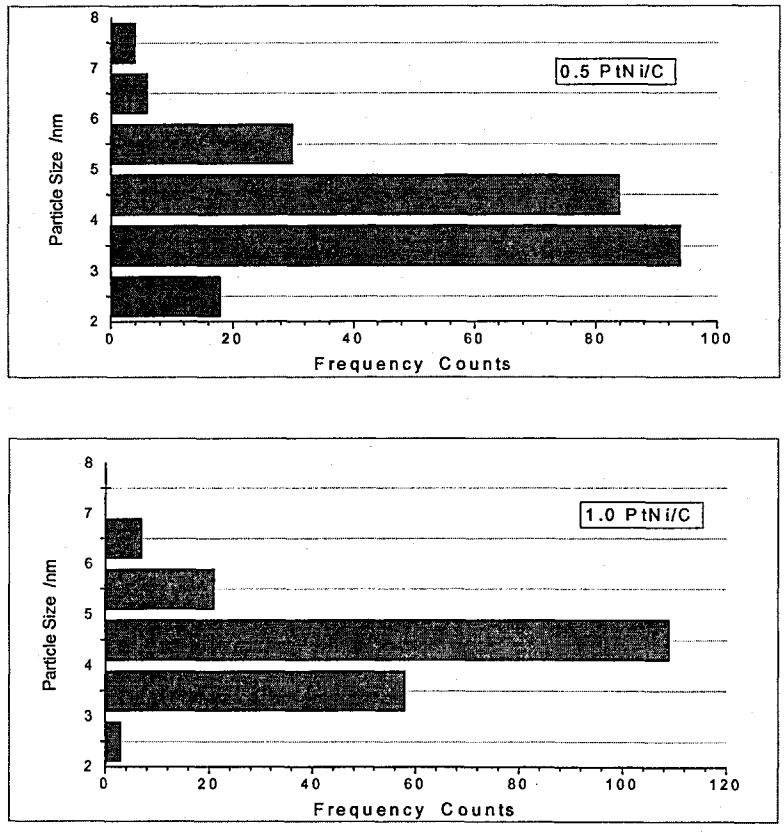

Figure 3.17 Histograms of particle size distribution for (a) 0.5PtNi/C and (b) 1.0PtNi/C catalysts.

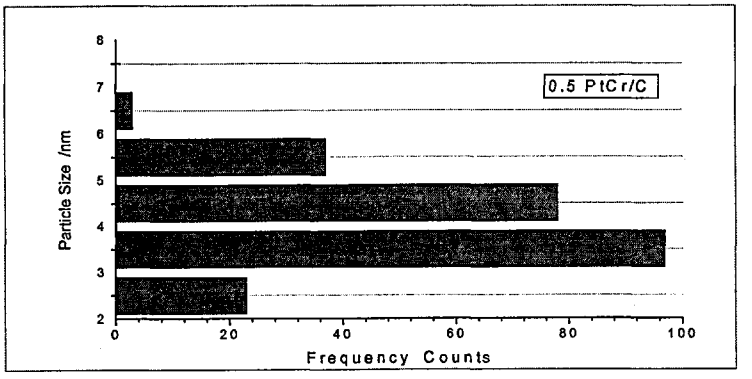

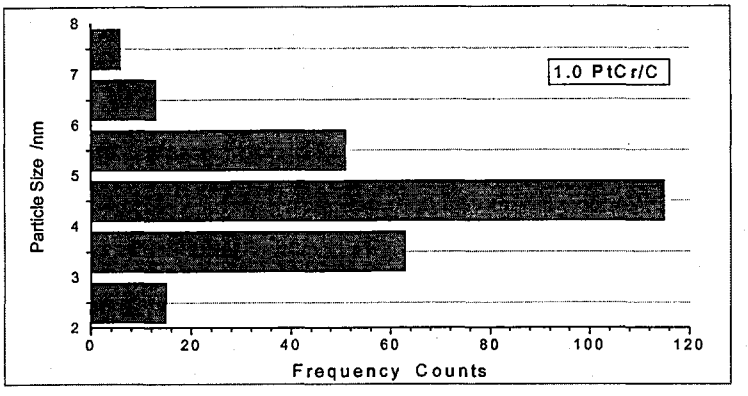

Figure 3.18 Histogram of particle size distribution for (a) 0.5PtCr/C and (b)1.0PtCr/C catalysts.

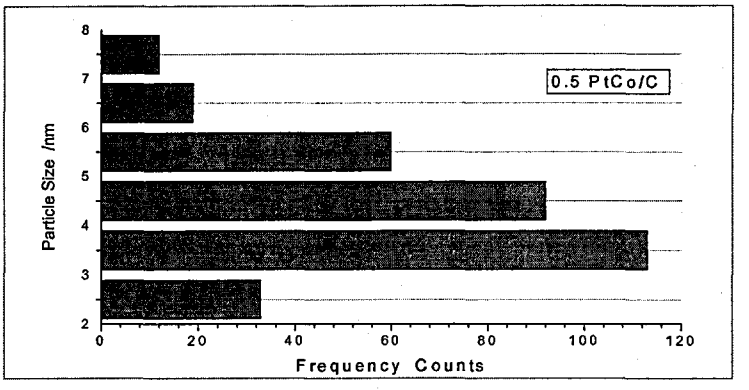

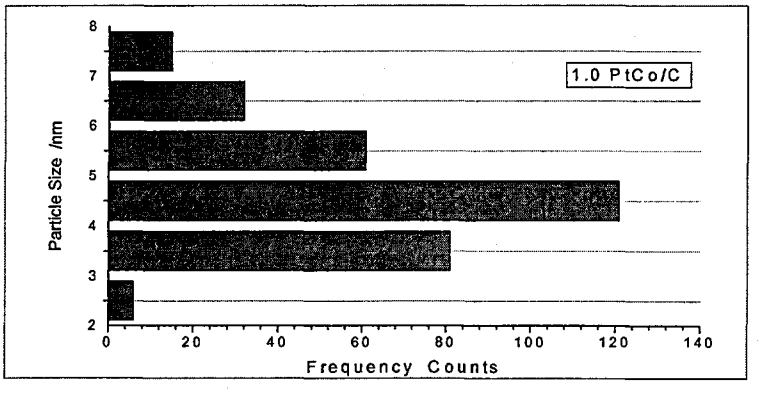

Figure 3.19 Histograms of particle size distribution for (a) 0.5PtCo/C and (b) 1.0PtCo/C catalysts.

Table 3.4 Particle size for Pt/C and PtM/C catalysts

Catalyst	Average particle size (TEM) / nm	Catalyst	Average particle size (TEM) / nm
Pt/C	2.7		
Pt/C (after 200°C)	3.2		
Pt/C (reaction)	3.5		
0.25FePt/C	4.3	0.25PtCr/C	4.2
0.5FePt/C	4.5	0.5PtCr/C	4.3
0.75FePt/C	4.6	0.75PtCr/C	4.3
1.0FePt/C	4.6	1.0PtCr/C	4.4
0.25NiPt/C	4.2	0.25PtCo/C	4.2
0.50NiPt/C	4.2	0.5PtCo/C	4.4
0.75NiPt/C	4.2	0.75PtCo/C	4.5
1.0NiPt/C	4.4	1.0PtCo/C	4.5

Energy dispersive X-ray microanalysis (EDX) analysis of catalysts was performed by reducing the size of the beam and focusing on different areas of the catalysts. The catalysts were held on carbon coated copper for the EDX experiment, so the Cu peak at 8.047 eV was also observed. On focusing the beam on areas of the Blank samples (M/C) - shown for Co/C in Figure 3.20 - no evidence for the second metal was found on the carbon support.

Focusing on random areas covered by metal particles of the bimetallic PtM/C catalysts, the presence of both the Pt and the second metal was observed. Typical EDX spectra of Co/C and PtCo/C bimetallic catalysts are shown in Figure 3.20. These spectra show the presence of both platinum and cobalt together in the area scanned. On focusing the beam on areas of the support where no platinum particle was present, there was no evidence for the second metal alone. Similar results were found for all four bimetallic catalyst (PtM/C) series. These results indicate that the second metal M was deposited on the Pt surface, not on the carbon.

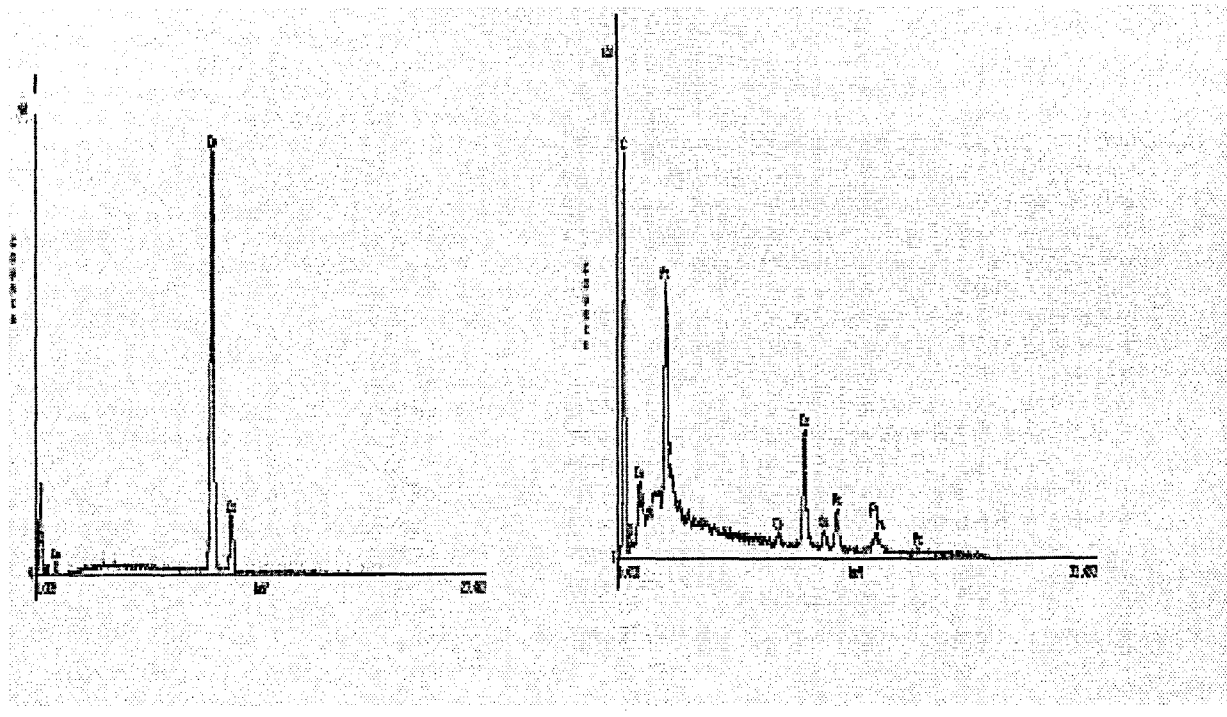

Co/C

0.25PtCo/C

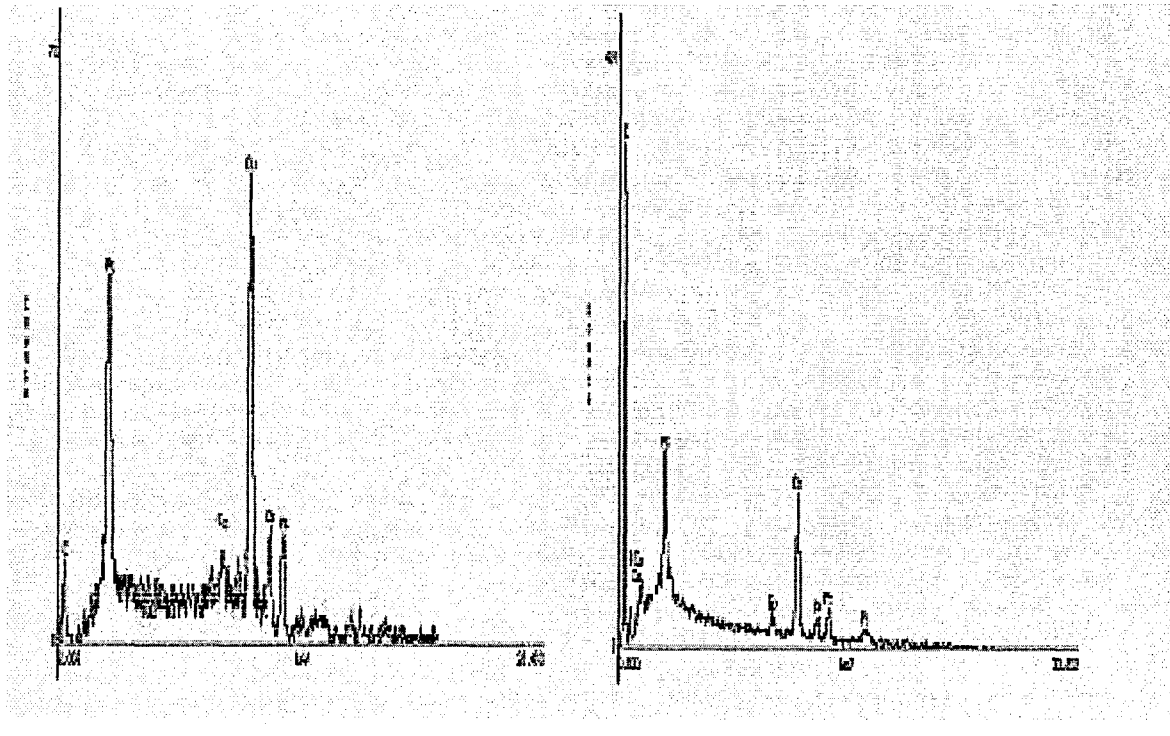

0.5PtCo/C

1.0PtCo/C

Figure 3.20 EDX spectrum of Co/C and PtCo/C catalysts

The composition of the Pt/C and PtM/C catalysts was also measured by EDX. The results are listed in Table 3.5. The compositions given in Table 3.5 will not represent an accurate analysis of the catalysts due to the local nature of the sampling process, however, it shows that both the Pt and second metal were present on PtM/C bimetallic catalysts, and that there was also no evidence of the second metal on the Blank samples (M/C). This is taken as evidence for a selective reaction between the platinum particles and the second metal organometallic precursor.

Table 3.5 Composition for Pt/C and PtM/C Catalysts by EDX

Catalyst	Weight %		Atomic %	
	Pt	M	Pt	M
Pt/C	18.9	81.1 (carbon)	1.4	98.6 (carbon)
0.25FePt/C	89.9	10.1	71.9	28.1
0.5FePt/C	86.2	13.8	64.1	35.9
0.75FePt/C	77.5	22.5	49.7	50.3
1.0FePt/C	84.6	15.4	61.2	38.8
Fe/C	0	0	0	0
0.25NiPt/C	97.5	2.5	92.1	7.9
0.50NiPt/C	95.5	4.5	86.4	13.6
0.75NiPt/C	98.6	1.4	95.5	4.5
1.0NiPt/C	81.9	18.1	57.7	42.3
Ni/C	0	0	0	0
0.25PtCr/C	93.0	7.0	21.9	78.1
0.5PtCr/C	88.3	11.7	66.8	33.2
0.75PtCr/C	97.8	2.2	92.3	7.7
1.0PtCr/C	95.1	4.9	83.8	16.2
Cr/C	0	0	0	0
0.25PtCo/C	95.3	4.7	85.9	14.1
0.5PtCo/C	90.7	9.3	74.6	25.4
0.75PtCo/C	84.2	15.8	61.6	38.4
1.0PtCo/C	91.4	8.6	76.2	23.8
Co/C	0	0	0	0

3.3.2 Total surface area and Pt metal dispersion of bimetallic catalysts

The BET total surface areas of the carbon, the Pt/C and the various PtFe/C, PtNi/C, PtCr/C and PtCo/C catalysts are given in Table 3.6.

BET total surface area measurements indicate that the total surface area of the Pt/C catalyst was smaller than that of the carbon alone. However, no further decrease in the BET total surface areas of the PtM/C bimetallic catalysts was observed in comparison with that of Pt/C.

The hydrogen chemisorption isotherms for Pt/C and PtM/C catalysts are shown in Figures 3.21 - 3.24. The Pt metal dispersion (H/Pt) estimated from the hydrogen chemisorption isotherms for each sample and the ratio of the second metal and surface Pt (from ICP) are tabulated in Table 3.6.

A theoretical value for H/Pt has also been given based on the assumptions:

- that H/Pt equals 0.40 if no second metal deposits on surface Pt, or $M/Pt_s = 0$. This assumption is based on the fact that the H/Pt for Pt/C is 0.40.
- that H/Pt equals zero if all surface Pt is covered by the second metal, or $M/Pt_s = 1$. This assumption is possible because hydrogen only adsorbs on surface Pt.

According to the two assumptions above, the theoretical Pt metal dispersion data (H/Pt) (fifth column in table 3.6) was calculated from the relation H/Pt *vs* M/Pt_s using the ICP data (Figure 3.25). The general trends of both chemisorption and theoretical data are in agreement, with the exception perhaps of the PtCr/C system.

Before the Pt metal dispersion data of the bimetallic catalysts are discussed further, the change of Pt metal dispersion on surface Pt after heating and SOMC reaction

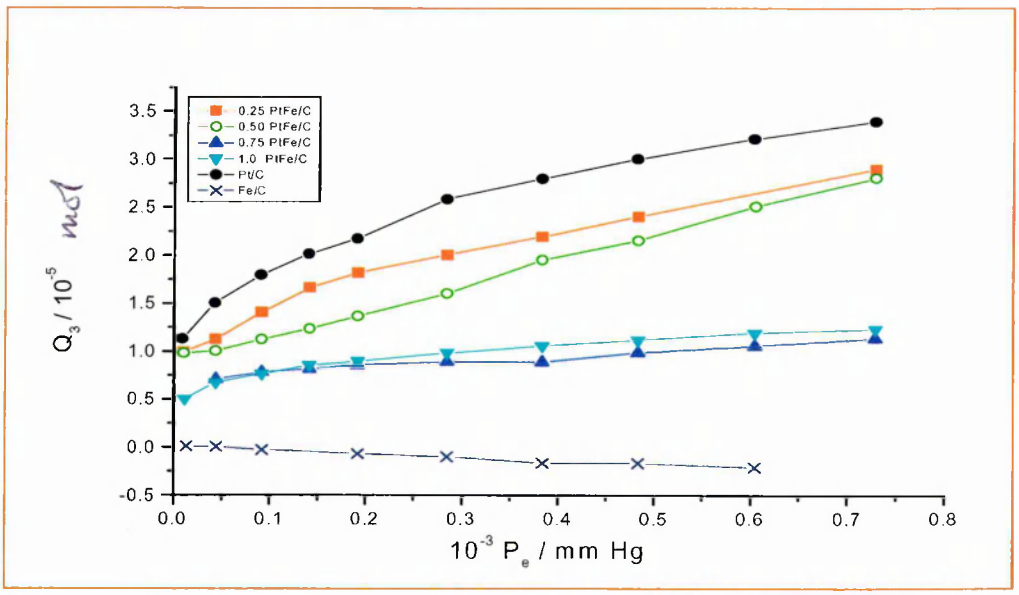

Figure 3.21 The hydrogen chemisorption isotherms for Pt/C and PtFe/C catalysts

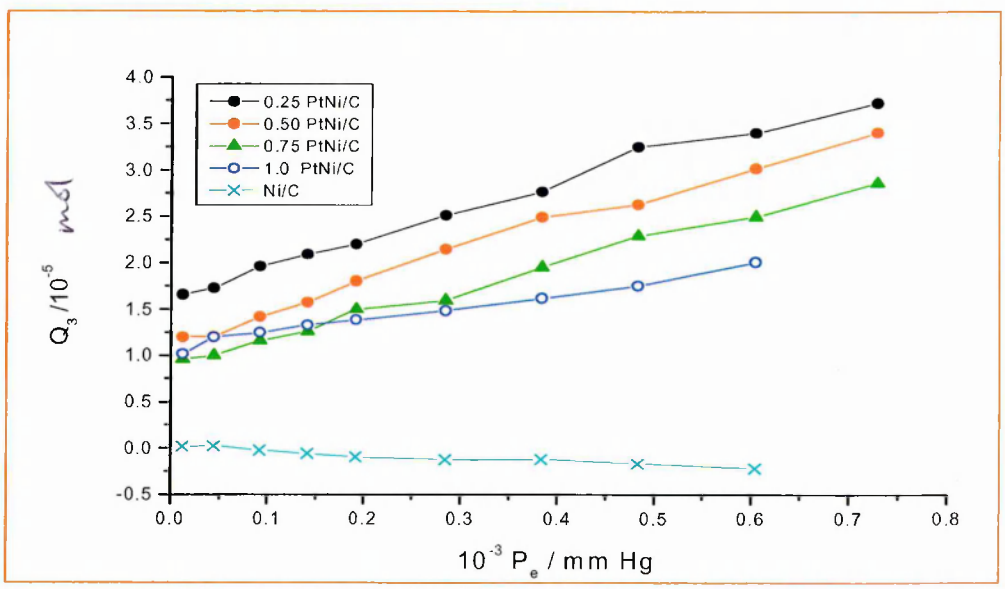

Figure 3.22 The hydrogen chemisorption isotherms for PtNi/C catalysts

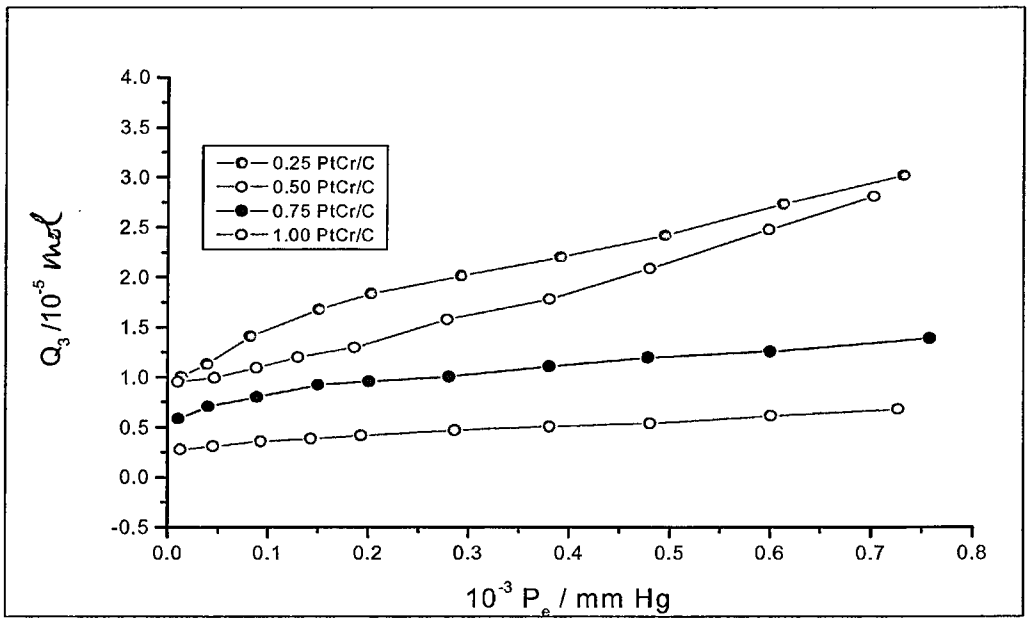

Figure 3.23 The hydrogen chemisorption isotherms for PtCr/C catalysts

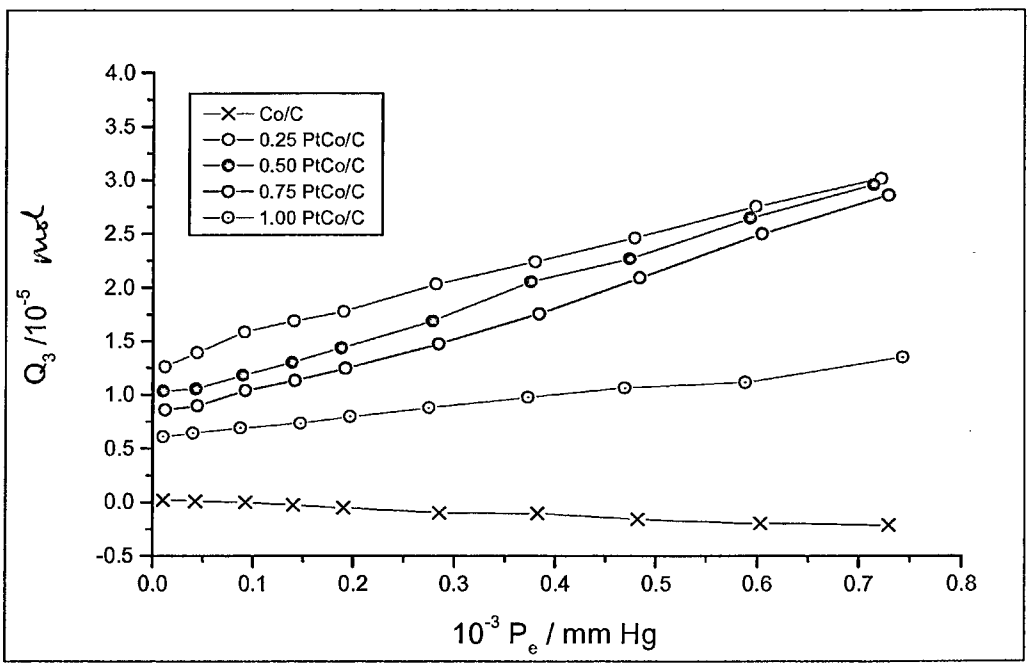

Figure 3.24 The hydrogen chemisorption isotherms for PtCo/C catalysts

Table 3.6 Total surface area and Pt metal dispersion

Catalyst	S_{BET} m^2/g	$Q_0 / 10^{-5}$ mol	H/Pt Chemisorption Data	H/Pt Theoretical Data	M:Pt_s atom ratio (ICP)
Carbon	213				
Pt/C			0.48		0
Pt/C (200°C)	158	2.00	0.40		0
Pt/C(Reaction)		1.85	0.37		0
0.25 PtFe/C	159	1.60	0.32	0.30	0.24
0.5 PtFe/C	157	1.10	0.22	0.23	0.43
0.75 PtFe/C	156	0.75	0.15	0.15	0.63
1.0 PtFe/C	159	0.50	0.10	0.08	0.8
Fe/C		0	0		
0.25 PtNi/C	158	1.75	0.35	0.36	0.11
0.50 PtNi/C	147	1.25	0.25	0.32	0.18
0.75 PtNi/C	155	1.00	0.20	0.28	0.29
1.0 PtNi/C	154	1.00	0.20	0.24	0.41
Ni/C	202	0	0		
0.25 PtCr/C	159	1.40	0.28	0.32	0.20
0.5 PtCr/C	157	0.80	0.16	0.20	0.50
0.75 PtCr/C	156	0.60	0.12	0.19	0.53
1.0 PtCr/C	159	0.30	0.06	0.15	0.61
0.25 PtCo/C	150	1.40	0.28	0.30	0.25
0.5 PtCo/C	162	1.10	0.22	0.23	0.37
0.75 PtCo/C	153	0.70	0.14	0.10	0.77
1.0 PtCo/C	160	0.60	0.12	0.10	0.77
Co/C		0	0		

will first be considered. The ratio of H/Pt for Pt/C decreased to 0.40 from 0.48 after reduction with H_2 at 200 °C, and further to 0.37 after treatment equivalent to the standard SOMC reaction procedure but without precursor. The average platinum particle size of the Pt/C was seen to increase to 3.2 and 3.5 nm, respectively from 2.7 nm (Table 3.7). This result suggested that the particle size of Pt increased during the conditions used in SOMC reaction. The average metal particle size of supported Pt and Pd catalysts can be estimated from the dispersion using the following equation[15]:

$$H/Pt = 1.13/d \qquad (3.10)$$

where d is the average diameter of a Pt or Pd particle. The estimated particle sizes of the Pt/C catalysts after different treatments are given in Table 3.7. The general trend agrees well with the TEM results. The particle size estimated from TEM is slightly higher as it is based on particles visible in the microscope, and depends on limits of detection of the microscope, whereas chemisorption gives an average value over all particles. This method was not appropriate for any bimetallic PtM/C catalysts, since the density of Pt is different from that of the second metal.

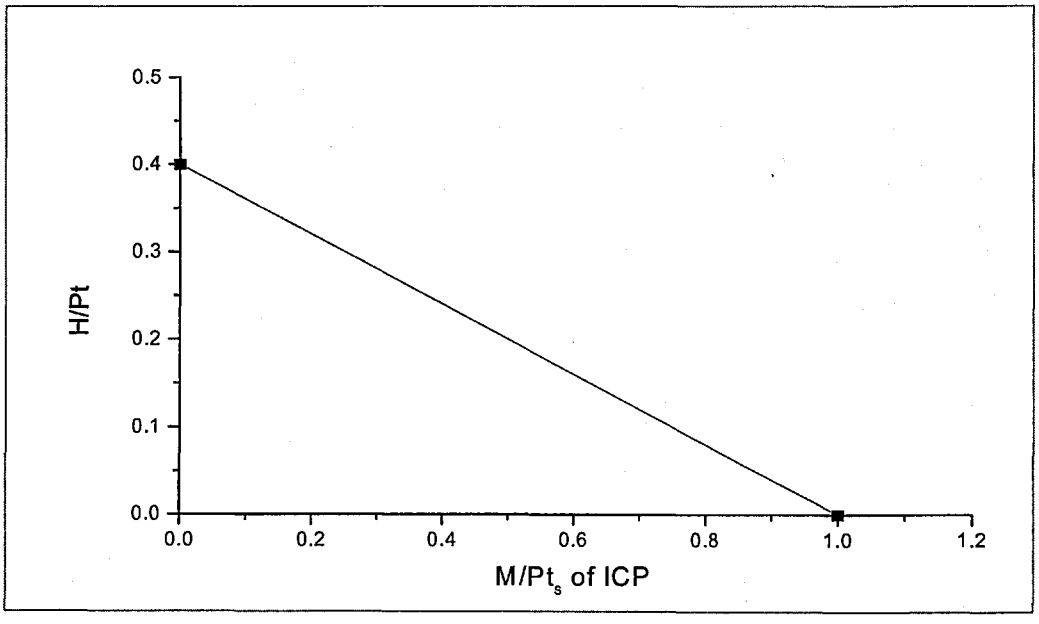

Figure 3.25 The relationship between H/Pt and M/Pt$_s$ of ICP

Table 3.7 The relation of the H/M and particles of Pt/C catalysts

Catalyst	H/Pt	Average diameter /nm (H/Pt)	Average diameter /nm (TEM)
Pt/C	0.48	2.4	2.7
Pt/C (200°C)	0.40	2.8	3.2
Pt/C (reaction)	0.37	3.1	3.5

It was confirmed that the carbon support did not chemisorb hydrogen as the value of H/Pt was found to equal zero for M/C in our experiments (Table 3.6). Similarly, Jung reported that hydrogen chemisorption did not occur on Fe/C catalysts [16]. Thus, assuming that each component retained its bulk properties, the second metal should not chemisorb hydrogen.

On addition of the second metal M to the Pt/C catalyst, the H/Pt values, both chemisorption and theoretical data, of the bimetallic PtM/C catalysts were all smaller than that of Pt/C (reaction). This indicated that the volume of hydrogen adsorbed by the bimetallic PtM/C catalysts decreased compared to the monometallic Pt/C catalyst, reflecting a decrease in the number of accessible surface Pt sites in the PtM/C catalysts. As the amount of the second metal on the surface platinum is increased, the atomic ratio of the second metal and surface Pt increased and the value of H/Pt became smaller.

3.3.3 Powder X-ray diffraction (XRD)

Powder X- ray diffraction techniques were used to characterize the structure of the catalysts and to determine the average size of the metal particles on carbon. XRD was carried out on very fine catalyst powder samples which were supported on a single crystal of silicon using grease.

Figure 3.26 and Figure 3.27 show the XRD patterns for grease, carbon (XCR72) and the Pt/C catalysts after different heat treatments. The value of 2θ and the full width at half maximum (FWHM) of the peaks reflect the lattice parameter and crystallite size of the material according to the Debye-Scherrer method [9]. The position and intensity of reference peaks from JCPDS files are shown in Table 3.8.

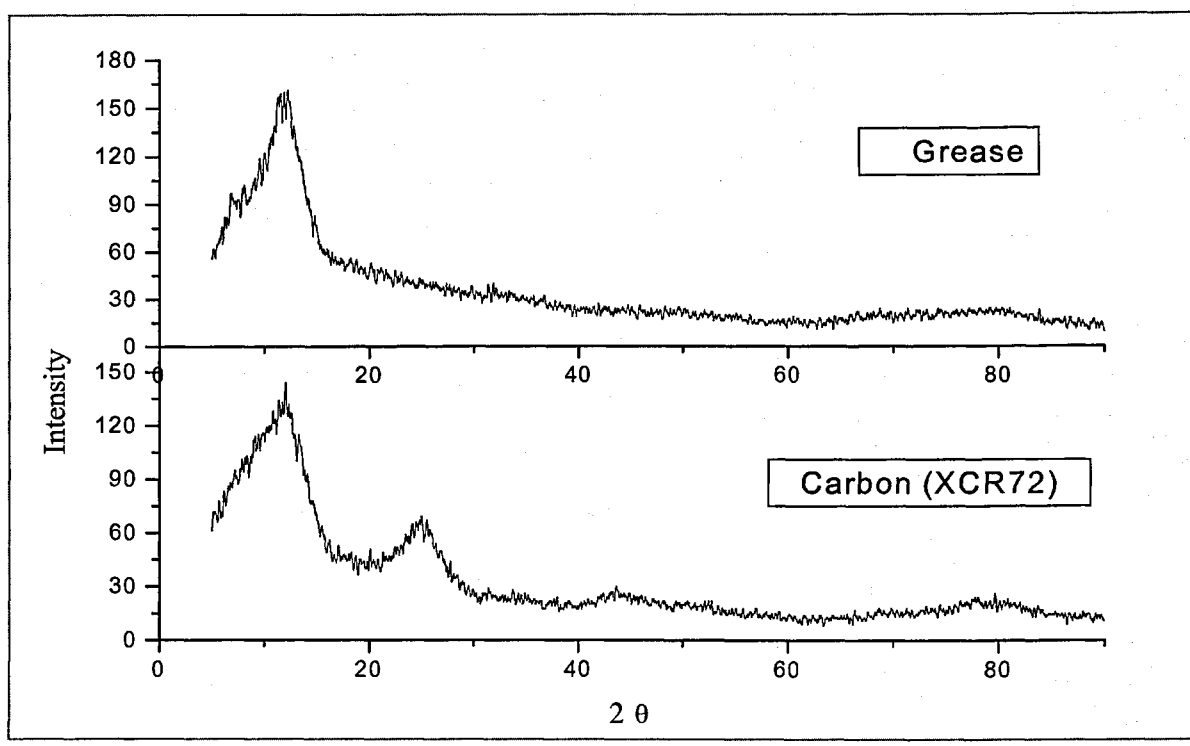

Figure 3.26 XRD pattern for grease and the carbon support

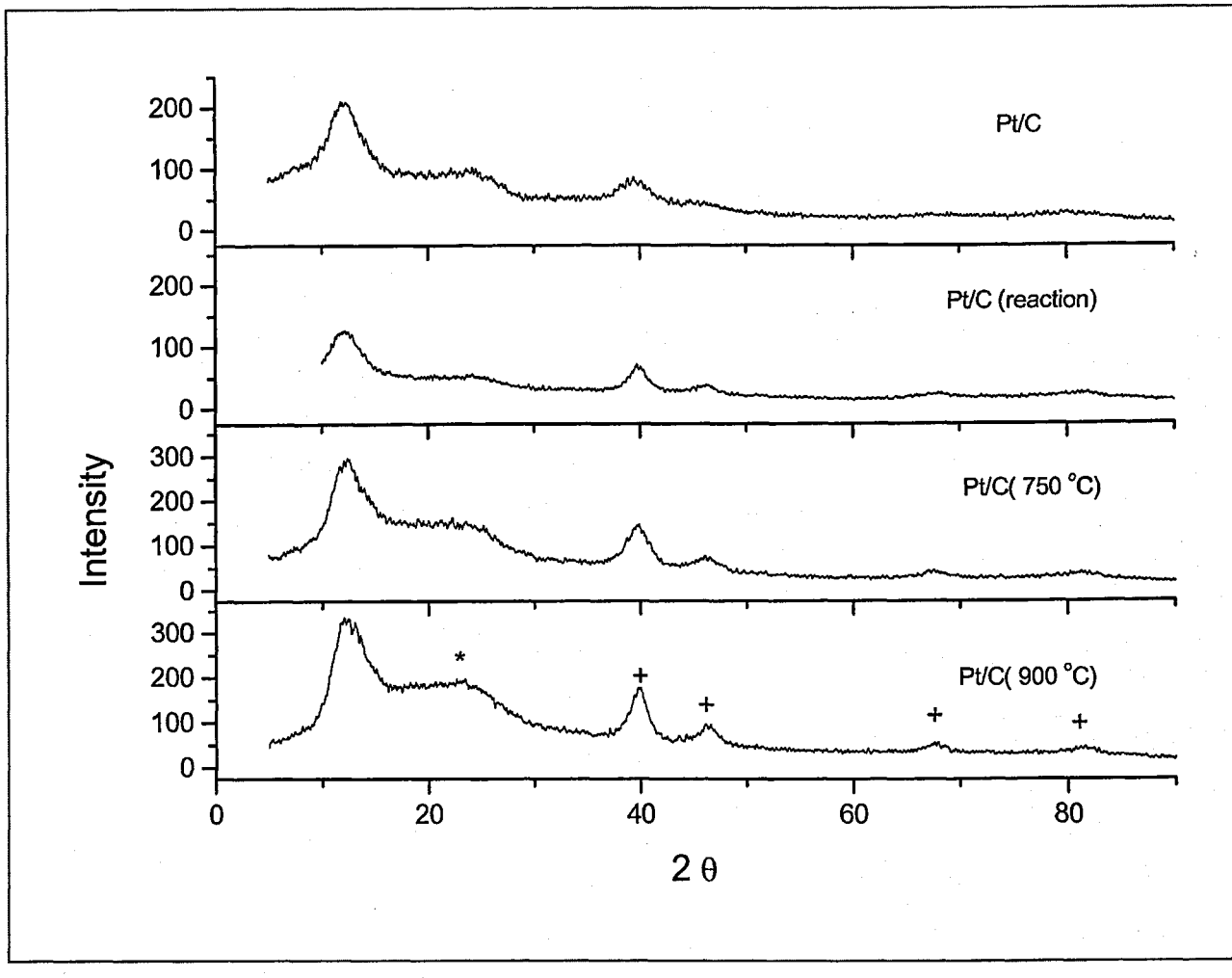

Figure 3.27 XRD pattern for Pt/C catalysts, * is C [13], and + is Pt [14].

Table 3.8 XRD reference peaks from JCPDS files.

2θ	**Intensity**	**Analysis**	**materials**
12.0	100		Grease
25.0	100	carbon	Carbon (XCR72) [17]
43.4	11	carbon	Carbon (XCR72) [18, 19]
39.7	100	Pt(111)	Pt/C [20]
46.2	53	Pt(200)	Pt/C [20]
67.4	31	Pt(220)	Pt/C [20]
81.2	33	Pt(311)	Pt/C [20]

After comparison with the XRD patterns of grease and the carbon support (Figure 3.26) and Pt/C (Figure 3.27), it was very clear that the additional peaks observed in the XRD pattern were due to the four major diffraction peaks of Pt (Table 3.8) [20]. The presence of the Pt(111) surface plane is thought to be very important for the electrocatalyst of a fuel cell because of the interaction of this surface with both reactants, oxygen and hydrogen, as well as the product, water [21-27].

The average crystallite size for the Pt was determined from the peak width Pt(111) at $2\theta = 39.7^{o}$ because it has the highest intensity value, and was calculated using the Debye-Scherrer equation [9]:

$$T = C\,\lambda / B\cos\theta = C\,\lambda / (U^2\text{-}S^2)^{1/2}\cos\theta \qquad (3.11)$$

where T is the crystallite size (the diameter of crystal particle Å); λ is the X-ray wavelength (1.5406 Å) for CuK_{α}; θ is the Bragg angle; C is a factor (typically from 0.9 to 1.0) depending on crystallite shape; B is the full width at half maximum, FWHM, of the peak (radians) corrected for instrumental broadening; U and S are the FWHM's of the unknown and standard peaks respectively. For our experiment, C = 1.0; λ = 1.5406(Å); S = 0.136; $B = (U^2 - S^2)^{1/2}/57.2727$ (radians). This equation shows an inverse relationship between crystallite size and peak profile width: the wider the peak, the smaller the crystallites. In order to obtain the full width at half maximum (FWHM), XRD patterns of catalysts were fitted using WinFit software [28]. As expected, the Pt peaks decreased in FWHM and the Pt crystallite size increased as the temperature of heat treatment was increased (Table 3.9).

Table 3.9 also lists the average diameter of a Pt particle based on TEM and chemisorption experiments. The crystallite size of XRD is smaller than the average diameter from TEM or chemisorption due to the different measurement method. Particles less than 1 nm were not observed in the TEM experiment. However all three techniques

showed similar trends with an increase in particle size as the heat treatment temperature of Pt/C catalysts was higher or longer.

Table 3.9 The crystallite size and particle size of Pt/C catalysts

Catalysts	FWHM (U)	Crystallite Size /nm	Diameter (H/Pt) /nm	Diameter (TEM) /nm
Pt/C	3.39	2.4	2.4	2.7
Pt/C(200°C)	3.08	2.7	2.8	3.2
Pt/C(reaction)	2.99	2.8	3.1	3.5

The powder X-ray diffraction patterns for the carbon black and the Blank samples for each second metal (M/C) were recorded with sodium chloride as an internal standard. Figures 3.28 – 3.31 show the XRD patterns of carbon black and the blank samples (M/C). Their patterns are similar, providing no evidence for crystalline iron, nickel, chromium and cobalt on carbon black. (The Bragg positions for NaCl and for Ni are indicated by reference lines taken from the JCPDS data files.)

Figures 3.32 – 3.35 show the powder X-ray diffraction patterns for the Pt/C and the various PtFe/C, PtNi/C, PtCr/C and PtCo/C catalysts, and peak positions and estimated crystallite size are tabulated in Table 3.10. The peaks of 100% intensity for the different metals, at: $2\theta = 44.7^{\circ}$ for iron, $2\theta = 44.8^{\circ}$ for nickel, $2\theta = 44.4^{\circ}$ for chromium, and $2\theta = 47.6^{\circ}$ for cobalt, were not found [29-33], suggesting that there was no evidence to indicate the presence of any crystalline metal phase. There were also no peaks corresponding to any metal oxide phases. This was probably because the second metal M loading was low, and also any second metal M species present was highly dispersed or was amorphous and so could not be detected.

Figure 3.32 shows that the Pt diffraction peaks of the higher Fe loaded PtFe/C

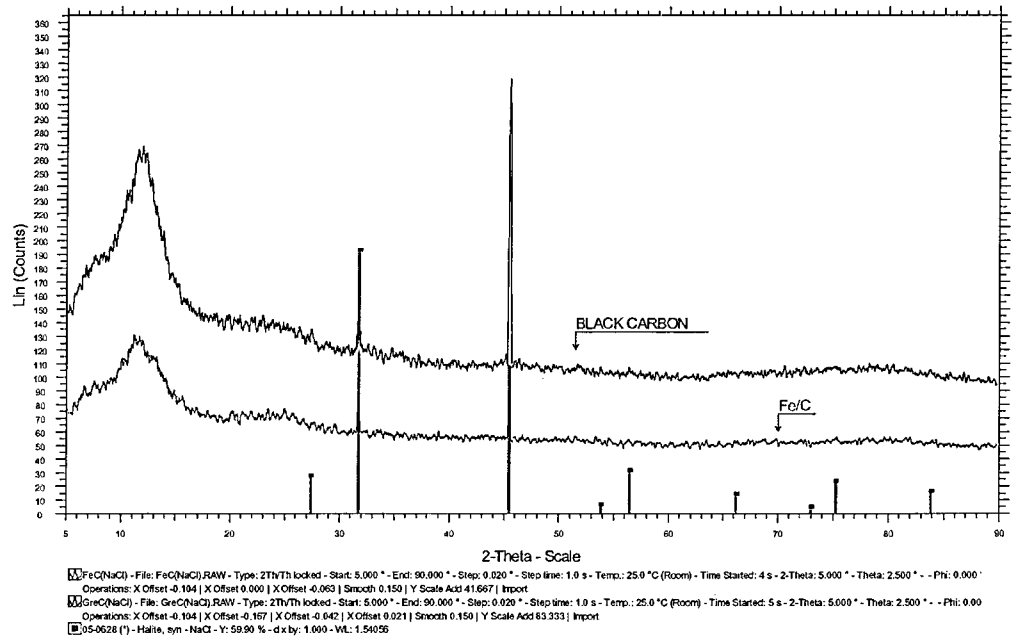

Figure 3.28 XRD Pattern for Fe/C and Carbon Catalyst Samples

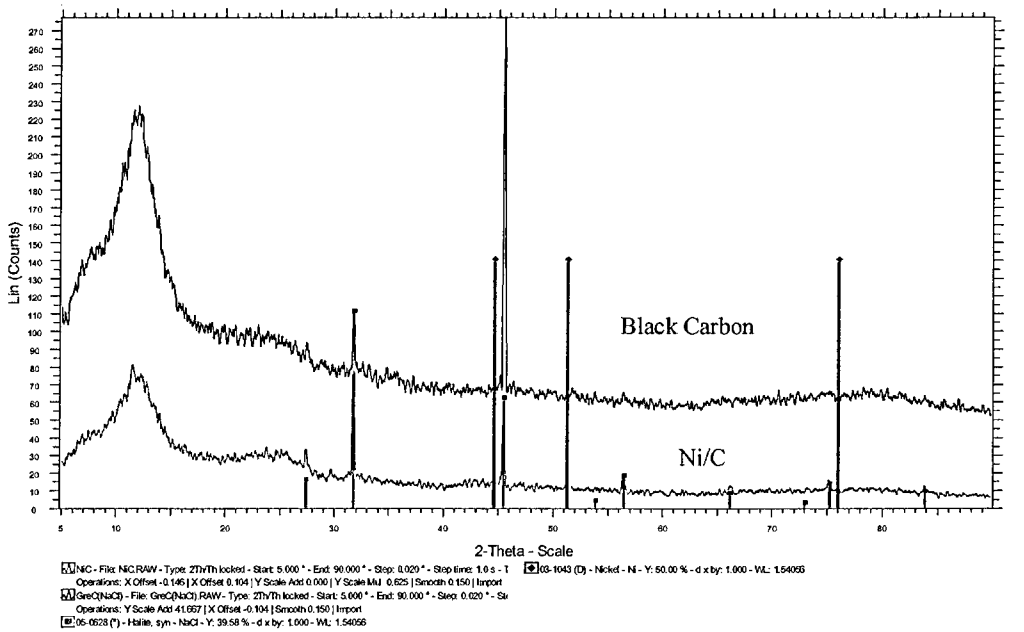

Figure 3.29 XRD Pattern for Ni/C and Carbon Catalyst Samples

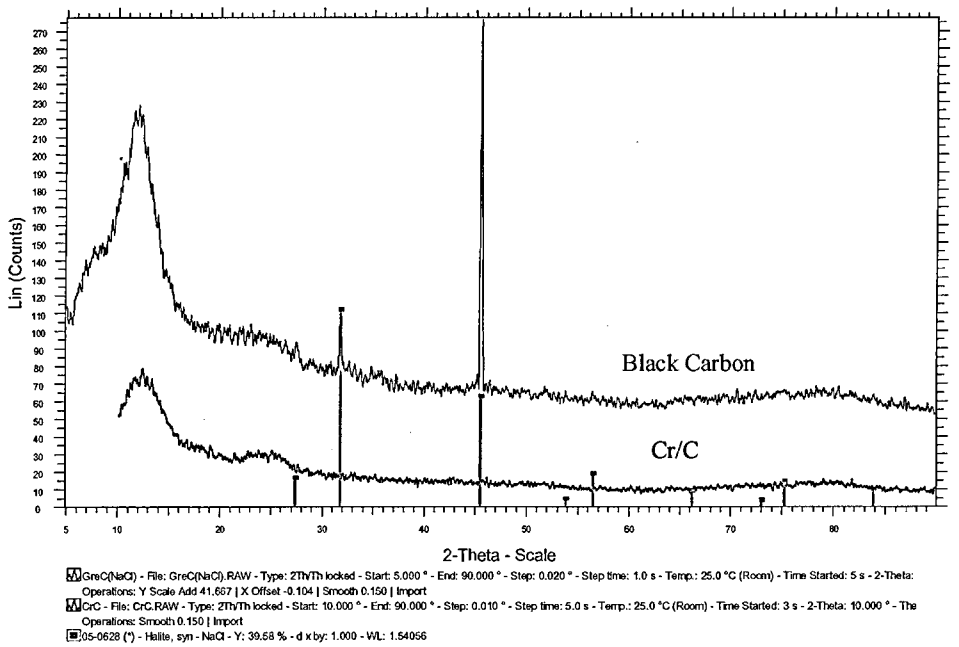

Figure 3.30 XRD Pattern for Cr/C and Carbon Catalyst Samples

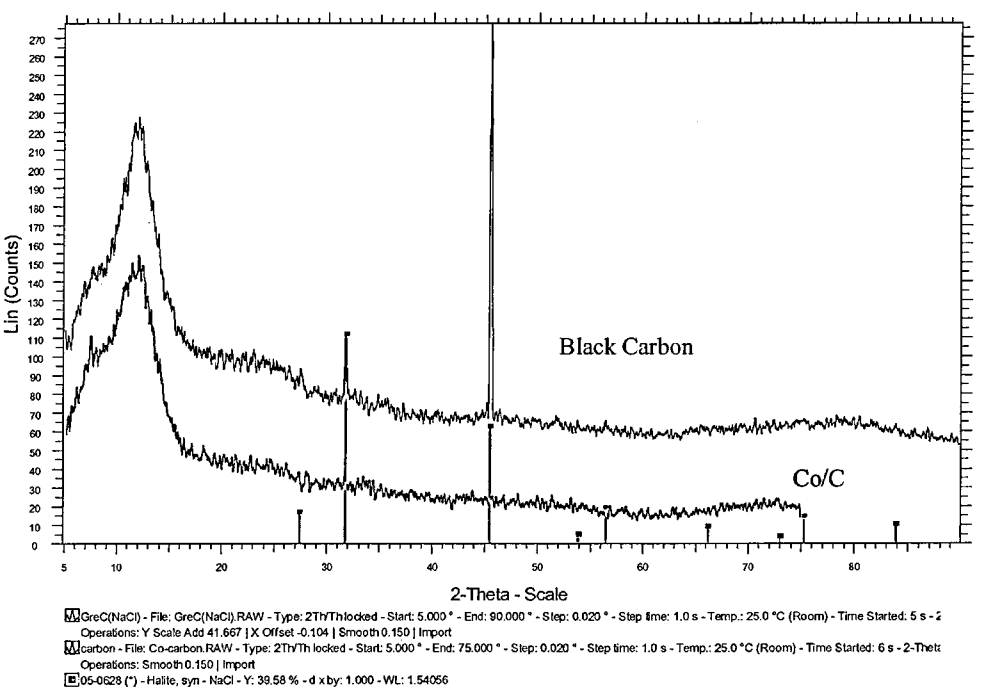

Figure 3.31 XRD Pattern for Co/C and Carbon Catalyst Samples

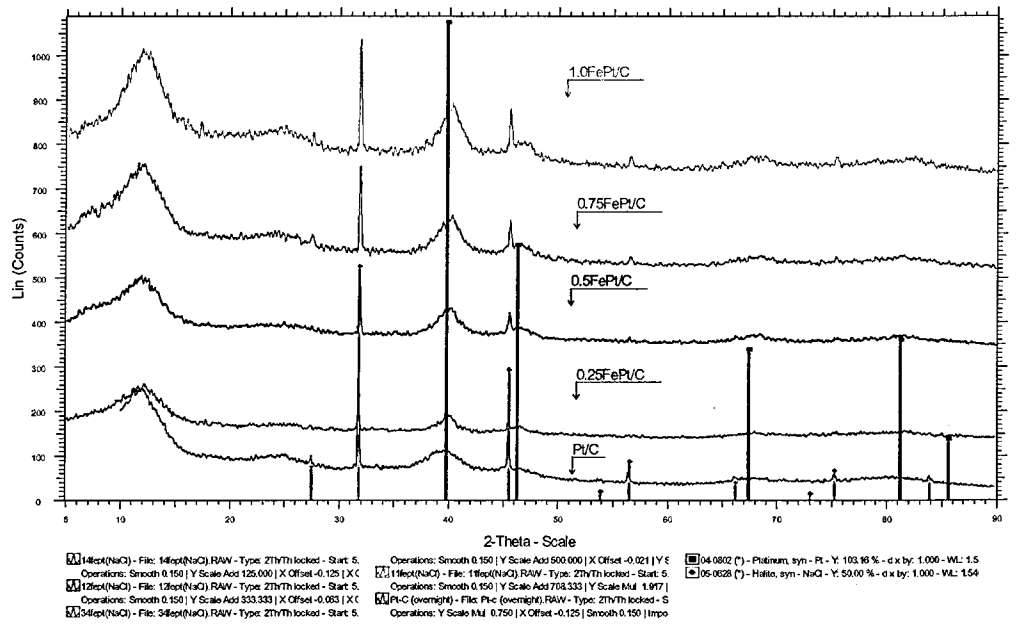

Figure 3.32 XRD Pattern for Pt/C and PtFe/C Catalyst Samples

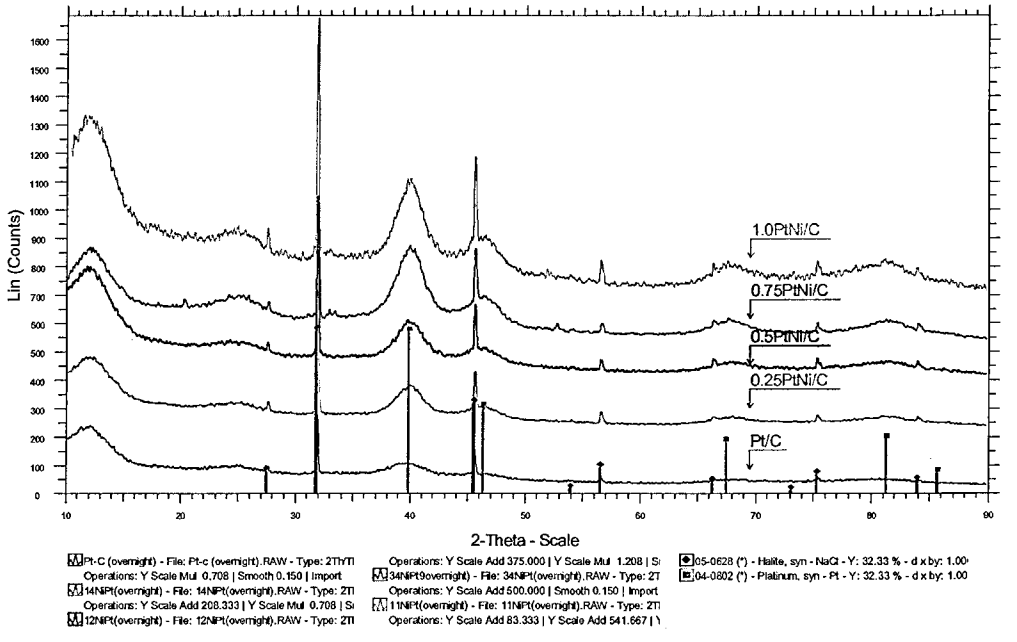

Figure 3.33 XRD Pattern for Pt/C and PtNi/C Catalyst Samples

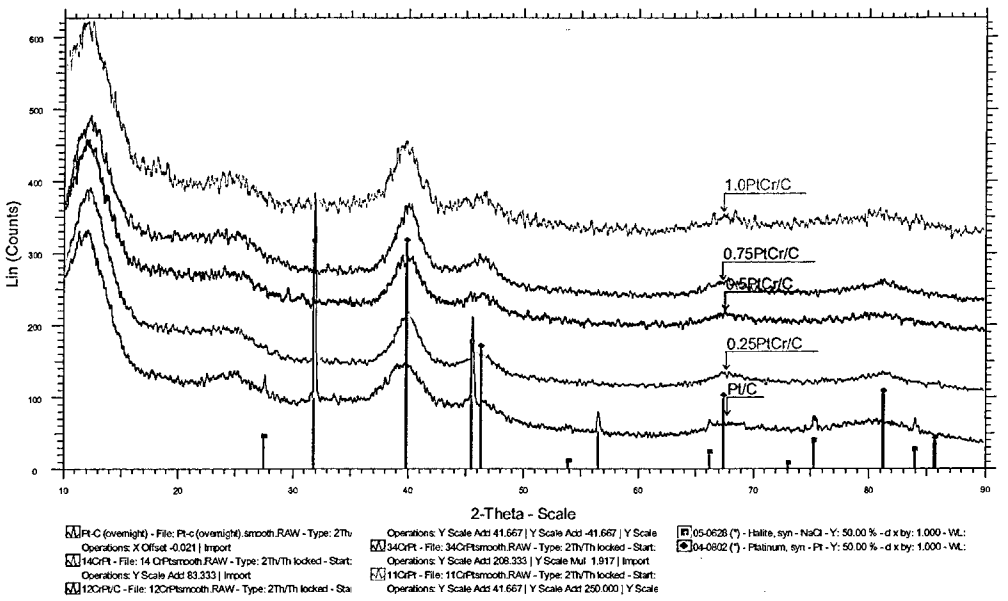

Figure 3.34 XRD Pattern for Pt/C and PtCr/C Catalyst Samples

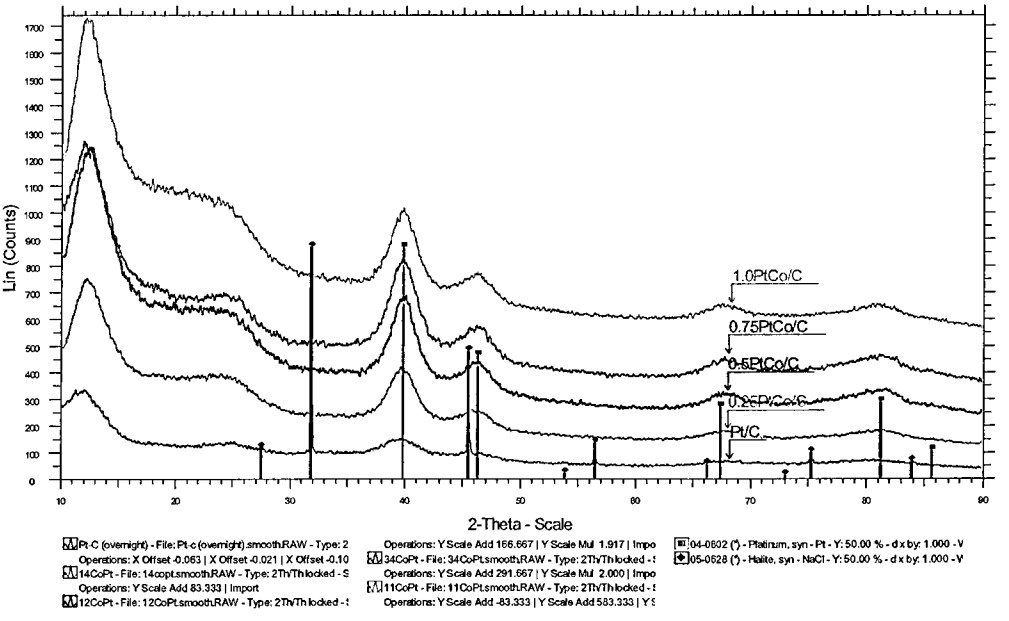

Figure 3.35 XRD Pattern for Pt/C and PtCo/C Catalyst Samples

catalysts were shifted to higher angle compared with the diffraction peaks of Pt/C catalyst, suggesting that the unit cell dimension of platinum has been decreased by substitution of the smaller iron atom into the Pt lattice. As the amount of iron deposited on the surface platinum increased, the shift in 2θ was found to increase further (Table 3.10). The Pt diffraction peaks in the PtNi/C, PtCr/C and PtCo/C catalysts were not shifted compared to those of Pt/C, suggesting that there was no evidence of alloy formation for the PtNi/C, PtCr/C and PtCo/C catalysts after the SOMC reaction alone(Figures 3.33 – 3.35).

Table 3.10 shows that all the PtM/C catalyst crystallite sizes estimated using the Debye-Scherrer equation were generally increased to 3.1 to 3.8 nm, compared with 2.8 nm of 20% Pt/C (reaction), this result supports the findings of the TEM/EDX. This again suggests that the second metal M did deposit on the Pt surface to form a Pt-M bimetallic in the PtM/C, although no evidence of alloy formation was found for PtNi/C, PtCr/C and PtCo/C catalysts. There was a larger increase observed for the PtFe/C system where evidence of alloy was also seen suggesting different properties for this system.

The results of TEM/EDX, H_2 chemisorption and XRD experiments have been discussed in section 3.3.1, 3.3.2 and 3.3.3. All results above support the fact that the second metal deposited on the surface Pt atoms of Pt/C catalyst. Thus the techniques of TEM/EDX, H_2 chemisorption and XRD have demonstrated the combination between the surface Pt atoms and the second metal during the preparation of PtM/C catalysts using SOMC method.

Table 3.10 XRD characterization and average diameter of PtM/C catalysts

Catalysts	2θ	Crystallite Size / nm	Lattice parameter /Å	Diameter (TEM) /nm
Pt/C (JCPDS)	39.8		3.92	
Pt_3Fe (JCPDS)	40.4		3.86	
Pt/C	39.8	2.4	3.92	2.7
Pt/C(200°C)	39.8	2.7	3.92	3.2
Pt/C(reaction)	39.9	2.8	3.92	3.5
0.25PtFe/C	39.9	3.5	3.90	4.3
0.5PtFe/C	40.0	3.5	3.90	4.5
0.75PtFe/C	40.1	3.7	3.89	4.6
1.0PtFe/C	40.3	3.8	3.87	4.6
0.25PtNi/C	39.9	3.1	3.90	4.2
0.5PtNi/C	39.9	3.1	3.91	4.2
0.75PtNi/C	39.8	3.2	3.92	4.2
1.0PtNi/C	39.9	3.2	3.90	4.4
0.25PtCr/C	39.9	3.4	3.92	4.2
0.5PtCr/C	39.9	3.3	3.92	4.3
0.75PtCr/C	39.9	3.4	3.90	4.3
1.0PtCr/C	39.7	3.3	3.93	4.4
0.25PtCo/C	39.7	3.1	3.92	4.2
0.5PtCo/C	39.8	3.2	3.92	4.4
0.75PtCo/C	39.7	3.1	3.92	4.5
1.0PtCo/C	39.8	3.1	3.92	4.5

3.3.4 Extended X-ray adsorption fine structure (EXAFS) [1]

In order to obtain direct structural information about the complicated microscopic structure of the PtM/C catalysts and to check the structural models proposed to explain their catalytic behaviour, the local structure around the iron, nickel and chromium atoms were determined by means of EXAFS at the Fe K-edge, Ni K-edge and Cr K-edge, respectively. Details on the EXAFS experiments and on the analysis of the data will be given in this section.

EXAFS data were collected for the 0.5PtFe/C, 1.0PtNi/C and 0.5PtCr/C catalysts, both in air and in H_2 (reduction for 1 hour at room temperature). The EXAFS experiments were carried out at room temperature in the fluorescence mode, and full details of the experimental conditions are given in Chapter 2. A description of the samples examined by EXAFS and their nomenclature are given in Table 3.11.

Table 3.11 The summary of samples examined by EXAFS

Samples	**Treatment method**
0.5PtFe/C(200 °C) in air	After SOMC , exposed and measured in air
0.5PtFe/C(200 °C) in H_2	Above sample, reduced in H_2 at room temperature for 1 hour, and measured under H_2
1.0PtNi/C(200 °C) in air	After SOMC, exposed and measured in air
1.0PtNi/C(200 °C) in H_2	Above sample, reduced in H_2 at room temperature for 1 hour, and measured under H_2
0.5PtCr/C(200 °C) in air	After SOMC, exposed and measured in air
0.5PtCr/C(200 °C) in H_2	Above sample, reduced in H_2 at room temperature for 1 hour, and measured under H_2

[1] This work was carried out jointly with Dr Andrea Russell and Ms Abbe Rose, Department of Chemistry, University of Southampton.

It should be noted that EXAFS is an averaging technique, so therefore we are not necessarily seeing what is happening at particular sites on the particle, but rather an average of what is happening in the system overall, for example, coordination numbers and distance between neighbouring atoms.

3.3.4.1 PtFe/C electrocatalysts

Figure 3.36 shows the EXAFS spectra and Fourier transforms (both experimental and theoretical) of the Fe K-edge in the samples of 0.5PtFe/C(200 °C) in air and in H_2. The results obtained from the analyses of these data are presented in Table 3.12. For the sample of the 0.5PtFe/C(200 °C) exposed in air, the spectrum was fitted to Fe surrounded by 2.5 oxygen atoms at a distance of 2.01 Å, with 1.3 Fe at a distance of 3.01 Å. The Fe–O bond length in crystalline Fe_2O_3 has an average value of 2.03 Å, and of Fe–O in FeO of 2.12 Å (Table 3.12); within experimental error, this refinement agrees with these values, supporting the fact that the Fe surface in the 0.5PtFe/C(200 °C) has oxidized after exposure to air, to give Fe–O species. (XPS data (see Section 3.3.5) indicates that the iron is present as Fe(III).) In this oxidized sample there was no evidence of any Pt neighbours.

When the 0.5PtFe/C(200 °C) electrocatalyst was reduced in hydrogen at room temperature for one hour, and the EXAFS measured under hydrogen, there was now evidence of Pt neighbours, with 2.5 Pt atoms at a distance of 2.63 Å. The coordination number of oxygen decreased to 1.2 indicating partial loss of oxygen, with the average Fe–O distance still ~2.02 Å. At the same time little evidence was seen of a Fe–Fe interaction. This suggests that the iron oxide species in the 0.5PtFe/C(200 °C) in H_2 were now in close contact with the Pt. As the treatment with the H_2 was only carried out at room temperature, this clearly was not sufficient to completely reduce the FeO_x species.

Suggested models of the surface of the 0.5PtFe/C(200 °C) electrocatalyst in air and in H_2, consistent with these results are shown in Figure 3.37. The coordination number of Fe–O in 0.5PtFe/C(200 °C) in the EXAFS experiments is 2.5 (oxidized) and 1.2 (reduced). This suggests that the iron is highly dispersed. A mixture of species (Fe and FeO_x) may be present in both cases (oxidized and reduced), and possibilities are shown in Figure 3.37. In the reduced sample some of the Fe in 0.5 PtFe/C may have entered the Pt crystalline lattice, although the XRD evidence for alloy formation is only compelling for the higher loading catalysts, 0.75 PtFe/C and 1.0 PtFe/C and at higher temperatures, so we have not shown it here.

Table 3.12 Best EXAFS fit parameters of 0.5PtFe/C(200°C) electrocatalysts in air and H_2, respectively (N: coordination numbers, R: distance from the Fe absorber, $2\sigma^2$: Debye-Waller factor, E_f: energy shift and R_{exafs}: a meaningful indication (below 40) of the quality of fit to the EXAFS data in k-space)

	Neighbour	**N**	**R / Å**	**$2\sigma^2$ / Å^2**	**E_f / eV**	**R_{exafs}**
In air	Fe – O	2.46 ± 0.17	2.01 ±0.12	0.012 ± 0.003	-12.00	32.05
	Fe – Fe	1.28 ± 0.29	3.01 ± 0.06	0.017 ±0.08		
In H_2	Fe – O	1.16 ± 0.11	2.02 ± 0.01	0.012 ±0.002	-2.05	30.99
	Fe – Pt	2.51 ± 0.25	2.63 ± 0.008	0.015 ±0.001		
	Fe – Fe	0.16 ± 0.08	2.55 ± 0.03	0.008 ± 0.006		
X-Ray Crystallographic data for comparison:						
Structure		**Bond distance/Å**		**Coordination number**		
Fe		Fe–Fe Fe–Fe	2.48 2.89	8 6		
FeO		Fe–O Fe–Fe	2.16 3.06	6 12		
Fe_2O_3		Fe–O Fe–O Fe–Fe	1.94 2.12 3.70	6 6 6		
Pt_3Fe		Pt–Fe Fe–Fe	2.74 3.87	12 6		

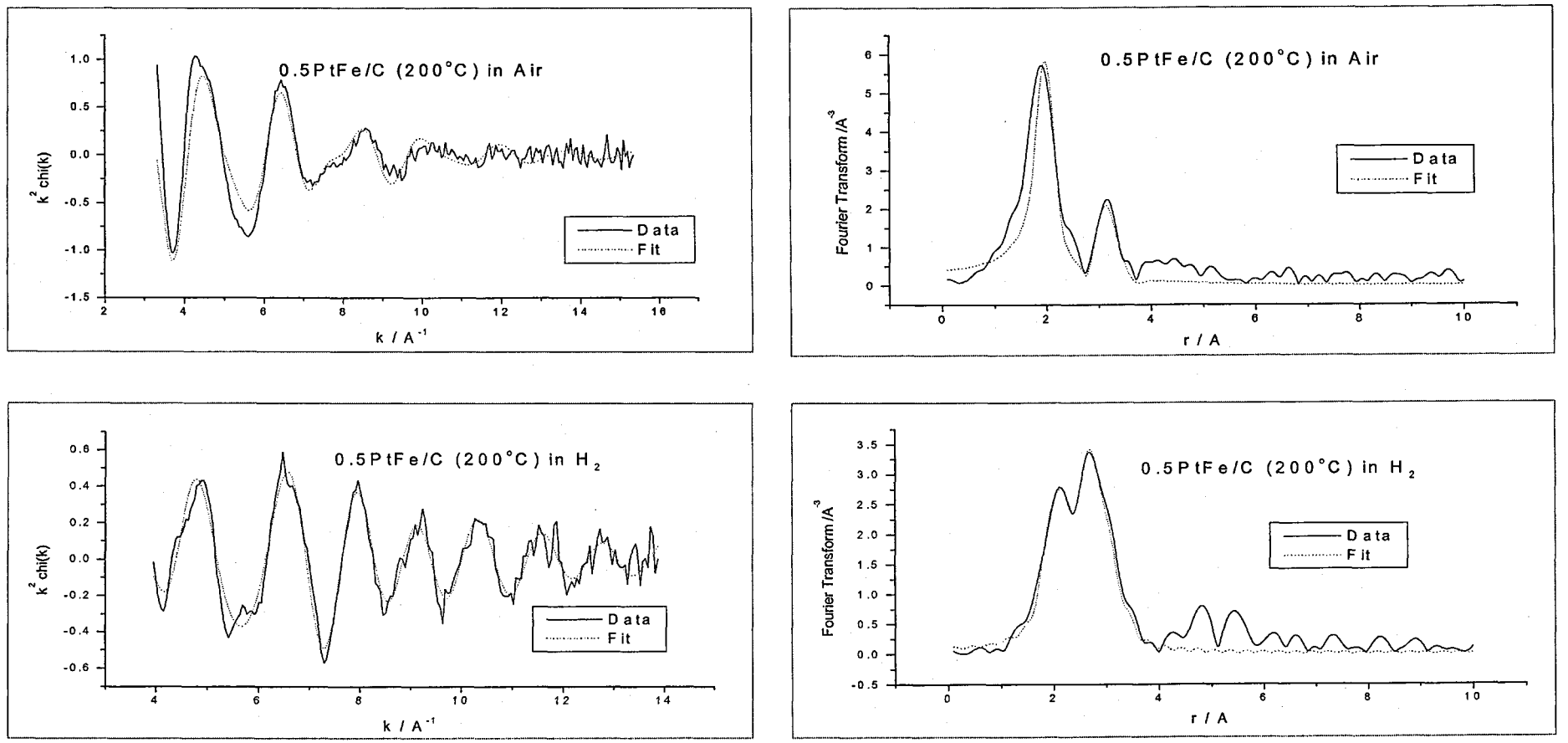

Figure 3.36 EXAFS k^2 weighted $x(k)$ spectra and k^2 weighted Fourier transforms of the Fe K-edge of 0.5PtFe/C(200°C) electrocatalysts in air and H_2, respectively. (solid line = data, dot line = fit)

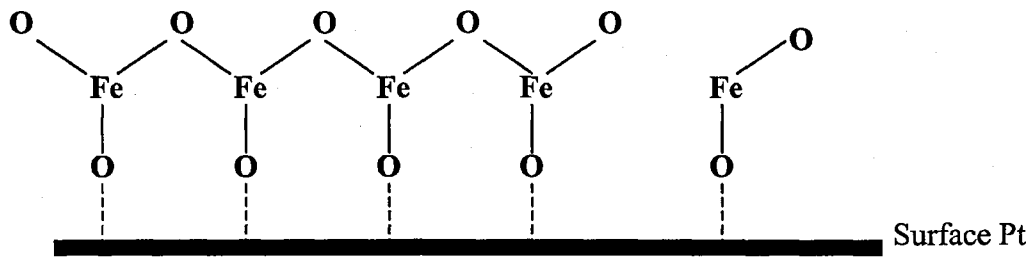

(a) in air

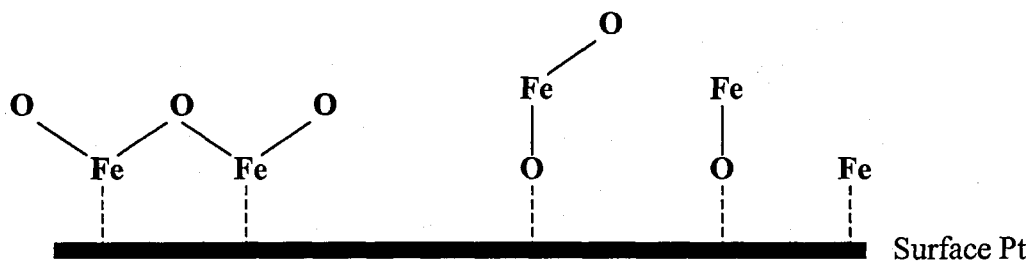

(b) in H_2

Figure 3.37 The models of 0.5PtFe/C(200°C) electrocatalysts (a) in air and (b) possible reduced species after treatment with H_2

3.3.4.2 PtNi/C electrocatalysts

EXAFS spectra and Fourier transforms (both experimental and theoretical) of the Ni K-edge in the samples of 1.0PtNi/C(200 °C) in air and in H_2 are shown in Figure 3.38. The results obtained from the analyses of these data are presented in Table 3.13. In 1.0PtNi/C(200 °C) in air, the Ni is fitted to 3.2 oxygen neighbouring atoms at a distance of 2.07 Å, and 1.7 Ni neighbouring atoms at a distance of 3.08 Å. No direct Ni–Pt bond was found although Ni has been shown to have deposited on the Pt/C catalyst. When 1.0PtNi/C(200 °C) catalyst was partially reduced and measured in H_2, there was now evidence of Pt neighbours around Ni, with 2.9 platinum atoms at a distance of 2.91 Å. The coordination number of oxygen decreased to 2.2. Both the Ni–O distance (~2.07 Å), and the Ni–Ni distance are consistent with a NiO-type species (the bond length of Ni–O in crystalline NiO is 2.08 Å, see Table 3.13). However the coordination number of Ni–O in NiO is 6 and the coordination number of Ni–O is 3.2 in our experiments, again

supporting high dispersion of the second metal. On reduction in H_2 the Ni now has Pt neighbours, but is still partially oxidized. A possible model of the surface of 1.0PtNi/C(200 °C) electrocatalysts in air and H_2 is shown in Figure 3.39. Similar to the PtFe/C results, this refinement showed that even after the reduction at room temperature, nickel was still coordinated to oxygen, but that the average coordination number of Ni–O decreased, and that Ni–Pt interactions had been formed.

Table 3.13 Best EXAFS fit parameters of 1.0PtNi/C (200°C) electrocatalysts in air and H_2, respectively (N: coordination numbers, R: distance from the Ni absorber, $2\sigma^2$: Debye-Waller factor, E_f: energy shift and R_{exafs}: a meaningful indication of the quality of fit to the EXAFS data in k-space)

	Neighbour	**N**	**R / Å**	**$2\sigma^2$ / Å^2**	**E_f / eV**	**R_{exafs}**
In air	Ni – O	3.21 ± 0.18	2.07 ± 0.01	0.010 ± 0.002	-4.72	34.36
	Ni – Ni	1.71 ± 0.27	3.08 ± 0.01	0.015 ± 0.003		
In H_2	Ni – O	2.20 ± 0.15	2.07 ± 0.01	0.008 ± 0.001	-3.90	35.77
	Ni – Ni	0.32 ± 0.20	2.56 ± 0.04	0.008 ± 0.001		
	Ni – Pt	2.88 ± 0.75	2.91 ± 0.03	0.016 ± 0.005		
	Ni – Ni	2.10 ± 0.26	3.04 ± 0.02	0.010 ± 0.003		

X-Ray Crystallographic data for comparison:

Structure	**Bond distance/Å**		**Coordination number**
Ni	Ni–Ni	2.50	12
	Ni–Ni	3.54	6
NiO	Ni–O	2.09	6
	Ni–Ni	2.95	12

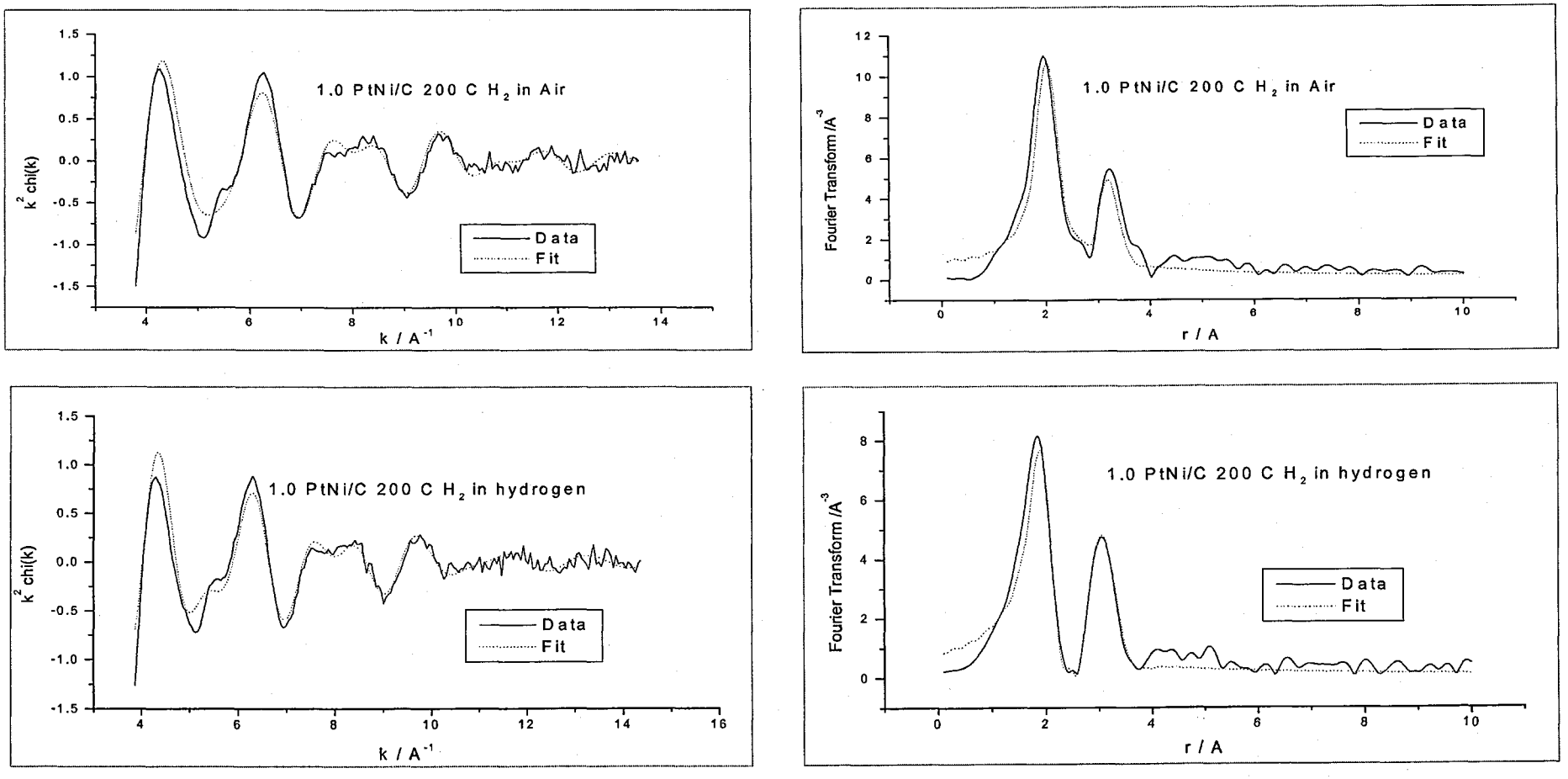

Figure 3.38 EXAFS k^2 weighted $x(k)$ spectra and k^2 weighted Fourier transforms of the Ni K-edge of 1.0PtNi/C(200°C) electrocatalysts in air and H_2, respectively. (solid line = data, dot line = fit)

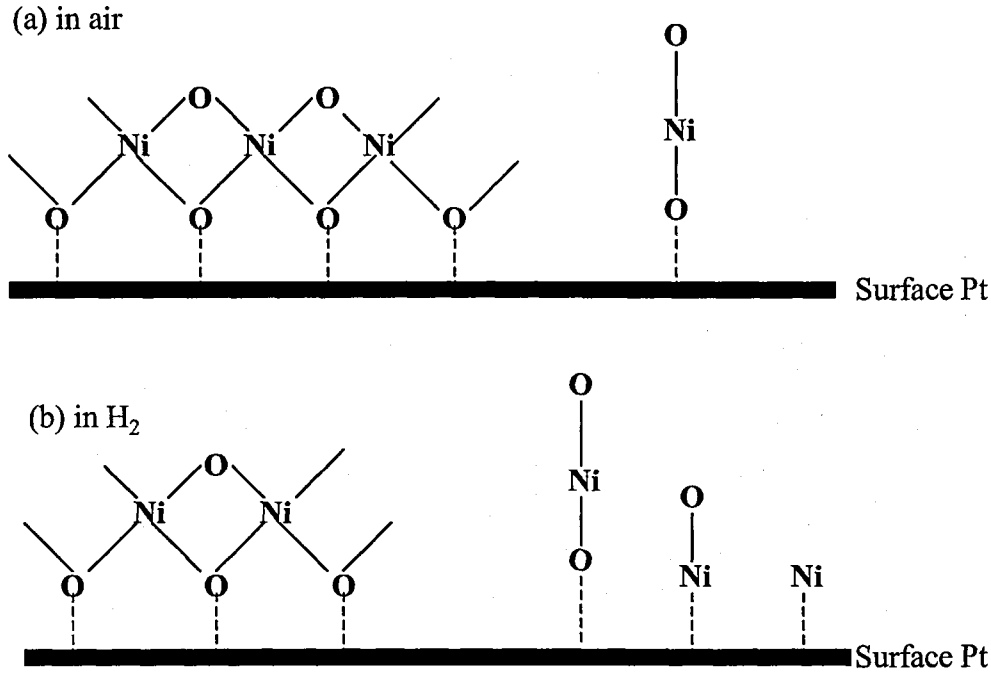

Figure 3.39 Possible models of the surface1.0PtNi/C(200°C) electrocatalysts (a) in air and (b) in H_2

3.3.4.3 PtCr/C electrocatalysts

Figure 3.40 shows the EXAFS spectra and Fourier transforms (both experimental and theoretical) of the Cr K-edge for the samples of 0.5PtCr/C(200 °C) in air and in H_2. The results obtained from the analyses of these data are presented in Table 3.14. When the sample of 0.5PtCr/C(200 °C) was exposed to air, the Cr was partially oxidized and refines to an environment of 1.7 oxygen atoms at a distance of 1.96 Å, and 1.2 Cr at a distance of 2.43 Å. In crystalline Cr_2O_3 the bond lengths for Cr–O average 1.99 Å and for Cr–Cr. is 3.66 Å; the Cr–Cr distance in the metal is 2.50 Å. This refinement supports that chromium metal is deposited on the Pt surface in the 0.5PtCr/C(200 °C) catalyst, but is partially oxidized after exposure to air to give Cr–O species with bond lengths similar to those found in Cr_2O_3. Unlike the samples of the 0.5PtFe/C(200 °C) in air and the 1.0PtNi/C(200 °C) in air, evidence for a direct Cr–Pt interaction was found for the 0.5PtCr/C(200 °C) electrocatalyst in air, refining 4.3 Pt neighbours at a distance of 2.64

Å. This suggesting that the interaction between Cr and surface Pt on the 0.5PtCr/C(200 °C) sample after SOMC reaction, was very strong. When the 0.5PtCr/C(200 °C) electrocatalyst was treated with H_2 at room temperature for one hour, and the EXAFS then measured in hydrogen, the Cr–Pt coordination number in the first coordination shell increased from 4.4 to 6.7 suggesting that on reduction some of the Cr moves into the bulk Pt with the possible formation of a Pt/Cr alloy. However, contrary to expectation, the Cr–O coordination number appeared to *increase* from 1.7 to 3.4 after treatment with H_2. This observation is difficult to explain; clearly the conditions of the experiment were not sufficient to reduce the Cr–O species present, but also air was carefully excluded from the experiment, so the overall amount of oxygen in the system could not increase. A possible explanation can found from the following literature and TPR experiments. According to the literature [34-37], a Pt–O bond contribution is observed at 2.03 Å in the Pt crystal structure of Pt/C and Pt-based alloy catalysts for EXAFS studies at the Pt L_{III}-edge. The TPR experiment (Section 3.3.6) for the 0.5PtCr/C(200 °C) catalyst shows that no peak for the Cr_2O_3 sample was found under the conditions of the TPR experiment, suggesting that Cr_2O_3 is very stable. However PtO is easy to reduce to Pt (section 3.3.6), so we suppose that the increase of the Cr–O coordination number on the 0.5PtCr/C (200 °C) after treatment with H_2, is due to the fact that oxygen from PtO combines with Cr on PtCr/C. At the same time some of the Cr moves into the Pt particle to form bulk Pt/Cr alloy. The overall reaction produces a net gain in the oxygen coordination around Cr. Another possible explanation is that a Cr–C species is formed, which would be difficult to distinguish from Cr–O by EXAFS. However, in view of the TEM/EDX results this seems less likely. It seems most likely that we have a heterogeneous Cr environment with a mixture of Cr metal, Cr_2O_3-type species, and Pt/Cr alloy all decorating the surface. Figure 3.41 shows a suggested model of the surface species for the 0.5PtCr/C(200 °C) electrocatalysts in air and H_2.

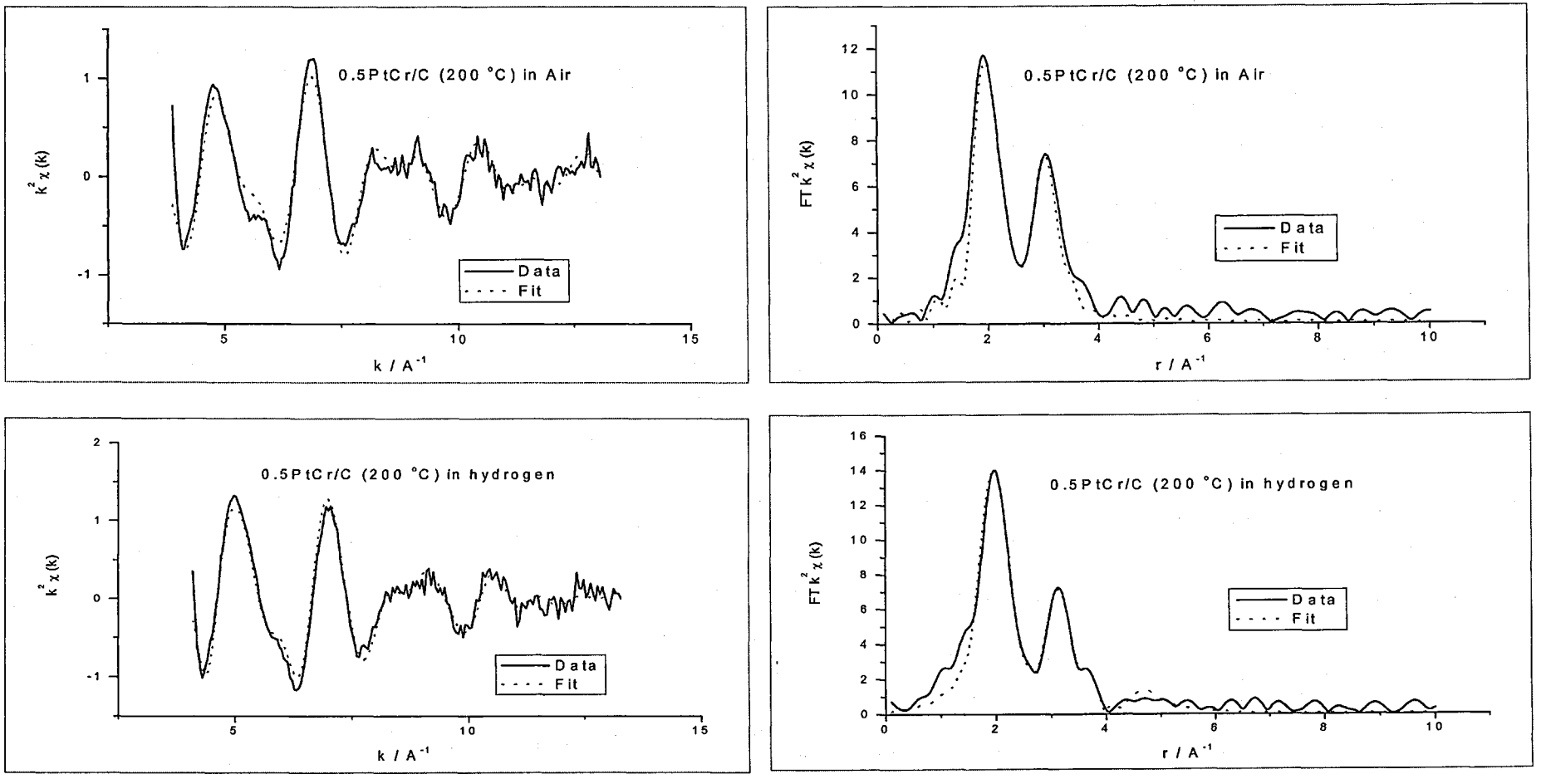

Figure 3.40 EXAFS k^2 weighted $x(k)$ spectra and k^2 weighted Fourier transforms of the Cr K-edge of 0.5PtCr/C(200°C) electrocatalysts in air and H_2, respectively. (solid line = data, dot line = fit)

Table 3.14 Best EXAFS fit parameters of 0.5PtCr/C (200°C) electrocatalysts in air and H_2, respectively (N: coordination numbers, R:distance from the Cr absorber, $2\sigma^2$: Debye-Waller factor, E_f: energy shift and R_{exafs}: a meaningful indication (below 40) of the quality of fit to the EXAFS data in k-space)

	Neighbour	N	R / Å	$2\sigma^2$ / Å^2	E_f / eV	R_{exafs}
In air	Cr – O	1.67 ± 0.15	1.96 ± 0.09	0.0014± 0.0014	2.34	30.69
	Cr – Cr	1.16 ± 0.29	2.43 ± 0.01	0.020 ± 0.004		
	Cr – Pt	4.38 ± 0.71	2.64 ± 0.02	0.017 ± 0.005		
	Cr – Cr	1.52 ± 0.38	2.84 ± 0.03	0.16 ± 0.048		
In H_2	Cr – O	3.41 ± 0.20	1.92 ± 0.09	0.011 ± 0.001	10.15	23.74
	Cr – Cr	1.37 ± 0.21	2.36 ± 0.01	0.017 ± 0.002		
	Cr – Pt	6.70 ± 1.01	2.58 ± 0.03	0.029 ± 0.002		
	Cr – Cr	1.14 ± 0.28	3.26 ± 0.012	0.010 ± 0.004		
	Cr – Cr	1.46 ± 0.052	3.79 ± 0.03	0.013 ± 0.005		

X-Ray Crystallographic data for comparison:

Structure	Bond distance/Å		Coordination number
Cr	Cr–Cr	2.50	8
	Cr–Cr	2.88	6
Cr_2O_3	Cr–O	1.96	6
	Cr–O	2.01	6
	Cr–Cr	3.65	6

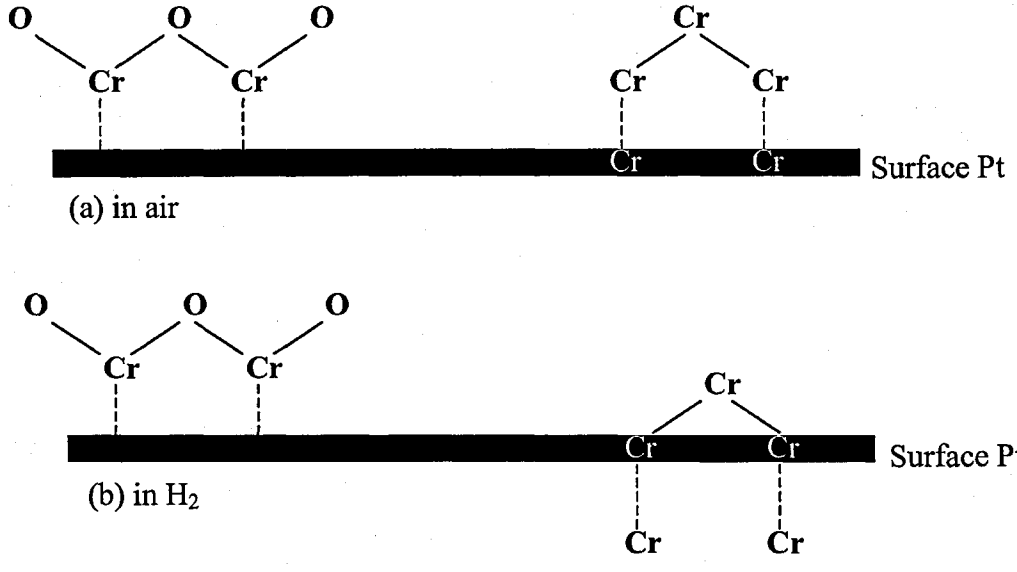

Figure 3.41 Surface species for the 0.5PtCr/C(200°C) electrocatalyst in air or in H_2

3.3.5 X-ray photoelectron spectra (XPS)

XPS was used to determine the oxidation-state of the iron and platinum metal for the PtFe/C series of catalysts. The binding energies and the relative peak intensities of the C-1s and O-1s X-ray photoelectron spectra for the carbon-supported Pt and PtFe/C samples are given in Table 3.15.

Table 3.15 Binding energies and relative intensities of various species from the C-1s and O-1s curve fitted X-ray photoelectron spectra in 20% Pt/C and PtFe/C catalysts

Catalyst	*Binding Energy C-1s* /eV	Binding Energy O-1s	
		Binding Energy /eV	Relative intensities /%
20% Pt/C	284.8		
0.25PtFe/C	284.8	531.0 532.3 533.8	10.5 57.9 31.6
0.5PtFe/C	284.8	531.1 532.4 534.0	18.5 59.3 22.2
0.75PtFe/C	284.8	530.1 532.3 534.1	17.2 62.1 20.7
1.0PtFe/C	284.8	530.7 532.2 533.8	28.0 48.0 24.0

The binding energy of C-1s from the carbon support was found at 284.8 eV, and the value is coincident with the value of 284.6 eV (graphitic carbon) shown in the literature [38]. The O-1s X-ray photoelectron spectra for the carbon-supported Pt and PtFe/C samples are composed of three components labeled as 1, 2 and 3. The peaks occurring at 530.1 – 531.1 eV (peak 1) could be due to the Pt-O species (530 V) and Pt-OH_{ads} species (531.5 eV) [39]. The peaks obtained at higher binding energies (532.2 – 532.4 eV) (peak 2) were probably derived from the carbon support, showing the strong

presence of –CO species [38]. The high binding energy peaks (peak 3) at 533.8 – 534.1 eV were ascribed to carboxylic groups from the carbon support. This is good agreement with the results of Arico et al [40] . They also reported that the O-1s X-ray photoelectron spectra for Pt/C, PtCo/C and PtCoCr/C had three peaks at the same binding energies [40].

The Pt-4f and Fe-2p X-ray photoelectron spectra are shown in Figures 3.42 and 3.43. The binding energies and relative intensities are given in Table 3.16. The Pt-4f XPS signal for bulk-platinum metal has been used from the literature [41] as a reference to interpret the Pt-4f X-ray photoelectron spectra of the 20% Pt/C and PtFe/C catalysts. The Pt 4f signal was derived from two pairs of Pt peaks. The most intense peaks were attributed to zero-valent platinum [42], whose binding energies for the Pt-$4f_{7/2}$ electrons and Pt-$4f_{5/2}$ electron were found to be located at 71.6-71.9 and 74.9-75.2 eV respectively. These values for all the supported catalysts are somewhat higher than those of bulk Pt, at 70.9 and 74.2 eV [38], , suggesting that the Pt in the Pt/C and PtFe/C catalyst was slightly electropositive, possibly due to a contribution from metal-support interaction [43]. This result is similar to that found for dispersed Pt metal on a support [10, 37]. The second set of doublets, with binding energies at about 72.9-73.4 and 76.5-76.8eV, were assigned to the Pt(II) state in PtO- and $Pt(OH)_2$- like species [44, 45]. Comparing the relative intensities of Pt(0)/Pt(II) between the 20% Pt/C and the PtFe/C catalysts, the amount of Pt(II) decreased after the SOMC reaction. This could be attributed to the reduction step during the preparation step, although the sample had subsequently been re-exposed to air. The peak of Pt(IV) on Pt/C and PtFe/C catalysts was difficult to detect in XPS due to the overlap with Pt(II), and also because Pt(IV) is easily reduced in the X-ray beam [40, 46].

The Fe-2p spectra were composed of only one pair of peaks at binding energies of 710.0 - 710.6 eV ($2p_{3/2}$) and 725.0 eV ($2p_{1/2}$). These are attributed to the presence of Fe_2O_3 species in the FePt/C catalyst [38]. The binding energies of Fe-2p (720 and 707 eV) for Fe^0 were not found. Thus, the XPS data show that after exposure to air the Fe in the samples was found to be oxidised, predominantly present as Fe_2O_3. The result was in good agreement with that of EXAFS where there appeared to be an Fe_2O_3–type phase in the 0.5PtFe/C (200°C) catalyst. As the amount of iron on the surface platinum is increased, the peak areas of the Fe $2p_{1/2}$ and Fe $2p_{3/2}$ were found to increase (Figure 3.43) as would be expected.

XPS studies were not performed on the Cr, Ni or Co series of catalysts.

Table 3.16 Binding energies and relative intensities of various species from the Pt-4f and Fe-2p curve fitted X-ray photoelectron spectra in 20% Pt/C and PtFe/C catalysts

catalyst	Binding Energy Pt-4f				Binding Energy Fe-2p		
	Species (*)	Binding Energy /eV		Relative intensities (%)	Binding Energy /eV		Relative intensities /%
		$4f_{7/2}$	$4f_{5/2}$		$2p_{3/2}$	$2p_{1/2}$	
20% Pt/C	Pt^0	71.9	75.2	73.7			
	Pt^{II}	73.4	76.5	26.3			
0.25PtFe/C	Pt^0	71.7	75.0	93.1	710.0	725.0	100
	Pt^{II}	73.2	76.6	6.9			
0.5PtFe/C	Pt^0	71.6	74.9	90.9	710.0	725.0	100
	Pt^{II}	73.5	76.8	9.1			
0.75PtFe/C	Pt^0	71.6	75.0	87.7	710.6	725.0	100
	Pt^{II}	72.9	76.5	12.3			
1.0PtFe/C	Pt^0	71.7	74.9	89.7	710.2	725.0	100
	Pt^{II}	72.9	76.7	10.3			

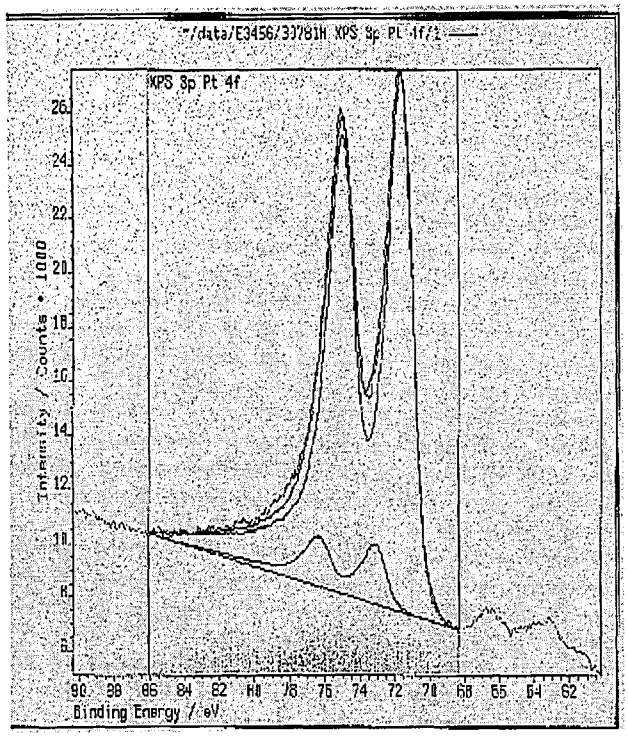

a

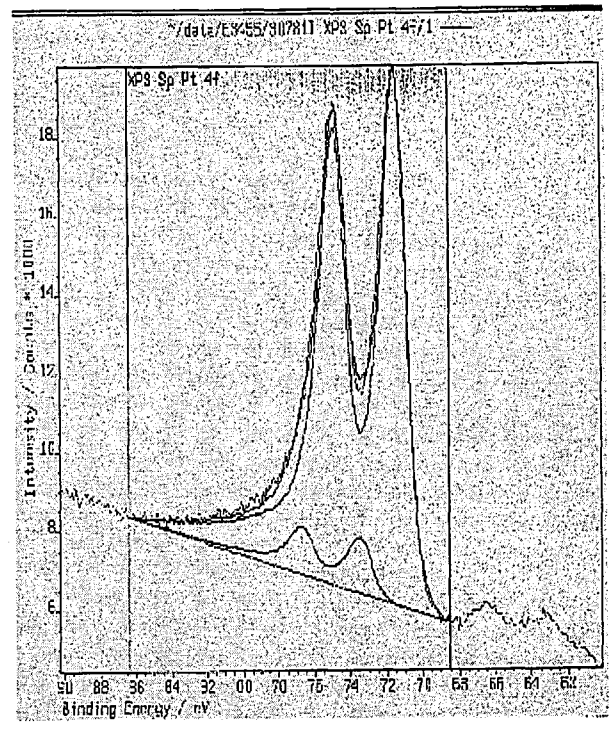

b

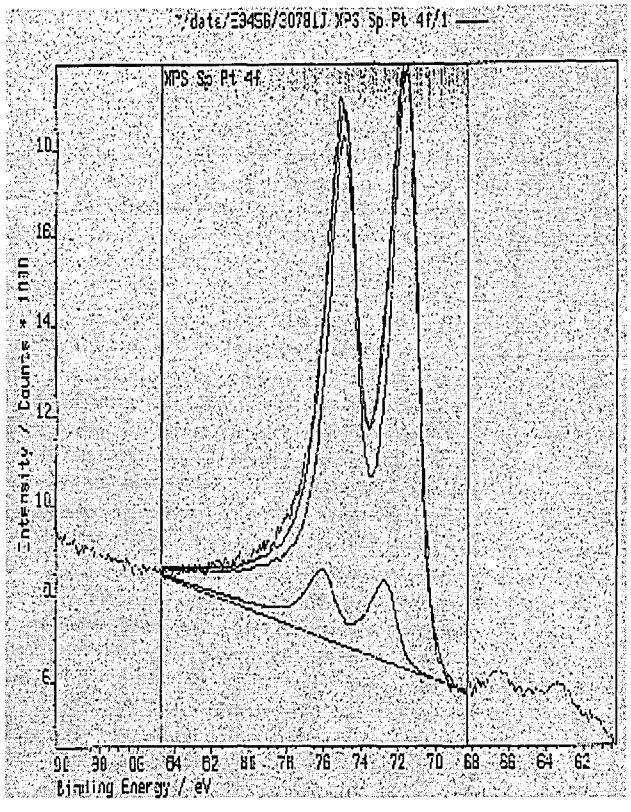

c

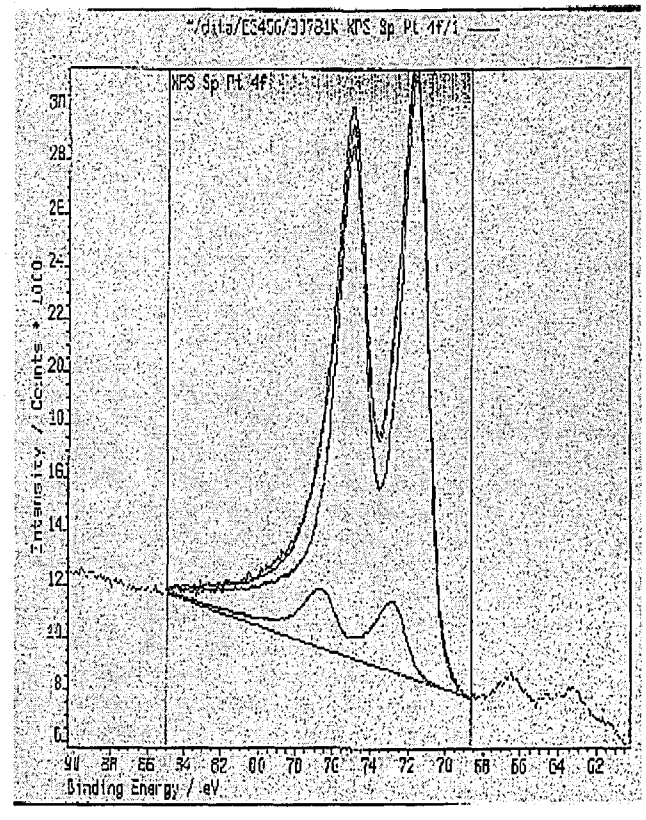

d

Figure 3.42 Pt-4f XPS of (a) 0.25PtFe/C, (b) 0.5PtFe/C, (c) 0.75PtFe/C, and (d) 1.0PtFe/C catalysts

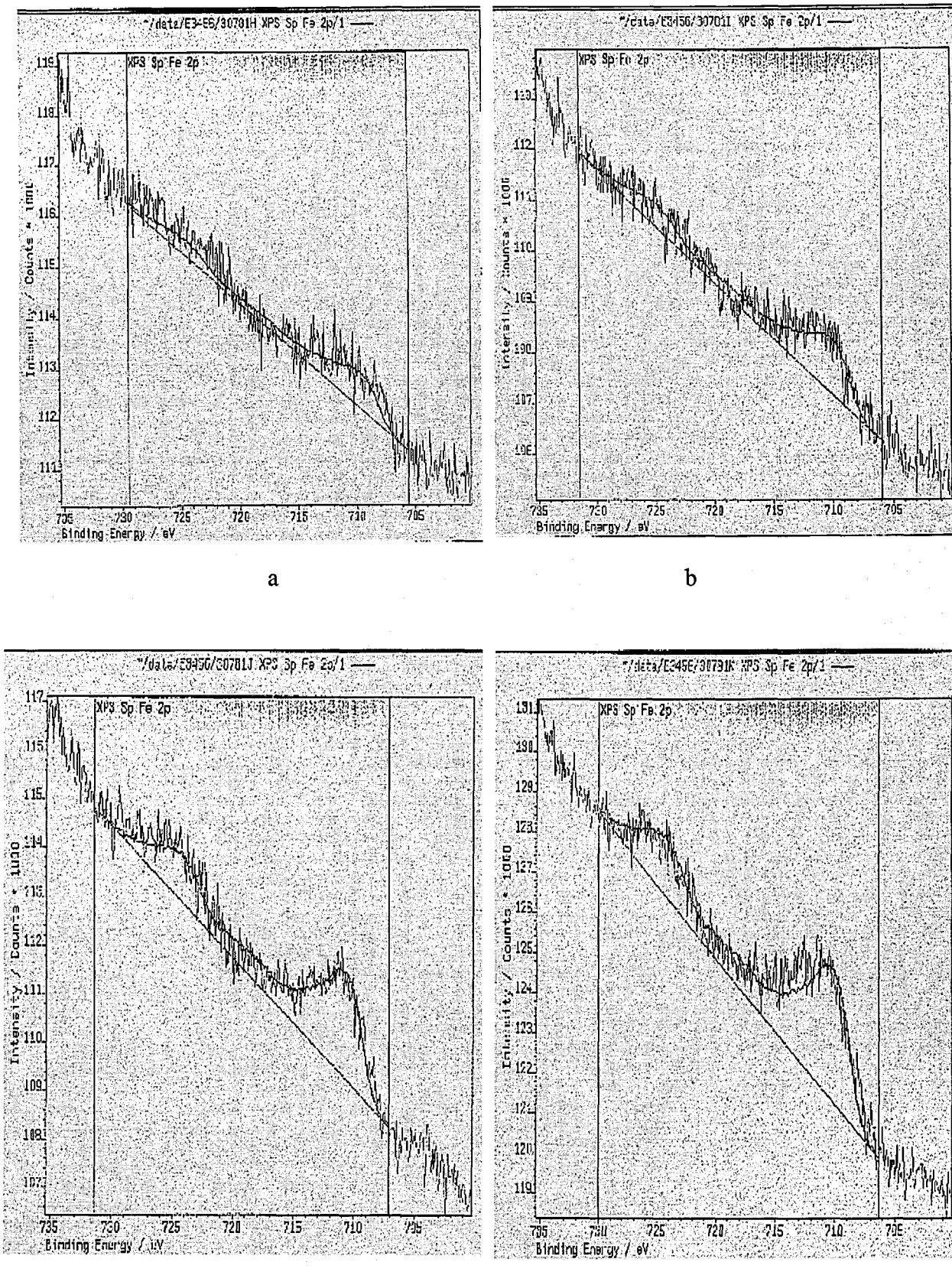

Figure 3.43 Fe-2p XPS of (a) 0.25PtFe/C, (b) 0.5PtFe/C, (c) 0.75PtFe/C, and (d) 1.0PtFe/C catalysts

3.3.6 Temperature-programmed reduction (TPR)

Temperature-programmed reduction (TPR) was carried out in an apparatus consisting of a flow controller and a reactor coupled to a gas chromatograph (refer to Chapter 2). A typical TPR profile is a record of the amount of hydrogen gas consumed by the sample as a function of temperature. It consists of a series of peaks. The position of a peak in the profile is determined by the chemical nature and environment of the chemical component, and the area of the peak reflects the hydrogen consumption by the samples. The hydrogen consumption was calculated by integration of the TPR profiles and the instrument was calibrated using by a series of standard external sample loops with a known volume of H_2. Figure 3.44 shows the calibration curve of hydrogen consumption versus the peak area for our instrument. A plot of the peak area as a function of the amount of hydrogen present was linear.

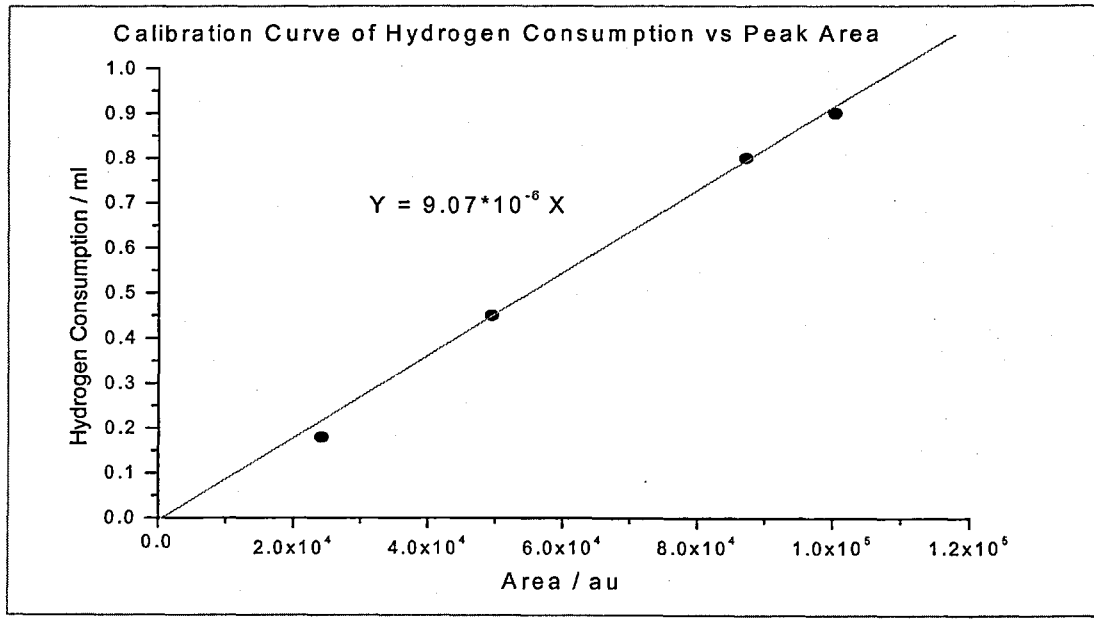

Figure 3.44 Quantitative analysis of hydrogen present

Figure 3.45 displays the TPR profiles of carbon and the 20% Pt/C catalyst, monitored in the range –78 °C to 950 °C. The TPR profile of the carbon displays a flat line indicating that no reduction of the carbon took place in the temperature range studied. The peaks before "heat on" resulted from consequences of turning on the valve. Three hydrogen consumption zones were observed for the TPR profile of the 20% Pt/C catalyst. These reduction peaks can be attributed to the metal. The two peaks at low temperature (peaks 1 and 2) were attributed to the reduction of Pt-oxygen compounds, PtO_X. The presence of two peaks suggests different forms of PtO_X or different sites on the metal surface. Evidence of a two-stage reduction has also been reported by McNicol and Short in the literature [47, 48]. For bulk platinum oxide they reported a double TPR profile at around 25 °C and 75 °C, the former being about twice as intense as the latter; and the total hydrogen consumption was found to equivalent to that of a four-electron reduction [47]; they attributed the double peaks to a two-step reduction of Pt^{4+} to Pt^{2+} and then Pt^{2+} to Pt^0. Yao et al [48] found using TPR that PtO_2 reduced in a similar temperature range to that found by McNicol [47]. TPR studies of the "reduced" catalysts [47] showed reduction peaks for Pt at temperatures substantially below that found for the bulk oxides. For "reduced" PtO_2, for instance, a reduction peak was found at –72 °C. For impregnated platinum supported carbon catalysts, McNicol et al reported a similar double TPR profile with two peaks at -96 and –78 °C with a hydrogen consumption corresponding to less than a two-electron reduction [47]; this is similar to our findings.

The third peak of the TPR profile (Figure 3.45) of Pt/C was at high temperature (580 °C). From the TPR result, and previous literature studies concerned with the reduction of Pt catalysts [49, 50], it would be anticipated that this can be attributed to hydrogen adsorbed at high temperature which has apparently penetrated into subsurface layers of Pt. Menon and Froment [51] studied H_2 adsorption and desorption from supported Pt (Al_2O_3, SiO_2, and TiO_2 supports) at various temperatures using TPD

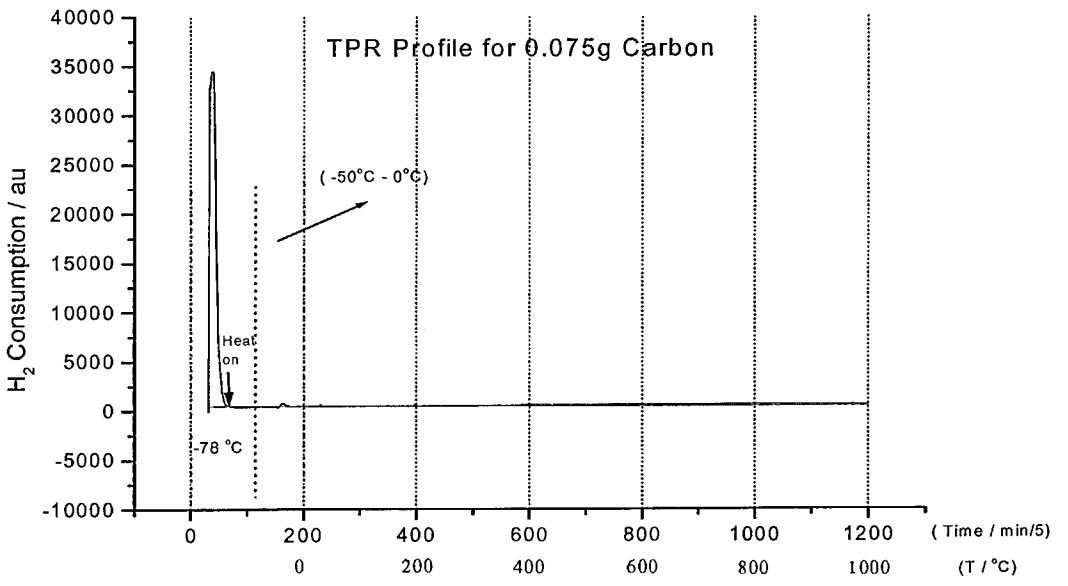

(a)

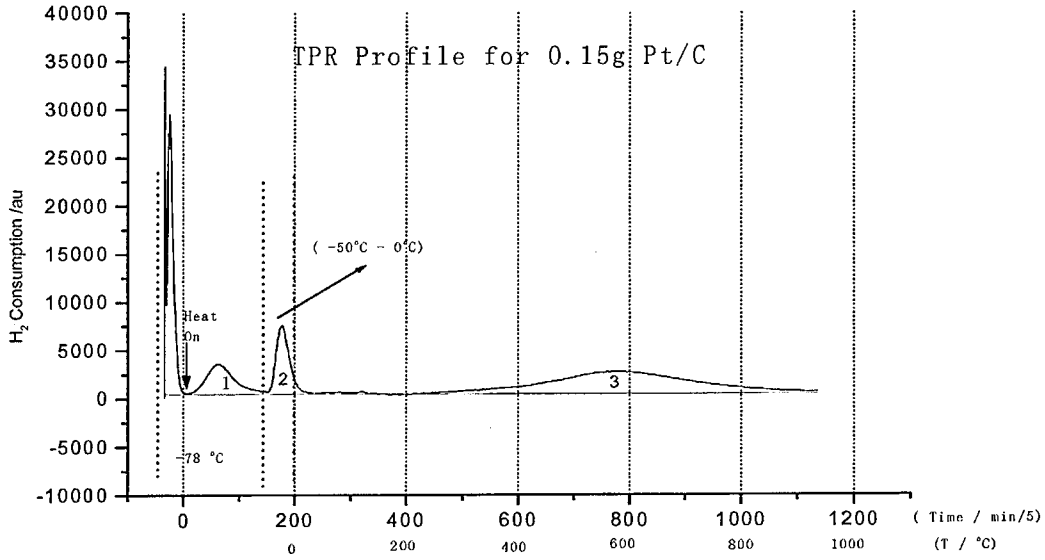

(b)

Figure 3.45 TPR profile for (a) carbon and (b) 20% Pt/C

technique to understand the processes on supported catalysts. They observed H_2 adsorption in the 300 -500 °C range. They attributed this adsorption to reduction of Pt and the fact that hydrogen adsorbed at high temperature penetrated into subsurface layers of Pt. They reported that hydrogen adsorbed at high temperature could only be desorbed at higher temperature [51].

The TPR profile of the PtFe/C, PtNi/C and PtCr/C catalysts are shown in Figures 3.46-3.48. The temperature range monitored was –78°C to 950°C. The hydrogen consumption estimated from the peak areas are tabulated in Table 3.17. As the amount of iron, nickel or chromium on the surface platinum is increased, the first peak at low temperature decreases or in some cases is not evident at all. It can be suggested that PtO_x species resposible for peak 1 present at surface sites on Pt/C have been reduced by reaction with H_2 or the second metal M during the SOMC reaction.

The effect of the second metal on the hydrogen consumption for peak 2 varied with different metals. The amount of hydrogen consumption of the second peak increased as Fe increased; decreased as Cr increased and did not change as Ni increased.

The hydrogen consumption of the third peak did not change significantly on addition of the second metal. The third peak splits into two for the PtFe/C catalysts, but not for the PtNi/C and PtCr/C catalysts. In addition we carried out TPR experiments for 30 – 50 mg Fe_2O_3 and Cr_2O_3 samples (Figure 3.49). No peak was observed for the Cr_2O_3 sample in the TPR experiment. However, the Fe_2O_3 was reduced in the range between 500 – 800 °C. This result suggests that the peak observed in this range for the PtFe/C probably also contains a contribution from the surface Fe_2O_3. Ayub et al [52] did a more detailed study looking at the redox characteristics of iron oxides using ^{57}Fe Mössbauer spectra recorded *ex situ* after each reduction step. Their results showed the initial reduction of Fe_2O_3 to Fe_3O_4 at 350 °C followed by partial reduction to FeO and metallic

iron (Fe) at *ca.* 720 °C [52]. The amount of hydrogen consumption at the third peak for Pt/C, PtFe/C, PtNi/C and PtCr/C catalysts are very similar.

Table 3.17 Quantitative analysis hydrogen consumption (ml g^{-1} catalyst)

Catalyst	**Peak 1**	**Peak 2**	**Peak 3**
Carbon	0	0	0
Pt/C	11	12	43
0.25PtFe/C	7	8	39
0.5PtFe/C	6	11	38
0.75PtFe/C	0	14	38
1.0PtFe/C	0	19	39
0.25PtNi/C	3	13	43
0.5PtNi/C	0	13	44
0.75PtNi/C	0	12	41
1.0PtNi/C	0	13	41
0.25PtCr/C	4	10	43
0.5PtCr/C	1	9	41
0.75PtCr/C	0	8	42
1.0PtCr/C	1	9	41

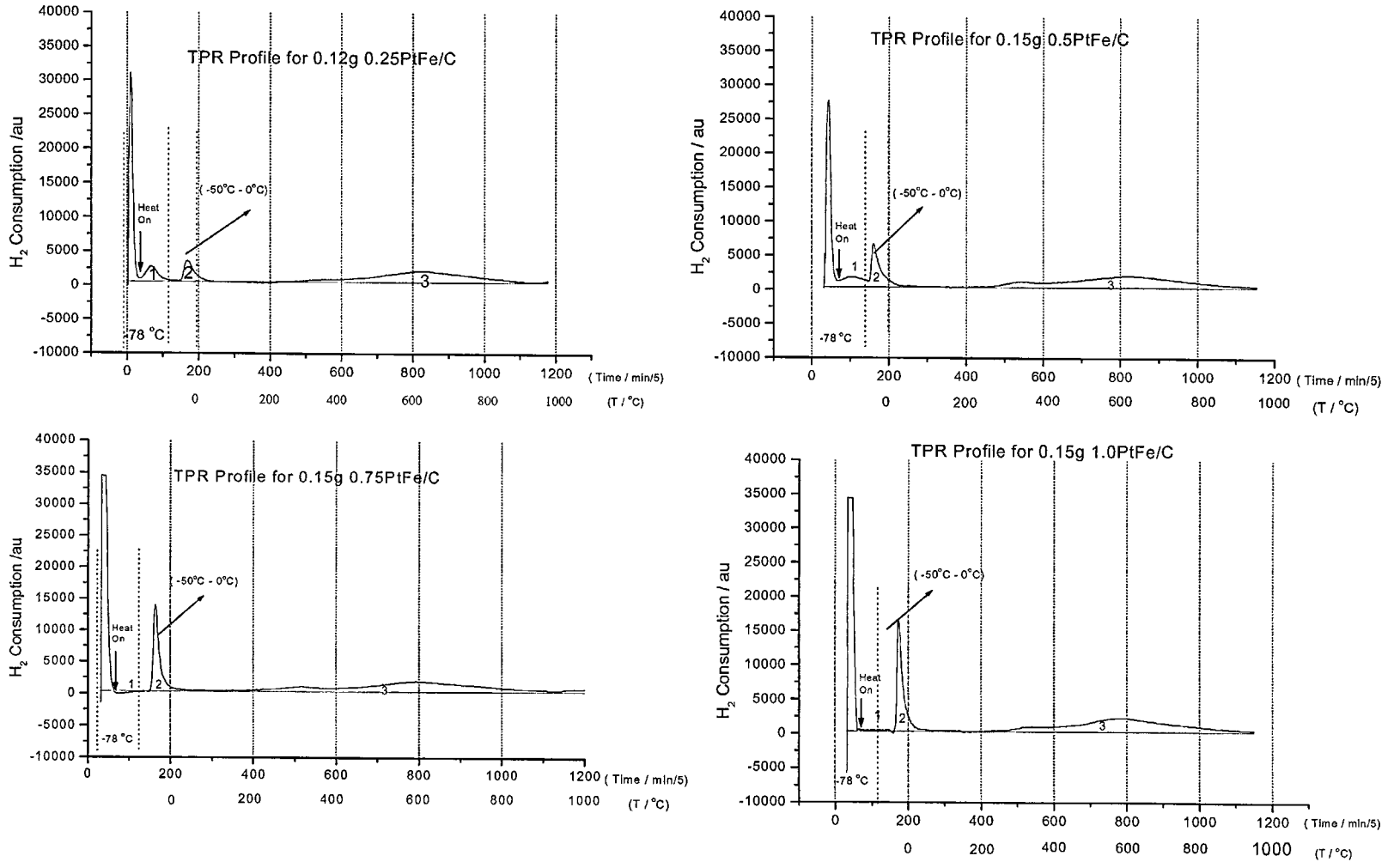

Figure 3.46 TPR profile for PtFe/C catalysts

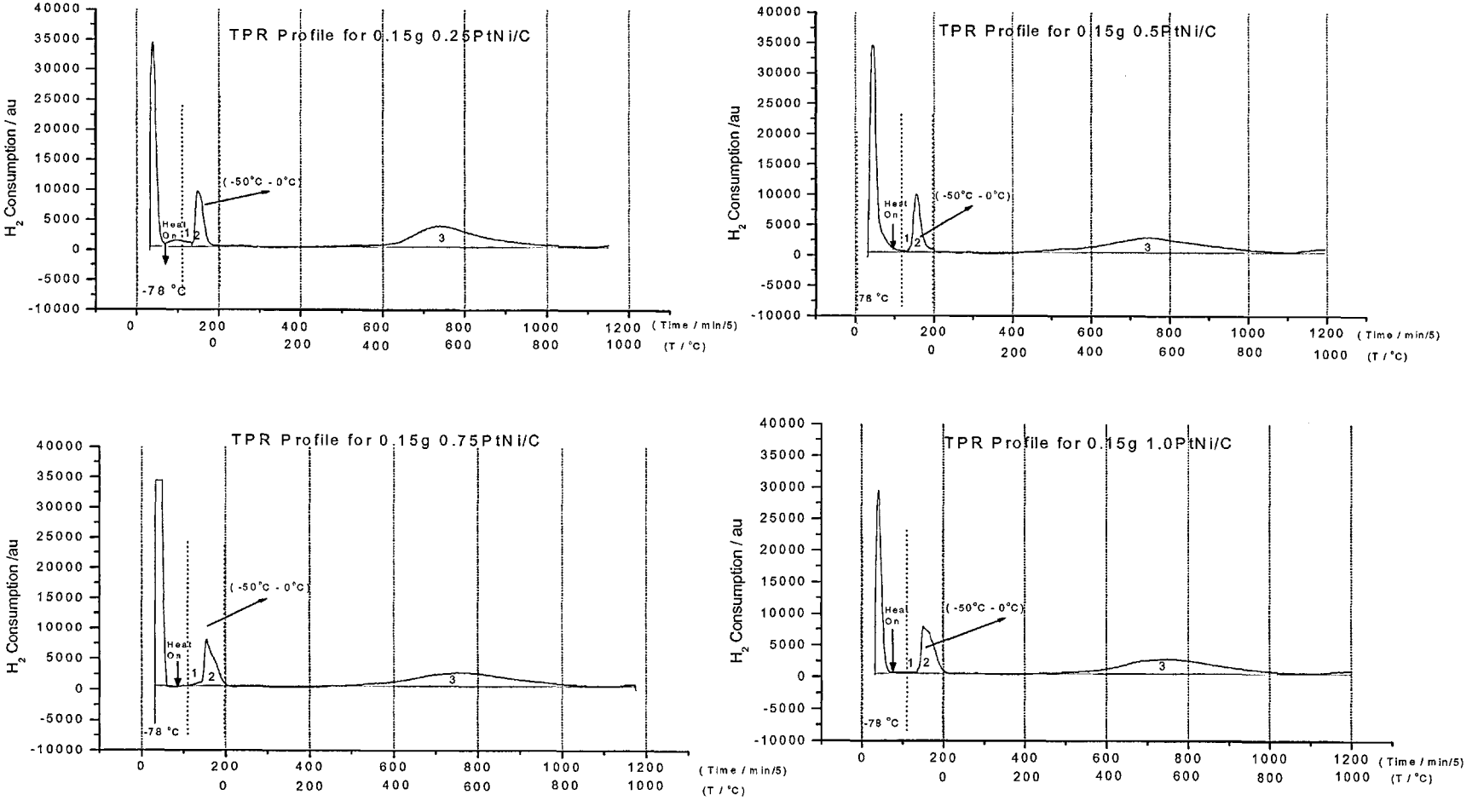

Figure 3.47 TPR profile for PtNi/C catalysts

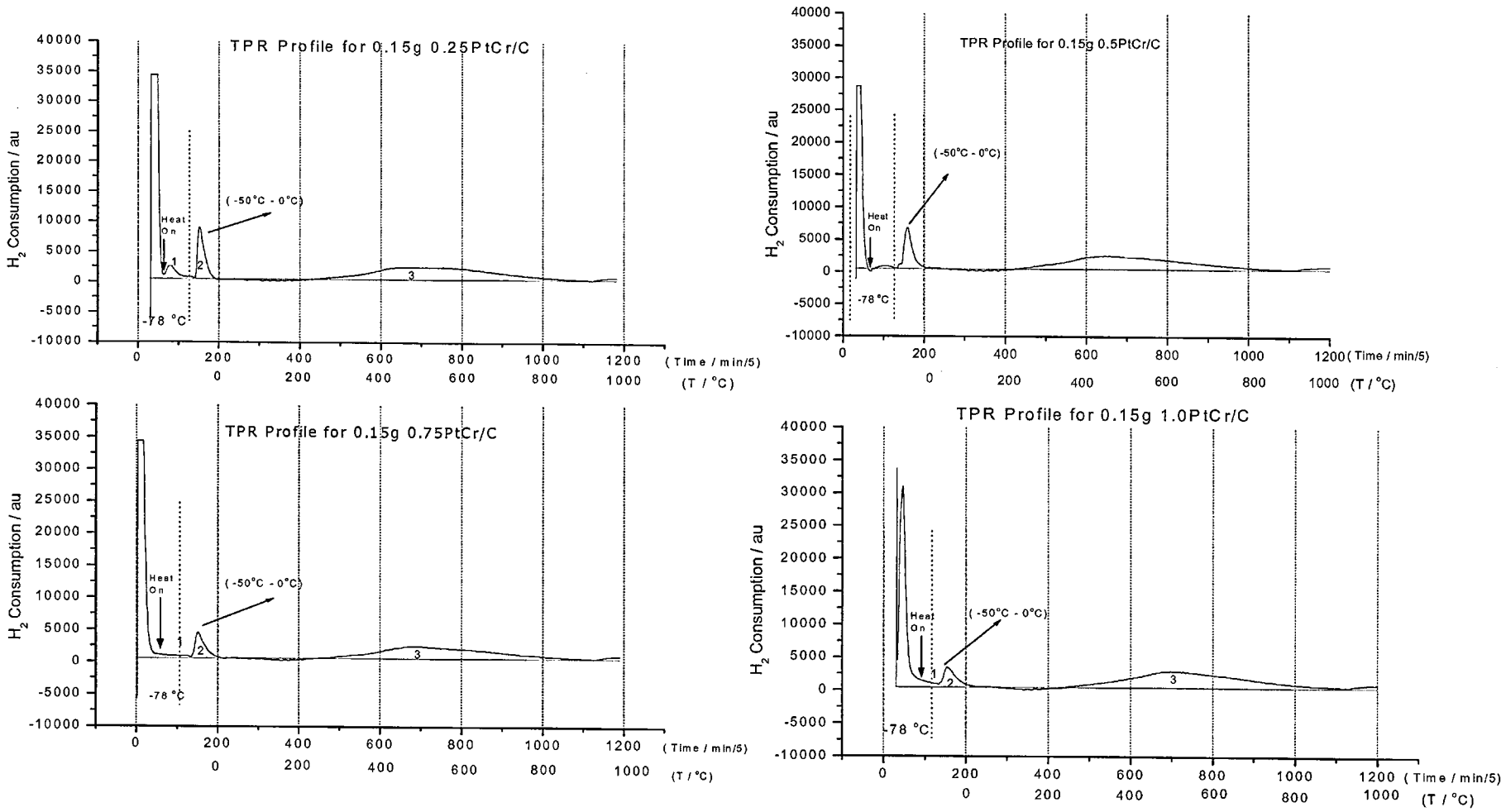

Figure 3.48 TPR profile for PtCr/C catalysts

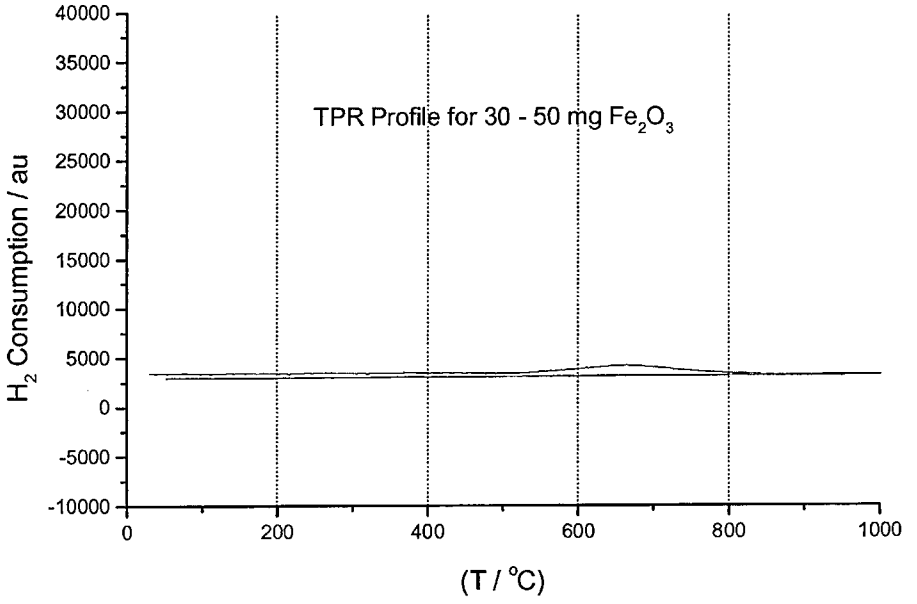

(a)

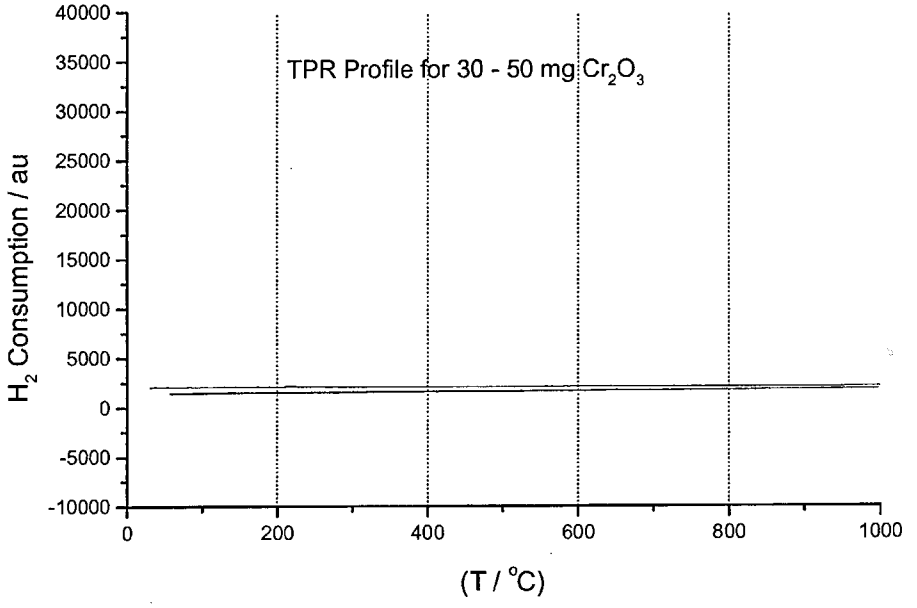

(b)

Figure 3.49 TPR profile for (a) Fe_2O_3 and (b) Cr_2O_3

3.4 Conclusions

A series of PtFe/C, PtNi/C, PtCo/C and PtCr/C bimetallic catalysts have been prepared from a Pt/C monometallic catalyst using the appropriate metallocene $M(C_5H_5)_2$ (where M is Co, Ni, Cr or Fe), and characterized using a range of techniques.

i) Under the reaction conditions employed during surface organometallic chemistry (SOMC), the reaction between the Pt/C catalyst and metallocene $M(C_5H_5)_2$ is believed to result in the selective deposition of the second metal, M, onto the Pt surface of a reduced Pt/C catalyst; the amount of the second metal deposited on carbon support appears to be negligible.

ii) UV-visible spectroscopy and ICP have been used to analyse the composition of the catalysts for the SOMC reaction during the catalyst preparation. It suggests that there is a limit for the deposition of the second metal on surface Pt, which varies with the metal used. $Co(C_5H_5)_2$ and $Ni(C_5H_5)_2$ appear to have decomposed under the reaction conditions used resulting in lower loadings than the nominal loading. According to the results of GC-MS and TGA/DSC, a reaction mechanism between the metallocene $M(C_5H_5)_2$ and Pt/C can be postulated: $Pt/C + 5H_2 + M(C_5H_5)_2 \rightarrow M\text{-}Pt/C + 2C_5H_{10}$

iii) TEM/EDX, BET, chemisorption and X-ray diffraction support that a selective reaction has occurred between the reduced surface Pt of the Pt/C catalyst and the organometallic precursor of the second metal. The metal particle size of the pure Pt/C and the PtM/C bimetallic catalysts increase as the second metal increase.

iv) EXAFS, TPR and XPS disclose the oxidation state of platinum and the second metal. XPS data indicates the presence of a Fe_2O_3 phase for PtFe/C catalysts; and EXAFS data indicates the presence of a Fe_2O_3, Cr_2O_3, NiO and the second metal phases in PtM/C catalysts.

3.5 References

1. N.N.Greenwood and A.Earnshaw, Chemistry of the Elements, Pergamon Press, 1984.
2. *http://ntp-server.niehs.nih.gov/ [Accessed: 16 December, 2003].*
3. E.M. Crabb, M.K. Ravikumar, D. Thompsett, A.E. Russell and A. Rose, *"Effect of Ru surface composition on the CO tolerance of carbon-supported PtRu" (in preparation).*
4. J.D. Roberts and M.C. Caserio, Basic Principles of Organic Chemistry, 2nd Edition, W. A. Benjamin, Inc., London, 1977: p. 77 and 92.
5. Ch. Elschenbroich and A. Salzer, Organometallics, VCH Publisher, New York, 1989: p. 345.
6. J. F. Faudon, F. Senocq, G. Bergeret, B. Moraweck, G. Clugnet, C. Nicot and A. Renouprez, J. Catal., 1993. **144**: p. 460.
7. C. M. Pleass and D. G. Schimmel, J. Catal., 1972. **24**: p. 424.
8. E.M. Crabb and Robert Marshall, Appl. Catal. A: Gen., 2001. **217**: p. 41.
9. B. D. Cullity, Elements of X-ray diffraction, Second Edition, Addision-Wesley Publishing Company, 1978.
10. E. M. Crabb, R. Marshall and D. Thompsett, J. Electrochem. Soc., 2000. **147**: p. 4440.
11. B. Coq, A. Bittar and R. Dutartre, J. Catal, 1991. **128**: p. 275.
12. M.E. Halttunen, M. K. Niemela, A. O. I. Krause, T. Vaara and A. I. Vuori, Appl. Catal. A: General, 2001. **205**: p. 37.
13. B. Didillon, C. Houtman and T. Shay, J. Am. Chem. Soc., 1993. **115**: p. 9380.
14. G. Neri, C. Milone, S. Galvagno, A.P.J. Pijpers and J. Schwank, Appl. Catal. A: Gen., 2002. **227**: p. 105.

15. K. Kunimori, T. Uchijima, M. Yamada, H. Matsumoto, T. Hattori and Y. Murakami, Appl. Catal., 1982. **4**: p. 67.

16. H. J. Jung, M. A. Vannice, L. N. Mulay, R.M. Stanfield and W. N. Delgass, J. Catal., 1982. **76**: p. 208.

17. A.S. Arico, V. Antonucci, N. Giordano, A.K. Shukla, M.K. Ravikumar, A. Roy, S.R. Barman and D.D. Sarma, Journal of Power Sources, 1994. **50**: p. 295.

18. H.P. Klug and L.E. Alexander, X-ray Diffraction Procedures for Polycrystalline and Amorphous Materials, Wiley, New York, 1974.

19. Powder Diffraction Files (Inorganic Volumes), *26-1079.* JCPDS International Center for Diffraction Data, USA.

20. Powder Diffraction Files (Inorganic Volumes), *4-802.* JCPDS International Center for Diffraction Data, USA.

21. L.K. Verheij and M.B. Hugenschmidt, Surf. Sci., 1988. **416**: p. 37.

22. C.T. Campbell, H.K. G. Ertl and J. Segner, Surf. Sci., 1981. **107**: p. 220.

23. A. C. Luntz, M.D. Williams and D.S. Bethune, J. Chem. Phys., 1988. **89**: p. 4381.

24. J. Wintterlin, R. Schuster and H.K. G. Ertl, Phys. Rev. Lett., 1996. **77**: p. 123.

25. L.K. Verheij, M.B. Hugenschmidt, A.B. Anton, B. Poelsema and G. Comsa, Surf. Sci., 1989. **210**: p. 1.

26. A.C. Luntz, J.K. Brown and M.D. Williams, J. Chem. Phys., 1990. **93**: p. 5240.

27. P.A. Thiel and T.E. Madey, Surf. Sci. Rep., 1987. **7**: p. 211.

28. S. Krumm, WinFit software, Geologisches Institut Eriagen, Schlobgarten.

29. Powder Diffraction Files (Inorganic Volumes), *6-696.* JCPDS International Center for Diffraction Data, USA.

30. Powder Diffraction Files (Inorganic Volumes), *29-716.* JCPDS International Center for Diffraction Data, USA.

31. Powder Diffraction Files (Inorganic Volumes), *3-1051.* JCPDS International Center for Diffraction Data, USA.

32. Powder Diffraction Files (Inorganic Volumes), *6-694.* JCPDS International Center for Diffraction Data, USA.

33. Powder Diffraction Files (Inorganic Volumes), *5-727.* JCPDS International Center for Diffraction Data, USA.

34. H.H.C.M. Pinxt, B.F.M. Kuster, D.C.Koningsberger and G.B. Marin, Catalysis Today, 1998. **39**: p. 351.

35. S.R de Miguel, O.A.Scelza, M.C.Roman-Martinez, C.Salinas-Martinze de Lecea, D.Cazorla-Amoros and A.Linares-Solano, Applied Catalysis A: General, 1998. **170**: p. 93.

36. M.C.Roman-Martinez, D.Cazorla-Amoros, A.Linares-Solano, C.Salinas-Martinze de Lecea, H. Yamashita and M. Anpo, Carbon, 1995. **33**: p. 3.

37. E. M. Crabb and M.K. Ravikumar, Electrochim. Acta, 2001. **46**: p. 1033.

38. C.D. Wagner, W.M. Riggs, L.E. Davis and J.F. Moulder, Handbook of X-ray Photoelectron Spectroscopy, Perkin-Elmer Corporation, MN,, 1978.

39. M. Peuckert, Electrochim. Acta, 1984. **29**: p. 1315.

40. A.S. Arico, A.K. Shukla, H. Kim, S. Park, M. Min and V. Antonucci, Appl. Surf. Sci., 2001. **172**: p. 33.

41. A.S. Arico, A.K. Shukla, K.M. El-Khatib, H. Kim, P.L. Antonucci and V. Antonucci, Appl. Surf. Sci., 1999. **137**: p. 20.

42. S. Hufner and G.K. Wertheim, Phys. Rev. B, 1975. **11**: p. 678.

43. W.E. Eberhardt, P. Fayet, D.M Cox, Z. Fu, A. Kalder, R. Sherwood and D. Sondericker, Phys. Rev. Lett., 1990. **64**: p. 780.

44. K.S. Kim and N. Vinograd, J. Am. Chem. Soc., 1974. **93**: p. 6296.

45. J. Knecht, G. Stark and Z. Frencius, Anal. Chem., 1978. **289**: p. 206.

46. M. Aria, T. Ebina and M. Shirai, Appl. Surf. Sci., 1999. **148**: p. 155.

47. B. D. McNicol and R. T. Short, J. Electroanal. Chem., 1978. **92**: p. 115.

48. H. C. Yao, M. Sieg and H.K.Plummer Jr., J. Catal., 1979. **59**: p. 365.

49. Alan Jones and Brian McNicol, Temperature-programmed reduction for solid materials characterization, Marcel Dekker, 1986.

50. J.L. Falconer and J.A. Schwarz, Catal. Rev. -Sci. Eng., 1983. **25**: p. 141.

51. P.G. Menon and G. F. Froment, Appl. Catal., 1981. **1**: p. 31.

52. I. Ayub, PhD Thesis, The Open University, 2002.

Chapter 4 Catalytic evaluation of the carbon supported Pt-based bimetallic electrocatalysts

This chapter describes the evaluation of the carbon supported Pt and Pt-based bimetallic catalysts using electrochemical methods.

The adsorption properties of the carbon supported Pt and Pt-based bimetallic catalysts prepared using SOMC where studied using the technique of cyclic voltammetry (CV) and described in Section 4.1. The electrode Pt surface area (EPSA) and electrochemical surface area (ECA) were determined using CO cyclic voltammetry described in Section 4.2. Section 4.3 gives catalyst evaluation for the oxygen reduction reaction (ORR) of the carbon supported Pt and Pt-based bimetallic catalysts.

4.1 Cyclic voltammetry

This section examines the adsorption properties of the electrocatalysts (Pt/C and representative Pt-based bimetallic catalysts) using the technique of cyclic voltammetry.

Noble metals adsorb hydrogen and oxygen in aqueous acidic electrolytes by Faradic charge transfer. The resulting cyclic voltammograms exhibit a general similarity in overall shape but display distinctive features which are characteristic of the particular metals. Figure 4.1 shows a typical profile for platinum for one 20% Pt/C catalyst electrode in 1M H_2SO_4 at 25 °C with sweep at 10 mV s^{-1}. A number of these characteristic features will now be discussed. Scanning from 0 V to 1.2 V versus SHE (standard hydrogen electrode) is called the anodic scan; scanning from 1.2 V to 0 V versus SHE is called the cathodic scan. Hwang, Ross, Lowed, Woods and Peuckert reported the results of oxide formation and hydrogen adsorption on platinum supported carbon electrodes and on platinum electrodes [1-5]. They deduced that between 0 - 0.4 V

the oxidation of hydrogen occurs ($Pt\text{-}H_{ads} \longleftrightarrow Pt + H^+ + e^-$) on the anodic sweep and the adsorption of hydrogen occurs on the cathodic sweep. Usually three peaks are observed on oxidation and two on adsorption. On well-characterized single crystalline (111) and (100) Pt surfaces these peaks have been interpreted as arising from H adsorbed on different Pt crystal faces[1, 3]. Between 0.4 and 0.8 V we encounter the "double-layer" region where no Faradaic processes occur. Above 0.8 V on the anodic sweep oxygen chemisorption starts. At about 1.1 V a monolayer of Pt-OH is formed:

$$Pt + H_2O \longleftrightarrow PtOH^+ + H^+ + 2e^-$$

At still higher anodic potentials PtO_2 is formed:

$$PtOH^+ + H_2O \longleftrightarrow PtO_2 + 3H^+ + 2e^-$$

and oxygen evolution commences at about 1.5 V (beyond the range used here). On the cathodic sweep reduction of the platinum-oxides takes place at about 0.75 V in a single peak ($PtO_2 + 4H^+ + 4e^- \longleftrightarrow Pt + 2H_2O$). Significantly this potential (0.75 V) is lower than the corresponding anodic potential (1.1 – 1.5 V) of the oxidation reaction indicating the irreversibility [3].

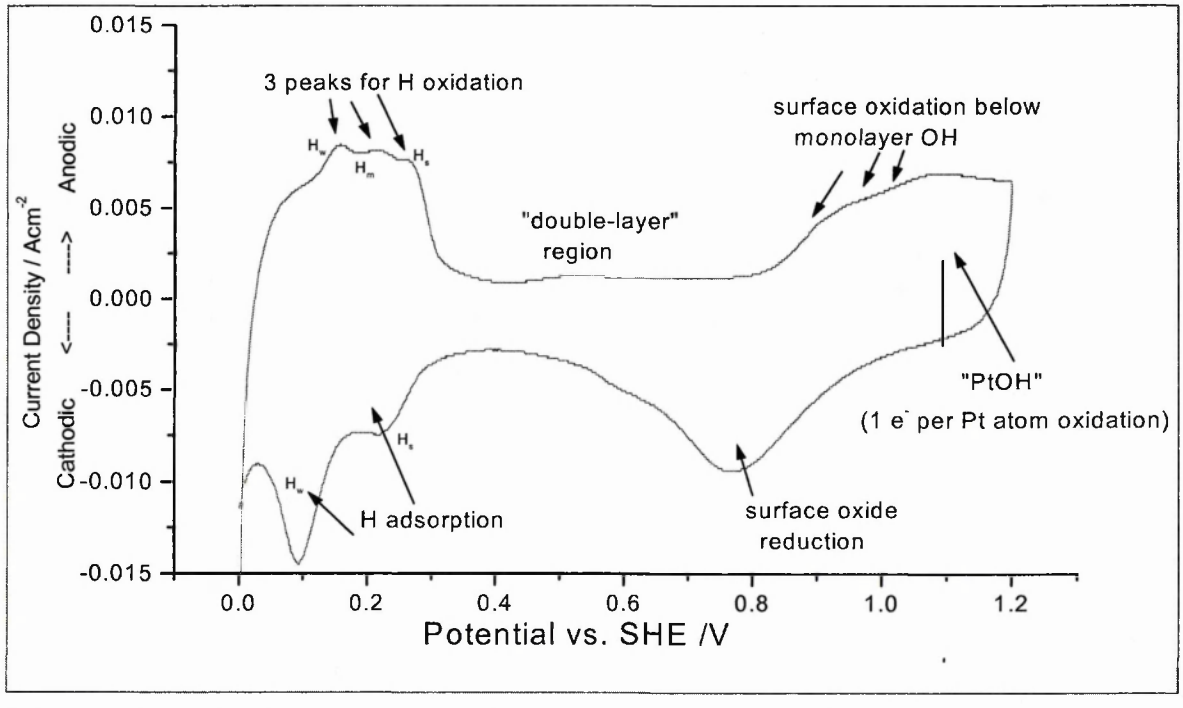

Figure 4.1 Cyclic voltammetry of 20 wt% Pt/C catalysed electrode (1 cm diameter, 1 mg Pt/cm^2) in 1M H_2SO_4 at 25°C

Figures 4.2 – 4.3 show typical profiles for 20% Pt/C and 0.5PtFe/C catalyst electrodes for a number of cycles. Whenever an electrode is made freshly (any electrode) it will have active redox sites as well as some impurities adsorbed from the air, specifically oxygen. This could have impacted on the redox characteristics of the electrode. In addition, the electrode morphology also will change when the electrode is subjected to a potential cycle. Hence, for most circumstances, the first few cycles will be recorded but only the reproducible redox peaks characteristics will be considered in the interpretation. In the case of Pt electrode, the roughness factor is an important parameter of the electrode. It will change from the first cycle to the second to the fifth cycle, stabilising after about three cycles as seen below in Figure 4.2. Hence, it is our practice to consider the CV of the fifth cycle for analysis.

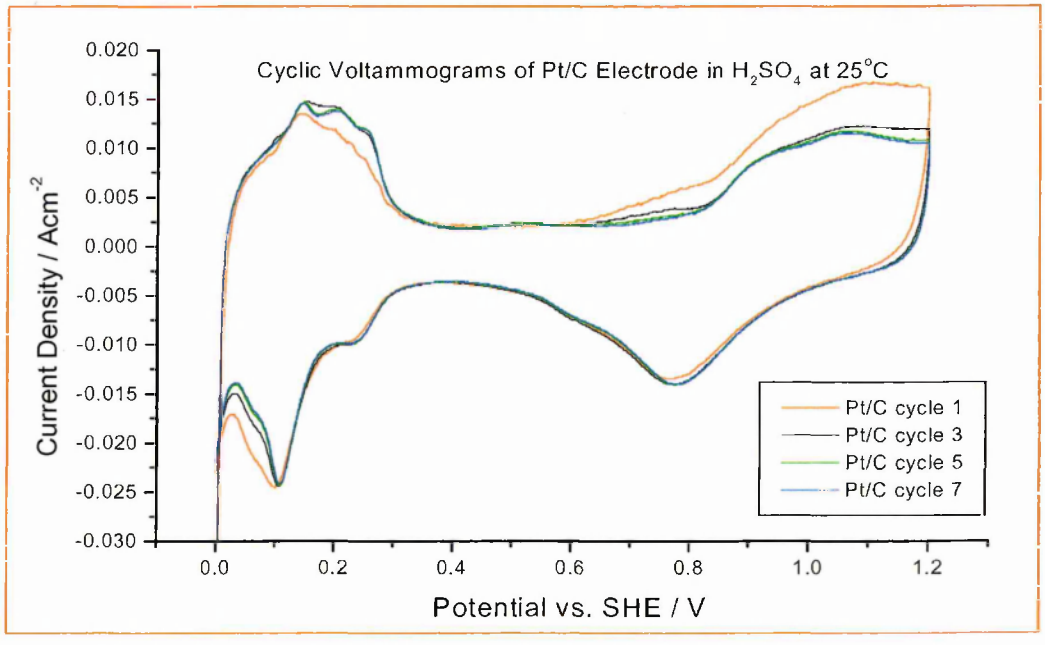

Figure 4.2 Cyclic voltammetry of 20 wt% Pt/C catalysed electrode at different cycles

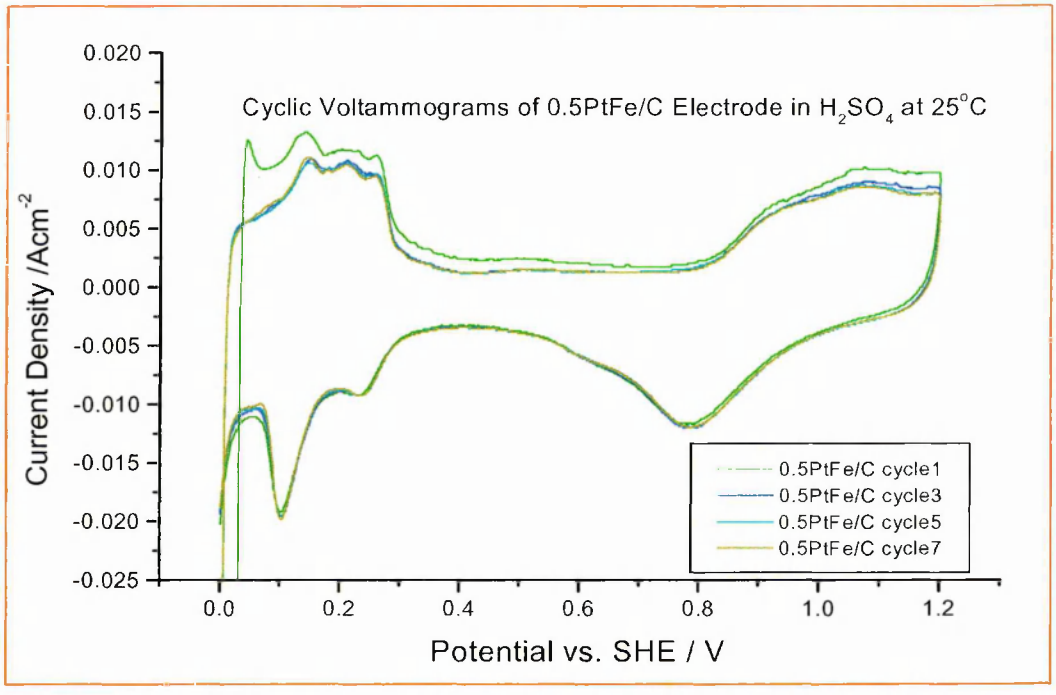

Figure 4.3 Cyclic voltammetry of 0.5PtFe/C electrode at different cycles

Figures 4.4 and 4.5 show cyclic voltammograms for the PtFe/C and PtNi/C catalysts after 5 cycles. The cyclic voltammograms were stable indicating that these catalysts did not dissolve in the electrolyte during the cyclic voltammetry experiments. The cyclic voltammograms of PtFe/C and PtNi/C catalysts were very similar to that of 20%Pt/C, suggesting that Pt was dominant. However, small shifts were obtained in the cyclic voltammetric profiles between the Pt/C and PtM/C and peak positions for each hydrogen species are summarized in Table 4.1. From the cathodic deposition of hydrogen, it can be observed that the peaks for the "strongly" (H_s) and "weakly" (H_w) deposited hydrogen of Pt/C catalyst are at 0.09 V and 0.21 V versus SHE, respectively. Those of PtFe/C and PtNi/C are slightly shifted compared with the peaks of Pt/C catalyst, at between 0.10 V and 0.12 V, and between 0.22 V and 0.25V, respectively. This was probably caused by a change in the electronic environment of Pt in the bimetallic catalysts, suggesting that the second metal is in close contact with the platinum.

The anodic peak (H_m) is located between the "strongly" (H_s) and "weakly" (H_w) adsorbed hydrogen peaks in the Pt/C and PtM/C catalysts. Lowde et al observed that this intermediate peak (H_m) increased in relative intensity as the Pt metal surface area increased, so they suggested that this anodic intermediate peak was due to hydrogen adsorbed on Pt atoms of low coordination e.g. edge atoms rather than due to H atoms dissolved in Pt [3].

The charge ratio (Q_s/Q_w) in Table 4.1 is the coulombic charge ratio of "strongly" (H_s) and "weakly" (H_w). Q is the coulombic charge and is measured by the area of the peak from the cathodic deposition profile. Q_s/Q_w can be obtained according to the following equation:

$$\frac{Q_s}{Q_w} = \frac{A_s}{A_w} \tag{4.1}$$

where A_s and A_w are the area of the peaks of H_s and H_w. A_s and A_w are calculated and obtained using Origin software (Figure 4.6)

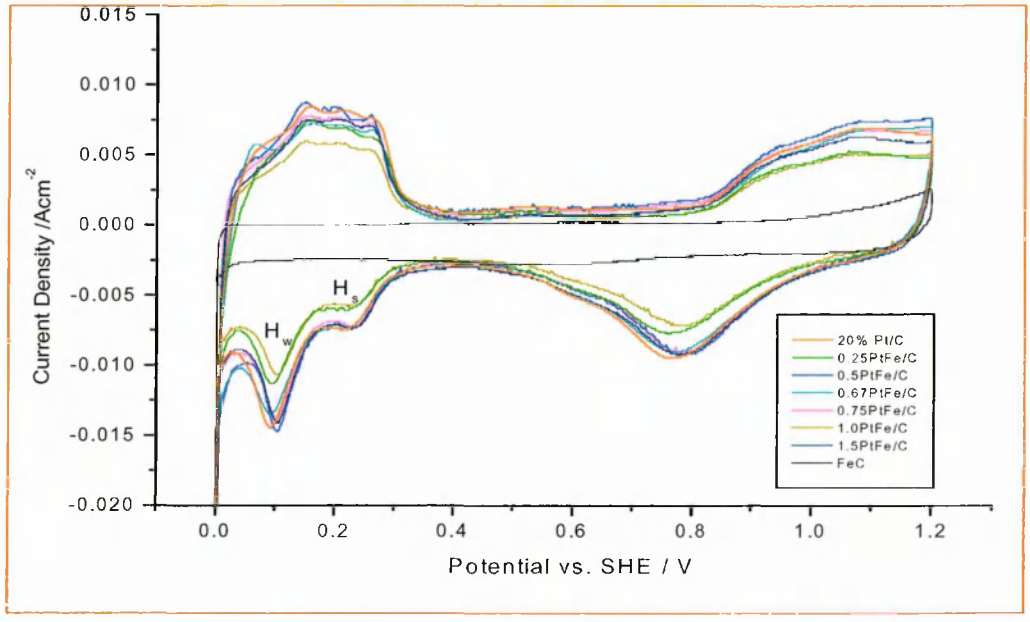

Figure 4.4 Cyclic Voltammetry of PtFe/C Electrodes (1 cm diameter, 1 mg Pt/cm^2) in 1M H_2SO_4 at 25°C

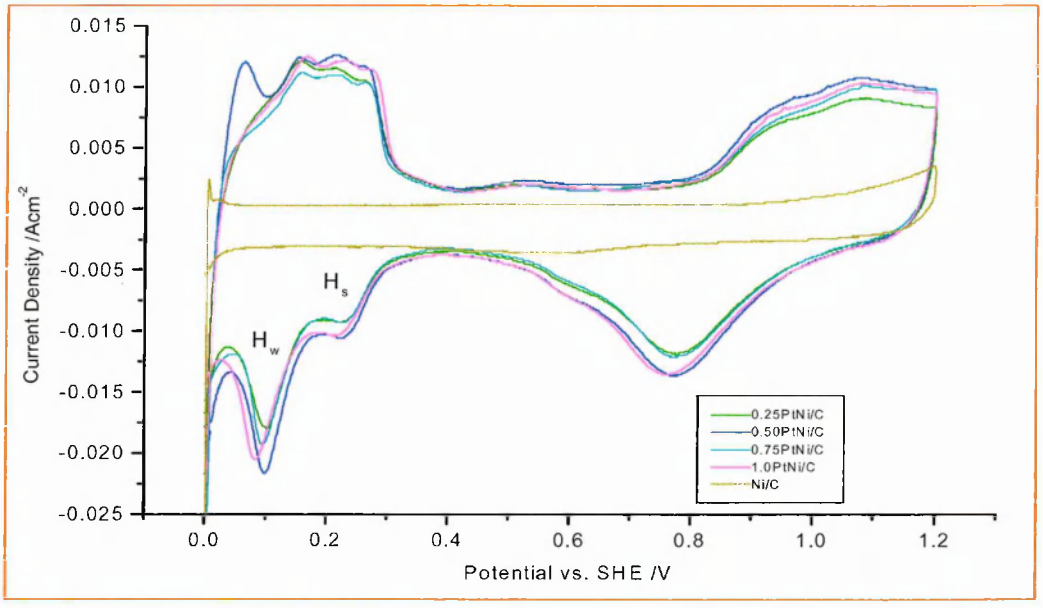

Figure 4.5 Cyclic Voltammetry of PtNi/C Electrodes (1 cm diameter, 1 mg Pt/cm^2) in 1M H_2SO_4 at 25°C

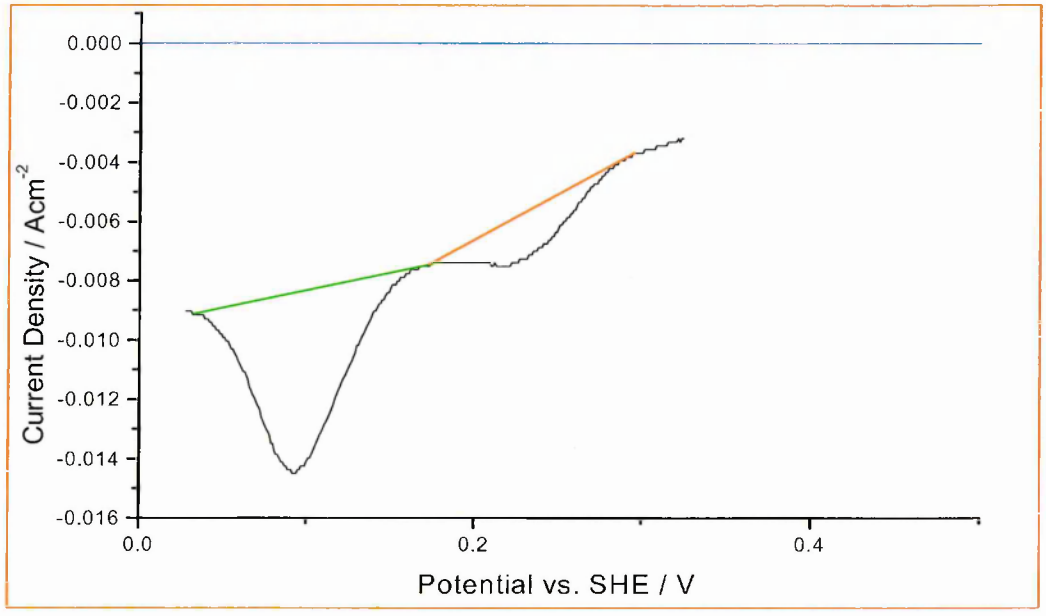

Figure 4.6 The area of H_s and H_w on the adsorption of hydrogen

Table 4.1 The peak position of hydrogen in the cyclic voltammogram for the cathodic deposition and anodic oxidation on the surface of Pt/C and PtM/C catalysts

Catalysts	Particle size / nm		Cathodic deposition		Anodic oxidation			Q_s/Q_w
	XRD	TEM	H_w	H_s	H_w	H_m	H_s	
Pt/C	2.4	2.7	0.09	0.21	0.16	0.22	0.25	0.45
0.25FePt/C	3.5	4.3	0.10	0.22	0.15	0.22	0.25	0.50
0.5FePt/C	3.5	4.5	0.10	0.23	0.14	0.21	0.27	0.51
0.75FePt/C	3.7	4.6	0.12	0.24	0.15	0.22	0.25	0.53
1.0FePt/C	3.8	4.6	0.12	0.25	0.15	0.21	0.25	0.53
0.25NiPt/C	3.1	4.2	0.10	0.22	0.15	0.20	0.25	0.50
0.5NiPt/C	3.1	4.2	0.10	0.22	0.16	0.20	0.26	0.50
0.75NiPt/C	3.2	4.2	0.10	0.22	0.17	0.21	0.26	0.51
1.0NiPt/C	3.2	4.4	0.08	0.22	0.17	0.23	0.27	0.52

Takasu et al [6] observed that the charge ratio of "strongly" (H_s) and "weakly" (H_w) deposited hydrogen increased with increasing Pt particle size. It is generally known that strongly and weakly deposited hydrogen peaks correspond to hydrogen adsorbed on the Pt(100) plane and Pt(111) plane, respectively [7, 8]. The charge ratio (Q_s/Q_w) of PtM/C was higher than that of pure Pt/C in all cases (Table 4.1). The results suggest that PtM/C bimetallic catalysts increased the ratio of the Pt(100) plane to the Pt(111) plane, which will increase the amount of the "strongly adsorbed" hydrogen species (H_s). This could be due to an increase in the particle size of PtM/C compared to that of pure Pt/C, or it is also possible that M on PtM/C bimetallic catalysts may be selectively adsorbed on one of the crystallite faces (Pt(100) and Pt(111)).

The change in Q_s/Q_w was not significant as the amount of the second metal was increased. Within a series TEM results show that the particle sizes are very similar. Hwang [9] showed that the peak height ratio and the coulombic charge ratio for

bimetallic Pt catalysts were the same even when their particle sizes were different. In other words, the ratio of the Pt (100) to Pt (111) plane was independent of the particle size, indicating that the second metal deposited selectively on one of the crystallite faces (Pt(100) and Pt(111)). Our results do not contradict this.

Cyclic voltammetry studies were not performed on the Cr or Co series of catalysts.

4.2 CO cyclic voltammetry

In order to observe the intrinsic activity of the Pt (current per cm^2 of available Pt) and the "intrinsic" kinetic performance of the pure Pt and Pt-based bimetallic electrocatalysts, the electrode Pt surface area (EPSA) and electrochemical surface area (ECA) need to be obtained. A detailed description of this is given in Chapter 2.

The cyclic voltammograms of the electrooxidation of CO to CO_2 generated for the Pt/C and some typical PtM/C catalysts are shown in Figures 4.7 and 4.8. The onset potential at which the CO oxidation reaction was initiated and the maximum position of the CO electrooxidation peak for all electrocatalysts are listed in Table 4.2. The oxidation of CO on Pt/C was found to begin at 0.57 V vs. SHE with the peak maximum position observed at 0.64 V vs. SHE. It can be observed that the onset potential and peak position of PtM/C for CO oxidation gave a small negative shift compared to the monometallic Pt/C catalyst, although this is not very significant. The onset of oxidation of the CO for the PtM/C electrocatalysts started at 0.48 – 0.53 V (Table 4.2). This indicates that the PtM/C catalysts have enhanced activity for CO electrooxidation with a reduction in the potential for oxidation. The results are in agreement with Markovic, Crabb and Gasteiger's works [10-12]. According to their results, the main peak above 0.6V can be assigned to strongly adsorbed CO on Pt sites [10-12]. The oxidation peak of CO was observed at lower potentials for the PtM/C electrocatalysts (Table 4.2), with a decrease in

the onset potential for CO oxidation to approximately 0.48 – 0.53 V. The change in the adsorption properties for the PtM/C electrocatalysts is believed to be mainly due to changes in the platinum surface structure on addition of the second metal [13].

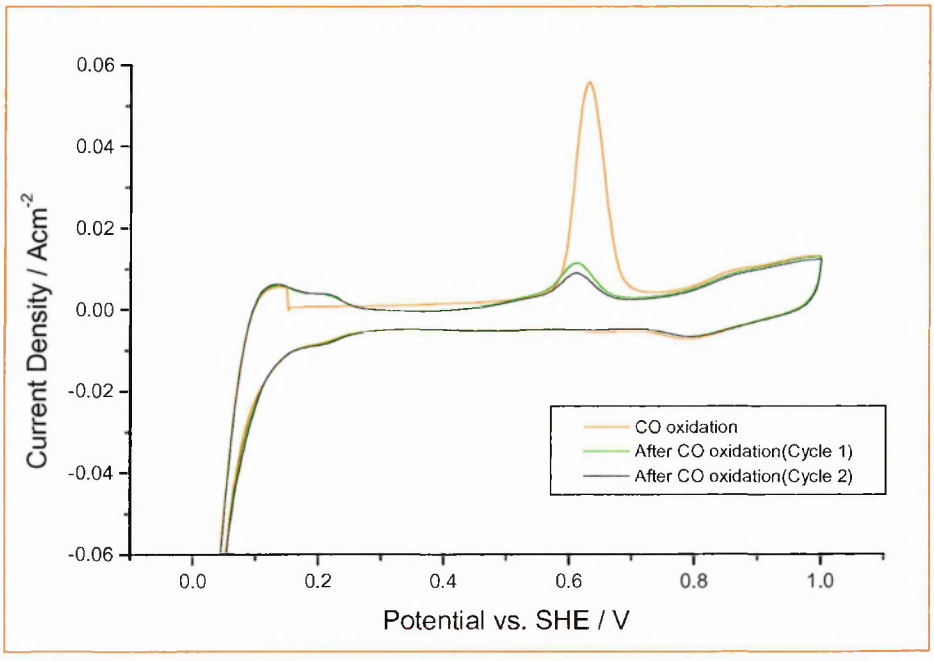

Figure 4.7 CO cyclic voltammograms of Pt/C catalyst in 1 M H_2SO_4 at 80 °C

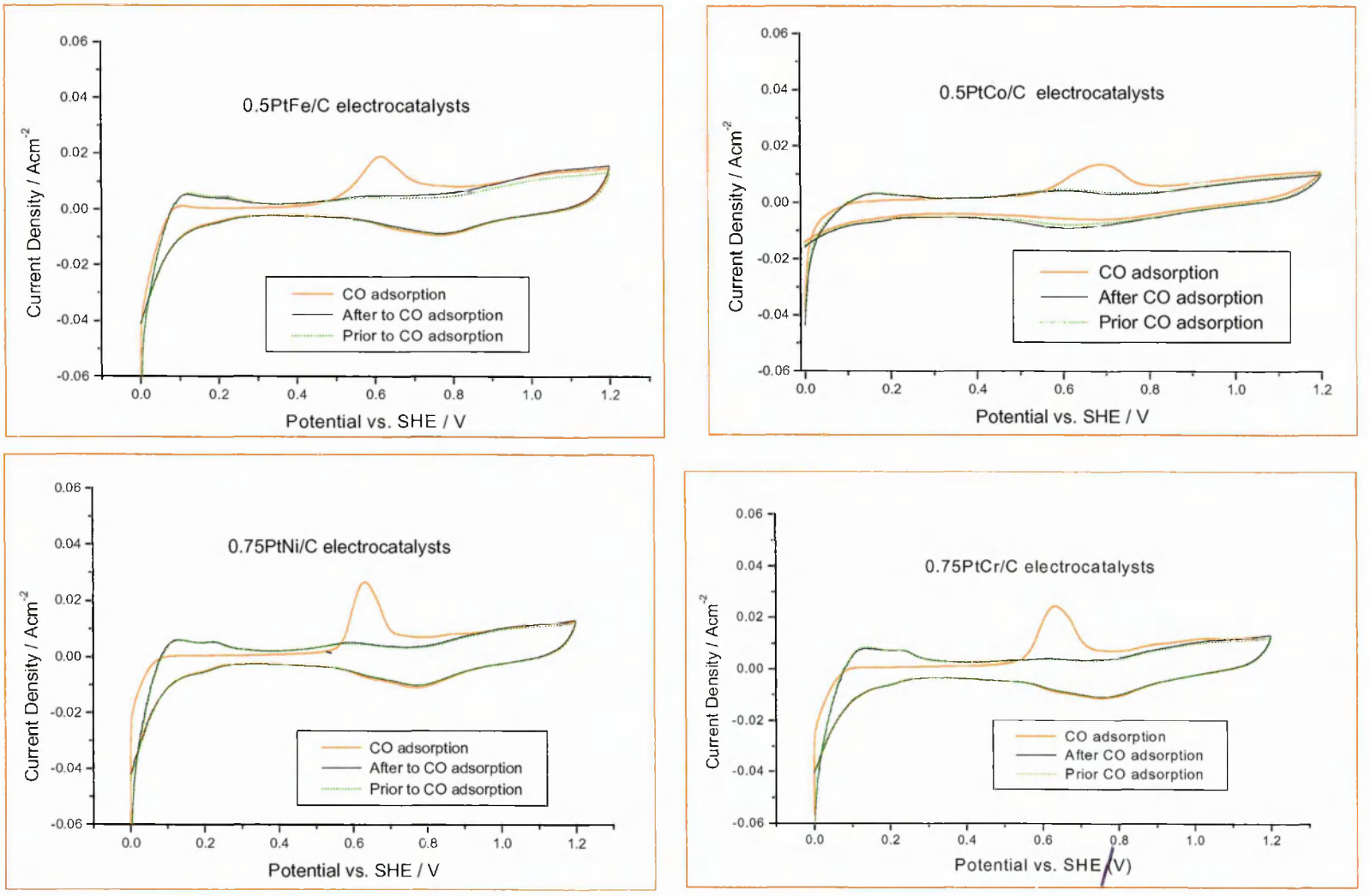

Figure 4.8 CO cyclic voltammograms of typical PtM/C catalysts in 1 M H_2SO_4 at 80 °C

Table 4.2 Onset potential and position of the peak maximum for CO oxidation for Pt/C and PtM/C catalysts

Catalyst	Onset potential /V	Peak position /V	Catalyst	Onset potential /V	Peak position /V
Pt/C	0.57	0.65	Pt/C	0.57	0.65
0.25PtFe/C	0.50	0.59	0.25PtNi/C	0.52	0.59
0.5PtFe/C	0.50	0.58	0.5PtNi/C	0.50	0.61
0.75PtFe/C	0.51	0.59	0.75PtNi/C	0.53	0.62
1.0PtFe/C	0.50	0.61	1.0PtNi/C	0.52	0.61
0.25PtCr/C	0.51	0.60	0.25PtCo/C	0.50	0.61
0.5PtCr/C	0.52	0.60	0.5PtCo/C	0.48	0.60
0.75PtCr/C	0.50	0.59	0.75PtCo/C	0.50	0.61
1.0PtCr/C	0.51	0.61	1.0PtCo/C	0.51	0.62

The electrode Pt surface area (EPSA) and electrochemical surface area (ECA) of Pt/C, and all the PtM/C catalysts are tabulated in Table 4.3. It can be seen that the PtM/C catalysts had a lower Pt surface area than the monometallic Pt/C catalyst in all cases. This was expected as some Pt surface atoms are covered by Fe, Ni, Co or Cr atoms. When Fe was deposited on the Pt/C catalyst, the EPSA had a larger decrease than expected for the 0.25PtFe/C electrocatalyst. The EPSA did not change significantly, however, with further addition of Fe. The EPSA of PtNi/C electrocatalysts followed the same trend as the PtFe/C electrocatalysts. The Cr series exhibited a quite different behaviour. 0.25PtCr/C and 0.5PtCr/C electrocatalysts had much higher EPSA compared to the other PtM/C electrocatalysts. 0.75PtCr/C and 1.0PtCr/C electrocatalysts, however, decreased significantly with further addition of Cr. The EPSA for PtCo/C electrocatalysts was different again, decreasing with an increase of Co. These results suggest that the change in the EPSA for PtM/C electrocatalyst is dependent on the second metal. The

EPSA or ECA data will be used to evaluate the specific activities of the electrocatalysts for the oxygen-reduction reaction.

Table 4.3 Electrode Pt Surface Area (EPSA) and Electrochemical Surface Area (ECA)

Catalyst	CO Area /mCcm^{-2} (1)	EPSA/ cm^{2}Pt (2)	ECA /m^{2}g^{-1}Pt (3)
20% Pt/C	306	728	104
0.25PtFe/C	189	450	64
0.5PtFe/C	186	442	63
0.75PtFe/C	182	434	62
1.0PtFe/C	174	413	59
0.25PtNi/C	205	487	69
0.5PtNi/C	215	511	73
0.75PtNi/C	206	490	70
1.0PtNi/C	211	501	71
0.25PtCr/C	285	679	96
0.50PtCr/C	290	691	98
0.75PtCr/C	219	522	74
1.00PtCr/C	200	476	68
0.25PtCo/C	238	566	87
0.50PtCo/C	215	511	80
0.75PtCo/C	198	471	67
1.00PtCo/C	175	416	59

(1) CO Area = X axis × Y axis ×(1/scan rate) = (A/cm^2) × (V) × (1/0.01 V/s) = 100(A × s)/cm^2 = 100C/cm^2 = 1×10^5 mC/cm^2

For CO: 0.42 mC/cm^2 = 1 cm^2 Pt

(2) EPSA= Area/0.42(cm^2 Pt)

(3)ECA = EPSA/W_{Pt}= EPSA/((2.01× 0.35) × 0.1) (m^2/g Pt)

4.3 Oxygen-reduction reaction at the cathode in PEM fuel cells

The evaluation of Pt/C and PtM/C catalysts prepared by SOMC for the oxygen reduction reaction (ORR) is discussed in this section. The steady state galvanostatic polarization experiment for the oxygen reduction reaction was carried out at 80 °C and 0.2 bar oxygen pressure. Three different analyses of the steady state galvanostatic polarization data were made:

- current-potential curves,
- Tafel plots, and
- specific activity plots.

After data analysis, the better PtM/C bimetallic catalysts were chosen for a further series of experiments after heat treatment to try to produce alloy electrocatalysts and optimize catalytic performance.

Figures 4.9 – 4.11 show the current-potential curves plot for the oxygen reduction reaction on the Pt/C and PtM/C electrocatalysts. The current-potential curves show that the catalytic activity for ORR on the PtM/C catalysts was slightly lower than that of the Pt/C catalyst, possibly reflecting the decrease in surface area on addition of the second metal.

The representative Tafel plots for monometallic Pt/C and PtM/C electrocatalysts for oxygen reduction reaction are shown in Figures 4.12 – 4.14. Even though it is clear that the Tafel slope for the ORR is changing continuously in the potential range examined [14, 15], two Tafel regions at low and high overpotential were found. The Tafel slopes for monometallic Pt/C and PtM/C electrocatalysts were well defined around RT/F (~60 mV/decade) for the low overpotential range (E>0.85 V) and 2RT/F(~120 mV/decade) for the high overpotential range (E<0.80 V), although some are slightly higher. They are in good agreement with Tafel slopes reported in the literature for single

crystal Pt electrodes [15], polycrystalline Pt [16], carbon supported Pt catalysts [17]. The appearance of two linear segments in the Tafel plot has typically been reported for the O_2 reduction reaction on platinum electrode in acidic medium and at the platinum/Nafion interface. Variations in the Tafel slopes are attributed to the influence of different adsorption and different rate-determining steps over the potential ranges investigated [6, 18, 19].

According to the literature [20, 21], the small Tafel slope corresponds to the ORR at a Pt surface covered with an oxide layer and the large slope corresponds to that on a clean Pt surface. The large Tafel slope region (~ 120 mV/decade) is a rather interesting potential region from the viewpoint of partical PEM fuel cells. The generalized reaction scheme for ORR in acidic medium and at the platinum/Nafion interface is as follows:

$$O_2 + Pt \rightarrow Pt\text{–}O_2 \qquad (4.2)$$

$$Pt\text{–}O_2 + H^+ + e^- \rightarrow Pt\text{–}HO_2 \quad \text{(rds)} \qquad (4.3)$$

$$Pt\text{–}HO_2 + Pt \rightarrow Pt\text{–}HO + Pt\text{-}O \qquad (4.4)$$

$$Pt\text{–}HO + Pt\text{–}O + 3H^+ + 3e^- \rightarrow 2Pt + 2H_2O \qquad (4.5)$$

Total reaction:

$$O_2 + 4H^+ + 4e^- \rightarrow 2H_2O \qquad (4.6)$$

The first electron-transfer step (Equation 4.3) is the rate-determining step (rds) and estimated from the Tafel slope for the ORR on the Pt electrode [20]. The Tafel slopes for the ORR on the PtM/C electrocatalysts shown in Figures 4.12 -4.14 were similar to that of the Pt/C electrocatalyst, suggesting that the rate-determining step for the ORR on the PtM/C electrocatalysts is the same as that of monometallic Pt/C electrocatalyst.

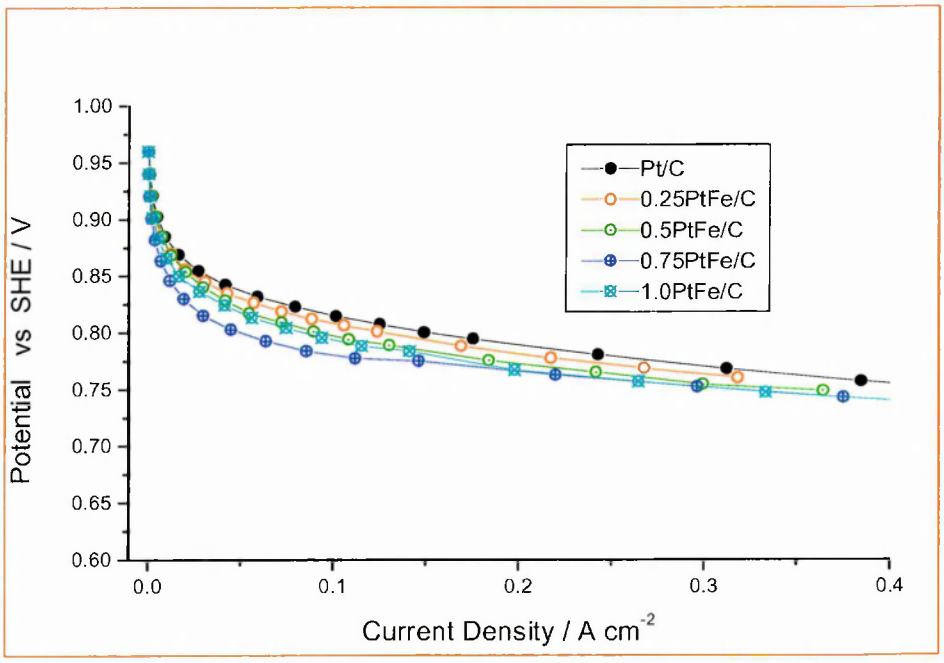

Figure 4.9 Steady galvanostatic polarization for oxygen-reduction reactions for the PtFe/C catalysts

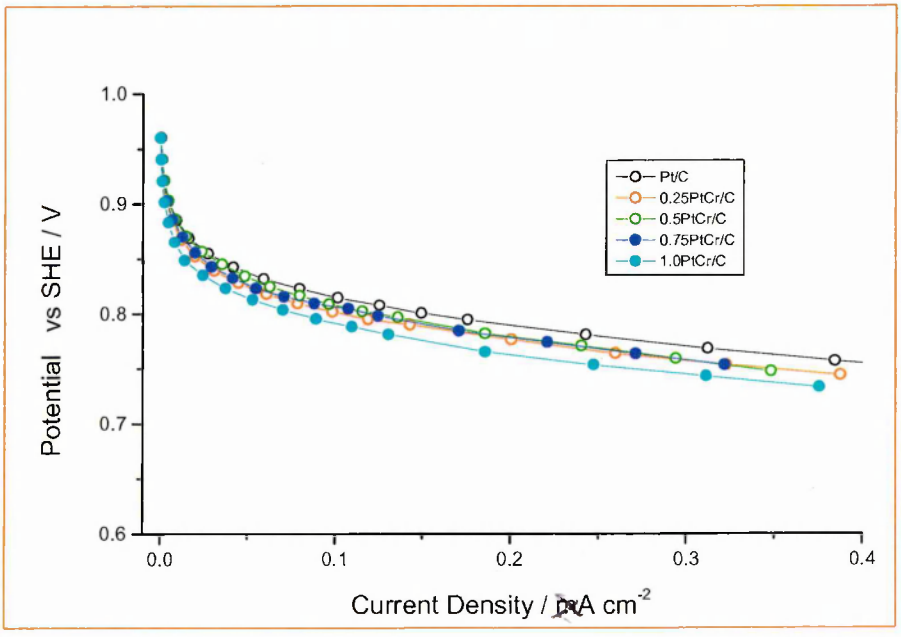

Figure 4.10 Steady galvanostatic polarization for oxygen-reduction reactions for the PtCr/C catalysts

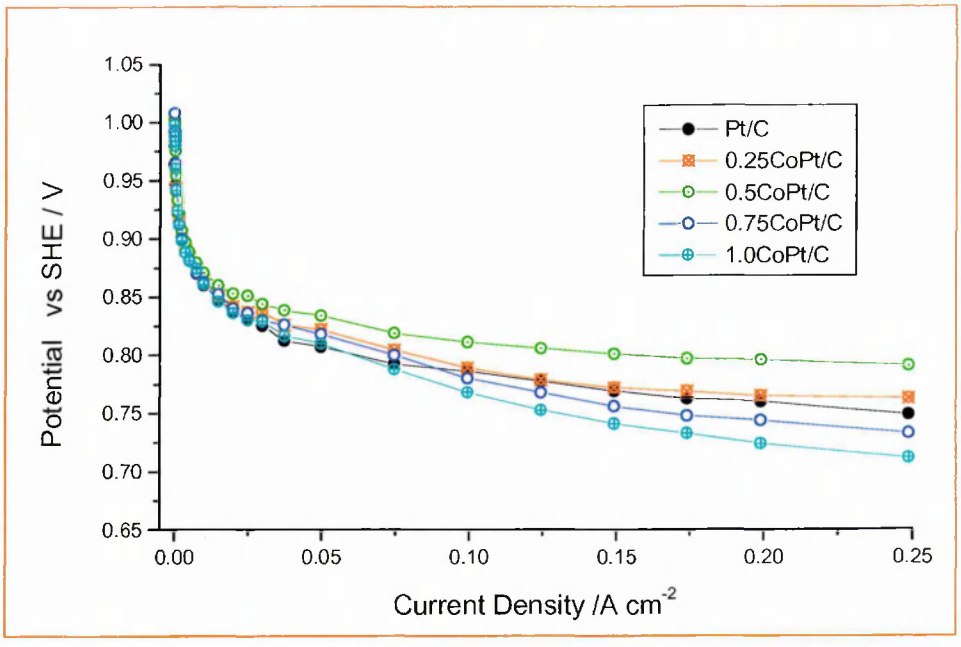

Figure 4.11 Steady galvanostatic polarization for oxygen-reduction reactions for the PtCo/C catalysts

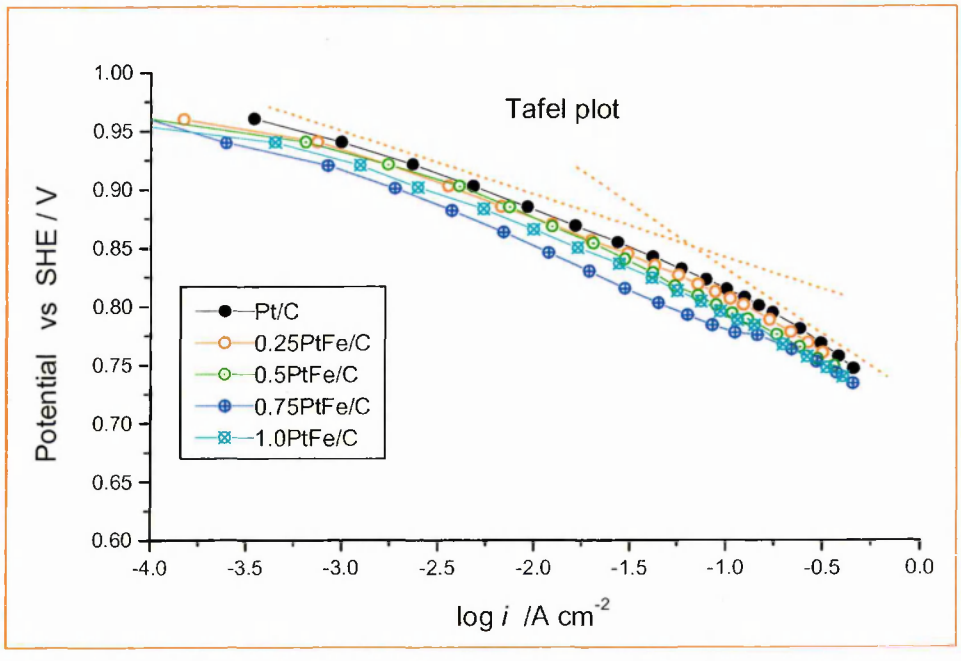

Figure 4.12 Tafel plot for the PtFe/C catalysts

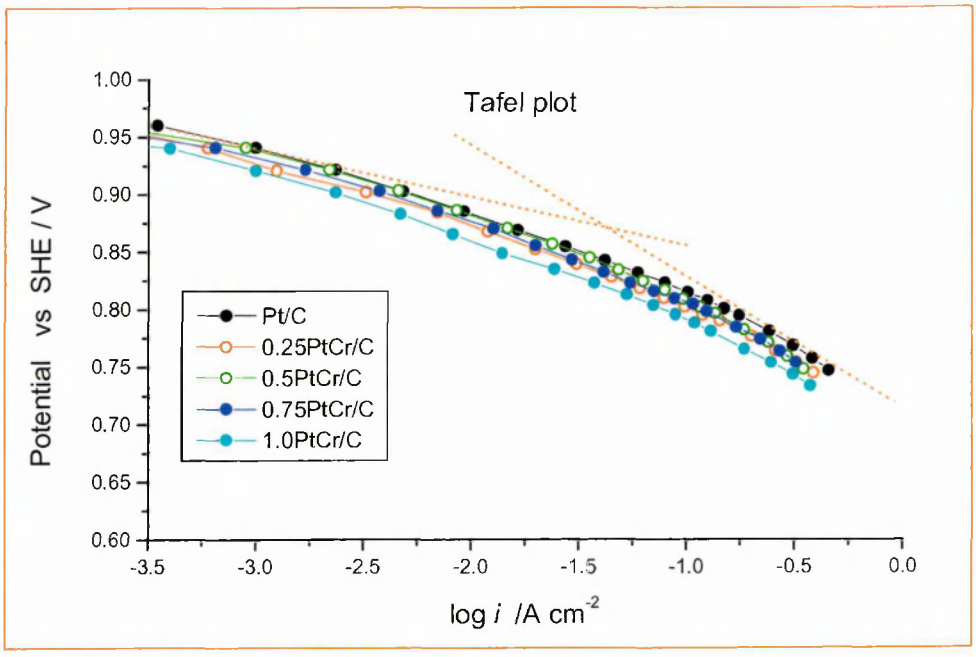

Figure 4.13 Tafel plot for the PtCr/C catalysts

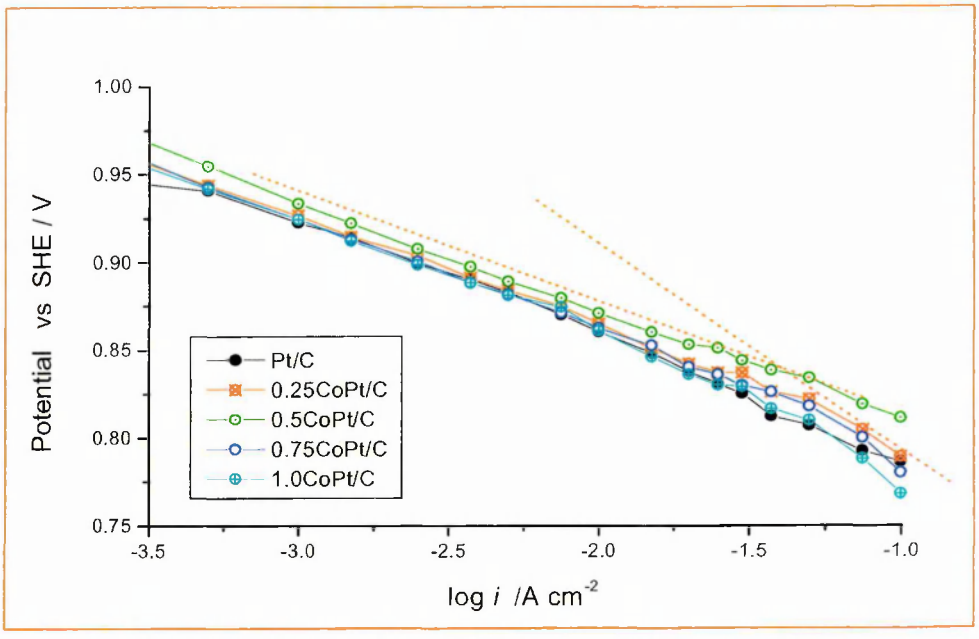

Figure 4.14 Tafel plot for the PtCo/C catalysts

Figures 4.15 – 4.17 show the specific activity *vs* cell potential plots for the oxygen reduction reaction of Pt/C and PtM/C electrocatalysts. The specific activity at 900 mV has been arbitrarily taken as a method to compare catalytic activity. Compared to the specific activity at 900 mV, the 0.5 PtFe/C, 0.5 PtCr/C and 0.5PtCo were the best catalysts for the oxygen-reduction reaction in their own series because they had the highest specific activity at 900 mV. Although some of the PtM/C catalysts had higher activity for oxygen-reduction reaction than the monometallic Pt/C catalyst, it was hoped to further improve the activity by heat treatment, and in particular to see if alloy formation improved performance significantly. Since the specific activity stands for the intrinsic activity of the Pt in PtM/C catalysts, the 0.5 PtFe/C, 0.5 PtCr/C, 0.5PtCo/C and 1.0PtNi/C (not shown here) catalysts were considered to have most potential to improve their catalytic activity for the oxygen-reduction reaction, and were thus selected for heat treatment to produce a series of Pt-based alloy electrocatalysts which are discussed in the next section.

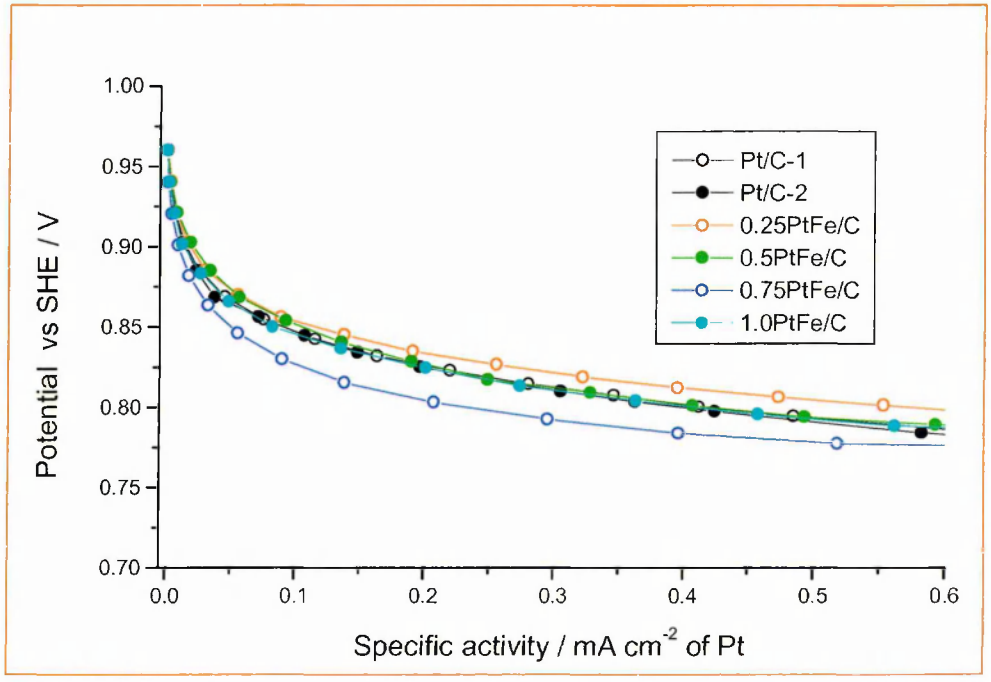

Figure 4.15 The specific activities of oxygen reduction reactions for PtFe/C catalysts

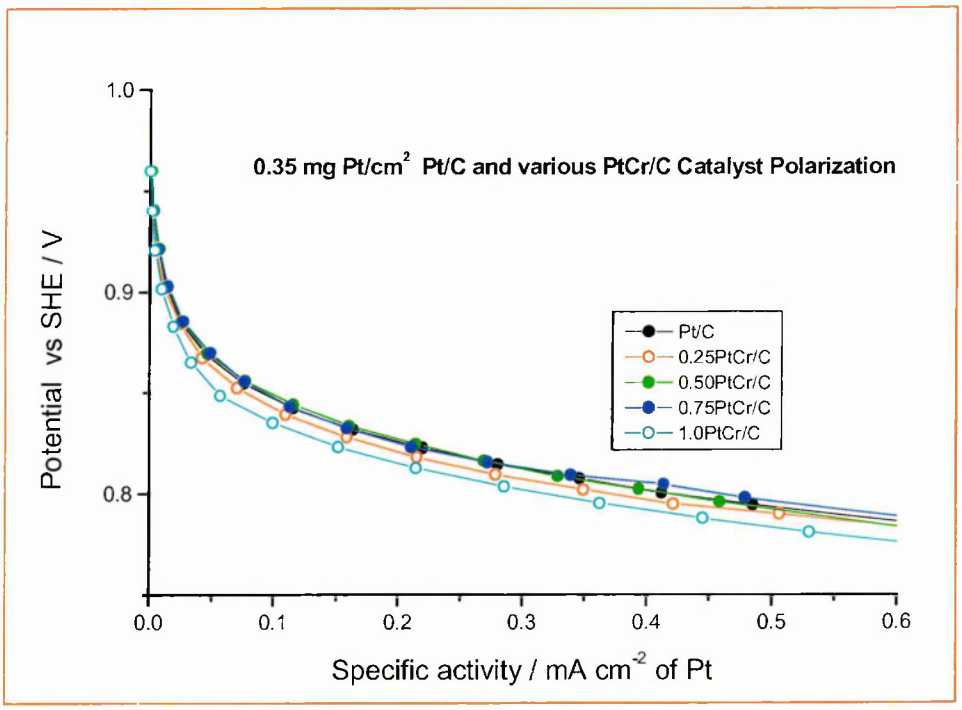

Figure 4.16 The specific activities of oxygen-reduction reactions for PtCr/C catalysts

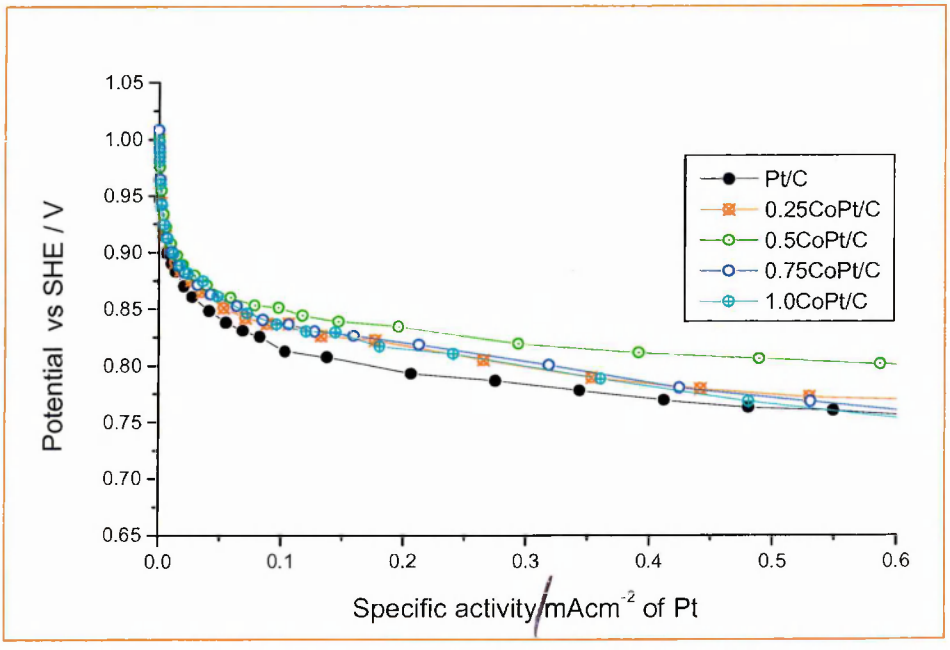

Figure 4.17 The specific activities of oxygen-reduction reactions for PtCo/C catalysts

4.4 Conclusion

Electrochemical studies of PtFe/C, PtNi/C, PtCo/C and PtCr/C bimetallic catalysts have been carried out.

i) The analysis of results for the cyclic voltammetry experiments for PtM/C catalysts, suggests that the second metal is in close contact with the platinum.

ii) CO cyclic voltammetry has been used to evaluate the electrode Pt surface area (EPSA) and electrochemical surface area (ECA) of Pt/C, and all the PtM/C catalysts. From the CO cyclic voltammetry results, the change in the adsorption properties for the PtM/C electrocatalysts is believed to be mainly due to changes in the platinum surface structure on addition of second metal.

iii) Tafel slopes for the Pt/C and PtM/C electrocatalysts suggest that the mechanism of the ORR is that the first electron-transfer is the rate-determining step.

iv) The results of the specific activity on the Pt/C and PtM/C suggest that some PtM/C catalysts have the potential to improve their catalyst activity for the oxygen-reduction reaction, and were selected for further study using heat treatment.

4.5 References

1. J.T. Hwang and J.S. Chung, Electrochim. Acta, 1993. **38**: p. 2723.
2. P.N. Ross Jr., Surf. Sci., 1981. **102**: p. 463.
3. D. R. Lowde and J.O. Williams, Appl. Surf. Sci., 1978. **1**: p. 215.
4. M. Peuckert, T. Yoneda, R.A. Dalla Betta and M. Boudart, J. Electrochem. Soc., 1986. **133**: p. 944.
5. R. Woods, J. Electroanal. Chem., 1974. **49**: p. 217.
6. Y. Takasu, Y. Fujii, K. Yasuda, Y. Iwanaga and Y. Matsuda, Electrochim. Acta, 1989. **34**: p. 452.
7. A.M. de Becdelievre and J. Clavilier, J. Electroanal. Chem., 1990. **294**: p. 97.
8. R. Gomez and J. Clavilier, J. Electroanal. Chem., 1993. **354**: p. 189.
9. J.T. Hwang and J.S. Chung, Electrochim. Acta, 1993. **38**: p. 2715.
10. N.M. Markovic, A. Widelov, P.N. Montriro and I.G. Brown, Catal. Lett., 1997. **43**: p. 161.
11. H.A. Gasteiger and M. Markovic, J. Phys. Chem., 1995. **99**: p. 8954.
12. E.M. Crabb and M.K. Ravikumar, Electrochim. Acta, 2001. **46**: p. 1033.
13. E. M. Crabb and M.K. Ravikumar, Electrochim. Acta, 2001. **46**: p. 1033.
14. U.A.Paulus, A. Wokaun, G.G. Scherer, T.J. Schmidt, V. Stamenkovic, N.M. Markovic and P.N. Ross, Electrochim. Acta, 2002. **47**: p. 3787.
15. B.N. Grgur, N.M. Markovic and P.N. Ross Jr., Can. J. Chem., 1997. **75**: p. 1465.
16. A. Danjanovic and D. B. Sepa, Electrochim. Acta, 1990. **39**: p. 1951.
17. J. Bett and J. Lundquist, Electrochim. Acta, 1973. **18**: p. 343.
18. S.L. Gojkovic, S.K. Zecevic and R.F. Savinell, J. Electrochem. Soc., 1998. **145**: p. 3713.
19. J. Jiang and A. Kucernak, Electrochem. Solid-State Lett., 2000. **3**: p. 559.

20. T. Toda, H. Igarashi, H. Uchida and M. Watanabe, J. Electrochem. Soc., 1999. **146**: p. 3750.

21. A. Danjanovic and J. O'M. Bockris, Electrochim. Acta, 1966. **11**: p. 376.

Chapter 5 Preparation and Characterization of heat-treated carbon supported Pt-based bimetallic catalysts

This chapter gives the preparation and characterization of heat-treated carbon supported Pt-based bimetallic catalysts. The preparation of heat-treated carbon supported Pt bimetallic catalysts (PtM/C(T), T = heat treatment temperature) will be described in Section 5.1. Section 5.2 will give the physical characterization of the PtM/C(T) bimetallic catalysts. The physical characterization of the PtM/C(T) bimetallic catalysts was performed using X-ray diffraction, TEM/EDX and EXAFS.

5.1 Preparation of heat-treated Pt-based bimetallic catalysts

Recent reports in the literature have shown that the Pt-based alloy electrocatalysts offer significantly higher electrocatalytic activities for oxygen reduction reaction than pure platinum for both phosphoric acid fuel cells [1-4] and PEM fuel cells [5-8]. In our work we treated Pt-based bimetallic catalysts prepared from SOMC at different temperatures to try to induce Pt alloy formation.

The preparation and characterisation of PtM/C bimetallic catalysts (where M = Fe, Ni, Cr or Co) by using SOMC method were described in detail in Chapter 3. In brief, the preparation of a series of PtFe/C, PtNi/C, PtCr/C and PtCo/C catalysts involved a surface organometallic chemistry (SOMC) reaction between the Pt/C catalyst and a metallocene $M(C_5H_5)_2$ (M is Co, Ni, Cr or Fe). The catalysts were then reduced under H_2 at 200 °C.

After the SOMC reaction, the PtM/C bimetallic catalysts were heated in a flowing reducing atmosphere (H_2/ N_2 = 10/90) at different heat treatment temperatures (denoted as PtM/C(T), T = heat treatment temperature (400 °C - 950 °C)) for 1 hour and allowed to cool to room temperature.

The Pt/C catalyst was subjected to a series of reaction and heat treatments in the same manner as the preparation of PtM/C(T) bimetallic catalysts (referred as Pt/C(T). The Pt/C(T) catalysts were used for the purposes of a comparative study.

5.2 Physical Characterization of heat-treated Pt-based bimetallic catalysts

5.2.1 Powder X-ray diffraction

Figures 5.1 – 5.6 show typical XRD patterns for the heat-treated Pt-based bimetallic catalysts at different heat treatment temperatures. The crystal structure and particle size of heat-treated Pt-based bimetallic catalysts could be verified by X-ray diffraction patterns. The position and intensity of reference peaks from JCPDS files are shown in Table 5.1[9-16].

The two major diffraction peaks of platinum are at $2\theta = 39.7^{o}$ (111) and 46.2^{o} (200) [9]. Peaks corresponding to the transition metals or their oxides for heat-treated Pt-based bimetallic catalysts were not observed probably due to the low second metal loadings, similar to the results for the 'as-prepared' Pt-based bimetallic catalysts using SOMC discussed in Chapter 3. This was because their phases were not fully developed or because their particle sizes were relatively small. Shifts in the Pt diffraction peaks of 0.5PtFe/C(T), 0.5PtCr/C(T) and 0.5PtCo/C(T) to higher diffraction angles were apparent for the heat-treated samples. The starting temperature at which shifts in the Pt diffraction peaks for 0.5PtFe/C(T), 0.5PtCr/C(T) and 0.5PtCo/C(T) became apparent, is 200°C, 500°C and 600°C, respectively. As the heat treatment temperature was increased, the shift was found to increase. This shift suggests that the interatomic distance of Pt was decreased due to the substitution of a smaller atom, such as a transition metal other than platinum [17]. After heat treatment temperature at 700 °C the main peaks for 0.5PtFe/C(T), shifted to near 40.6^{o} from 39.7^{o} and 46.9^{o} from 46.2^{o}, indicating Pt_3Fe

alloy formation. Figure 5.2 shows the PtFe/C(T) patterns of XRD for the catalysts with different atom ratios of Pt/Fe at 750 °C. There is evidence of possibly the Pt_3Fe alloy phase for all the compositions because the main peak of the Pt diffraction for catalysts above shifted to ~ 40.6° from 39.7°. A similar shift in the Pt diffraction peaks was observed for 0.5PtCr/C(T) to 40.4° from 39.7° and 47.0° from 46.2° (Figure 5.3) after heat treatment at 750 °C, suggesting formation of Pt_3Cr. Although the XRD Pt diffraction peaks for 0.5PtCo/C(T) were shifted to higher angle after heat treatment above 600°C (Figure 5.4), they did not shift to ~ 40.5 from 39.7° and ~ 47.1° from 46.2° reported in the literature for Pt_3Co[11] even after heat treatment at 950°C. The XRD patterns in Figure 5.5 and 5.6 show that the Pt diffraction peaks of 0.5PtNi/C(T) and 1.0PtNi/C(T) were not shifted compared with the diffraction peaks of Pt/C catalyst even after heat treatment at 800 °C or 950 °C.

Table 5.1 XRD reference peaks from JCPDS files

materials	**2θ**	**Intensity**
Pt	39.7	100
	46.2	53
Pt_3Fe	40.6	60
	46.9	100
Pt_3Cr	40.4	100
	47.0	25
Pt_3Co	40.5	100
	47.1	45
Fe	44.7	100
Ni	44.8	100
Cr	44.4	100
Co	47.5	100

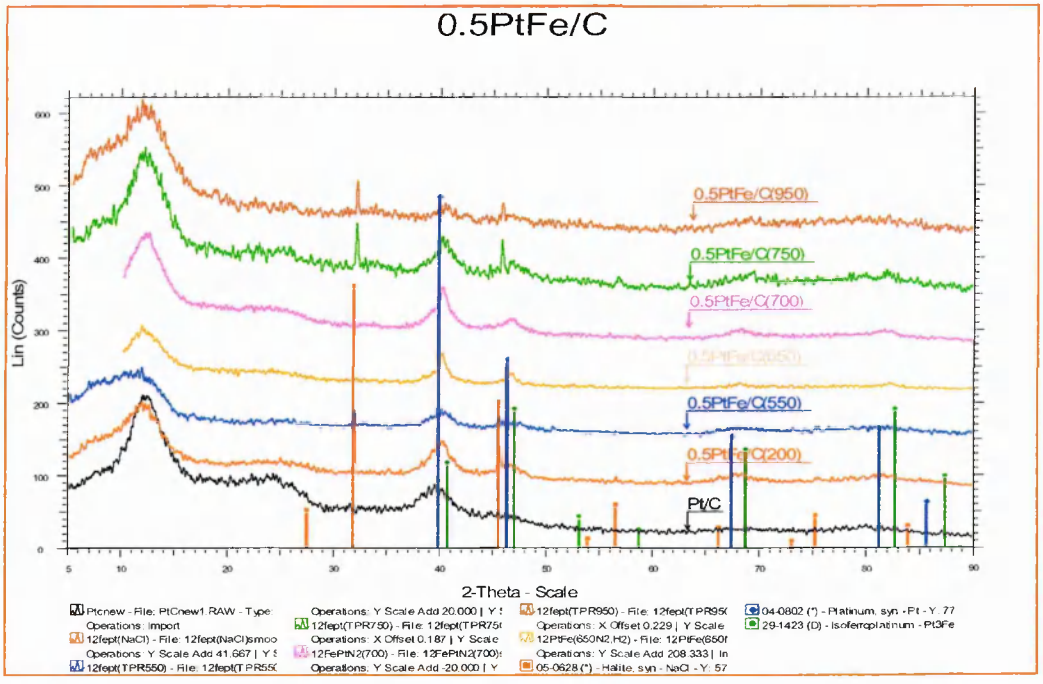

Figure 5.1 XRD Pattern for 0.5PtFe/C(T) Catalysts

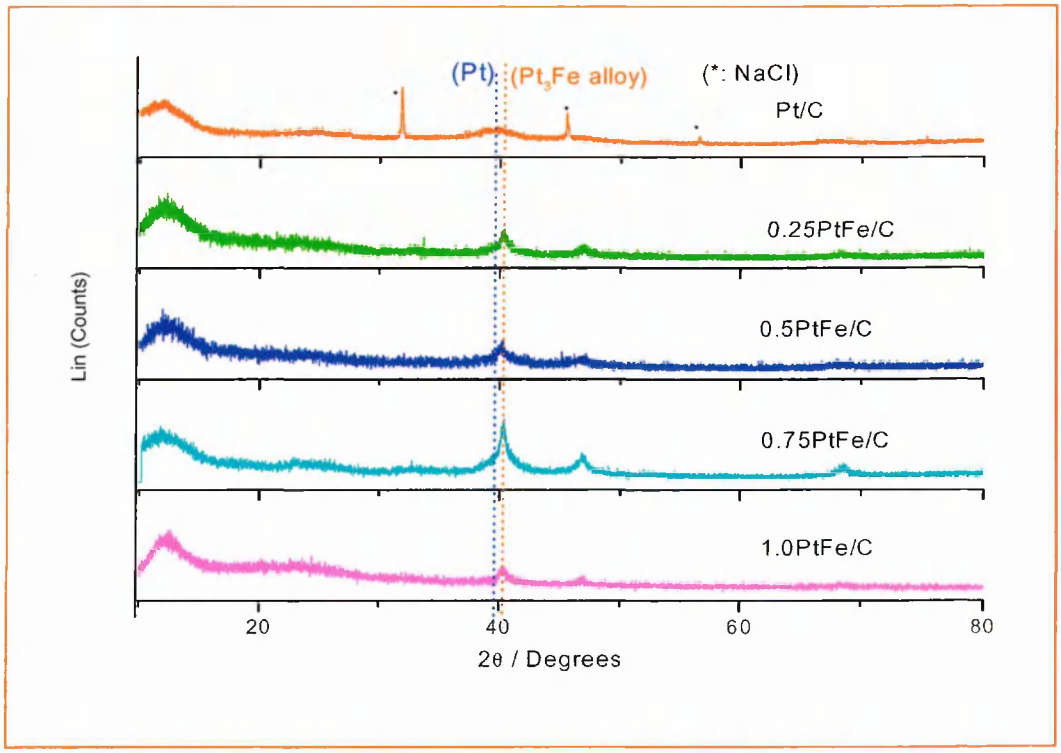

Figure 5.2 XRD Pattern for PtFe/C(750 ^{o}C) Catalysts

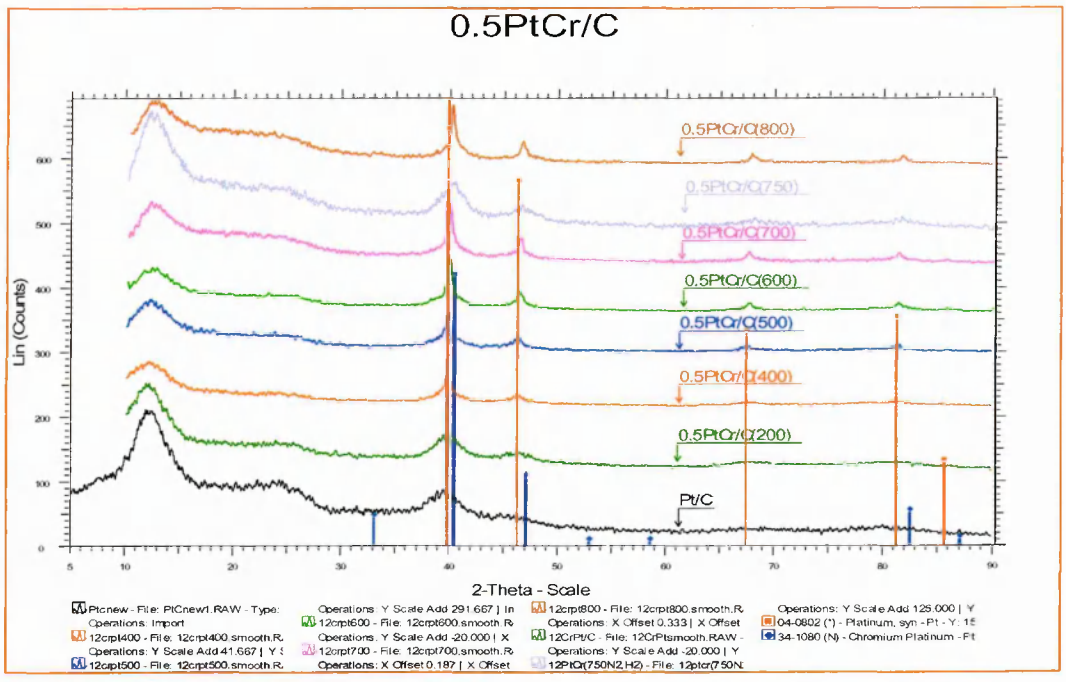

Figure 5.3 XRD Pattern for 0.5PtCr/C(T) Catalysts

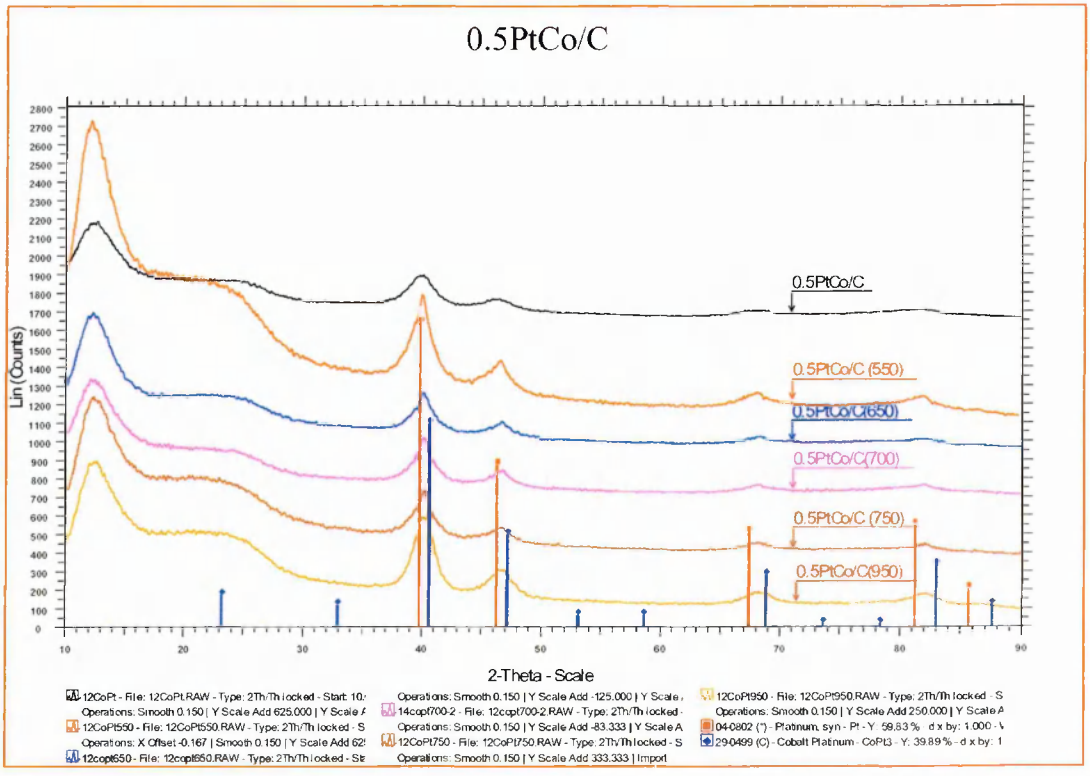

Figure 5.4 XRD Pattern for 0.5PtCo/C(T) Electrocatalysts

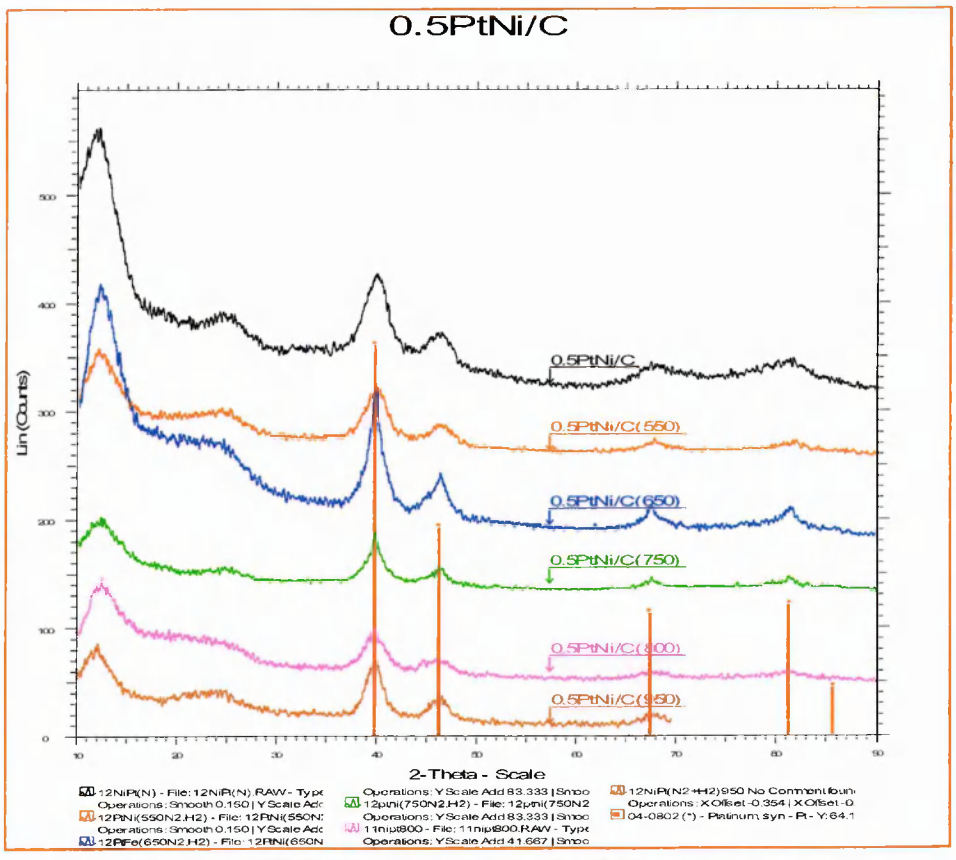

Figure 5.5 XRD Pattern for 0.5PtNi/C(T) Electrocatalysts

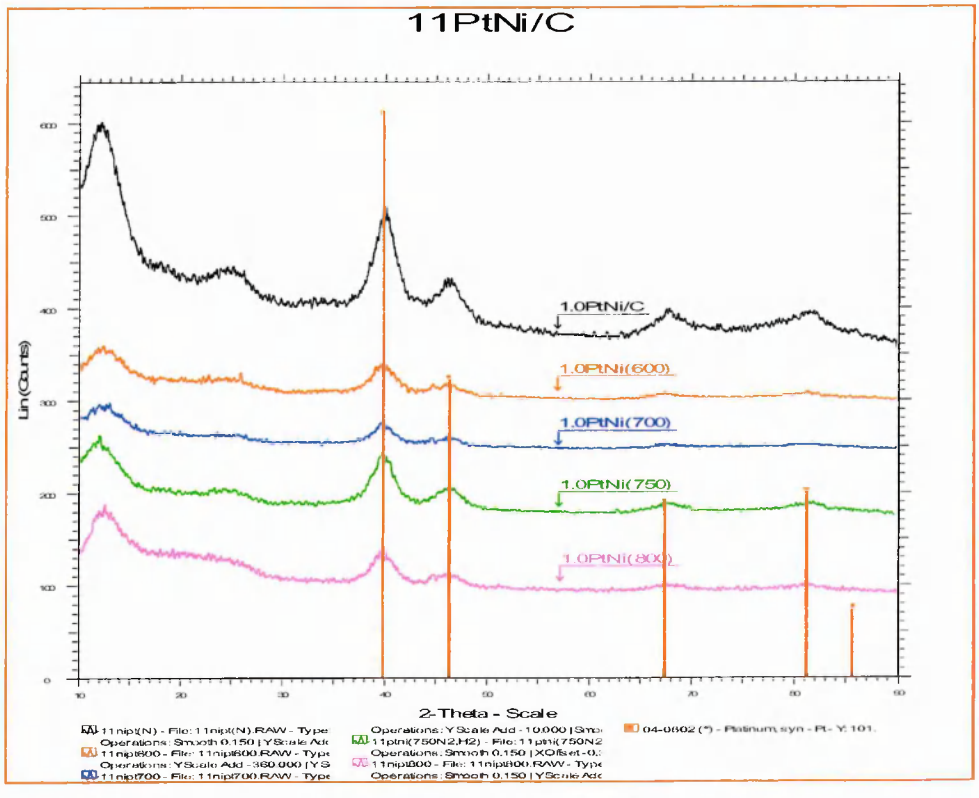

Figure 5.6 XRD Pattern for 1.0PtNi/C(T) Electrocatalysts

In all cases the second metal was at similar but low loading and highly dispersed on the Pt/C catalyst. There is evidence from the XRD that Fe, Cr and Co all entered into the Pt crystal after heat treatment. There was no such evidence for Ni using XRD. No shift in the Pt diffraction peaks for PtNi/C(T) is likely to be evident in XRD pattern if Ni enters into the Pt crystals after heat treatment. It appears to be energetically more favourable for the Pt/Ni system to form a continuous solid solution with Ni substituting on the Pt sites than for the rearrangement to a different crystal structure to take place.

The preparation of platinum alloyed with transition metals such as Ti, Cr, Co, Fe, using a precipitation method, been reported by Luczak and Landsman [18-20]. They claimed that alloying reduces sintering and gives better activity. Since then a number of different preparation methods for Pt-based alloy catalysts have been reported by a number of different authors. Hwang and Chung described PtFe/C alloy catalysts prepared by impregnating Pt/C with an aqueous solution of iron nitrate. After drying and reducing the impregnated samples at 100 °C for 1 h and at 400 °C for 2 h in flowing hydrogen, they were subjected to additional heat treatment at 900 °C in He atmosphere for 2h to form a Pt-Fe alloy [21]. Neergat used the same impregnation method to prepare PtCo/C, PtNi/C and PtCo/C catalysts. These were heat-treated at 900 °C in nitrogen atmosphere for 1 h to form the respective binary alloy catalysts [7]. Talismanic [22] used ultrasonic technique to prepare PtCu/C and PtCo/C catalysts. The solution, $Co(OH)_2$ or $Cu(NO_3)_2$, was ultrasonically blended with Pt/C for 2 h at about 60 °C. After drying the mixture in air, the alloying was carried out by heat treating the dried mixture at 900 °C for 2 h in a flowing argon atmosphere. The methods above, all needed heat treatment at 900 °C to form the Pt alloy. Obviously heating at such high temperatures may cause a reduction in the surface area.

In our work we used a Surface Organometallic Chemistry (SOMC) method described elsewhere [23-26] to prepare Pt-based bimetallic catalysts. This approach has

the advantage that an organometallic precursor only reacts with surface Pt on Pt/C. Thus the second metal is in close contact with the Pt and so it appears that a lower temperature is required to form the alloy. After SOMC, the PtCr and PtFe alloy were formed at lower heat treatment temperature, 750 °C and 700 °C, respectively. Lower heat treatment temperature is important for bimetallic catalysts to form an alloy because it reduces sintering. The use of a lower heat treatment temperature to form the alloy may be beneficial, resulting in less sintering of the catalyst.

The average sizes of the Pt and Pt-based alloy crystallites were calculated from the FWHM (full width at half-maximum) of the most prominent Pt (111) peak using Scherrer's equation (Section 3.3.3) [27]. Assuming a spherical shape for the particles, the specific area S (m^2g^{-1}) for the crystallites was calculated using the following equation (5.1) [28]:

$$S = 6 \times 10^3 \rho^{-1} d^{-1} \qquad (5.1)$$

where d is the diameter of the particle (nm) obtained from the XRD and ρ is the platinum density (21.4 g cm^{-3}). The features of XRD for representative electrocatalysts are summarized in Table 5.2.

It is evident from Table 5.2 that the crystallite size of PtM/C bimetallic catalysts even after heat treatment at 750 °C, was still small (< 4 nm) and not greatly increased compared with PtM/C (200 °C) bimetallic catalysts. This result is different with that of literatures [22, 29]. The crystallite sizes of the bimetallic catalysts in these literatures [22, 29] were > 6 nm after heat treatment at 900 °C. This shows that PtM/C bimetallic catalysts using SOMC method can form Pt/M alloy at lower heat treatment temperature and hence reduce the extent of sintering.

Table 5.2 XRD data of Pt/C and PtM/C(T) electrocatalysts

Electrocatalysts	Particle size/nm*	Metal area / $m^2 g^{-1}$	Lattice parameter /Å
Pt/C	2.4	117	3.92
Pt/C(200 °C)	2.7	104	3.92
Pt/C(reaction)	2.8	100	3.92
0.5PtNi/(200 °C)	3.1	90	3.91
0.5PtNi/(750 °C)	3.1	90	3.92
0.5PtCo/(200 °C)	3.2	88	3.92
0.5PtCo/(750 °C)	3.5	80	3.90
0.5PtCr/(200 °C)	3.3	85	3.92
0.5PtCr/(750 °C)	3.8	74	3.88
0.5PtFe/(200 °C)	3.5	80	3.90
0.5PtFe/(750 °C)	3.9	72	3.87

* Estimated from the FWHM using the Debye-Scherrer equation.

5.2.2 Transmission electron microscopy and Energy Dispersive X-ray

Figure 5.7 shows the morphology and the particle size distribution obtained by TEM of 0.5PtCr/C(750 °C), a typical Pt-based heat-treatment catalyst. A homogeneous dispersion of metal particles for 0.5PtCr/C (750 °C) catalyst was observed with a low degree of agglomeration, suggesting little sintering had occurred. This was similar to the micrographs for the Pt/C and the 0.5PtCr/C (200 °C) catalysts. EDX analysis of 0.5PtCr/C (750 °C) catalyst was carried out by reducing the size of the beam and focusing on different areas of the catalyst. The EDX analysis of the area occupied by an individual particle from the 0.5PtCr/C (750 °C) catalyst is also shown in Figure 5.7. The lines characteristic of Pt and Cr are visible, suggesting the presence of both chromium and platinum in the same region. On focusing the beam on areas of the support where no platinum metal particle was present there was no evidence of chromium. Similarly no Cr

was found on the carbon for the blank product (Cr/C) obtained between chromium precursor ($Cr(C_5H_5)_2$) and the carbon support under the same preparation process.

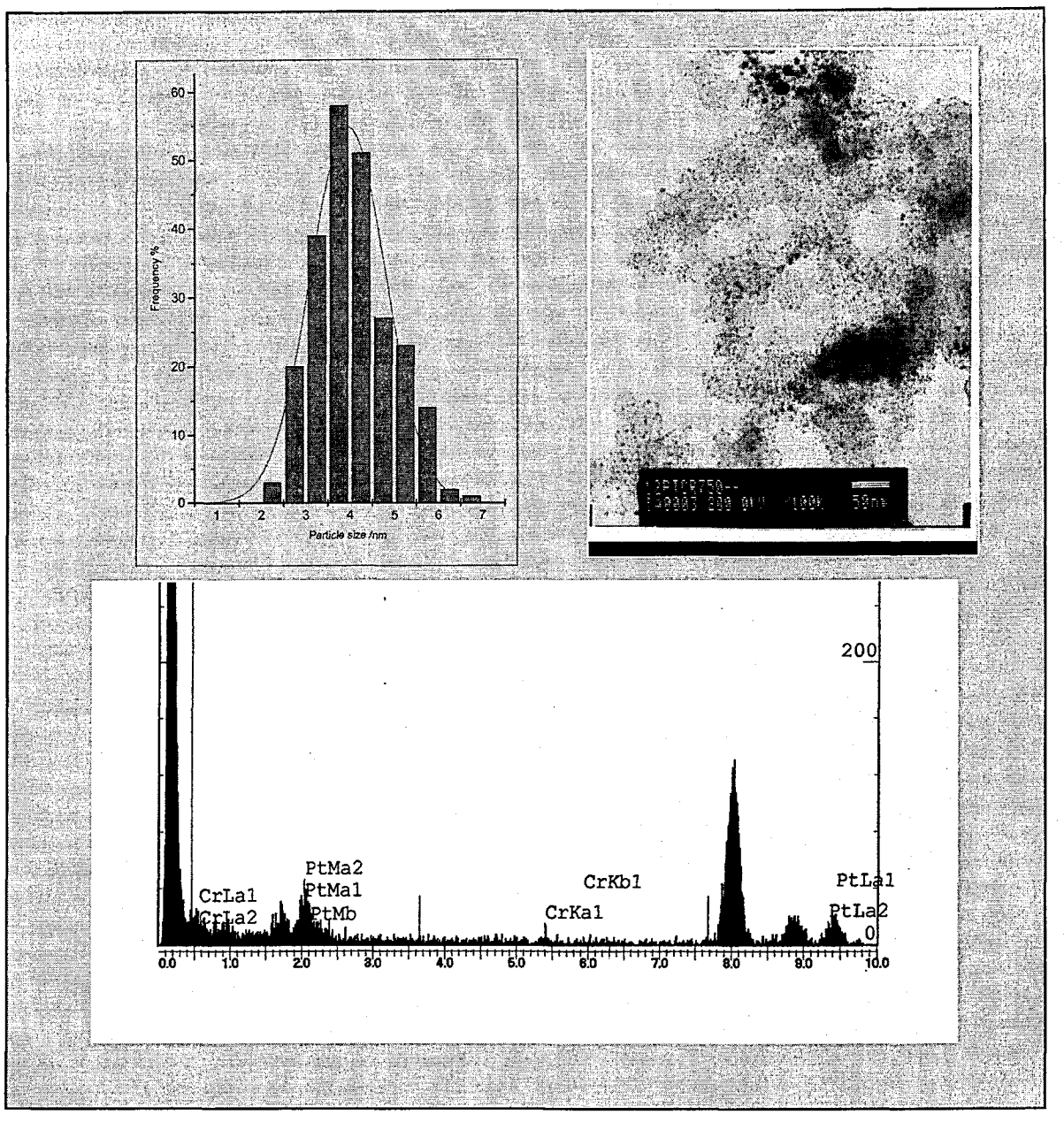

Figure 5.7 TEM and EDX analysis of 0.5PtCr/C(750 °C)

To elucidate any change in the morphologies and particle size of the Pt-based bimetallic catalysts at different heat treatment temperature, typical electron micrographs and particle size distribution are shown in Figure 5.8 – 5.17 after heat treatment at 200 °C, 700 °C and 950 °C. The particle size was measured directly from TEM photographs

using NIH image software. The average metal particle size for each catalyst was calculated using equation (5.2) and is listed in Table 5.3.

$$d = \frac{\sum n_i d_i}{\sum n_i} \tag{5.2}$$

The average particle size of the Pt/C (200 °C), Pt/C (700 °C) and Pt/C (950 °C) catalysts is 3.2, 3.9, 4.6 nm, respectively, suggesting that the particle size increased as heat-treatment temperature was increased. The histograms in Figure 5.9 show that the particle size distribution is narrow for Pt/C catalysts even after heat treatment at 950 °C.

When the Pt_3M phase of Pt-based bimetallic catalysts was formed at 700 – 750 °C, the TEM images show that the metal particle sizes of catalysts were quite uniform and only slightly increased (< 5 nm) compared with PtM/C (200 °C) (4.2 – 4.5 nm). The histograms show that the particle size distribution is still narrow for PtM/C (700 °C) catalysts. As the heat-treatment temperature was increased to 950 °C, the TEM images show that some sintering has occurred with some larger particles (≥ 10 nm) evident and the average metal particle size of catalysts has increased to 5.5 – 8.5 nm, particularly for PtNi/C (950 °C). The histograms show that the particle size distribution is not narrow for PtM/C (950 °C) catalysts unlike PtM/C (200 °C) catalysts. The degree of sintering appeared to depend on the second metal. The PtCo/C(950 °C), PtFe/C(950 °C) and PtCr/C(950 °C) catalysts show less sintering, whereas sintering was severe for the PtNi/C(950 °C) catalysts where the Pt_3M alloy did not form.

EDX analysis was carried out by decreasing the size of the electron beam it was possible to focus on areas occupied by individual metal particles on the surface of the support. EDX analysis (Table 5.3) of these individual particles provided evidence for the two metals coexisting in the same although not a very quantitative technique. By

examining a large number of particles by EDX no isolated particles of the second metal were observed on the support.

Table 5.3 Characterization of Pt-based bimetallic catalysts at different heat-treatment by EDX and TEM

Electrocatalysts	**Atomic ratio % (Pt:M)**	**Particle size / nm**
Pt/C(200 °C)	---	3.2
Pt/C(700 °C)	---	3.9
Pt/C(950 °C)	---	4.6
0.5PtNi/C(200 °C)	88.2 : 11.9	4.2
0.5PtNi/C(700 °C)	91.3 : 8.7	4.8
0.5PtNi/C(950 °C)	57.7 : 42.3	8.3
0.5PtFe/C(200 °C)	71.5 : 28.5	4.5
0.5PtFe/C(700 °C)	69.2 : 30.8	4.9
0.5PtFe/C(950 °C)	73.6 : 26.4	6.4
0.5PtCr/C(200 °C)	85.8 : 14.2	4.3
0.5PtCr/C(700 °C)	66.8 : 33.2	5.0
0.5PtCr/C(950 °C)	78.1 : 21.9	6.5
0.5PtCo/C(200 °C)	72.6 : 27.4	4.4
0.5PtCo/C(700 °C)	83.7 : 16.3	4.8
0.5PtCo/C(950 °C)	77.5 : 22.5	5.5

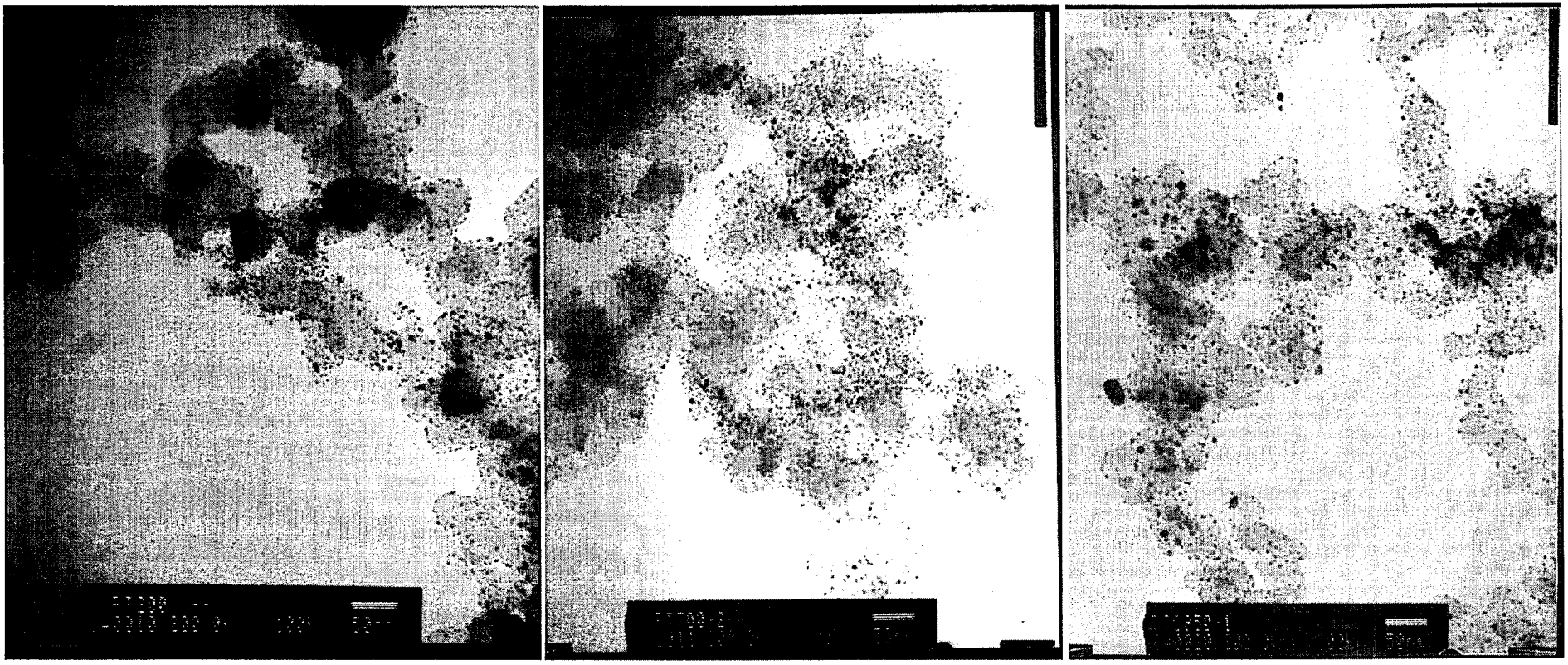

Figure 5.8 TEM micrographs of (a) Pt/C(200 °C), (b) Pt/C(700 °C) and (c) Pt/C(950 °C) catalysts

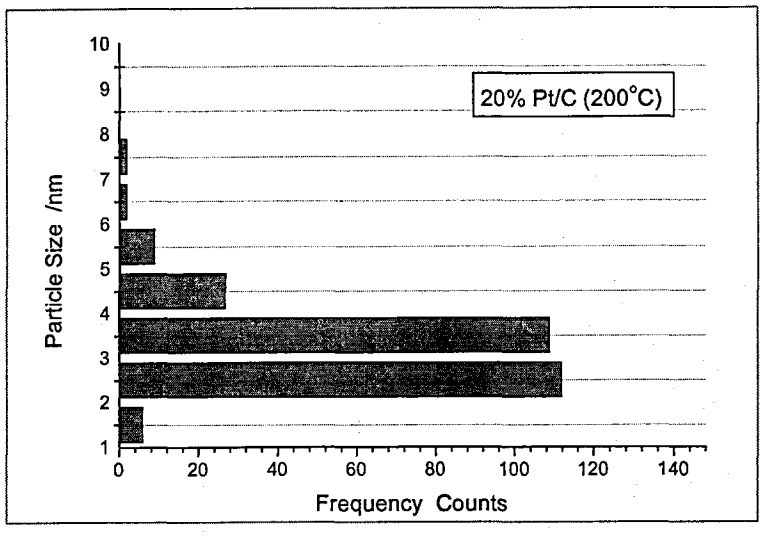

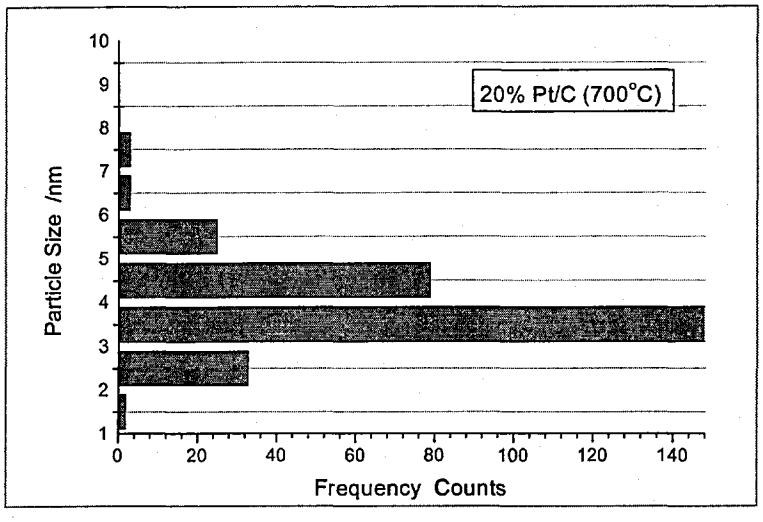

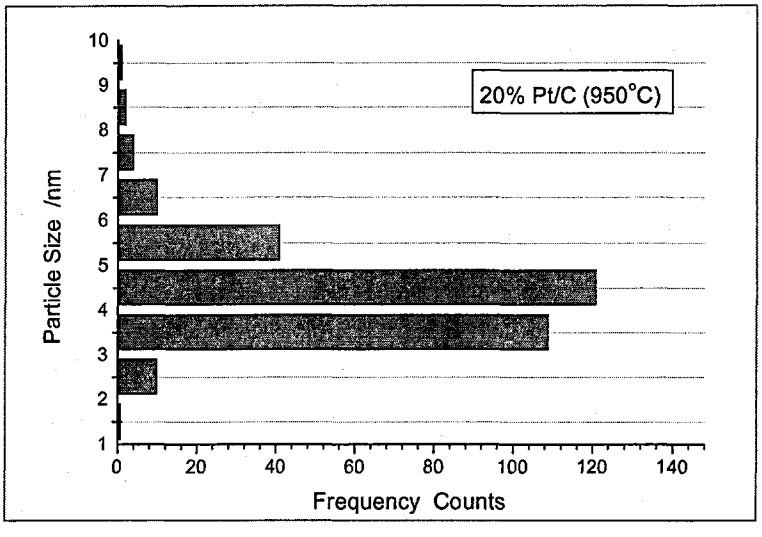

Figure 5.9 Histograms of particle size distribution for (a) Pt/C(200 °C), (b) Pt/C(700 °C) and (c) Pt/C(950 °C) catalysts

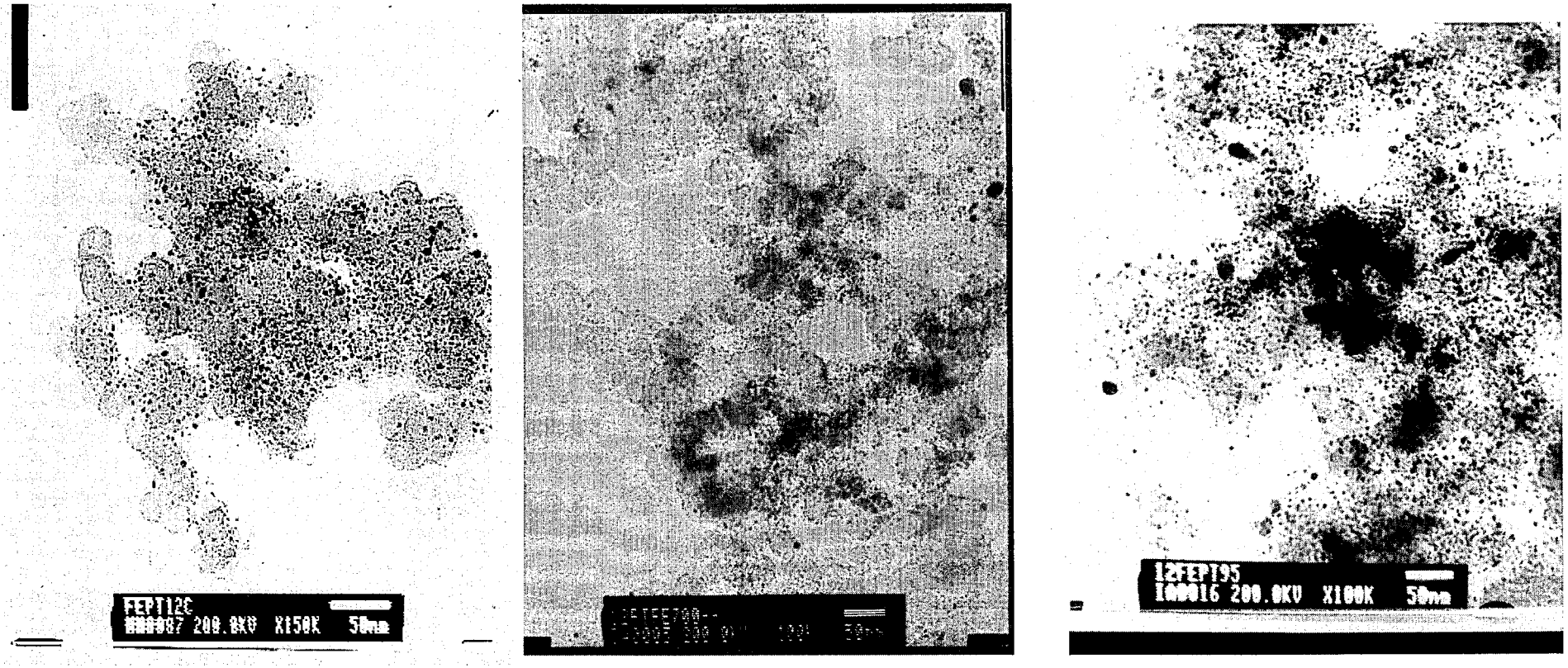

Figure 5.10 TEM images of (a) 0.5PtFe/C(200 °C), (b) 0.5PtFe/C(700 °C) and (c) 0.5PtFe/C(950 °C) catalysts

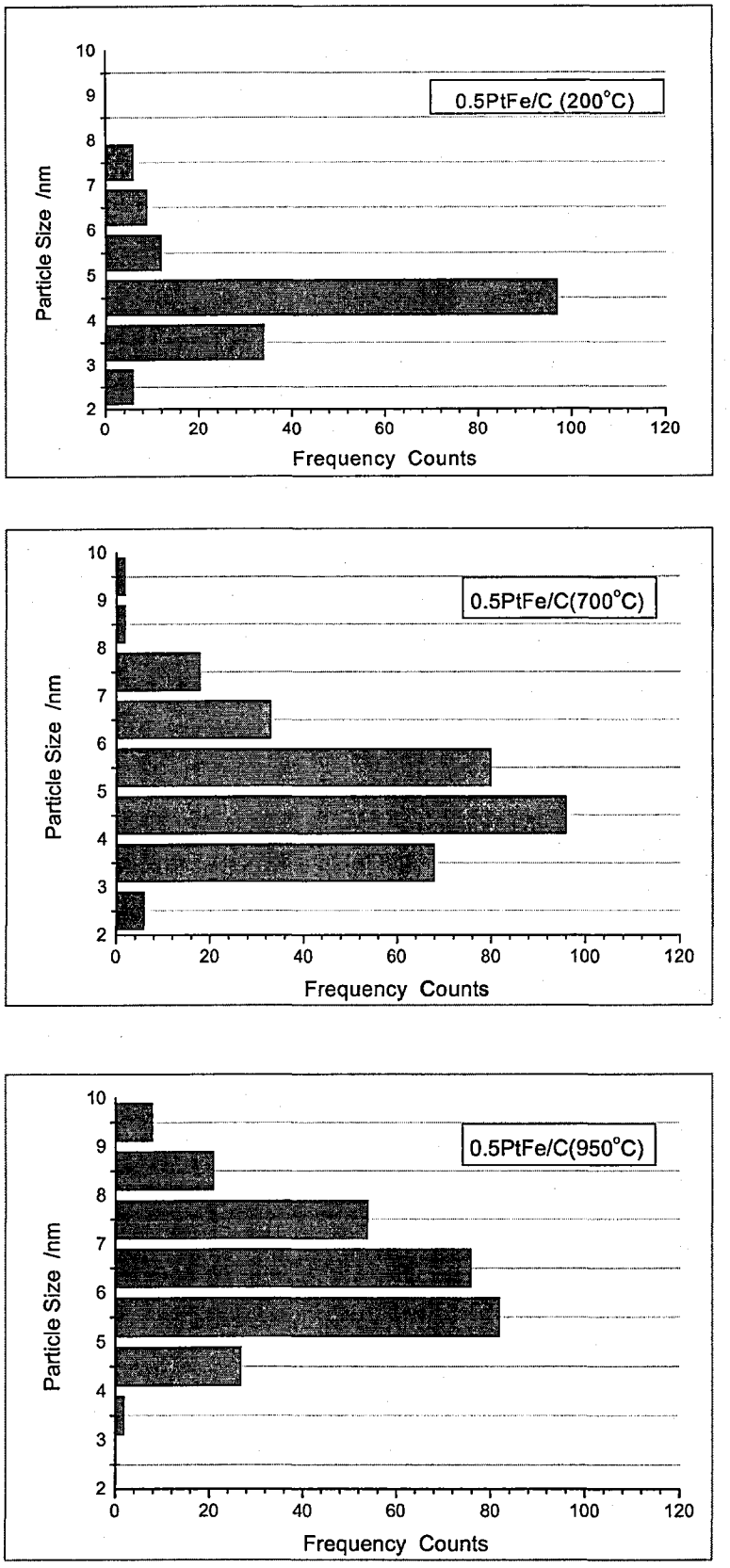

Figure 5.11 Histograms of particle size distribution for (a) 0.5PtFe/C(200 °C), (b) 0.5PtFe/C(700 °C) and (c) 0.5PtFe/C(950 °C) catalysts

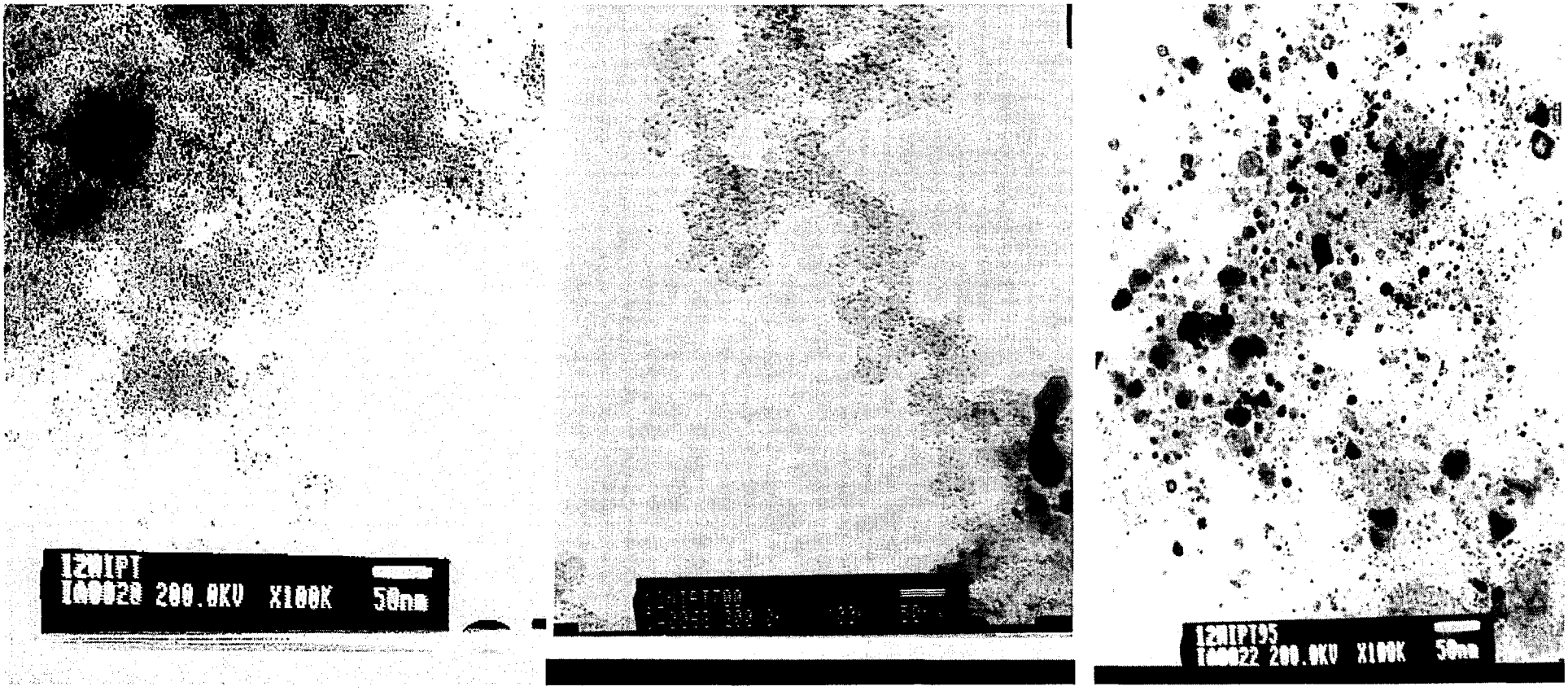

Figure 5.12 TEM images of (a) 0.5PtNi/C(200 °C), (b) 0.5PtNi/C(700 °C) and (c) 0.5PtNi/C(950 °C) catalysts

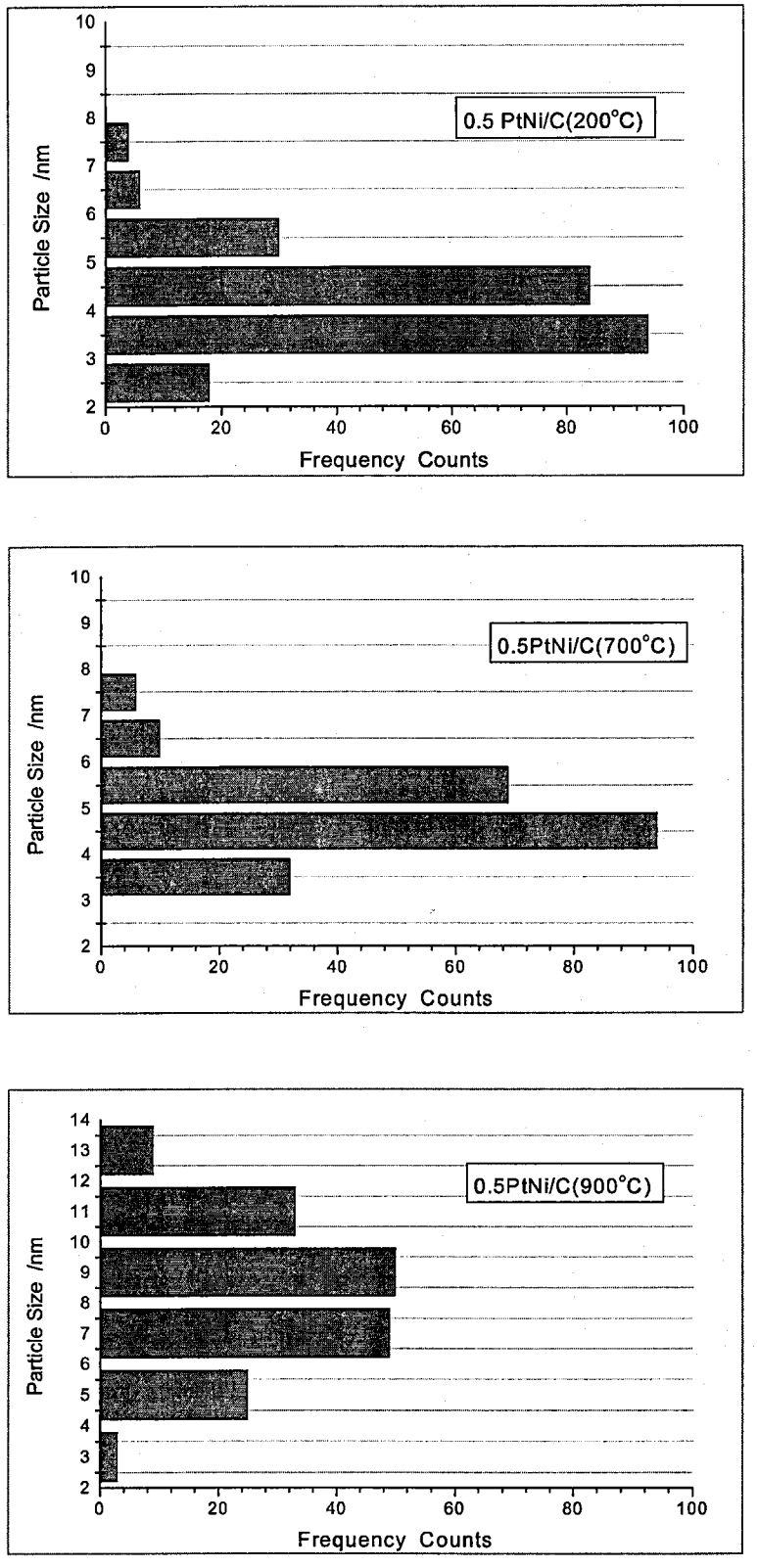

Figure 5.13 Histograms of particle size distribution for (a) 0.5PtNi/C(200 °C), (b) 0.5PtNi/C(700 °C) and (c) 0.5PtNi/C(950 °C) catalysts

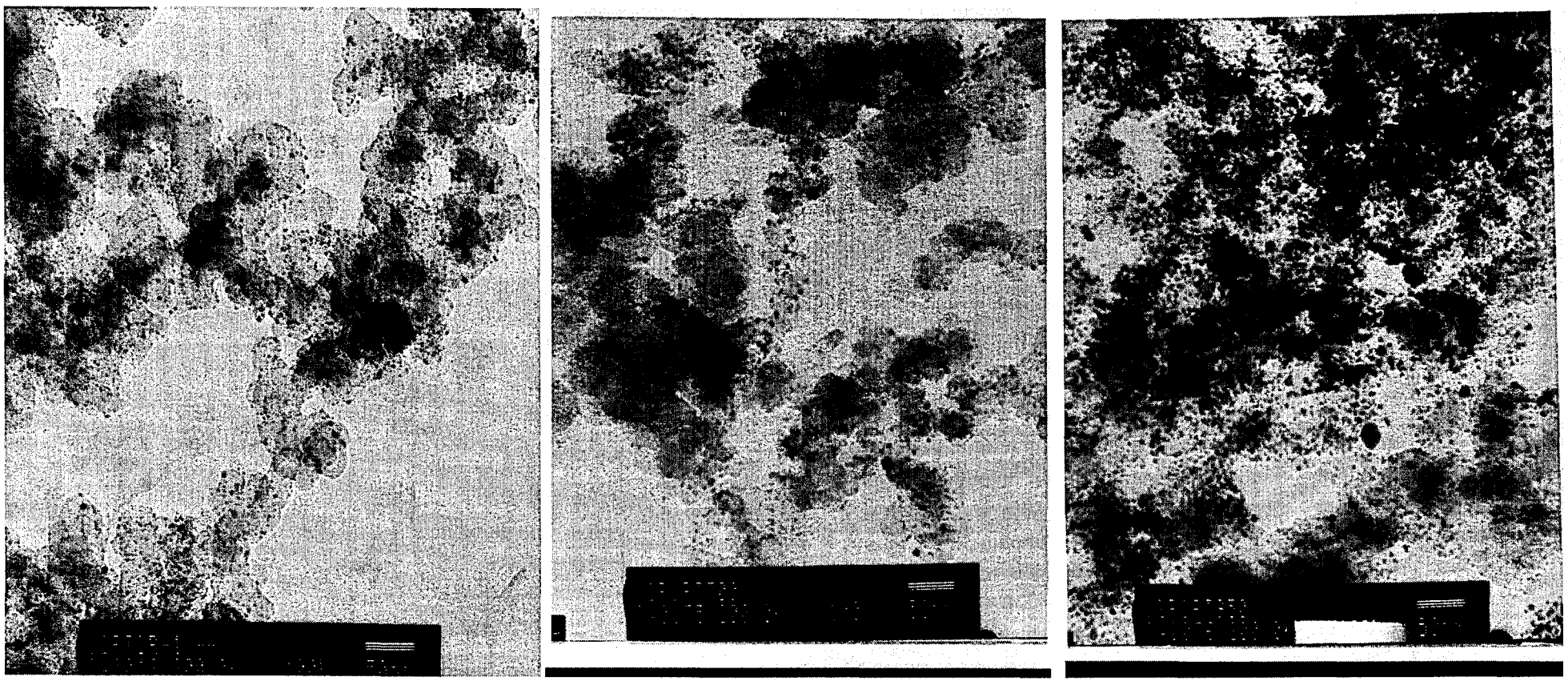

Figure 5.14 TEM images of (a) 0.5PtCr/C(200 °C), (b) 0.5PtCr/C(700 °C) and (c) 0.5PtCr/C(950 °C) catalysts

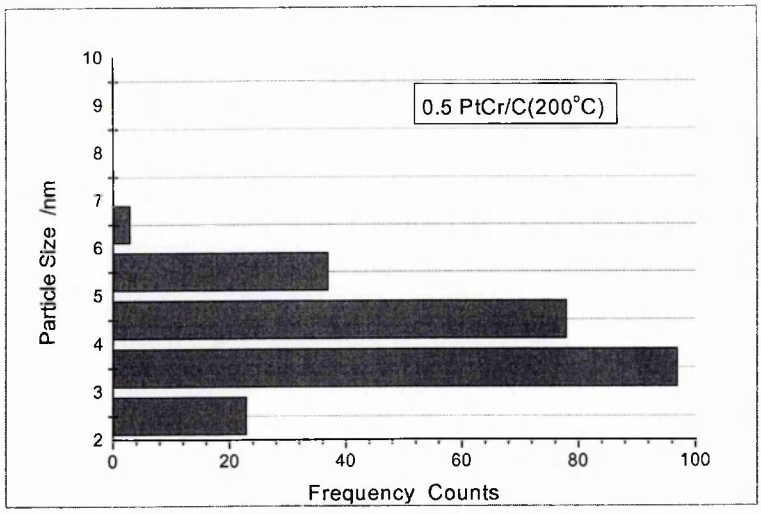

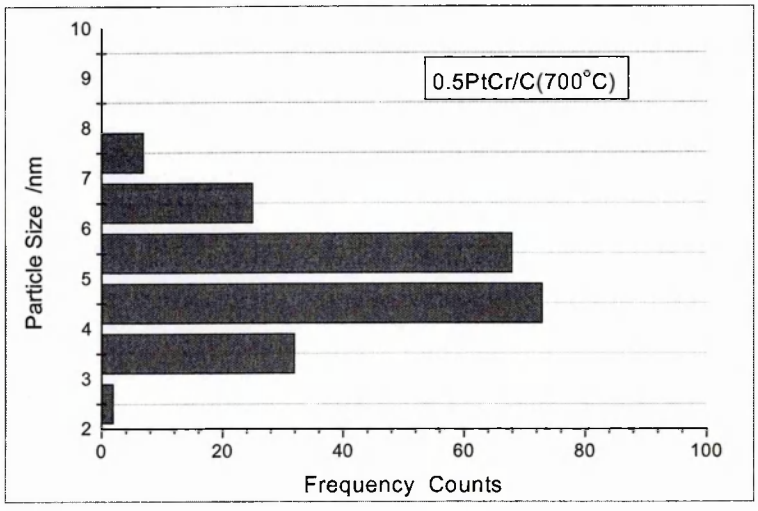

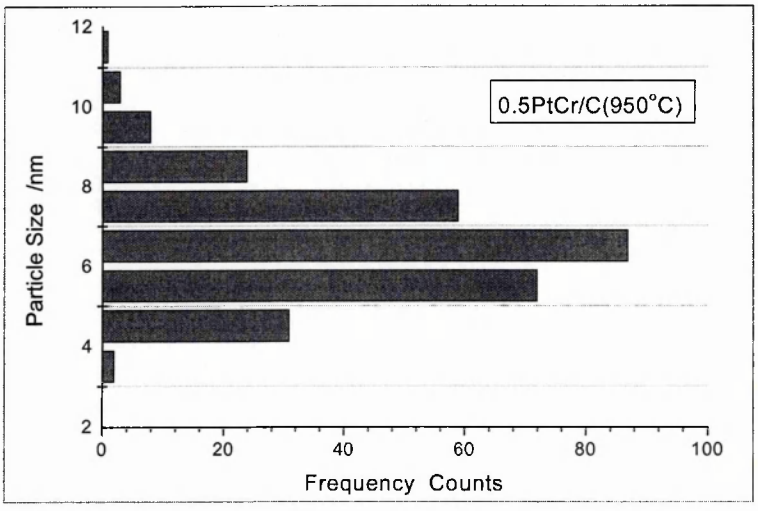

Figure 5.15 Histograms of particle size distribution for (a) 0.5PtCr/C(200 °C), (b) 0.5PtCr/C(700 °C) and (c) 0.5PtCr/C(950 °C) catalysts

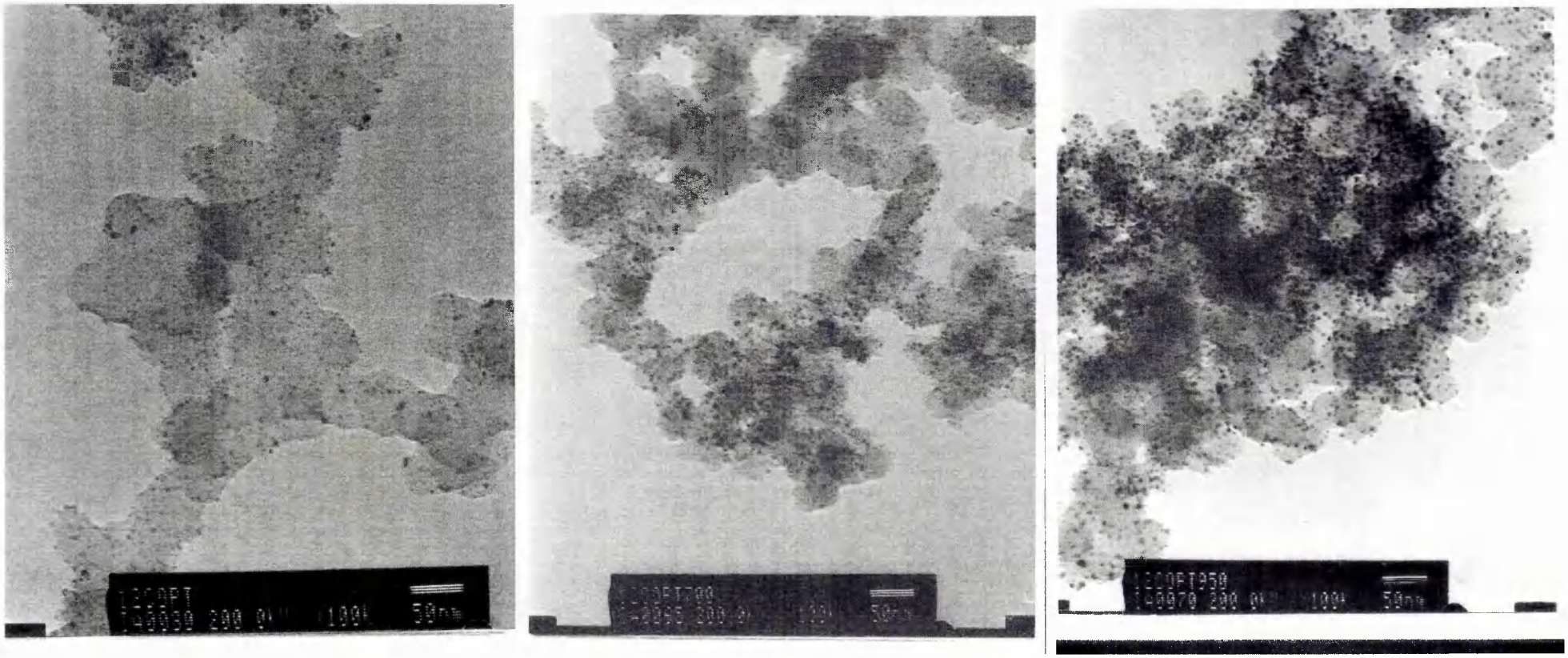

Figure 5.16 TEM images of (a) 0.5PtCo/C(200 ^{o}C), (b) 0.5PtCo/C(700 ^{o}C) and (c) 0.5PtCo/C(950 ^{o}C) catalysts

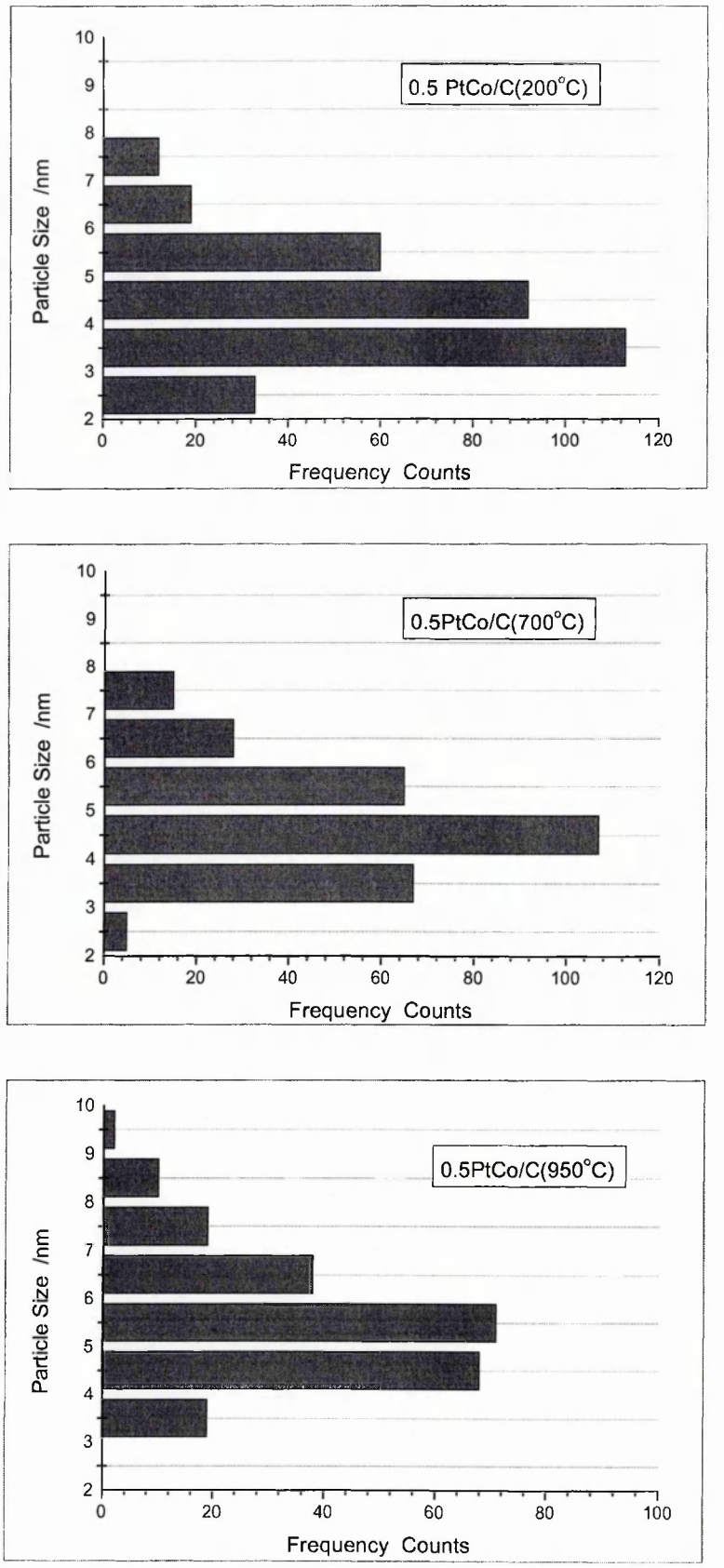

Figure 5.17 Histograms of particle size distribution for (a) 0.5PtCo/C(200 °C), (b) 0.5PtCo/C(700 °C) and (c) 0.5PtCo/C(950 °C) catalysts

5.2.3 Extended X-ray adsorption fine structure (EXAFS)

Details on the EXAFS experiments and on the analysis of the data of the PtM/C(T) bimetallic electrocatalysts will be given in this section.

EXAFS data were collected for the 0.5PtFe/C(T), 1.0PtNi/C(T) and 0.5PtCr/C(T) electrocatalysts both in air and H_2 (reduction for 1 hour at room temperature). The EXAFS experiments were carried out at room temperature in the fluorescence mode, and full details of the experimental conditions are given in Chapter 2. A description of the samples examined by EXAFS and their nomenclature are given in Table 5.4.

Table 5.4 The summary of samples examined by EXAFS

Samples	**Treatment method**
0.5PtFe/C(700 °C) in air	Heat treatment at 700 °C, exposed and measured in air
0.5PtFe/C(700 °C) in H_2	Above sample was reduced for 1 hour and measured in H_2
0.5PtFe/C(750 °C) in air	Heat treatment at 750 °C, exposed and measured in air
0.5PtFe/C(750 °C) in H_2	Above sample was reduced for 1 hour and measured in H_2
0.5PtFe/C(900 °C) in air	Heat treatment at 900 °C, exposed and measured in air
0.5PtFe/C(900 °C) in H_2	Above sample was reduced for 1 hour and measured in H_2
1.0PtNi/C(700 °C) in air	Heat treatment at 700 °C, exposed and measured in air
1.0PtNi/C(700 °C) in H_2	Above sample was reduced for 1 hour and measured in H_2
1.0PtNi/C(750 °C) in air	Heat treatment at 750 °C, exposed and measured in air
1.0PtNi/C(750 °C) in H_2	Above sample was reduced for 1 hour and measured in H_2
1.0PtNi/C(900 °C) in air	Heat treatment at 900 °C, exposed and measured in air
1.0PtNi/C(900 °C) in H_2	Above sample was reduced for 1 hour and measured in H_2
0.5PtCr/C(700 °C) in air	Heat treatment at 700 °C, exposed and measured in air
0.5PtCr/C(700 °C) in H_2	Above sample was reduced for 1 hour and measured in H_2

0.5PtCr/C(750 °C) in air	Heat treatment at 750 °C, exposed and measured in air
0.5PtCr/C(750°C) in H_2	Above sample was reduced for 1 hour and measured in H_2
0.5PtCr/C(900 °C) in air	Heat treatment at 900 °C, exposed and measured in air
0.5PtCr/C(900 °C) in H_2	Above sample was reduced for 1 hour and measured in H_2

5.2.3.1 0.5PtFe/C(T) electrocatalysts

EXAFS spectra and Fourier transforms (both experimental and theoretical) of the Fe K-edge in the samples of 0.5PtFe/C(T) electrocatalysts in air and in H_2 (T = 700 °C, 750 °C and 900 °C) are shown in Figures 5.18 – 5.20 and analyses of these data are presented in Tables 5.5 - 5.7 respectively. The results are very different to those for the catalysts treated at 200 °C (Section 3.3.4.1). We now see a Fe-Pt interaction both for the 0.5PtFe/C electrocatalyst exposed to air, and for the sample treated using a reducing atmosphere (H_2/N_2 = 10/90) at high temperature; in both cases the Fe-Pt distance and the coordination number of Pt in the first coordination shell are ≈ 2.73 Å and 5-6, respectively, compared to 2.63 Å and 2.5 for the 0.5PtFe/C(200 °C) reduced electrocatalyst. A new coordination number for Pt in the second coordination shell was also found at a Fe-Pt distance ≈ 3.95 Å. Both these results indicated the diffusion of Fe into the Pt crystal, and with possibly some Pt_3Fe alloy formation in 0.5PtFe/C(T) electrocatalysts.

Figure 5.21 shows the crystal structures of Pt and Pt_3Fe. In Pt_3Fe crystal structure the corner iron atoms, of which there are eight, are each shared between eight neighbouring unit cells; and the face-centred Pt atoms, of which there are six, count as ½ each. So in one Pt_3Fe crystal cell the ratio of Fe and Pt atoms is 1:3. The distance and coordination number of Fe–Pt of Pt_3Fe crystal in the first coordination shell is 2.74 Å and 12. The distance and average coordination number of Fe–Pt of the 0.5PtFe/C(T)

electrocatalysts in the first coordination shell using EXAFS experiments is 2.73 Å and 5-6, respectively. The distance of Fe–Pt in the 0.5PtFe/C(T) electrocatalysts suggests that there is some Pt_3Fe alloy formation on the 0.5PtFe/C(T) electrocatalysts. However, the coordination number of Fe–Pt in the 0.5PtFe/C(T) electrocatalysts of 5 – 6, is less than the 12-coordination found in the Pt_3Fe crystal structure, suggesting that a mixture of species (Pt_3Fe, Pt, Fe *etc*) are present in the 0.5PtFe/C(T) electrocatalysts.

The coordination number of Fe–Pt in the first coordination shell was slightly different at different heat treatment temperatures, and increased as temperature rose, suggesting that diffusion of Fe into the Pt surface, and the formation of Pt_3Fe is easier at high temperature. After heat treatment at 700°C or above, Pt_3Fe alloy in the 0.5PtFe/C(T) electrocatalysts seems to be a stable system and is still present after exposure to air.

The Fe–O bond length of ~ 2.0 Å and the coordination number of one oxygen atom were almost unaltered in the 0.5PtFe/C(T) electrocatalysts, compared to that of 0.5PtFe/C(200 °C) electrocatalyst (Section 3.3.4.1). The results showed that some iron was present as oxide when 0.5PtFe/C(T) electrocatalysts exposed in air, even after reduction at high temperature.

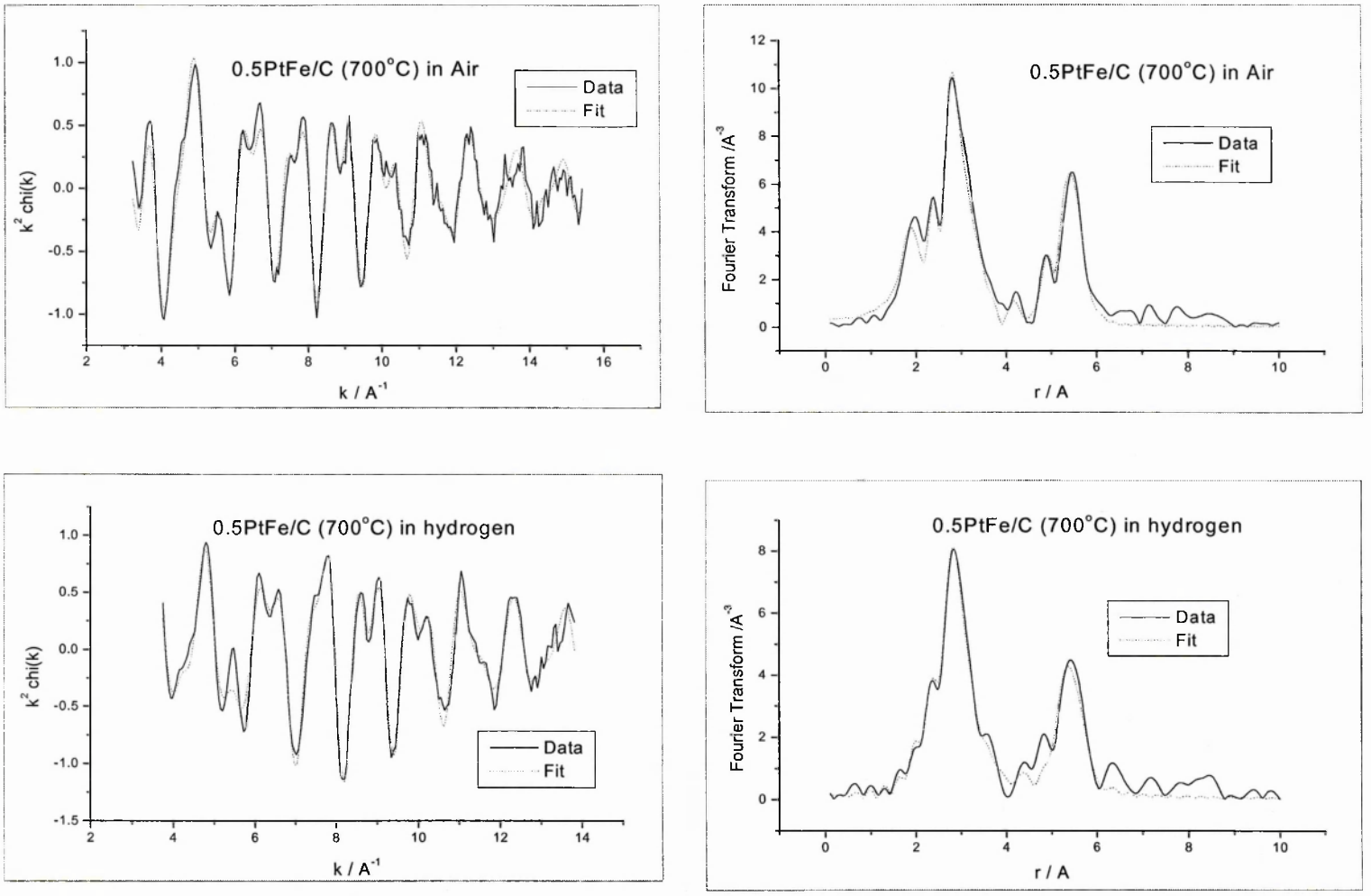

Figure 5.18 EXAFS k^2 weighted $x(k)$ spectra and k^2 weighted Fourier transforms of the Fe K-edge of 0.5PtFe/C(700°C) electrocatalysts in air and H_2, respectively. (solid line = data, dot line = fit)

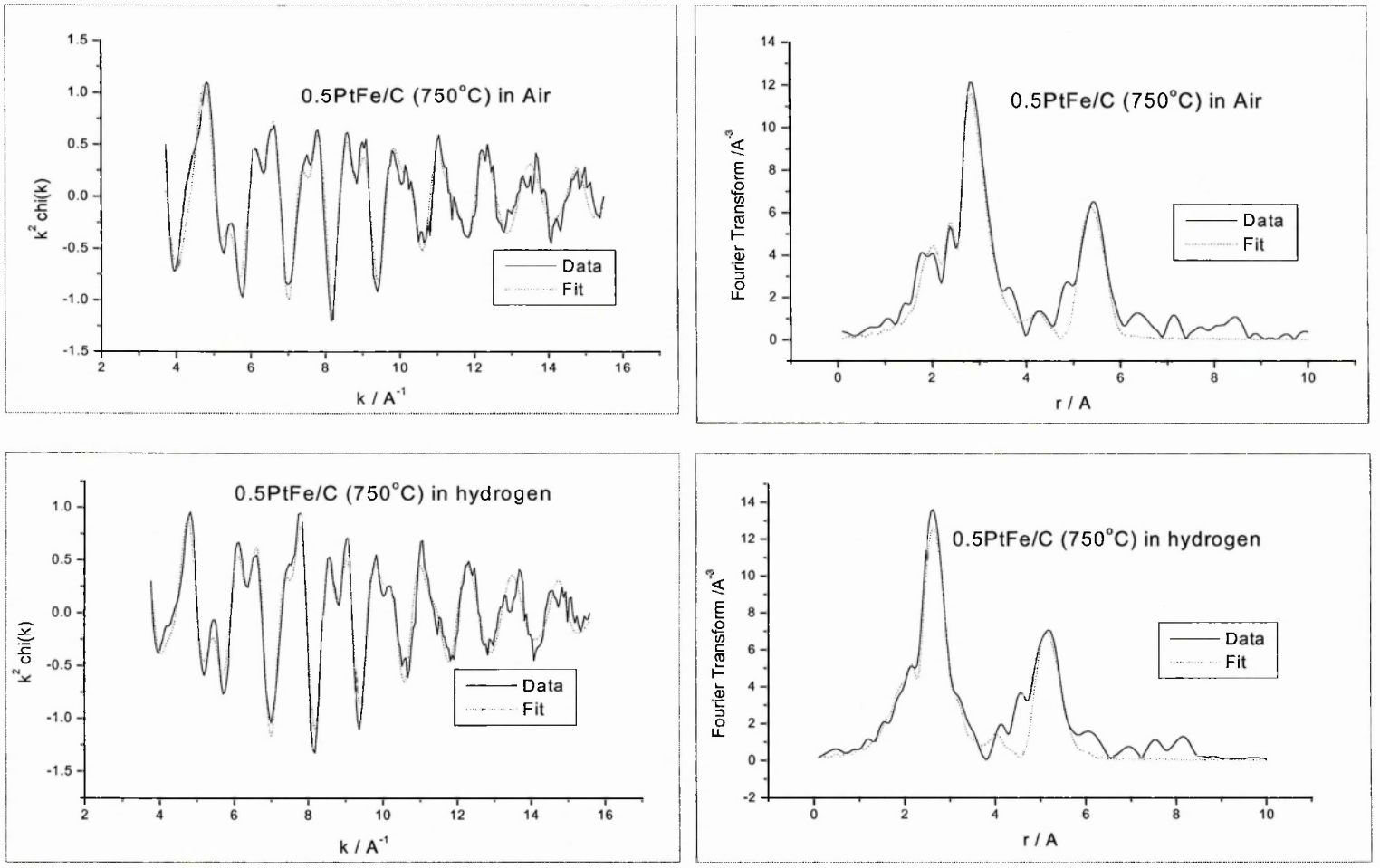

Figure 5.19 EXAFS k^2 weighted $x(k)$ spectra and k^2 weighted Fourier transforms of the Fe K-edge of 0.5PtFe/C(750°C) electrocatalysts in air and H_2, respectively. (solid line = data, dot line = fit)

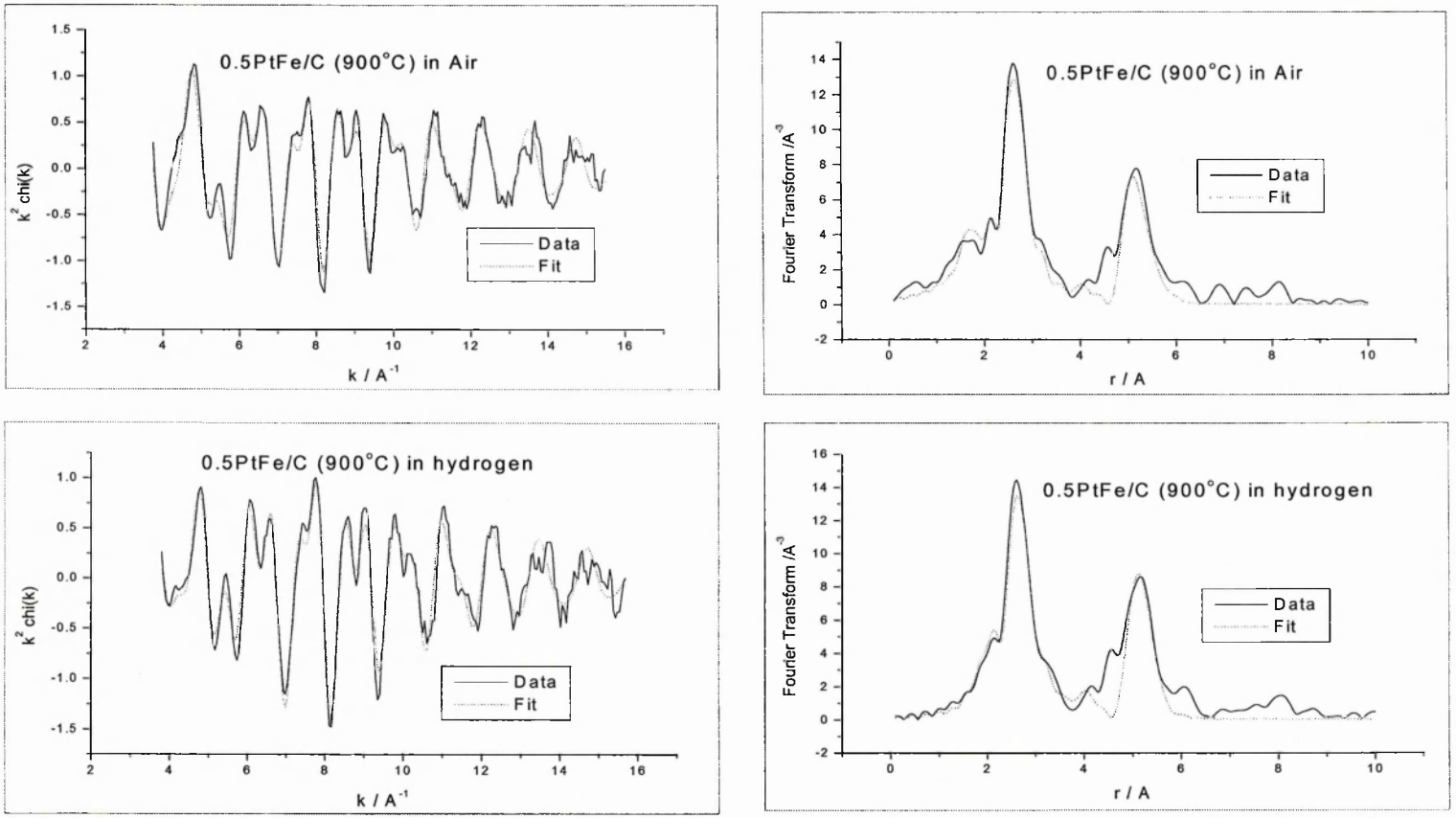

Figure 5.20 EXAFS k^2 weighted $x(k)$ spectra and k^2 weighted Fourier transforms of the Fe K-edge of 0.5PtFe/C(900°C) electrocatalysts in air and H_2, respectively. (solid line = data, dot line = fit)

Table 5.5 Best EXAFS fit parameters of 0.5PtFe/C(700 °C) electrocatalysts in air and H_2, respectively (N: coordination numbers, R: distance from the Fe absorber, $2\sigma^2$: Debye-Waller factor, E_f: energy shift and R_{exafs}: a meaningful indication (below 40) of the quality of fit to the EXAFS data in k-space)

	Neighbour	N	R / Å	$2\sigma^2$ / Å^2	E_f / eV	R_{exafs}
In air	Fe – O	1.23 ± 0.11	1.94 ± 0.01	0.015 ± 0.003	–1.59	27.98
	Fe – Fe	0.12 ± 0.09	2.48 ± 0.04	0.007 ± 0.015		
	Fe – Pt	4.91 ± 0.24	2.71 ± 0.004	0.014 ± 0.0007		
	Fe – Pt	2.70 ± 1.16	3.92 ± 0.03	0.027 ± 0.009		
In H_2	Fe – O	1.41 ± 0.29	2.09 ± 0.016	0.031 ± 0.01	–9.06	23.26
	Fe – Fe	0.19 ± 0.11	2.66 ± 0.03	0.004 ± 0.01		
	Fe – Pt	5.51 ± 0.37	2.73 ± 0.01	0.014 ± 0.0006		
	Fe – Pt	4.75 ± 1.38	3.96 ± 0.02	0.028 ± 0.01		

Table 5.6 Best EXAFS fit parameters of 0.5PtFe/C(750 °C) electrocatalysts in air and H_2, respectively (N: coordination numbers, R: distance from the Fe absorber, $2\sigma^2$: Debye-Waller factor, E_f: energy shift and R_{exafs}: a meaningful indication (below 40) of the quality of fit to the EXAFS data in k-space)

	Neighbour	N	R / Å	$2\sigma^2$ / Å^2	E_f / eV	R_{exafs}
In air	Fe – O	1.65 ± 0.20	2.01 ± 0.012	0.018 ± 0.004	–6.45	30.54
	Fe – Pt	5.02 ± 0.29	2.72 ± 0.005	0.013 ± 0.0006		
	Fe – Pt	1.38 ± 0.71	3.98 ± 0.029	0.013 ± 0.005		
In H_2	Fe – O	1.37 ± 0.27	2.09 ± 0.02	0.025 ± 0.007	–9.97	30.98
	Fe – Pt	5.70 ± 0.29	2.73 ± 0.004	0.013 ± 0.0005		
	Fe – Pt	2.14 ± 0.81	3.99 ± 0.02	0.017 ± 0.005		

Table 5.7 Best EXAFS fit parameters of 0.5PtFe/C(900 °C) electrocatalysts in air and H_2, respectively (N: coordination numbers, R: distance from the Fe absorber, $2\sigma^2$: Debye-Waller factor, E_f: energy shift and R_{exafs}: a meaningful indication (below 40) of the quality of fit to the EXAFS data in k-space)

	Neighbour	N	R / Å	$2\sigma^2$ / Å^2	E_f / eV	R_{exafs}
In air	Fe – O	1.29 ± 0.20	2.01 ± 0.014	0.015 ± 0.004	5.00	29.34
	Fe – Pt	5.31 ± 0.30	2.73 ± 0.005	0.012 ± 0.0006		
	Fe – Pt	4.43 ± 1.55	3.95 ± 0.03	0.028 ± 0.007		
In H_2	Fe – O	1.53 ± 0.32	2.13 ±0.02	0.029 ± 0.008	0.01	31.43
	Fe – Pt	6.27 ± 0.33	2.73 ± 0.004	0.014 ± 0.0006		
	Fe – Pt	4.39 ± 1.32	3.97 ± 0.02	0.023 ± 0.005		

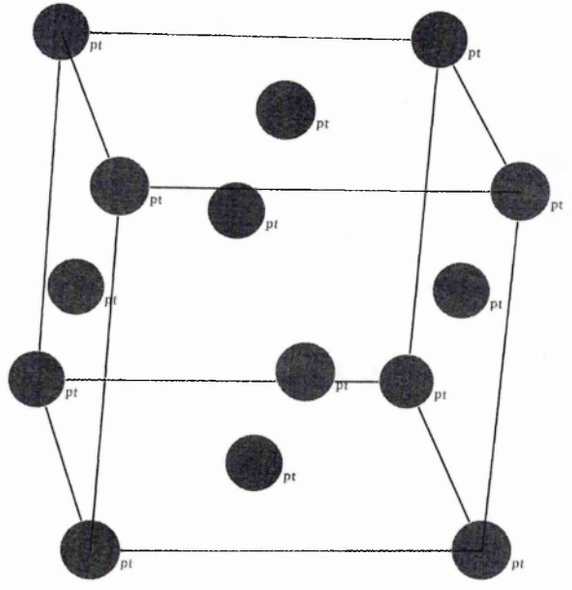

Pt crystal

(a)

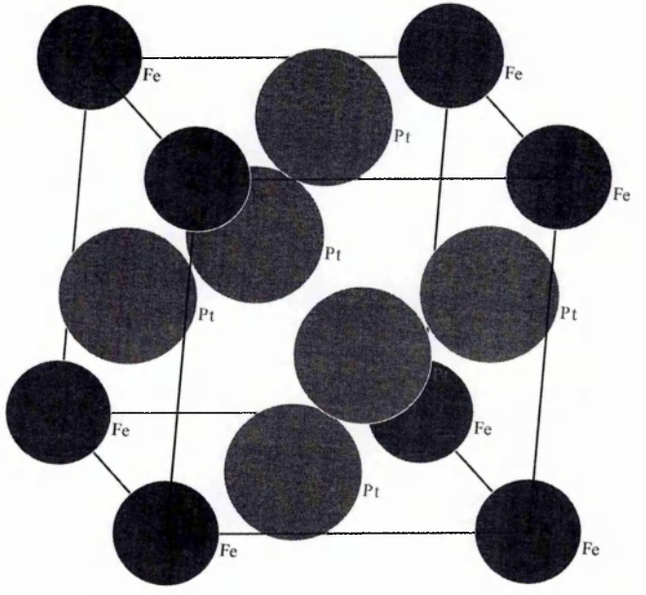

Pt_3Fe alloy

(b)

Figure 5.21 the crystal structures of (a) Pt and (b) Pt_3Fe

5.2.3.2 1.0PtNi/C(T) electrocatalysts

EXAFS spectra and Fourier transforms (both experimental and theoretical) of the Ni K-edge in the samples of 1.0PtNi/C(700 °C) and 1.0PtNi/C(750 °C) electrocatalysts in air and in H_2 are shown in Figure 5.22 – 5.23 and analyses of these data are presented in Table 5.8 – 5.9. When the 1.0PtNi/C electrocatalyst was treated using a reducing atmosphere (H_2/ N_2 = 10/90) at 700 °C and 750 °C, comparison with the1.0PtNi/C (200 °C) electrocatalyst (Section 3.3.4.2), shows that the Ni–Ni bond length decreased to 2.48 Å from 3.08 Å and the coordination number of Ni–Ni in the first coordination shell increased to 7-8 from 2. The X-ray data for the distance and coordination number of Ni–Ni in crystalline Ni are 2.49 Å and 12, respectively in the first coordination shell [30]. The increase of coordination number and the decrease of bond length of Ni–Ni suggests that there was some agglomeration of Ni atoms in 1.0PtNi/C(700 °C) and 1.0PtNi/C(750 °C) electrocatalysts, and that the heat treatment at 700 °C and 750 °C induced a migration of Ni atoms to form larger particles. Ni was surrounded by 6-7 platinum atoms at a distance of 4.02 Å, meaning however, that the Ni atom was still in contact with surface Pt. The increase of the average distance of Ni–Pt, compared with the 1.0PtNi/C(200 °C) electrocatalyst (from 2.91 Å to 4.02 Å, Section 3.3.4.2), is due to the agglomeration of Ni atoms. At the same time, the Ni–O bond has all but disappeared, meaning that the NiO was easily reduced with H_2. Thus Ni seems to have segregated into larger clumps in the samples of 1.0PtNi/C(700 °C) and 1.0PtNi/C(750 °C).

Figure 5.24 shows EXAFS spectra and Fourier transforms (both experimental and theoretical) of the Ni K-edge and analyses of these data in the samples of 1.0PtNi/C(900 °C), respectively. When the heat treatment temperature was up to 900 °C, the coordination number of Ni–Ni decreased to 1-2 at a distance of 2.52 Å, and the average distance of Ni–Pt decreased to 2.69 Å from 4.02 Å. This result suggested that

large clumps of segregated Ni atoms disappeared, and Ni atoms entered and dispersed into the Pt crystal. This is consistent with the change in atomic ratio seen in the EDX results for this catalyst (section 5.2.2). The average distance of Ni–Pt 2.69 Å is similar to that expected for the Ni–Pt bond distance of a Pt/Ni alloy in the first coordination shell. A Ni–O bond appeared again in the 1.0PtNi/C(900 °C) electrocatalyst; this would suggest that the Pt/Ni species formed when the Ni migrates into the Pt crystallite, has an oxide coating. According to the literature [26, 31-33], a Pt–O bond is present in the Pt crystal structure of Pt/C and Pt-based alloy catalysts. Miguel and Roman-Martinez's EXAFS results revealed the formation of a Pt–O bond in a Pt/C catalyst using Pt-L_{III} edge [32, 33]. Crabb and Ravikumar detected the formation of PtO in Pt/C and PtGe/C catalysts using XPS [26]. It is possible that when Ni atoms entered into Pt crystal structure, Ni atoms could contact the O already in the system as Pt–O.

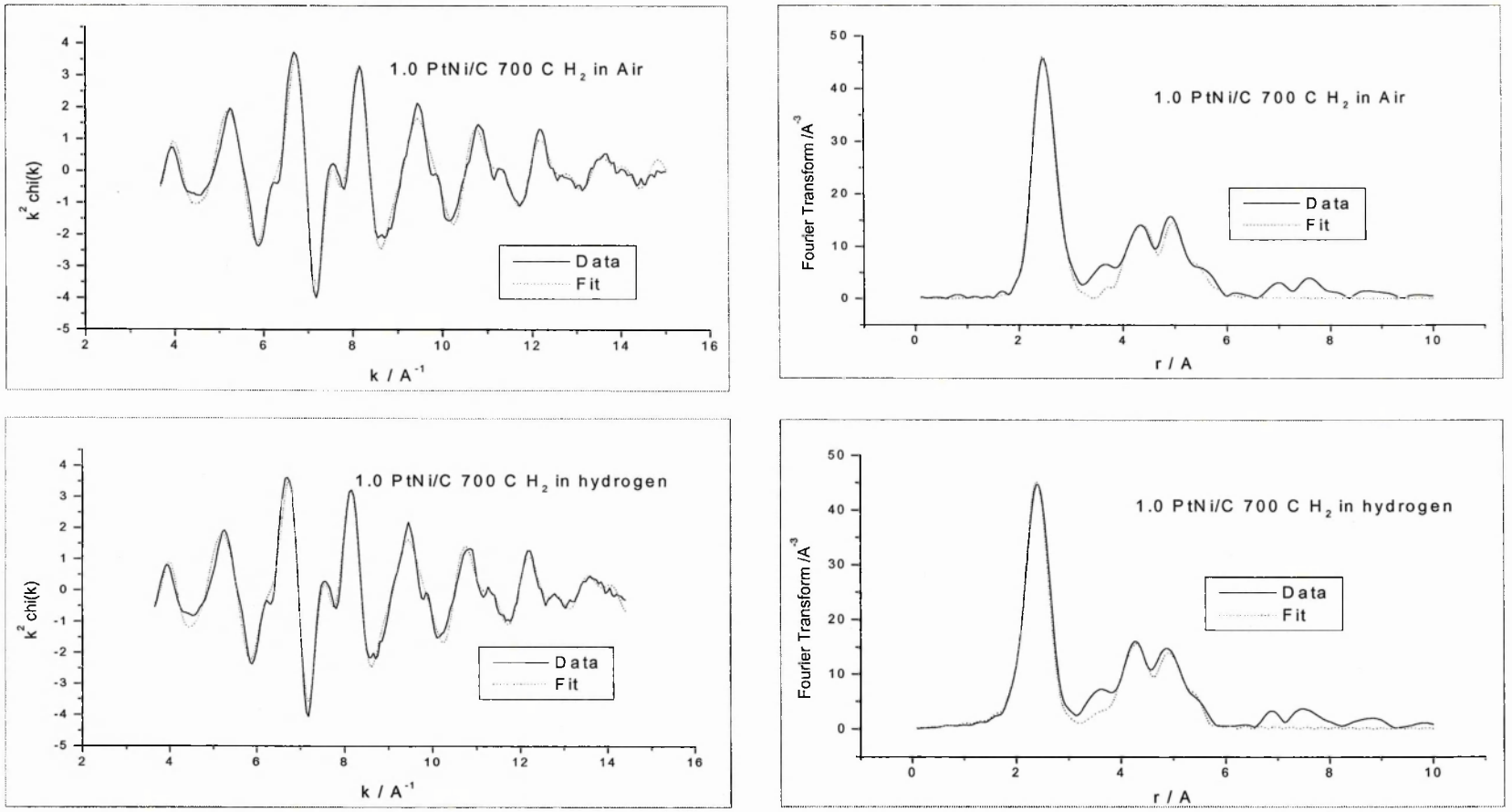

Figure 5.22 EXAFS k^2 weighted $x(k)$ spectra and k^2 weighted Fourier transforms of the Ni K-edge of 1.0PtNi/C(700 °C) electrocatalysts in air and H_2, respectively. (solid line = data, dot line = fit)

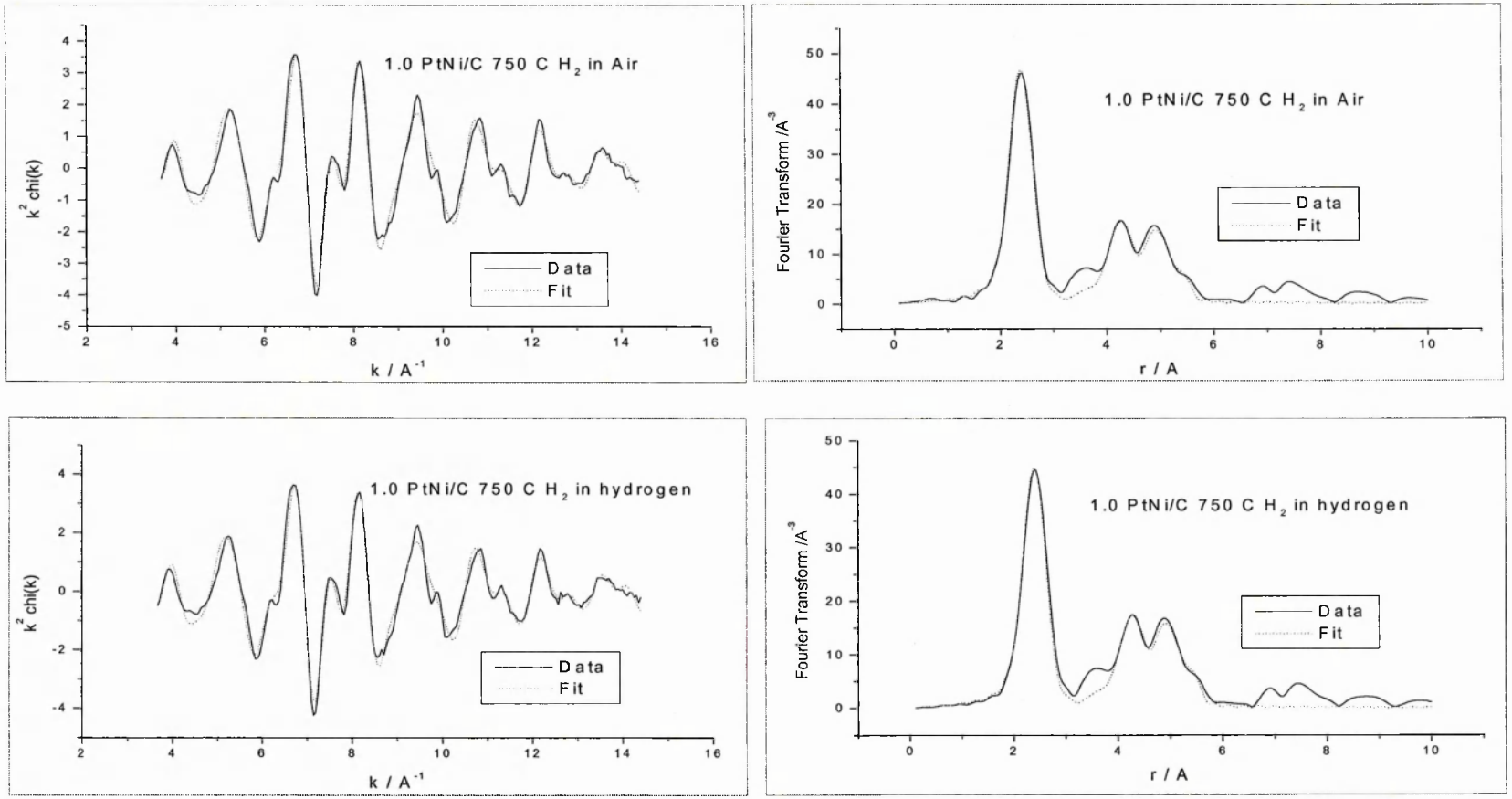

Figure 5.23 EXAFS k^2 weighted $x(k)$ spectra and k^2 weighted Fourier transforms of the Ni K-edge of 1.0PtNi/C(750 °C) electrocatalysts in air and H_2, respectively. (solid line = data, dot line = fit)

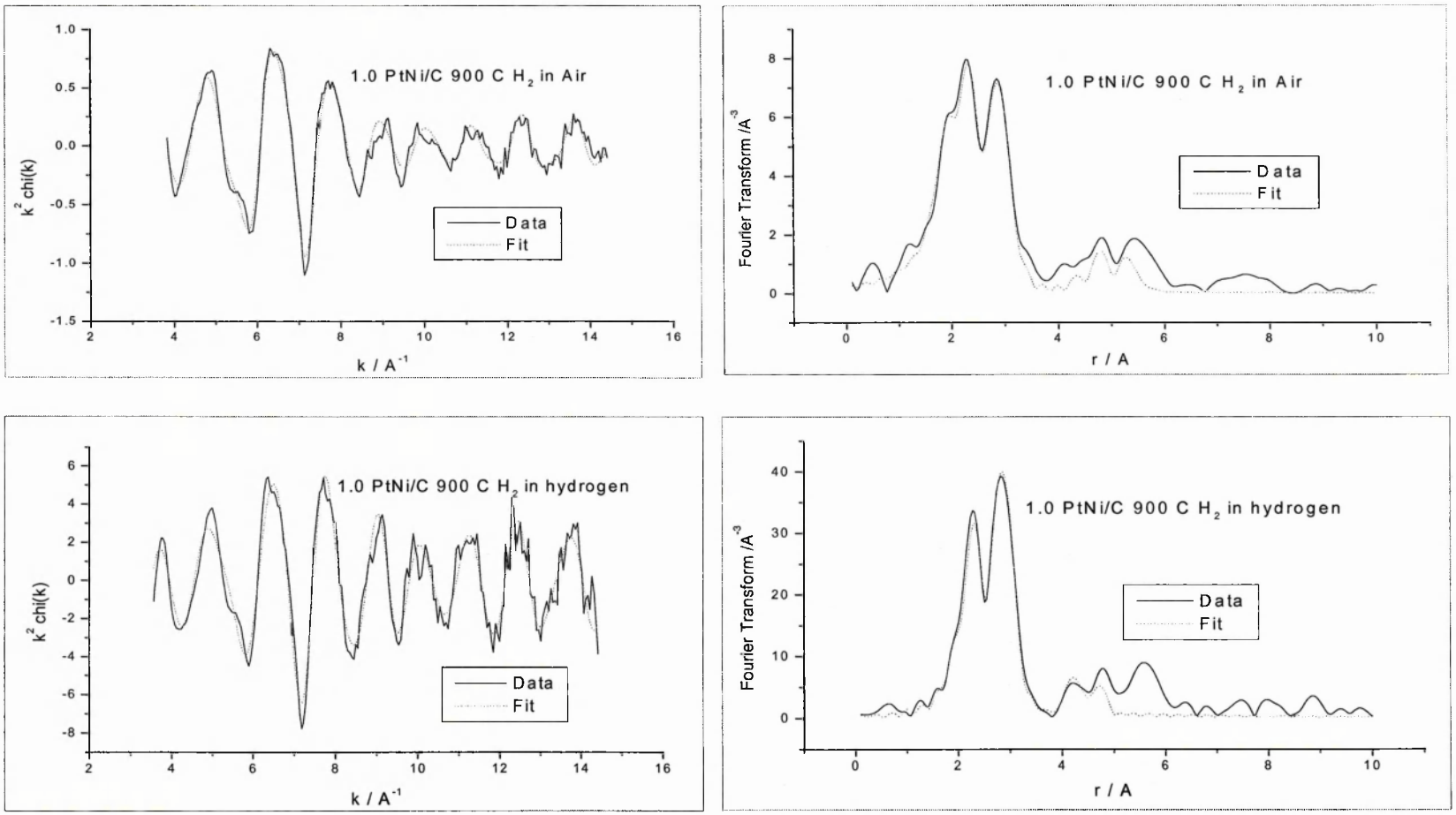

Figure 5.24 EXAFS k^2 weighted $x(k)$ spectra and k^2 weighted Fourier transforms of the Ni K-edge of 1.0PtNi/C(900 °C) electrocatalysts in air and H_2, respectively. (solid line = data, dot line = fit)

Table 5.8 Best EXAFS fit parameters of 1.0PtNi/C (700 °C) electrocatalysts in air and H_2, respectively (*N*: coordination numbers, *R*: distance from the Ni absorber, $2\sigma^2$: Debye-Waller factor, E_f: energy shift and R_{exafs}: a meaningful indication (below 40) of the quality of fit to the EXAFS data in *k*-space)

	Neighbour	***N***	***R* / Å**	**$2\sigma^2$ / Å^2**	**E_f / eV**	**R_{exafs}**
In air	Ni – O	0.44 ± 0.30	2.08 ± 0.06	0.014 ± 0.022	0.52	21.14
	Ni – Ni	7.89 ± 0.23	2.48 ± 0.03	0.011 ± 0.0004		
	Ni – Ni	12.71 ± 1.82	4.34 ± 0.01	0.019 ± 0.003		
	Ni – Pt	6.11 ± 1.86	4.02 ± 0.02	0.014 ± 0.004		
In H_2	Ni – Ni	7.31 ± 0.22	2.48 ± 0.003	0.011 ± 0.0004	0.47	20.42
	Ni – Ni	10.93 ± 1.5	4.35 ± 0.011	0.017 ± 0.003		
	Ni – Pt	6.82 ± 1.6	4.01 ± 0.015	0.012 ± 0.003		

Table 5.9 Best EXAFS fit parameters of 1.0PtNi/C (750 °C) electrocatalysts in air and H_2, respectively (*N*: coordination numbers, *R*: distance from the Ni absorber, $2\sigma^2$: Debye-Waller factor, E_f: energy shift and R_{exafs}: a meaningful indication (below 40) of the quality of fit to the EXAFS data in *k*-space)

	Neighbour	***N***	***R* / Å**	**$2\sigma^2$ / Å^2**	**E_f / eV**	**R_{exafs}**
In air	Ni – Ni	7.30 ± 0.22	2.48 ± 0.004	0.010 ± 0.0004	0.82	20.81
	Ni – Ni	13.9 ± 2.07	4.35 ± 0.013	0.020 ± 0.003		
	Ni – Pt	6.21 ± 1.48	4.01 ± 0.015	0.011 ± 0.002		
In H_2	Ni – Ni	7.20 ± 0.23	2.48 ± 0.004	0.011 ± 0.0005	–0.55	21.85
	Ni – Ni	16.69 ± 2.31	4.35 ± 0.01	0.022 ± 0.003		
	Ni – Pt	7.17 ± 1.78	4.01 ± 0.02	0.013 ± 0.003		

Table 5.10 Best EXAFS fit parameters of 1.0PtNi/C (900 °C) electrocatalysts in air and H_2, respectively (*N*: coordination numbers, *R*:distance from the Ni absorber, $2\sigma^2$: Debye-Waller factor, E_f: energy shift and R_{exafs}: a meaningful indication (below 40) of the quality of fit to the EXAFS data in *k*-space)

	Neighbour	***N***	***R* / Å**	**$2\sigma^2$ / Å^2**	**E_f / eV**	**R_{exafs}**
In air	Ni – O	1.21 ± 0.13	2.02 ± 0.009	0.012 ± 0.002	0.18	25.53
	Ni – Ni	1.67 ± 0.15	2.52 ± 0.008	0.018 ± 0.001		
	Ni – Pt	3.33 ± 0.23	2.69 ± 0.006	0.015 ± 0.001		
	Ni – Pt	2.12 ± 0.64	4.76 ± 0.016	0.011 ± 0.003		
In H_2	Ni – O	0.42 ± 0.20	2.01 ± 0.04	0.018 ± 0.012	0.61	29.90
	Ni – Ni	2.11 ± 0.24	2.51 ± 0.01	0.023 ± 0.002		
	Ni – Pt	4.22 ± 0.26	2.68 ± 0.01	0.016 ± 0.001		
	Ni – Pt	0.73 ± 0.33	3.99 ± 0.02	0.009 ± 0.003		

5.2.3.3 0.5PtCr/C(T) electrocatalysts

EXAFS spectra and Fourier transforms (both experimental and theoretical) of the Cr K-edge in the samples of 0.5PtCr/C(T) electrocatalysts (T = 750, 800 and 900 °C) in air and in H_2 are shown in Figures 5.25 – 5.27. The results obtained from the analyses of these data are presented in Tables 5.11 – 5.13.

The coordination number of oxygen is 1-3 at a distance of 1.95 – 1.98 Å, similar to the 0.5PtCr/C(200 °C) electrocatalyst, suggesting that part of the Cr is present on the surface as a Cr_2O_3-type species for all the 0.5PtCr/C(T) electrocatalysts.

The EXAFS data of 0.5PtCr/C(750 °C) electrocatalysts in air and in H_2 are similar to that of 0.5PtCr/C(200 °C) electrocatalysts in air and in H_2, apart from the loss of the short Cr–Cr distance in the air sample. The high Pt coordination number around Cr in the reduced sample indicates that the Cr is diffusing into the bulk Pt. It would seem that

Cr_2O_3, Cr and a Pt/Cr bulk alloy (possibly Pt_3Cr) are present on the 0.5PtCr/C(750 °C) electrocatalysts in air and in H_2.

The coordination number of Cr–O, Cr–Cr and Cr–Pt in the 0.5PtCr/C(800 °C) electrocatalyst in air was similar to that in 0.5PtCr/C(750°C) in hydrogen, but not 0.5PtCr/C(750 °C) in air. The result suggested that the Pt/Cr bulk alloy on 0.5PtCr/C electrocatalyst was more stable in air after heat treatment at higher temperature (800 °C). A significant change is seen however for the 0.5PtCr(800 °C) in H_2 and both 0.5PtCr(900 °C) samples: there is a dramatic decrease in the number of Pt neighbours at a distance of 2.61 Å, and a new Cr–Pt bond of 3.35 Å also appeared, suggesting a change in the Pt/Cr bulk alloy in this sample. The new Cr–Pt bond at a distance of 3.35 Å and the overall decrease in coordination number suggests the possible segregation of Cr from bulk alloy towards the surface at the higher temperatures.

Table 5.11 Best EXAFS fit parameters of 0.5PtCr/C (750°C) electrocatalysts in air and H_2, respectively (N: coordination numbers, R:distance from the Ni absorber, $2\sigma^2$: Debye-Waller factor, E_f: energy shift and R_{exafs}: a meaningful indication (below 40) of the quality of fit to the EXAFS data in k-space)

	Neighbour	***N***	***R* / Å**	**$2\sigma^2$ / Å^2**	**E_f / eV**	**R_{exafs}**
In air	Cr – O	1.80 ± 0.17	1.95 ± 0.01	0.006 ± 0.002	3.92	39.28
	Cr – Pt	3.74 ± 0.49	2.56 ± 0.01	0.020 ± 0.002		
	Cr – Cr	1.41 ± 0.66	3.93 ± 1.61	0.004 ± 0.005		
In H_2	Cr – O	3.16 ± 0.32	1.93 ± 0.01	0.012 ± 0.002	10.60	32.65
	Cr – Cr	1.22 ± 0.34	2.32 ± 0.02	0.016 ± 0.004		
	Cr – Pt	10.13 ± 1.59	2.55 ± 0.01	0.030 ± 0.002		

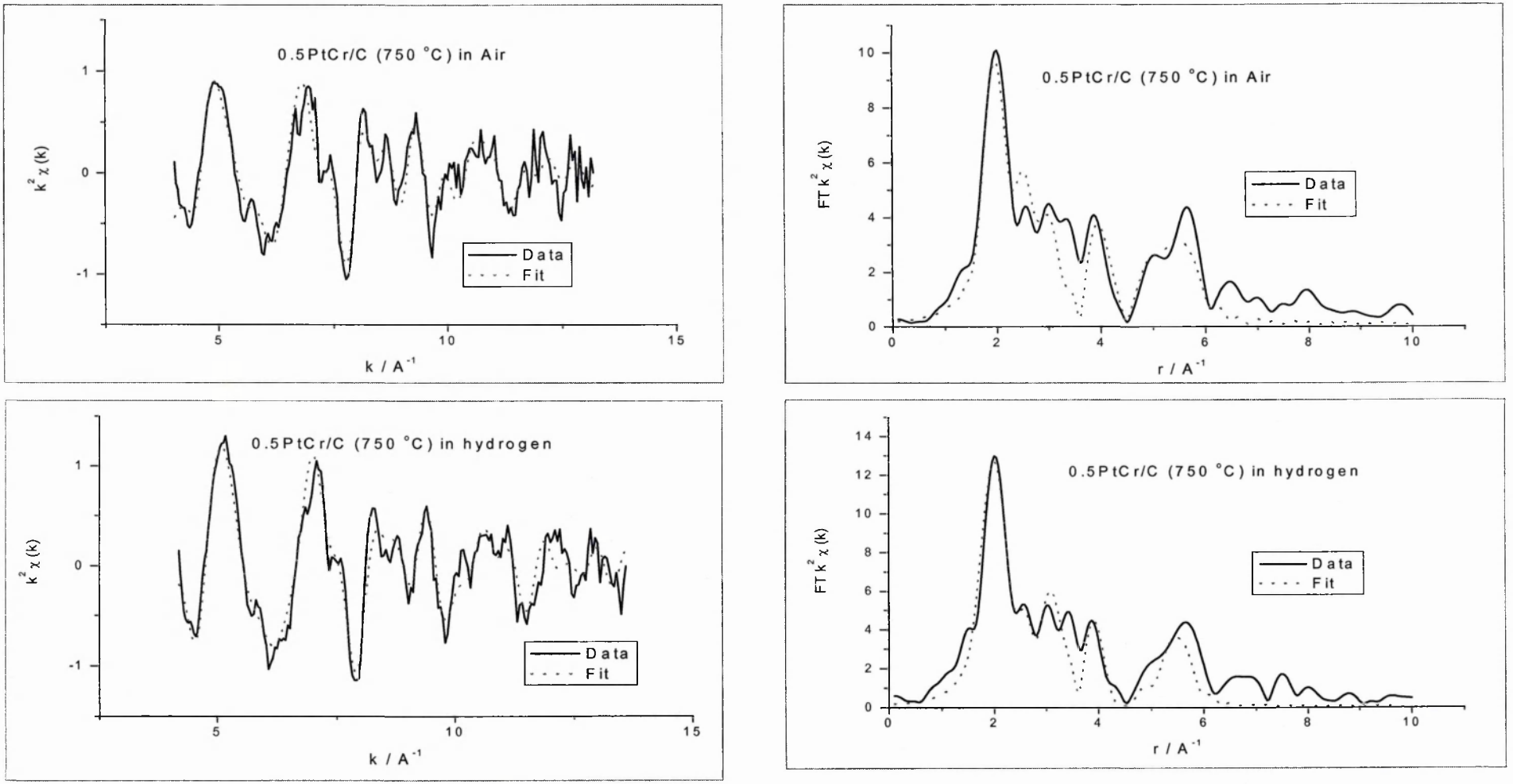

Figure 5.25 EXAFS k^2 weighted $x(k)$ spectra and k^2 weighted Fourier transforms of the Cr K-edge of 0.5PtCr/C(750°C) electrocatalysts in air and H_2, respectively. (solid line = data, dot line = fit)

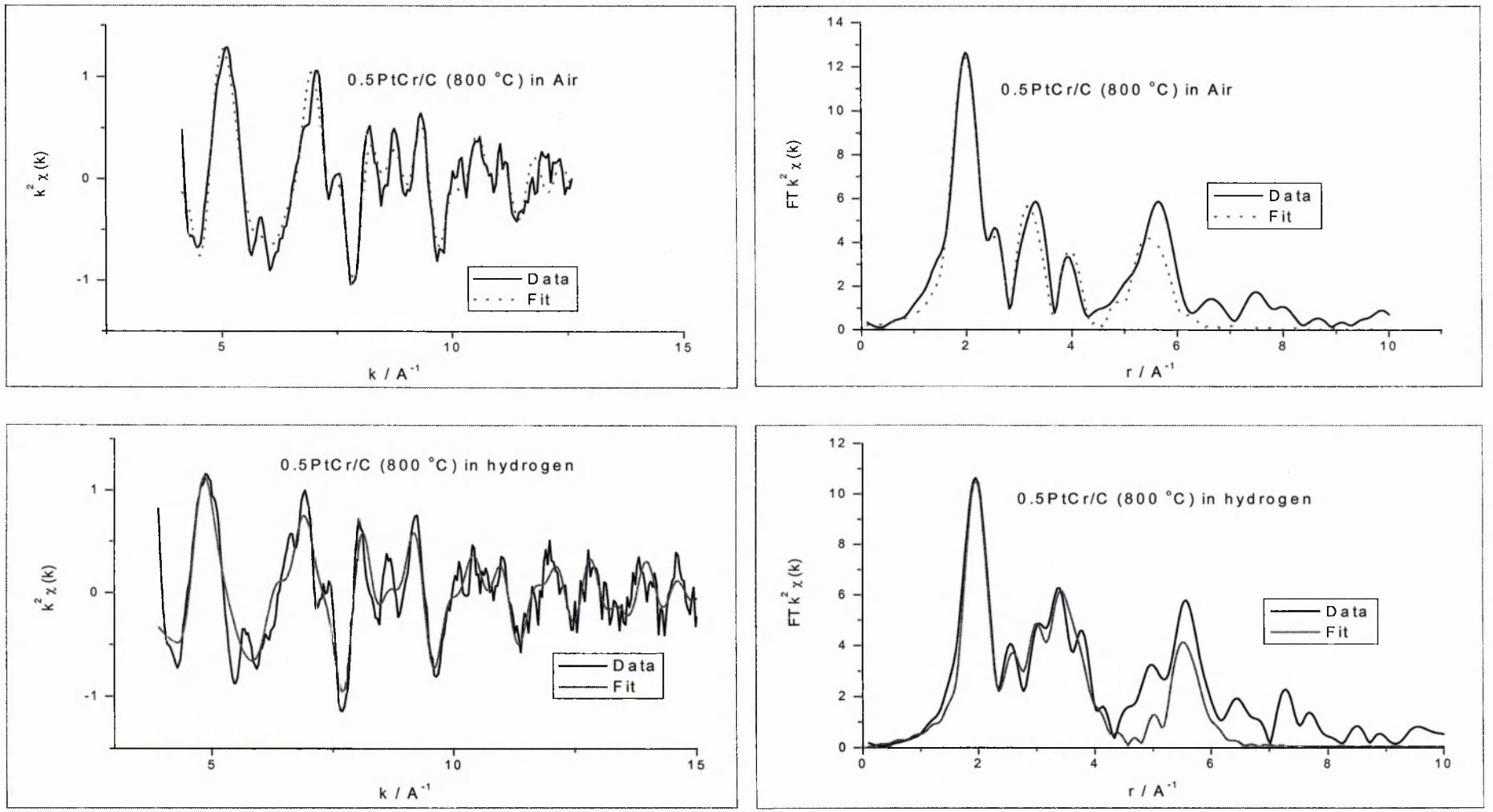

Figure 5.26 EXAFS k^2 weighted $x(k)$ spectra and k^2 weighted Fourier transforms of the Cr K-edge of 0.5PtCr/C(800 °C) electrocatalysts in air and H_2, respectively. (solid line = data, dot line = fit)

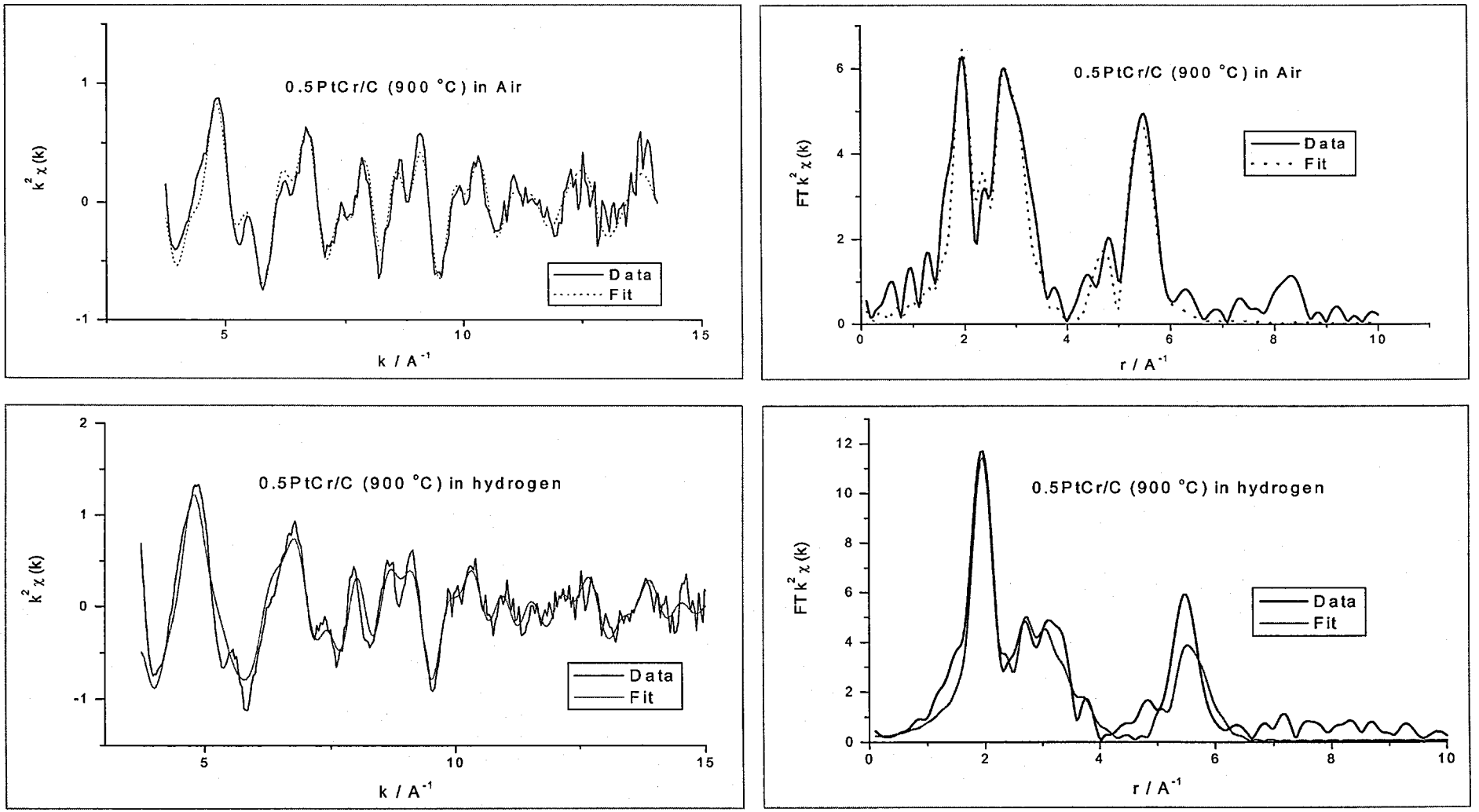

Figure 5.27 EXAFS k^2 weighted $x(k)$ spectra and k^2 weighted Fourier transforms of the Cr K-edge of 0.5PtCr/C(900 °C) electrocatalysts in air and H_2, respectively. (solid line = data, dot line = fit)

Table 5.12 Best EXAFS fit parameters of 0.5PtCr/C(800 °C) electrocatalysts in air and H_2, respectively (*N*: coordination numbers, *R*:distance from the Ni absorber, $2\sigma^2$: Debye-Waller factor, E_f: energy shift and R_{exafs}: a meaningful indication (below 40) of the quality of fit to the EXAFS data in *k*-space)

	Neighbour	***N***	***R* / Å**	**$2\sigma^2$ / Å^2**	**E_f / eV**	**R_{exafs}**
in air	Cr – O	3.02 ± 0.31	1.95 ± 0.01	0.034 ± 0.003	8.88	33.98
	Cr – Cr	1.66 ± 0.45	2.34 ± 0.01	0.021 ± 0.004		
	Cr – Pt	11.07 ± 2.10	2.59 ± 0.01	0.034 ± 0.003		
in H_2	Cr – O	2.08 ± 0.19	1.96 ± 0.009	0.005 ± 0.002	2.34	45.39
	Cr – Cr	0.26 ± 0.16	2.33 ± 0.033	0.007 ± 0.007		
	Cr – Pt	3.63 ± 0.61	2.61 ± 0.012	0.021 ± 0.002		
	Cr – Pt	4.16 ± 0.64	3.35 ± 0.011	0.013 ± 0.002		

Table 5.13 Best EXAFS fit parameters of 0.5PtCr/C(900 °C) electrocatalysts in air and H_2, respectively (*N*: coordination numbers, *R*:distance from the Ni absorber, $2\sigma^2$: Debye-Waller factor, E_f: energy shift and R_{exafs}: a meaningful indication (below 40) of the quality of fit to the EXAFS data in *k*-space)

	Neighbour	***N***	***R* / Å**	**$2\sigma^2$ / Å^2**	**E_f / eV**	**R_{exafs}**
in air	Cr – O	1.07 ± 0.10	1.99 ± 0.003	0.004 ± 0.002	–6.19	36.42
	Cr – Pt	2.31 ± 0.21	2.70 ± 0.007	0.012 ± 0.001		
	Cr – Cr	1.58 ± 0.58	4.72 ± 0.028	0.011 ± 0.006		
in H_2	Cr – O	2.33 ± 0.19	1.98 ± 0.009	0.005 ± 0.001	–2.46	39.56
	Cr – Cr	0.53 ± 0.29	2.41 ± 0.05	0.027 ± 0.013		
	Cr – Pt	3.23 ± 0.45	2.69 ± 0.010	0.016 ± 0.002		
	Cr – Pt	1.75 ± 0.63	3.39 ± 0.02	0.014 ± 0.004		

5.3 Conclusions

The preparation and physical characterization of the PtM/C(T) bimetallic catalysts were discussed.

i) The results of X-ray diffraction showed a shift in the Pt lattice peak consistent with the formation of the Pt_3Fe alloy on PtFe/C (T) after heat treatment at 700°C. A similar shift in the heat-treated Pt/Cr catalysts at 750°C is evidence for the formation of a Pt/Cr alloy. However, no evidence for the formation either a Pt/Co alloy on PtCo/C(T) or a Pt/Ni alloy on PtNi/C(T) was found using the XRD technique.

ii) TEM images showed that the particle size of Pt and second metal increased as heat treatment increased. The PtCo/C(T), PtFe/C(T) and PtCr/C(T) catalysts show less sintering, whereas sintering was severe for the PtNi/C(T) catalysts.

iii) EXAFS data verified the formation of the Pt_3Fe alloy on PtFe/C(T), and gave evidence of alloy formation for the PtCr/C(T) and PtNi/C(T) catalysts.

5.4 References

1. M. Watanabe, K. Tsurumi, T. Mizukami, T. Nakamura and P. Stonehart, J. Electrochem. Soc., 1994. **141**: p. 2659.
2. W. Roh, J. Cho and J.A.E. H. Kim, J. Appl. Electrochem., 1996. **26**: p. 623.
3. K.T. Kim, J.T. Hwang, Y.G. Kim and J.S. Chung, J. Electrochem. Soc., 1993. **140**: p. 31.
4. B.C. Beard and P.N. Ross Jr., J. Electrochem. Soc., 1990. **137**: p. 3368.
5. S. Mukerjee and S. Srinivasan, J. Electroanal. Chem., 1993. **201**: p. 357.
6. M.T. Paffet, G.J. Beery and S. Gottesfeld, J. Electrochem. Soc., 1998. **135**: p. 1431.
7. M. Neergat, A.K. Shukla and K.S. Gandhi, J. Appl. Electrochem., 2001. **31**: p. 373.
8. G. Thamizhmani and G.A. Capuano, J. Electrochem. Soc., 1994. **141**: p. 968.
9. Powder Diffraction Files (Inorganic Volumes), *4-802.* JCPDS International Center for Diffraction Data, USA.
10. Powder Diffraction Files (Inorganic Volumes), *29-1423.* JCPDS International Center for Diffraction Data, USA.
11. Powder Diffraction Files (Inorganic Volumes), *29-499.* JCPDS International Center for Diffraction Data, USA.
12. Powder Diffraction Files (Inorganic Volumes), *34-1080.* JCPDS International Center for Diffraction Data, USA.
13. Powder Diffraction Files (Inorganic Volumes), *5-727.* JCPDS International Center for Diffraction Data, USA.
14. Powder Diffraction Files (Inorganic Volumes), *3-1051.* JCPDS International Center for Diffraction Data, USA.

15. Powder Diffraction Files (Inorganic Volumes), *6-694.* JCPDS International Center for Diffraction Data, USA.

16. Powder Diffraction Files (Inorganic Volumes), *6-696.* JCPDS International Center for Diffraction Data, USA.

17. J.T. Hwang and J.S. Chung, Electrochim. Acta, 1993. **38**: p. 18.

18. D.A.Landsman and F.J.Luczak, U.S. Patent 4,316,944, 1982.

19. F.J.Luczak and D.A.Landsman, U.S. Patent 4,47,506, 1984.

20. F.J.Luczak and D.A.Landsman, U.S. Patent 4,677,092, 1987.

21. J.T. Hwang and J.S. Chung, Electrochim. Acta, 1993. **38**: p. 2715.

22. G. TamizhMani, J.P.Dodelet, D.Guay and L.Dignard-Bailey, J. Electroanal. Chem., 1998. **444**: p. 121.

23. E. M. Crabb, R. Marshall and D. Thompsett, J. Electrochem. Soc., 2000. **147**: p. 4440.

24. E.M. Crabb and Robert Marshall, Appl. Catal. A: Gen., 2001. **217**: p. 41.

25. E.M. Crabb, M.K. Ravikumar, Y.Qian, A.E. Russell, S. Maniguet, J. Yao, D. Thompsett, M. Hurford and S.C. Ball, Electrochemical and Solid-State Letters, 2002. **5**: p. 5.

26. E. M. Crabb and M.K. Ravikumar, Electrochimica Acta, 2001. **46**: p. 1033.

27. B. D. Cullity, Elements of X-ray diffraction, Second Edition, Addision-Wesley Publishing Company, 1978.

28. P. Stonehart, J. Appl. Electrochem., 1992. **22**: p. 995.

29. M. Min, J. Cho, K. Cho and H. Kim, Electrochim. Acta, 2000. **45**: p. 4211.

30. *http://www.cds.dl.ac.uk/cgi-bin/icsd/icsd.cgi [Accessed 9 October 2003].*

31. H.H.C.M. Pinxt, B.F.M. Kuster, D.C.Koningsberger and G.B. Marin, Catalysis Today, 1998. **39**: p. 351.

32. S.R de Miguel, O.A.Scelza, M.C.Roman-Martinez, C.Salinas-Martinze de Lecea, D.Cazorla-Amoros and A.Linares-Solano, Appl. Catal. A: General, 1998. **170**: p. 93.

33. M.C.Roman-Martinez, D.Cazorla-Amoros, A.Linares-Solano, C.Salinas-Martinze de Lecea, H. Yamashita and M. Anpo, Carbon, 1995. **33**: p. 3.

Chapter 6 Catalytic evaluation of the carbon supported Pt-based bimetallic PtM/C(T) catalysts after heat treatment, and optimization of the catalysts.

The CO cyclic voltammograms and the catalyst evaluation for the oxygen reduction reaction of the heat-treated Pt-based bimetallic electrocatalysts, PtM/C(T), will be presented and discussed in this chapter. The method of electrode preparation for the PtM/C(T) electrocatalysts was the same as that of the 'as-prepared' carbon supported Pt-based bimetallic catalysts described in Chapter 2 and Chapter 4.

The electrode Pt surface area (EPSA) of the PtM/C(T) electrocatalysts is discussed in section 6.1. Section 6.2 describes the oxygen reduction reaction (ORR) of the PtM/C(T) electrocatalysts. Optimization electrocatalysts for oxygen reduction reaction are investigated and described in section 6.3.

6.1 CO stripping voltammetry

Figures 6.1 – 6.5 show some typical CO stripping voltammograms for various Pt/C, 0.5PtFe/C, 1.0PtNi/C, 0.5PtCo/C and 0.5PtCr electrocatalysts in 1.0 M H_2SO_4 at 80 °C. The onset of oxidation of the CO, the position of the CO peak, CO area, EPSA and ECA for each of these electrocatalysts are listed in Table 6.1.

The CO stripping voltammograms of the three Pt/C electrocatalysts with different heat treatment temperatures, show in all cases that the onset of the CO oxidation current always commenced at 0.56 ± 0.02 V and CO stripping peak maximum was at 0.65 ± 0.02 V. The fact that there was no significant difference in the onset of the CO oxidation current and the position of CO stripping peak for the three Pt/C electrocatalysts suggests that these two electrochemical properties were not affected by the temperature of the heat treatment.

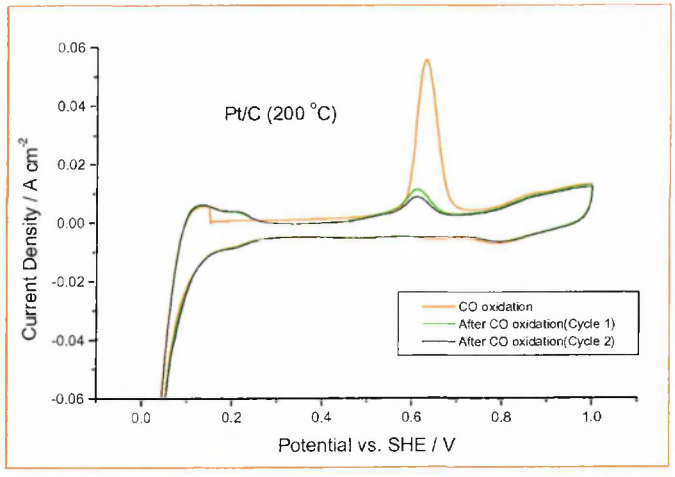

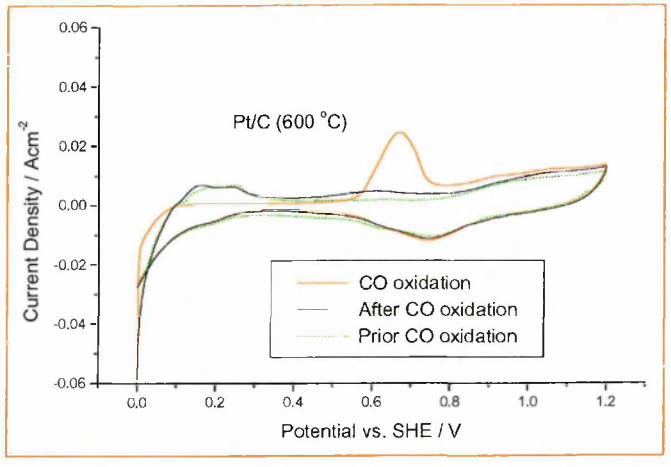

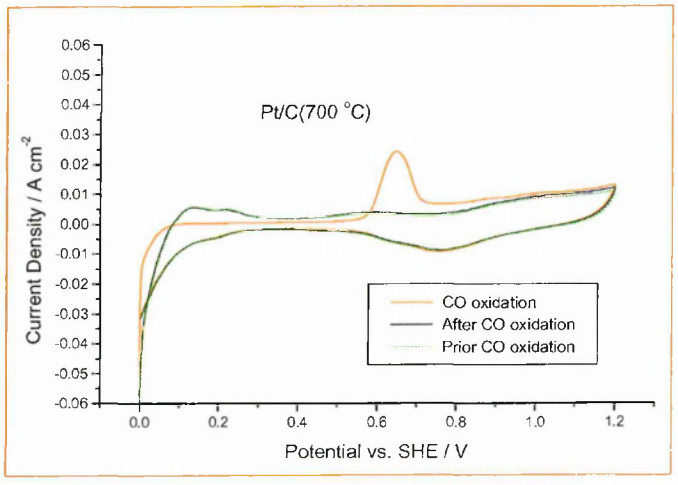

Figure 6.1 CO stripping voltammograms for different Pt/C electrocatalysts in 1.0 M H_2SO_4 at 80 °C

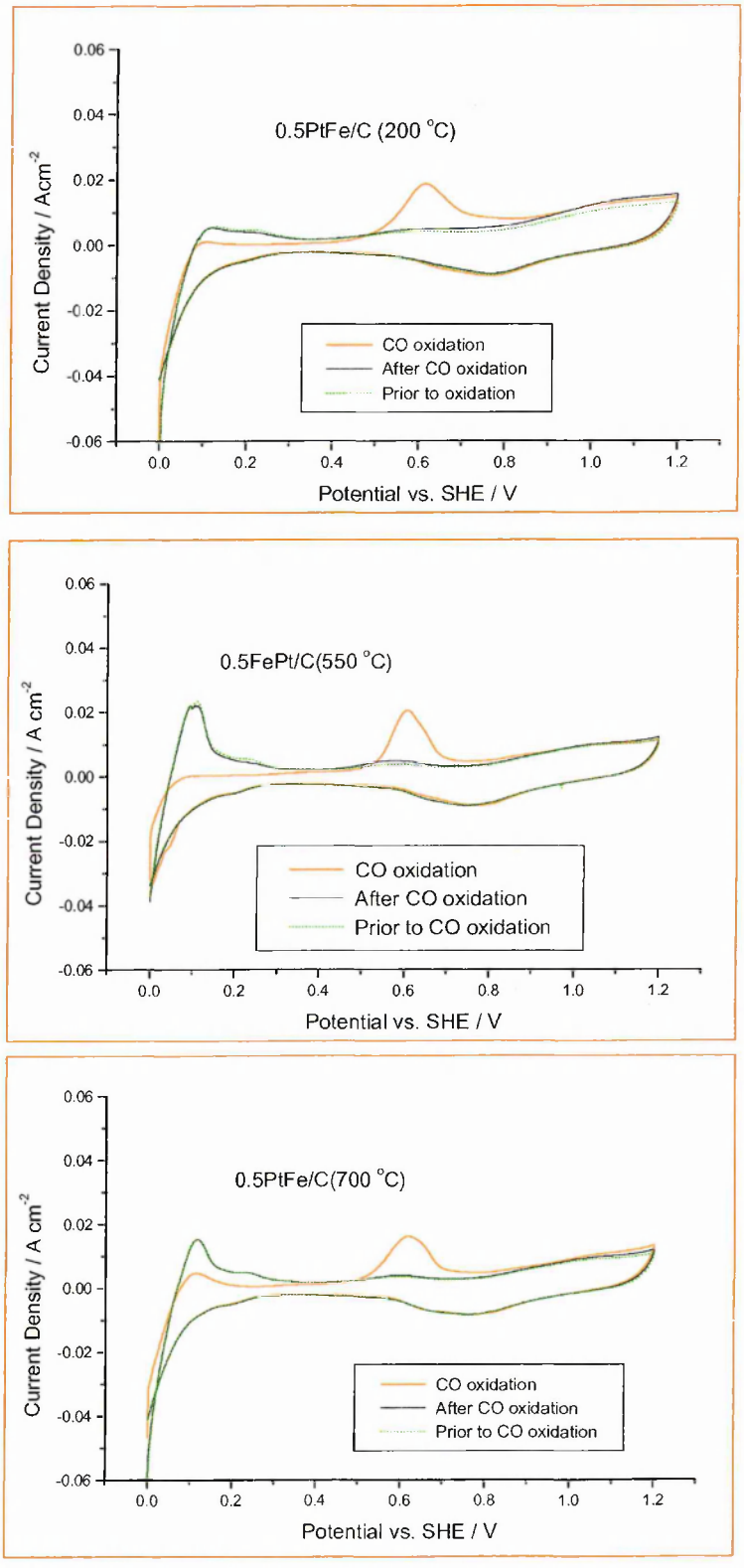

Figure 6.2 CO stripping voltammograms for different 0.5PtFe/C electrocatalysts in 1.0 M H_2SO_4 at 80 °C

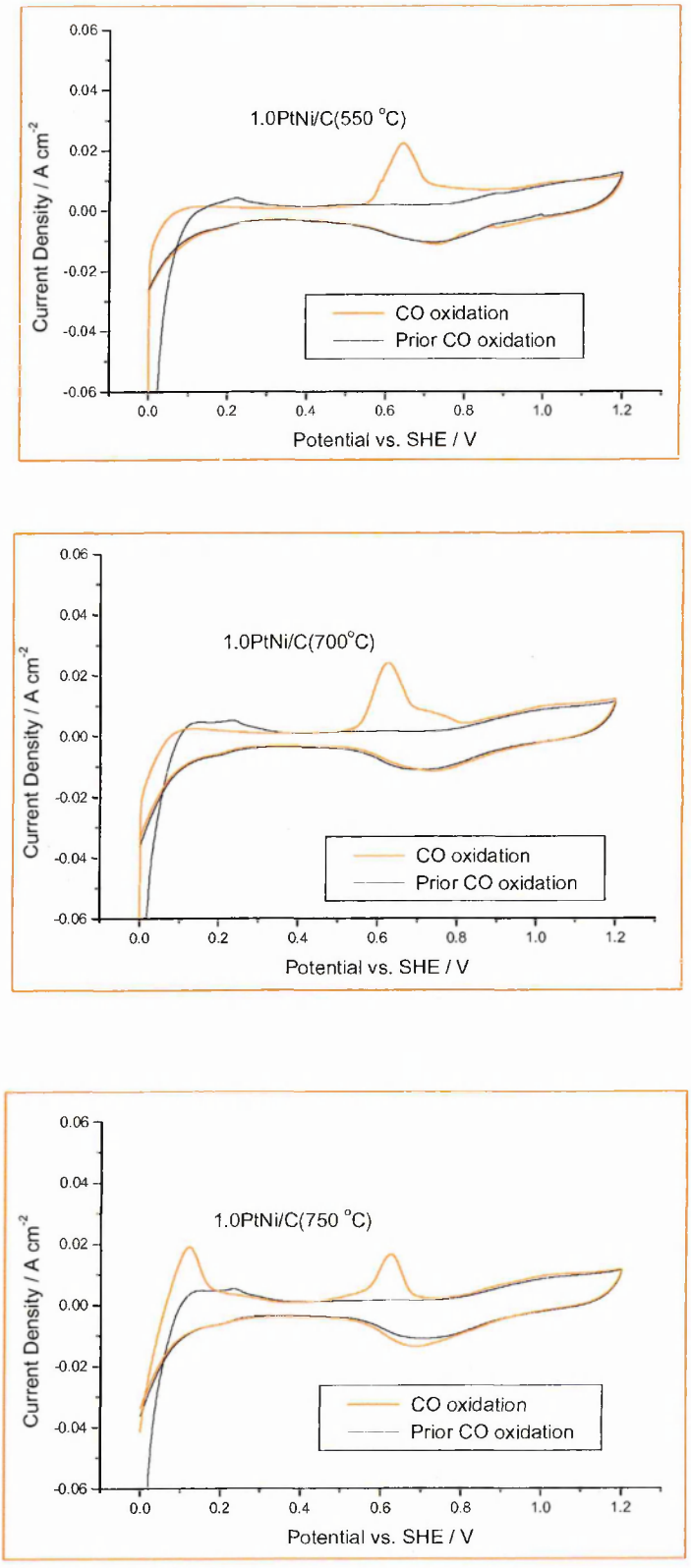

Figure 6.3 CO stripping voltammograms for different 1.0PtNi/C electrocatalysts in 1.0 M H_2SO_4 at 80 °C

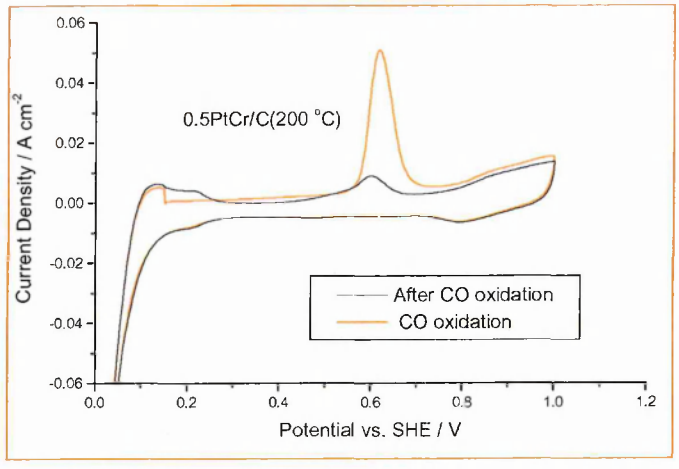

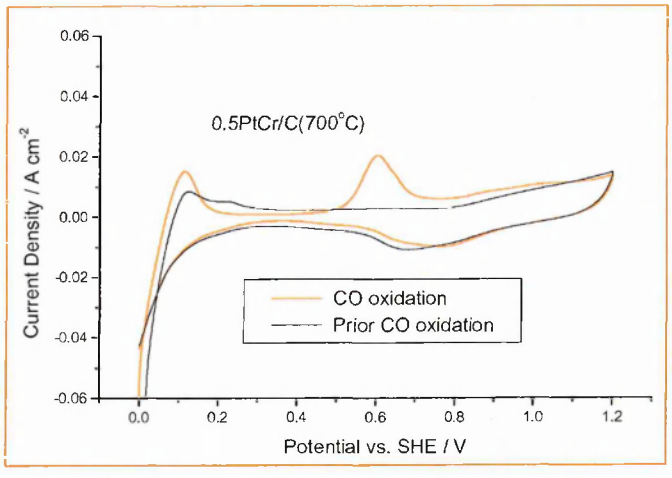

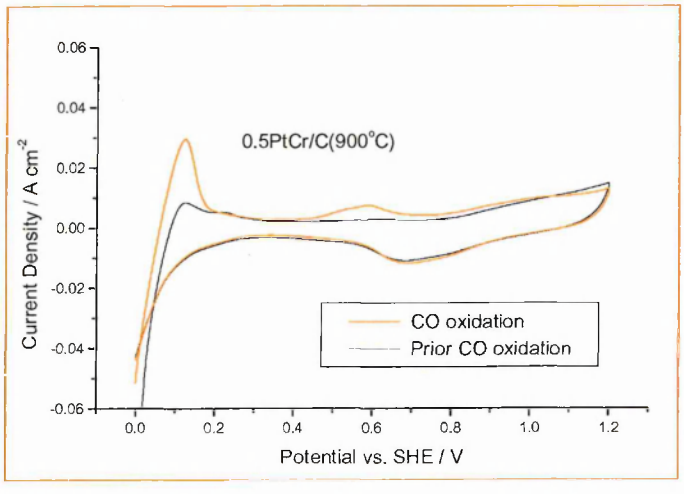

Figure 6.4 CO stripping voltammograms for different 0.5PtCr/C electrocatalysts in 1.0 M H_2SO_4 at 80 °C

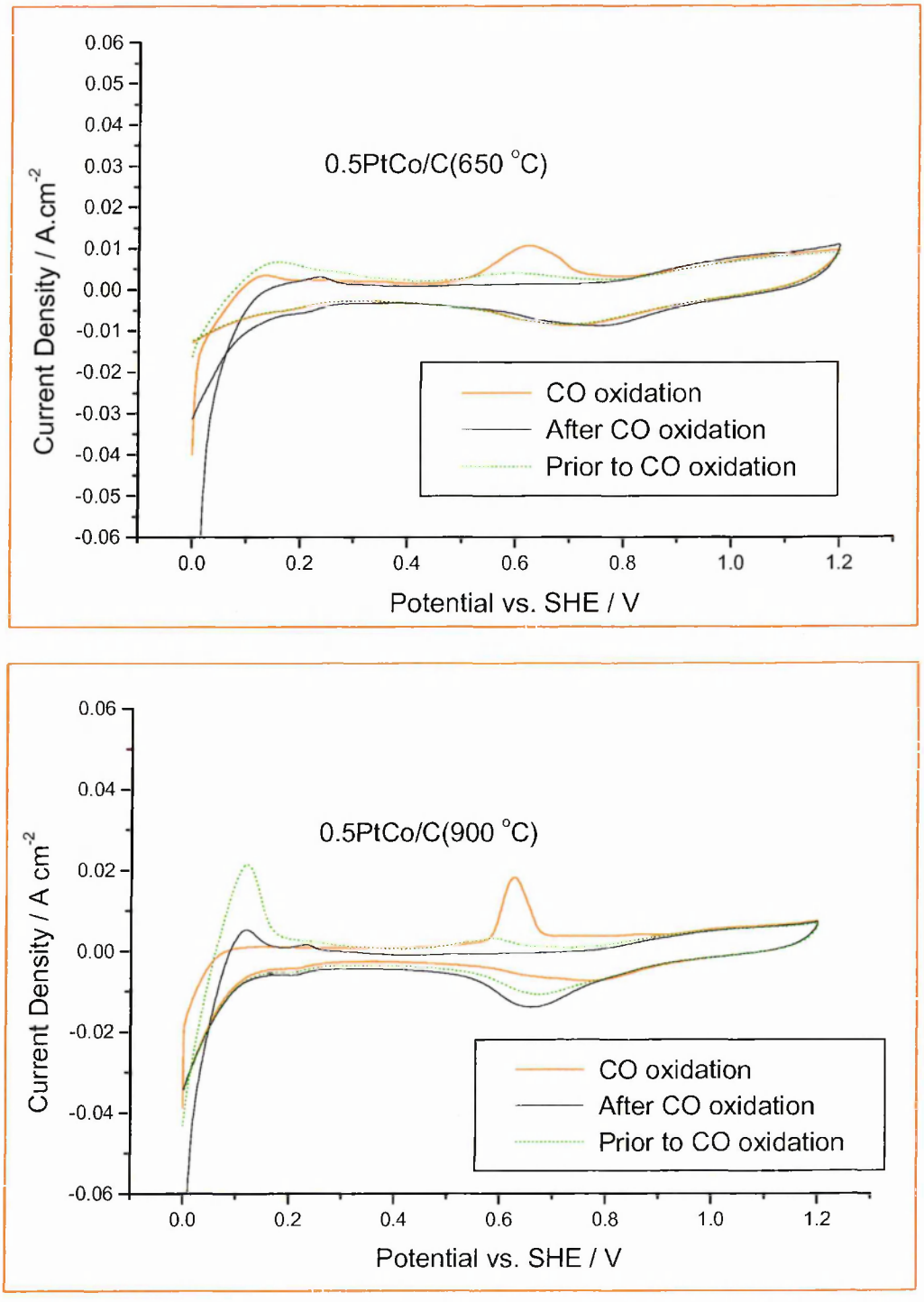

Figure 6.5 CO stripping voltammograms for different 0.5PtCo/C electrocatalysts in 1.0 M H_2SO_4 at 80 °C

The EPSA of the Pt/C electrocatalyst decreased as heat treatment temperature increased, indicating that heat treatment caused sintering of the metal particles with a loss of surface area.

When the second metal was added to the Pt/C electrocatalyst, the average onset of the CO oxidation current corresponding to the CO stripping peak began at lower potentials for PtM/C bimetallic and PtM/C(T) electrocatalysts compared to Pt/C electrocatalyst, but for the heat-treated samples was always within ±0.03 V of the potential for the 'as-prepared' samples, and therefore not significantly different. Similarly, the CO stripping peak on PtM/C bimetallic and PtM/C(T) was shifted about 0.05 V lower than the Pt/C electrocatalyst. No attempt was made to determine why the onset of the CO oxidation current and the position of CO stripping peak for PtM/C bimetallic and PtM/C(T) electrocatalysts had a negative shift compared to Pt/C electrocatalysts, however, it is likely that this negative shift on PtM/C bimetallic and PtM/C(T) electrocatalysts can be attributed to the presence of the second metal. The similarity of both the onset of the CO oxidation current and the position of CO stripping peak for PtM/C bimetallic and PtM/C(T) electrocatalysts at different heat treatment temperature strongly suggested that again these two chemical properties were controlled by platinum and the second metal, but was not relevant to the temperature of the heat treatment, and hence the particle size.

As for the monometallic catalyst, the EPSA of the PtM/C(T) catalysts decreased in each series as the heat treatment temperature increased. The PtCr series appeared to be the most stable, with surface areas close to that of the monometallic sample at each temperature. The EPSA for the PtCo/C(T) system were significantly lower after heat treatment at 650 °C, changing little beyond that point. The PtCr/C(JM), from Johnson Matthey Technology Center, was prepared using different preparation method.

Table 6.1 Electrochemical properties of electrocatalysts

Electrocatalyst	Onset potential/V	Peak position/V	CO Area /mC cm^{-2}	EPSA /cm^{-2} Pt	ECA /m^2 g^{-1} Pt
Pt/C	0.57	0.65	306	728	104
Pt/C(600°C)	0.56	0.66	219	521	74.1
Pt/C(700°C)	0.56	0.65	188	447	63.6
0.5PtFe/C(200°C)	0.50	0.61	186	442	62.9
0.5PtFe/C(400°C)	0.50	0.61	181	430	61.2
0.5PtFe/C(550°C)	0.51	0.60	162	385	54.8
0.5PtFe/C(700°C)	0.49	0.61	146	347	49.4
0.5PtFe/C(750°C)	0.50	0.59	122	290	41.2
0.5PtFe/C(900°C)	0.50	0.60	97.5	232	33.2
1.0PtNi/C(200°C)	0.52	0.62	210	501	71.3
1.0PtNi/C(550°C)	0.49	0.62	189	450	64.0
1.0PtNi/C(600°C)	0.47	0.61	186	443	63.0
1.0PtNi/C(700°C)	0.51	0.62	204	486	69.0
1.0PtNi/C(750°C)	0.48	0.62	174	414	58.9
1.0PtNi/C(800°C)	0.47	0.61	128	305	43.3
0.5PtCo/C(200°C)	0.48	0.62	215	511	80.0
0.5PtCo/C(650°C)	0.47	0.62	113	269	38.3
0.5PtCo/C(700°C)	0.45	0.63	120	285	40.6
0.5PtCo/C(750°C)	0.46	0.62	98	233	33.2
0.5PtCo/C(900°C)	0.45	0.59	94	223	31.8
0.5PtCr/C(200°C)	0.50	0.61	290	691	98.2
0.5PtCr/C(400°C)	0.50	0.60	282	672	95.5
0.5PtCr/C(500°C)	0.51	0.60	246	586	83.2
0.5PtCr/C(600°C)	0.50	0.59	214	510	72.4
0.5PtCr/C(700°C)	0.48	0.60	192	457	65.0
0.5PtCr/C(750°C)	0.49	0.59	188	448	63.6
0.5PtCr/C(800°C)	0.49	0.59	171	407	57.9
0.5PtCr/C(900°C)	0.48	0.58	105	250	35.5
PtCr/C(JM)	0.48	0.62	165	393	55.8

6.2 The oxygen-reduction reaction

Of the performance controlling components in a PEM fuel cell, the cathode is recognized to be one of the most influential components. The oxygen reduction reaction (ORR) occurs at the cathode:

$$O_2 + 4H^+ + 4e^- \rightarrow 2H_2O \qquad (6.1)$$

The half reaction at the cathode can only occur at a high rate in the presence of a catalyst. The reaction of one O_2 molecule at the cathode is a 4-electron reduction process which occurs in a multi-step sequence. So far, Pt based electrocatalysts seem to be the best catalysts, capable of generating high rates of O_2 reduction at the low temperature at which PEM fuel cells operate. Unfortunately the reaction mechanism on the Pt is not clear.

To improve the efficiency of PEM fuel cells operating at low temperature, the electrocatalysts of the oxygen reduction reaction have been widely studied due to the fact that the rate of the O_2 reduction half reaction is more than 100 times slower than the H_2 oxidation half reaction [1-9].

The work in chapter 4 has suggested that there is an opportunity to develop more active cathode electrocatalysts for ORR. Here, the electrocatalytic activity of the various Pt/C, 0.5PtFe/C, 1.0PtNi/C, 0.5PtCo/C and 0.5PtCr/C electrocatalysts was investigated in order to find the best electrocatalyst for ORR.

To evaluate the electrocatalytic activity of the Pt/C, 0.5PtFe/C, 1.0PtNi/C, 0.5PtCo/C and 0.5PtCr/C electrocatalysts for ORR, steady-state galvanostatic polarization measurements in 1M H_2SO_4 at 80 °C and 0.2 bar pure oxygen using Nafion electrodes were performed. Three analysis methods of the steady state galvanostatic

polarization data were made using Tafel plots, Specific Activity plots and Mass Activity plots [10-12].

6.2.1 Tafel plots

Figures 6.6 and 6.7 shows Tafel plots for the ORR on 0.5PtFe/C(T), 1.0PtNi/C(T), 0.5PtCo/C(T) and 0.5PtCr/C(T) electrocatalysts in comparison with that of pure Pt/C electrocatalyst. Variations in the Tafel slopes resulted from the influence of different adsorption and different rate-determining steps over the potential ranges investigated [12].

Most of the Tafel slopes for the ORR on the 0.5PtFe/C(T), 1.0PtNi/C(T), 0.5PtCo/C(T) and 0.5PtCr/C(T) electrocatalysts shown in Figure 6.4 and 6.5 were similar to that of pure Pt/C electrocatalyst, suggesting that the rate-determining step for the ORR on these electrocatalysts is the same as that of the monometallic Pt/C electrocatalyst. An enhancement in the activity is seen for some of the heat treated samples.

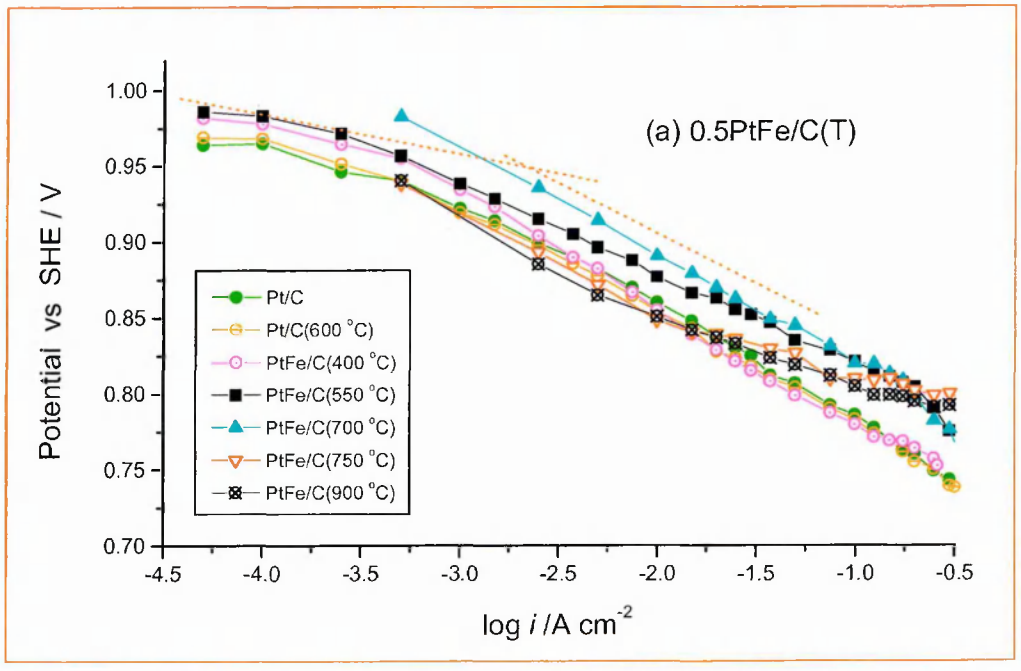

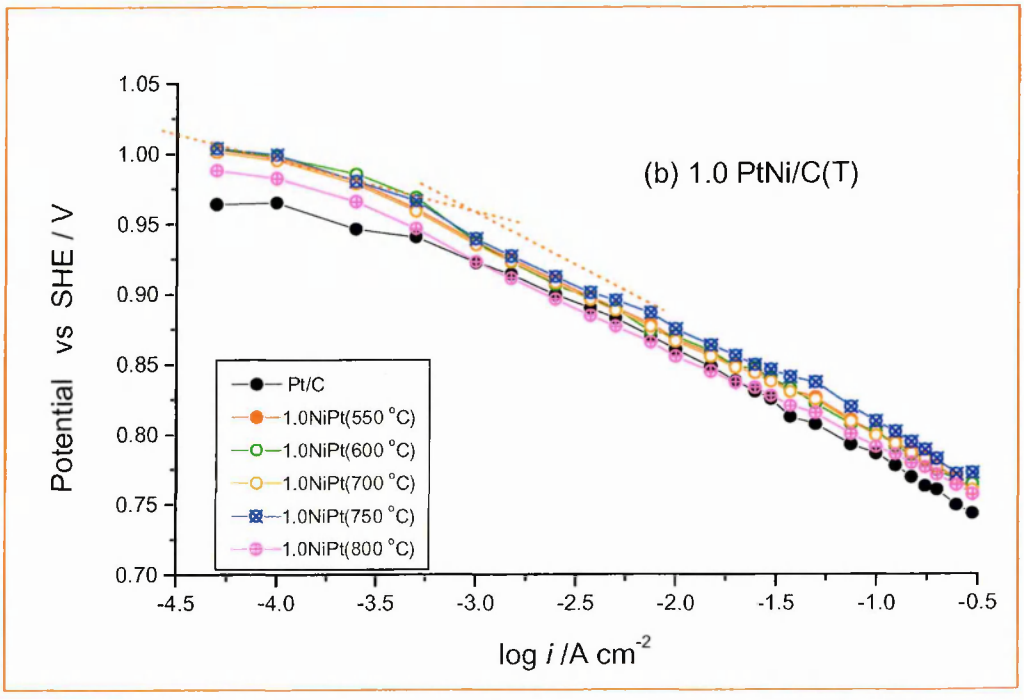

Figure 6.6 Tafel plots for the ORR on (a) 0.5PtFe/C, and (b) 1.0PtNi/C electrocatalysts

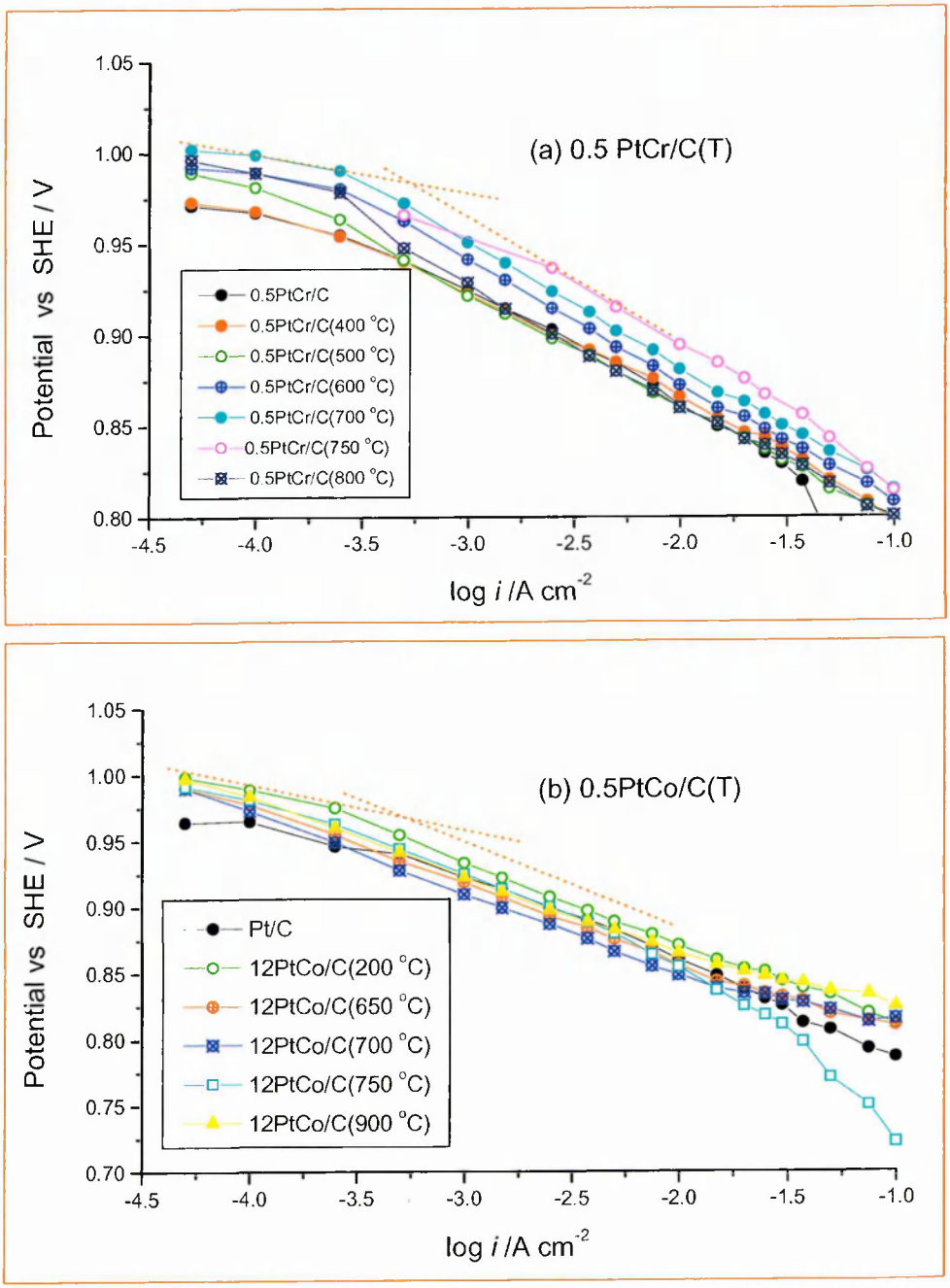

Figure 6.7 Tafel plots for the ORR on (a) 0.5PtCr/C and (b) 0.5PtCo/C electrocatalysts

6.2.2 Specific activity

A Specific Activity plot is the PEM fuel cell potential (corrected for cell resistance) *vs.* specific activity. Specific activities were calculated from the current, I, and the electrode Pt surface area (EPSA):

$$\text{Specific activity} = I/EPSA\ (mA \cdot cm^{-2}\ Pt) \qquad (6.2)$$

The specific activities compares the intrinsic activity of the Pt present in different catalysts in terms of current per unit area of electrochemically available Pt. Specific activity is especially meaningful for structure-sensitive reactions.

Specific activity for the ORR on 0.5PtFe/C(T), 1.0PtNi/C(T), 0.5PtCo/C(T) and 0.5PtCr/C(T) electrocatalysts are shown in Figures 6.8 - 6.11. The relationship between the heat-treatment temperature and the specific activity of pure Pt/C and PtM/C(T) electrocatalysts was studied. As the heat-treatment temperature increased and the EPSA decreased for certain electrocatalysts, the specific activities were different although their Pt loadings were same. This meant that the oxygen-reduction on the platinum surface of pure Pt/C or PtM/C(T) electrocatalysts was indeed a structure-sensitive reaction, otherwise the specific activity should be constant due to the fact that the Pt amount was same. The enhancement in the specific activity for ORR on these electrocatalysts compared to the pure Pt/C electrocatalyst suggested that the Pt structure was slightly changed by adding the second metal.

Figure 6.12 shows the relationship between the specific activity at 900 mV and heat treatment temperature for the 0.5PtFe/C(T), 1.0PtNi/C(T), 0.5PtCo/C(T) and 0.5PtCr/C(T) electrocatalysts. Kim et al. claimed that the specific activity generally increased as the EPSA decreased [5]. However, our studies showed that the specific activity maximized at a specific temperature for each catalyst, before decreasing again.

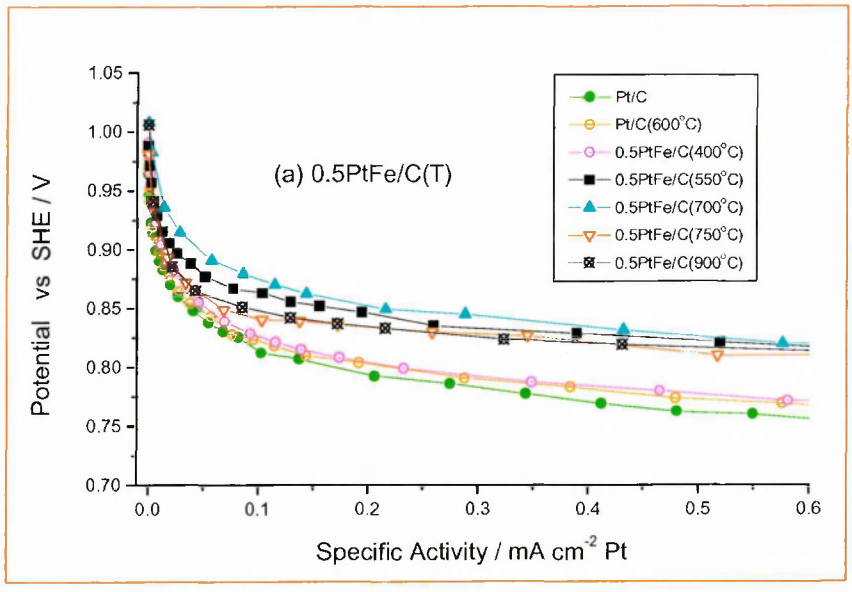

Figure 6.8 Specific activity for the ORR on 0.5PtFe/C

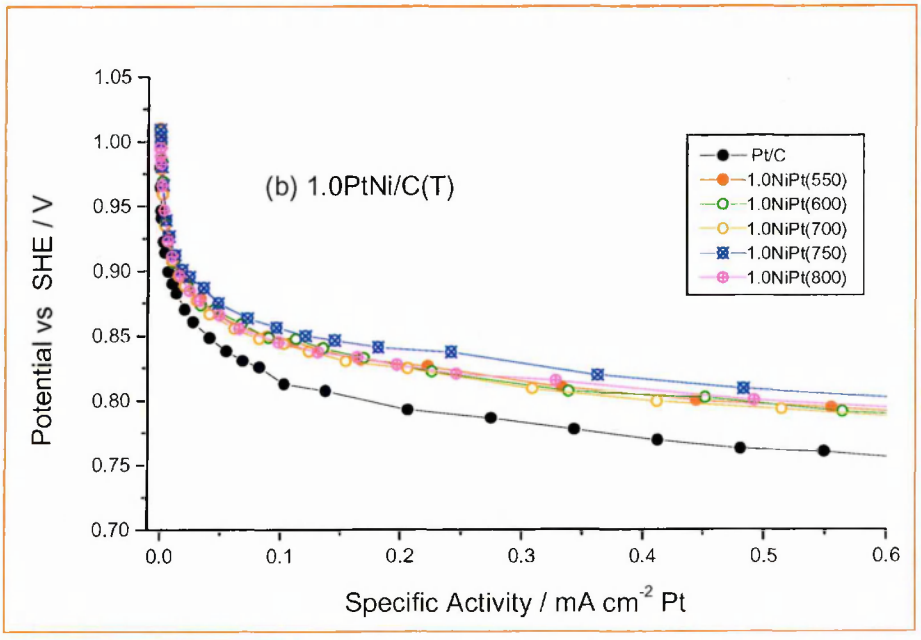

Figure 6.9 Specific activity for the ORR on 1.0PtNi/C

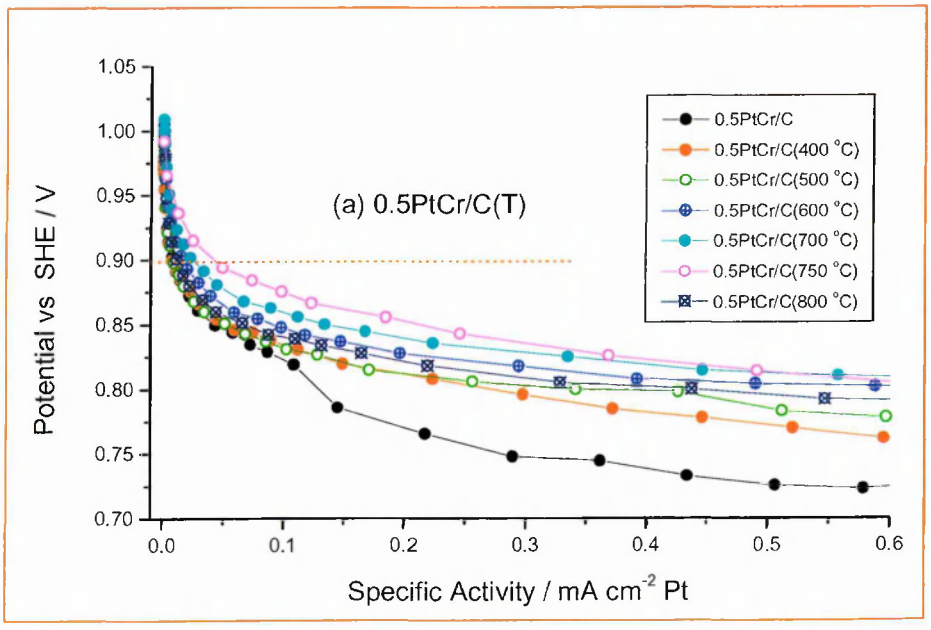

Figure 6.10 Specific activity for the ORR on 0.5PtCr/C

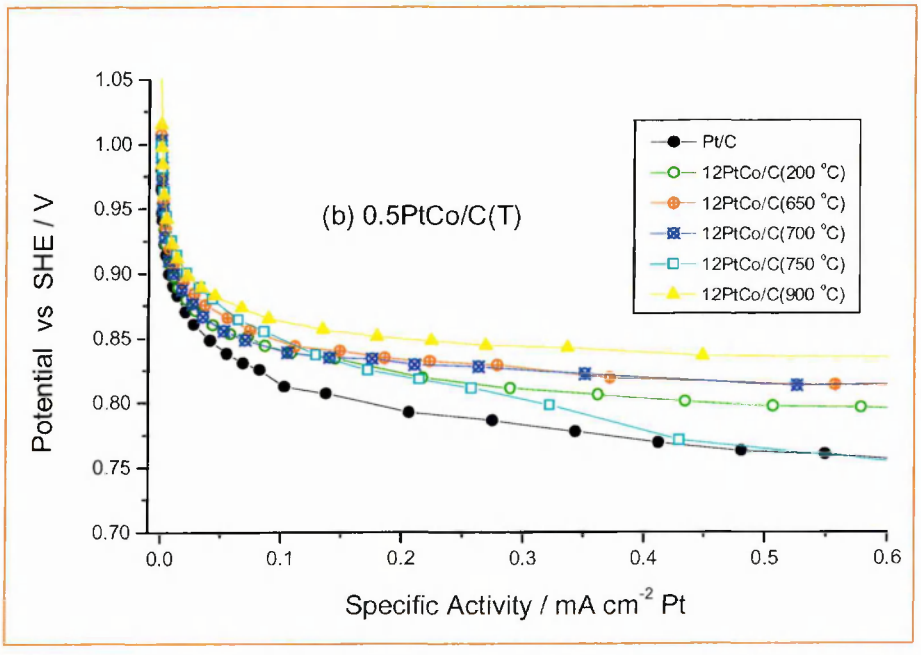

Figure 6.11 Specific activity for the ORR on 0.5PtCo/C

The maximum activity was found at 700 °C for Pt/Fe, and 750 °C for Pt/Cr, Pt/Ni and Pt/Co electrocatalysts. Large enhancements were seen for the Pt/Fe and Pt/Cr systems at these temperatures. This suggested that it is important to find the optimal heat treatment temperature for the formation of alloys on each electrocatalyst. The 0.5PtFe/C (700°C) and 0.5PtCr/C (750°C) were good electrocatalysts for ORR because their specific activities were high.

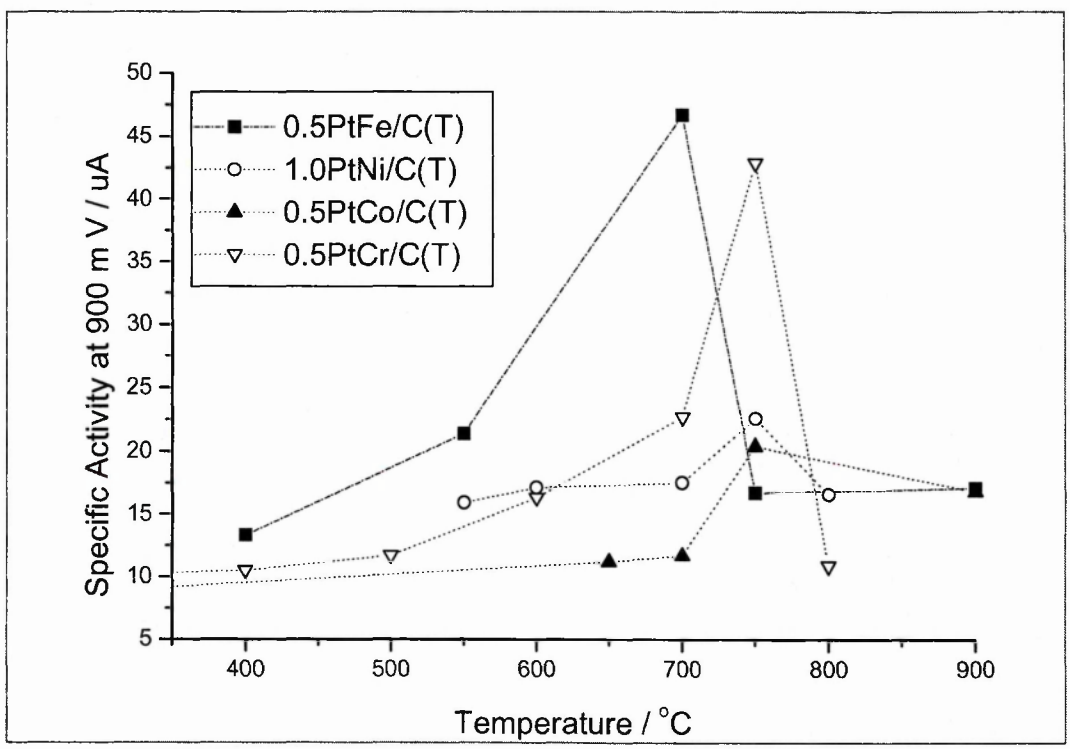

Figure 6.12 The relationship between the specific activity and the heat-treatment temperature

6.2.3 Mass activity

The Mass Activity plot is the PEM fuel cell potential *E,* (corrected for cell resistance) *vs.* mass activity. Mass activities were calculated from the current, I, and the electrode Pt loading:

Mass activity = I/Pt loading (A/g Pt) (6.3)

The electrode area and Pt loading in our experiments were 2.01 cm^2 and 0.35 mg/cm^2. Thus, the total Pt loading was 2.01 × 0.35 = 0.704 mg. So the Mass Activity plot

is *E vs. i*/0.704×10^{-3} A/g Pt. If the assumption is made that only Pt atoms on the surface of the Pt particles in the electrocatalysts take part in the ORR, the more sintered the catalyst, the bigger the particles and so less of the Pt is likely to be available on the surface for the ORR. The mass activity has a practical meaning in terms of PEM fuel cells because the cost of the electrode depends on the amount of platinum used, so companies that make MEA's and fuel cell stacks tend to consider metal loadings in terms of mass when considering the cost of fuel cells.

Figures 6.13 and 6.14 show the mass activity plots of ORR for the 0.5PtFe/C(T), 1.0PtNi/C(T), 0.5PtCo/C(T) and 0.5PtCr/C(T) electrocatalysts. The relationship between the mass activity at 900 mV and the heat-treatment temperature on these electrocatalysts is shown in Figure 6.15.

The mass activities of 1.0PtNi/C (T) and 0.5PtCo/C(T) electrocatalyst were 6.5 - 10.5 and 5.8 – 9.8 A/g at 900 mV, respectively. These were similar to that of the Pt/C electrocatalyst (7.1 A/g at 900 mV), which suggested that the 1.0PtNi/C(T) and 0.5PtCo/C(T) electrocatalysts were not significantly better electrocatalysts for the oxygen reduction reaction at the cathode for the PEM fuel cell. This would agree with characterisation results which show no evidence for PtM alloy formation for these systems.

The mass activities of the oxygen reduction reaction on the 0.5PtFe/C(T) and 0.5PtCr/C(T) showed higher mass activity at some of the heat treatment temperatures compared to the pure Pt/C electrocatalyst. According to Johnson Matthey Technology Centre's own data, the mass activity of ORR on monometallic Pt/C electrocatalyst was 5-10 A/g at 900 mV and that of good Pt-alloys was 15-30 A/g at 900 mV. The mass activities of 0.5PtFe/C(700°C) and 0.5PtCr/C(750°C) were 23.5 and 25.1 A/g at 900 mV, suggesting that the formation of Pt/Cr and Pt/Fe alloys at these temperatures on both

electrocatalysts, was beneficial for the oxygen-reduction reaction at the cathode of the PEM fuel cell. As the heat treatment temperature was increased to values greater than 700 °C for 0.5PtFe/C, and 750 °C(T) for 0.5PtCr/C(T), the mass activity was found to decrease again. When the heat-treatment temperature increased, the particle size of the electrocatalysts increased and thereby the dispersion was reduced; the increase in the metal particle size of the electrocatalysts, after heating to high temperature, is to the disadvantage of the oxygen reduction reaction.

Table 6.2 lists the best mass activities and specific activities of the 0.5PtFe/C(T), 1.0PtNi/C(T), 0.5PtCo/C(T) and 0.5PtCr/C(T) electrocatalysts. The order of mass activity for ORR on these tested electrocatalysts was: PtCr/C(T) ~ PtFe/C(T) > PtNi/C(T) ~ PtCo/C(T) ~ Pt/C. The best electrocatalyst was 0.5PtCr/C (750 °C) according to the mass activity.

Table 6.2 The best mass activity and specific activity at 900 mV on electrocatalysts

Electrocatalyst	**Mass Activity /A g^{-1}Pt**	**Specific Activity /μA cm^{-2}Pt**
20%Pt/C	7-8	10
(1.0)PtNi/C(T)-SOMC	10	23
(0.5)PtCo/C(T)-SOMC	12	20
(0.5)PtFe/C(T)-SOMC	23	47
(0.5)PtCr/C(T)-SOMC	25	43

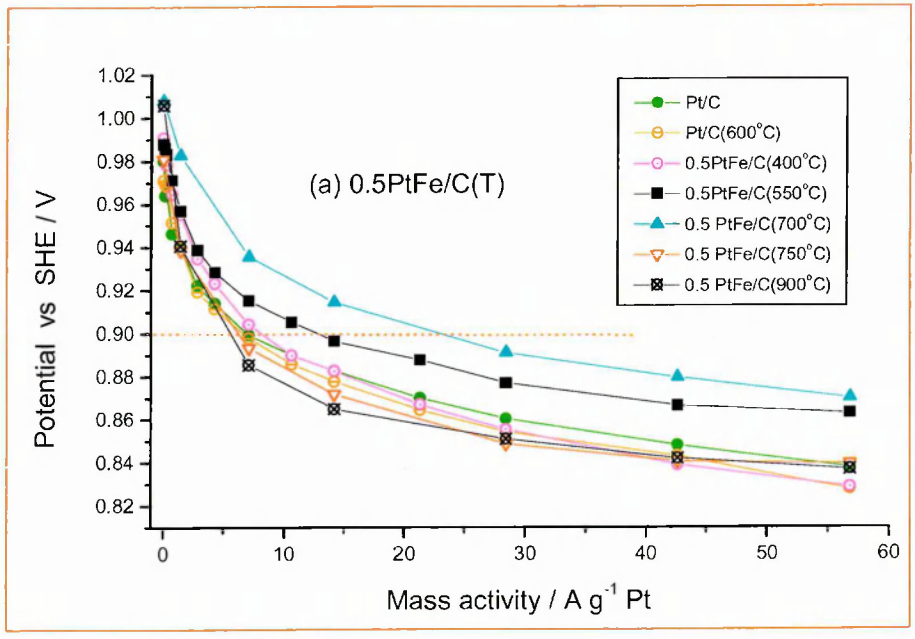

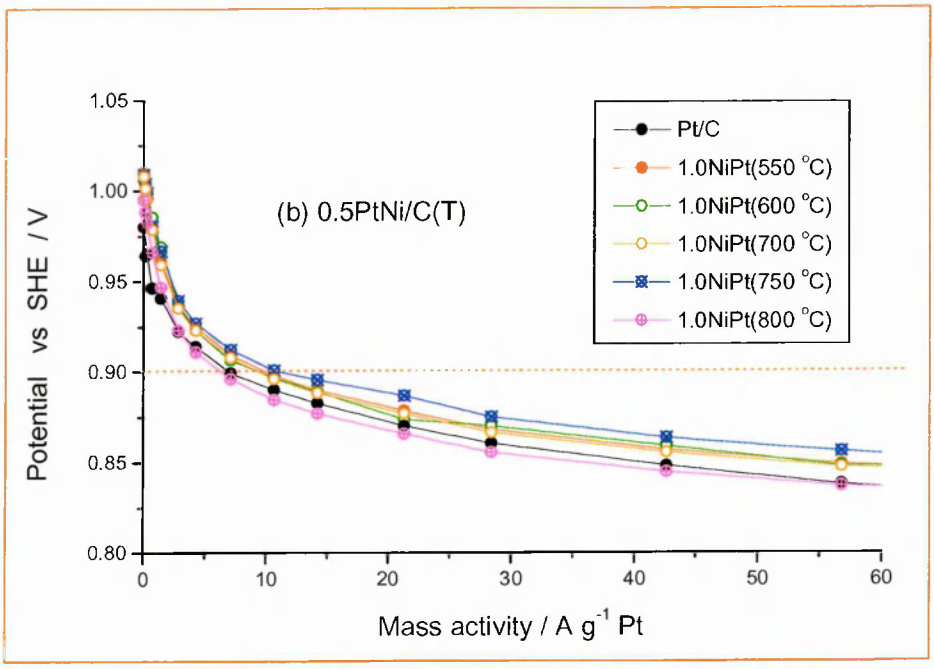

Figure 6.13 Mass activity for the ORR on (a) 0.5PtFe/C, and (b) 1.0PtNi/C electrocatalysts

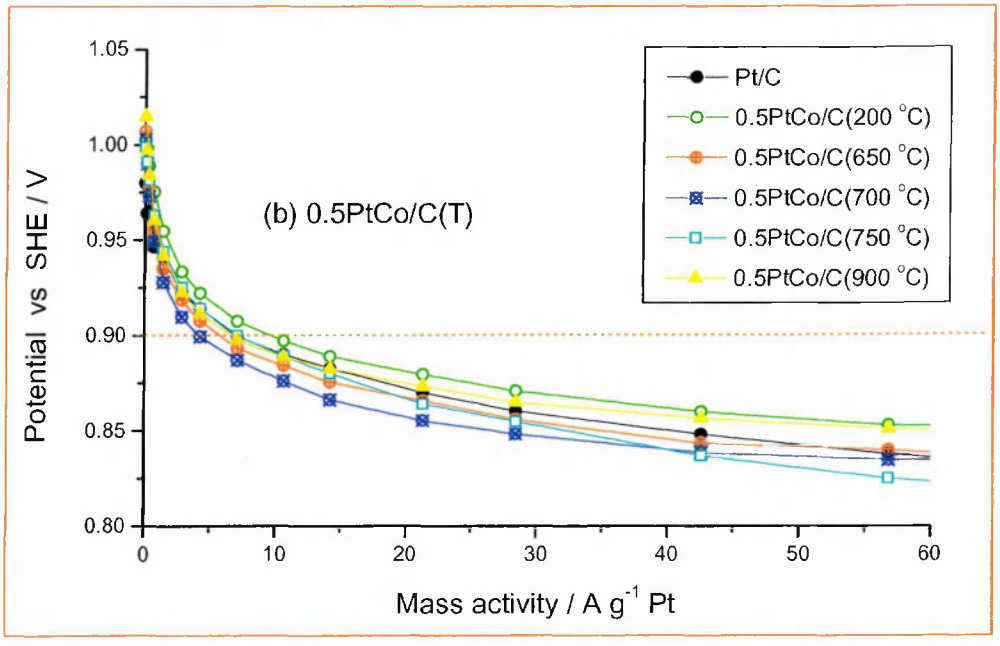

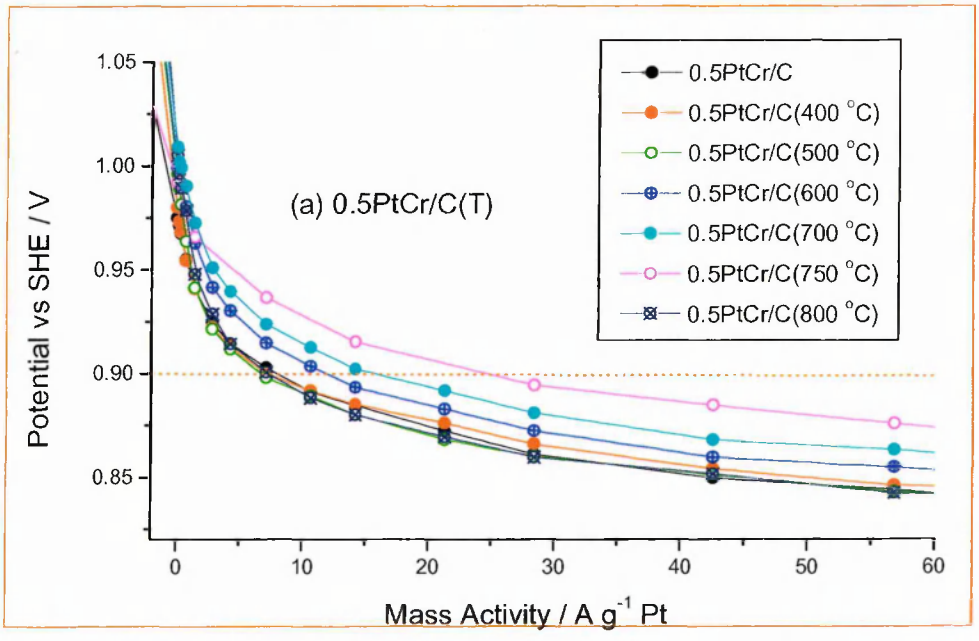

Figure 6.14 Mass activity for the ORR on (c) 0.5PtCo/C and (d) 0.5PtCr/C electrocatalysts

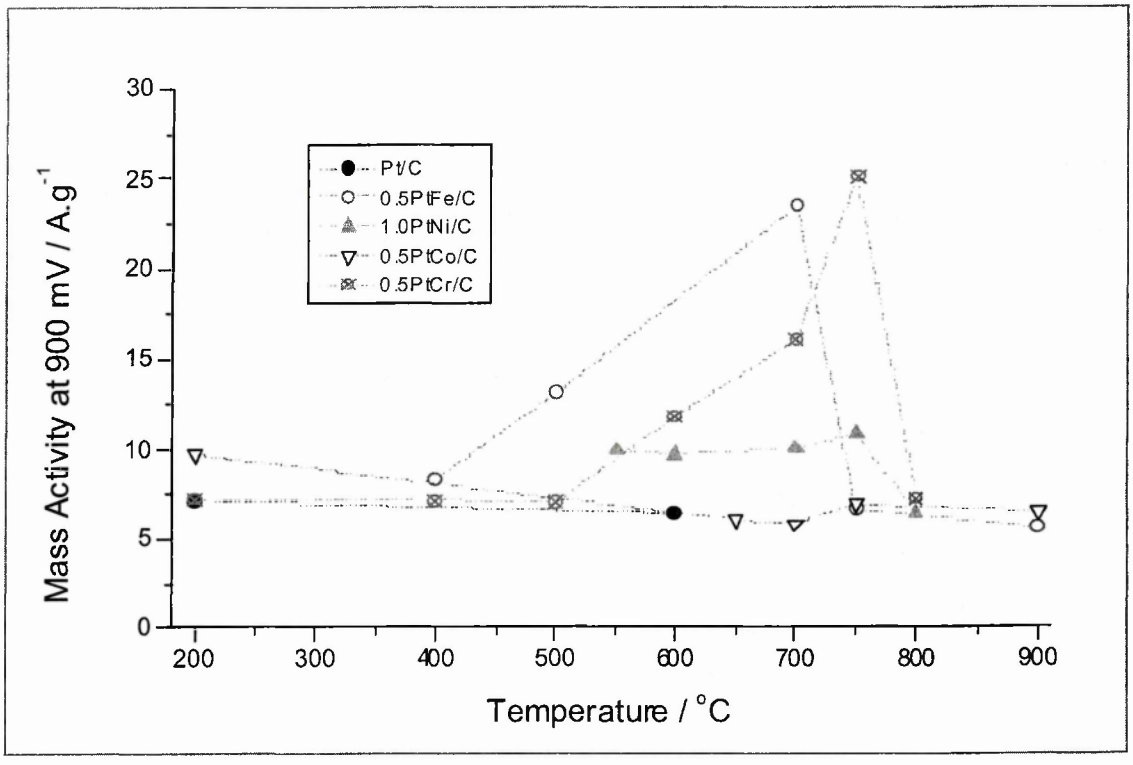

Figure 6.15 The relationship between the mass activity and heat treatment temperature

6.2.4 Discussion and further experiments

PtM/C alloy electrocatalysts, where M is usually a transition metal (e.g. Ti, Cr, V, Mn, Fe, Co, Ni, Cu, etc), have previously been shown to have enhanced electrocatalytic activities for the oxygen-reduction reaction at the cathode with respect to Pt/C alone [6-8]. Jalan and Taylor claimed that the increased Pt electrocatalytic activity of ORR observed for PtM/C was related to the shortening of the Pt–Pt interatomic distance [1], and this was supported by Appleby [4, 6] and Mukerjee [6]. However, Glass [2] found that the decreased lattice spacing of a Pt/Cr alloy was not correlated with an increase in ORR activity, and that activity enhancement was attributed to a highly dispersed Pt/Cr alloy rather than to the bulk Pt/Cr alloy. Toda et al [8] studied PtM (M = Fe, Co and Ni) electrocatalysts for ORR and found that maximum activity was observed at 30, 40 and 50% content of Ni, Co and Fe, respectively. They claimed that the enhancement of

activity for ORR was based on an increased d-electron vacancy of the thin Pt surface layer caused by the underlying alloy. As seen by these studies, the role of the second metal on PtM/C electrocatalysts for the ORR is elusive.

To summarize the work here briefly, four kinds of bimetallic electrocatalysts, 0.5PtFe/C(T), 1.0PtNi/C(T), 0.5PtCo/C(T) and 0.5PtCr/C(T), were prepared under different heat-treatment temperature conditions, and were characterized by electrocatalytic activity tests for ORR. According to the shift of onset potential from CO CV and the relationship between the EPSA and specific activity, the structure-sensitivity of pure Pt/C or PtM/C(T) electrocatalysts for the oxygen reduction reaction (ORR) was found. The study of mechanism using Tafel plot showed that (i) the same electrocatalytic mechanism for the ORR occurs on the monometallic Pt/C and PtM/C (T) electrocatalysts (ii) the first electron-transfer step was the rate-determining step for the oxygen reduction reaction at the cathode on the Pt/C and PtM/C(T) electrocatalysts. As the heat treatment temperature increased, the particle size increased and the surface area and EPSA decreased. XRD and EXAFS indicated that in most electrocatalysts, a Pt/M alloy was formed over 700 – 750°C. This may break down again at very high temperatures. Heat treating 0.5PtCr/C(T) and 0.5PtFe/C(T) electrocatalysts increased the electrocatalytic performance. Both mass activity and specific activity for the PtM/C(T) electrocatalysts showed an optimal heat treatment temperature. The 0.5PtCr/C(700°C) and 0.5PtFe/C(750°C) electrocatalysts showed significantly higher mass and specific activities than monometallic Pt/C electrocatalyst with the same Pt loading. Different ratios of the second metals perform differently and a ratio between 0.5 and 1.0 gives optimum results.

As stated previously the main aim of this research work is to find the best Pt-based alloy electrocatalysts and optimal preparation condition for oxygen reduction reaction. Accordingly, PtCr/C was found to be best electrocatalyst for ORR of the four

types studied, and in view of these results, we decided to try and optimize the best-performing Cr system, and a series of different ratio PtCr/C(750 ^{o}C) catalysts was made for further study. The optimal commercial electrocatalyst, PtCr/C(JM), from Johnson Matthey Technology Centre was also investigated.

6.3 Optimization of electrocatalysts for oxygen reduction reaction

6.3.1 Comparison of mass activity for different composition PtCr/C electrocatalysts

The mass activity of the 0.5PtCr/C(T) electrocatalysts increased with temperature and attained the highest value at 750 °C, decreasing thereafter with further increase of temperature. This temperature coincides with the detection of a Pt/Cr alloy formation (XRD and EXAFS). This suggests that the Pt/Cr alloy formation is beneficial to ORR at the cathode. However at high temperatures sintering occurs, the alloy may decompose, and activity decreases again. Thus the temperature of 750 °C was found to be the optimal heat-treatment for 0.5PtCr/C(T) electrocatalysts.

Figures 6.16 and 6.17 show the Tafel plot and mass activity plot for the Pt/C and PtCr/C(750 °C) electrocatalysts with different ratios (0.25, 0.5, 0.67, 0.75 and 1.00) of Cr/Pt. The relationship between the mass activity at 900 mV and the ratio of $Cr/Pt_{(S)}$ on PtCr/C electrocatalysts at the optimal temperature of 750 °C is shown in Figure 6.18. The Tafel plot suggested that the performance of the 0.5PtCr/C(750 °C) electrocatalyst was of the order of 10 – 30 mV higher than that of the monometallic Pt/C electrocatalyst. The mass activity plot indicated that the best Cr/Pt ratios for ORR were 0.5 - 0.67.

It seems likely from our evidence, that activity optimizes at 750 °C because a Pt/Cr alloy formed at this temperature. From all the ratios of $Cr/Pt_{(S)}$, the 0.67 PtCr/C(750 °C) electrocatalyst was found to exhibit the highest mass activity at 900 mV (26.2 A/g Pt). It was interesting that the 0.67 PtCr/C catalyst has a bulk atomic ratio Cr/Pt of 1:3 that expected for a Pt_3Cr alloy, which is similar to the known ordered crystalline Pt/Fe alloy, Pt_3Fe. If an assumption is made that all Pt and Cr formed a Pt_3Cr alloy on 0.67 PtCr/C(750 °C)

electrocatalyst, no superfluous Pt or Cr atoms would exist on the 0.67 PtCr/C(750°) electrocatalyst.

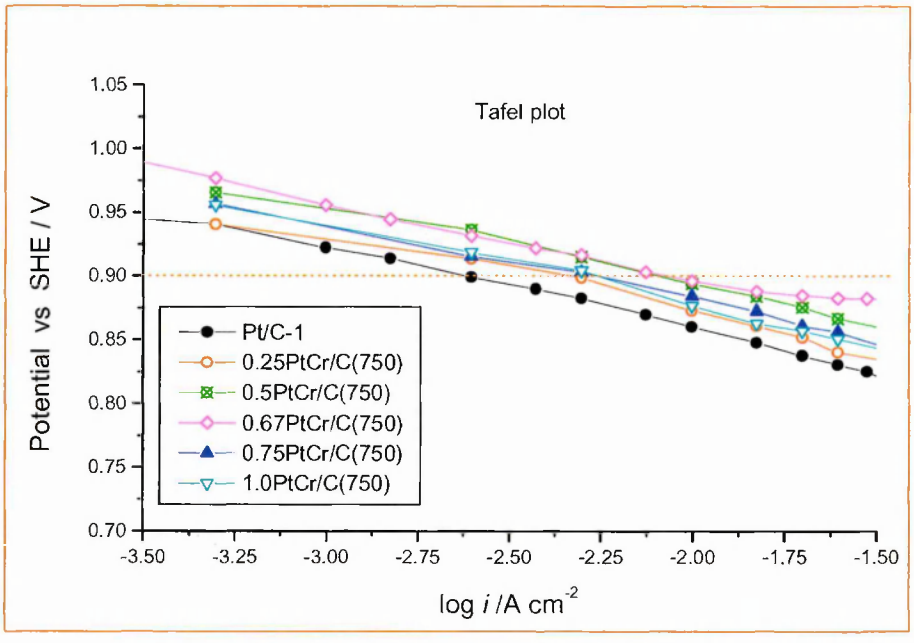

Figure 6.16 Tafel plots for the ORR for various composition PtCr/C electrocatalysts

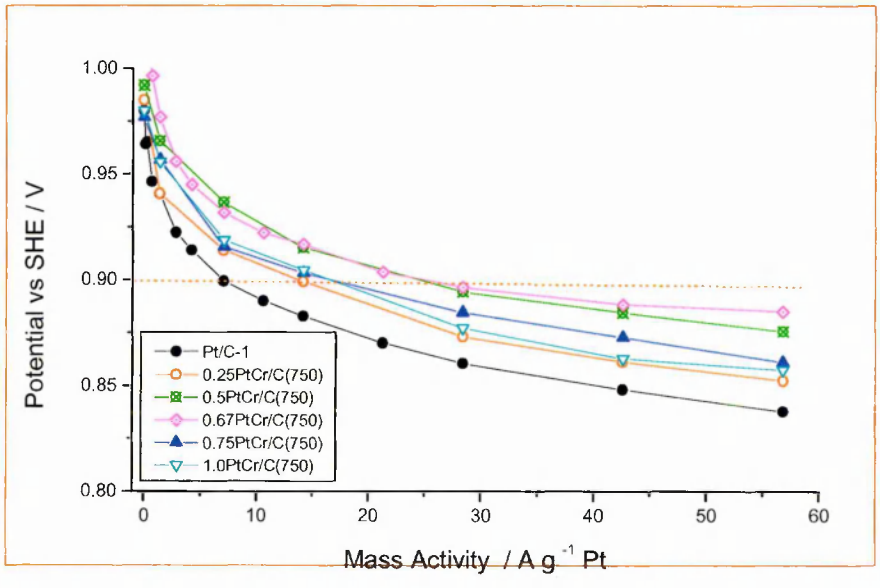

Figure 6.17 Mass activity for the ORR for various composition PtCr/C electrocatalysts

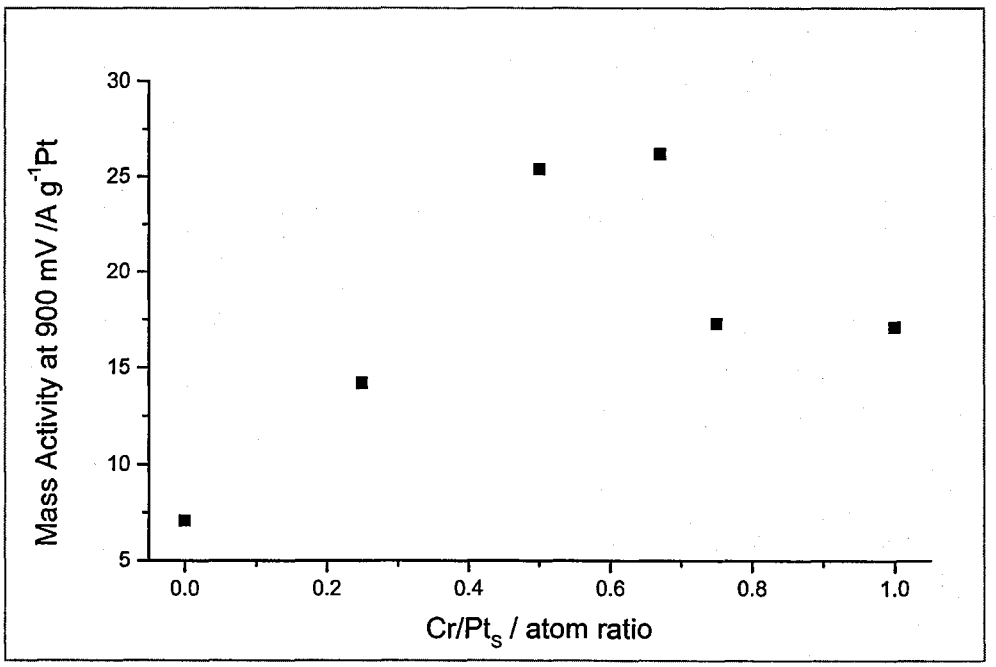

Figure 6.18 The relationship between the mass activity at 900 mV and the different ratios of $Cr/Pt_{(S)}$ on PtCr/C electrocatalysts at 750 °C

The 0.67 Cr/Pt ratio was thus chosen as the most promising to make the optimum catalyst, and further optimization temperature treatments were then carried out on this catalyst.

Figures 6.19 and 6.20 show the mass activity plots for ORR on 0.67PtCr/C(T) electrocatalysts with different heat-treatment temperatures, and the relationship between the mass activity at 900 mV and heat treatment temperature, respectively. Unlike the 0.5PtCr/C(T) electrocatalyst, the mass activity on 0.67PtCr/C(T) electrocatalysts remained high at 800 °C and 850 °C although the highest value of mass activity was still at 750 °C. This suggested that for ratios other than the optimum 0.67, as the heat-treatment temperature was increased, the drop of mass activity might result from superfluous Pt or Cr after Pt_3Cr

alloy formation. There is little superfluous Pt or Cr after Pt_3Cr alloy formation on 0.67PtCr/C(T) electrocatalysts, which corresponds to only a small drop in mass activity on 0.67PtCr/C(T) electrocatalysts was very small, and possibly comes from partial decomposition of the alloy at higher temperatures.

Min and Hwang [5, 13] studied the ORR on Pt-based alloy electrocatalysts and indicated that the particle size of the electrocatalyst and alloying effect are two important factors affecting the electrocatalytic activity towards the oxygen reduction reaction. They claimed that the Pt-based alloy electrocatalysts have a mass activity superior to monometallic Pt/C electrocatalyst when the particle size of the alloy electrocatalyst was as small as possible [5, 13]. As the heat-treatment temperature increased, the particle size of PtCr/C(T) electrocatalysts increased. This suggested that, for the PtCr/C(T) alloy electrocatalysts, the Pt/Cr alloy needed to be formed at heat-treatment temperatures as low as possible. This is in agreement with our findings, and the SOMC method has proved to be a good way to prepare Pt-based Cr alloy electrocatalysts since PtCr/C(T) alloy electrocatalyst was synthesized at 750 °C rather than the temperature of 900 °C needed using conventional methods, thus reducing the degree of sintering.

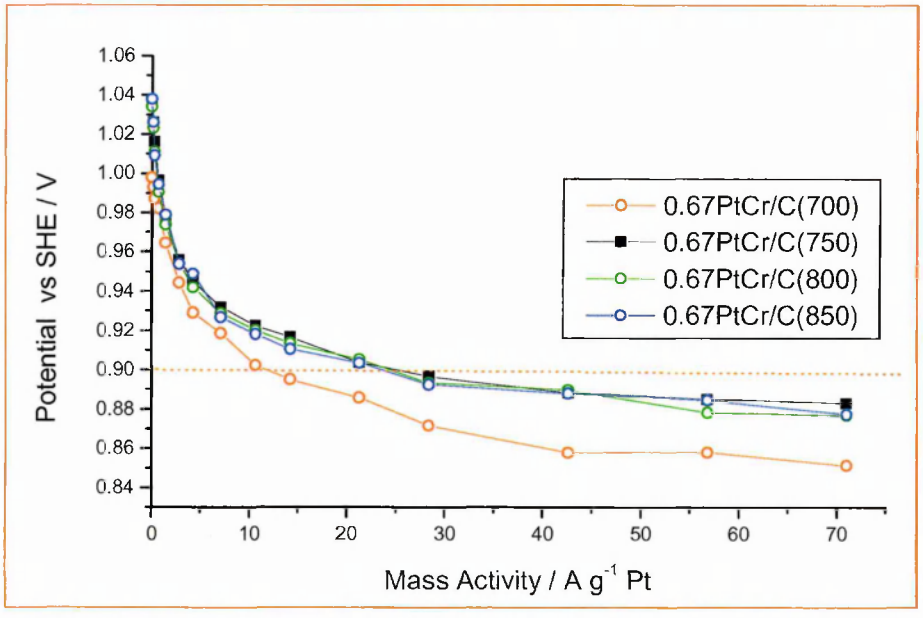

Figure 6.19 Mass activity for the ORR on 0.67PtCr/C electrocatalysts at different heat treatment temperatures

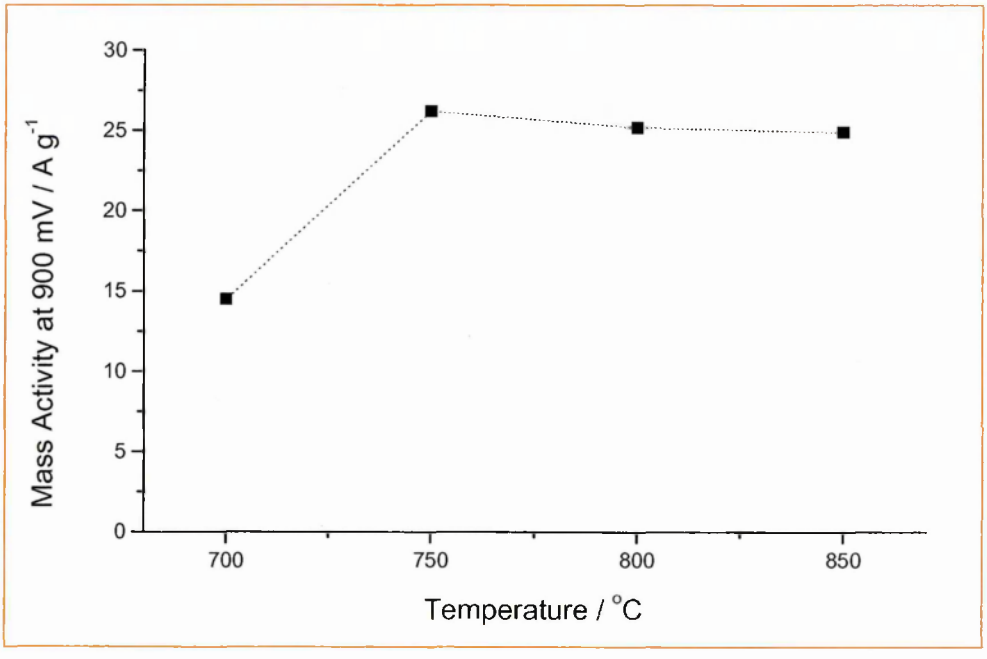

Figure 6.20 The relationship between the mass activity at 900 mV and heat treatment temperature for 0.67PtCr/C electrocatalysts

Figure 6.21 shows the mass activity plots for the ORR for the 0.5PtCr/C(750 °C), 0.67PtCr/C(750 °C) and PtCr/C(JM) electrocatalysts. Particle size based on XRD and some electrochemistry properties of these electrocatalysts are also shown in Table 6.3. The PtCr/C(JM) electrocatalyst is an optimal commercial electrocatalyst from Johnson Matthey Technology Centre for ORR, synthesized using a special method to form a Pt/Cr alloy. Our 0.67PtCr/C(750°C) electrocatalyst can be seen to attain the standard of an optimal commercial electrocatalyst for ORR. In addition, the particle size of the 0.67PtCr/C(750°C) alloy electrocatalyst is smaller than that of the PtCr(JM) alloy electrocatalyst. The 0.67PtCr/C(750°C) alloy electrocatalyst also has more resistance to sintering on heat treatment compared with the PtCr(JM) alloy electrocatalyst, a very important property for commercial electrocatalysts because this ensures that they will have a long life time.

Table 6.3 Particle size based on XRD and electrochemical properties

Electrocatalysts	**Particle size /nm**	**EPSA /cm^2 Pt**	**ECA/m^2 g^{-1}Pt**	**Mass activity at 900 mV/A g^{-1}Pt**
20%Pt/C	2.4	728	104	7.1± 0.5
0.5PtCr/C(200°C)	3.3 ± 0.2	691 ± 10	98 ± 2	7.5± 0.5
0.5PtCr/C(700°C)	3.6 ± 0.2	457 ± 10	65 ± 2	15.4 ± 0.5
0.5PtCr/C(750°C)	3.8 ± 0.2	448 ± 10	64 ± 2	25.1 ± 0.5
0.5PtCr/C(800°C)	3.7 ± 0.2	407 ± 10	58 ± 2	8.2± 0.5
0.67PtCr/C(700°C)	3.6 ± 0.2	433 ± 10	61 ± 2	14.9 ± 0.5
0.67PtCr/C(750°C)	3.7 ± 0.2	424 ± 10	60 ± 2	26.2 ± 0.5
0.67PtCr/C(800°C)	3.7 ± 0.2	409 ± 10	58 ± 2	25.2 ± 0.5
PtCr(JM)	4.5 ± 0.2	393 ± 10	56 ± 2	27.1 ± 0.5

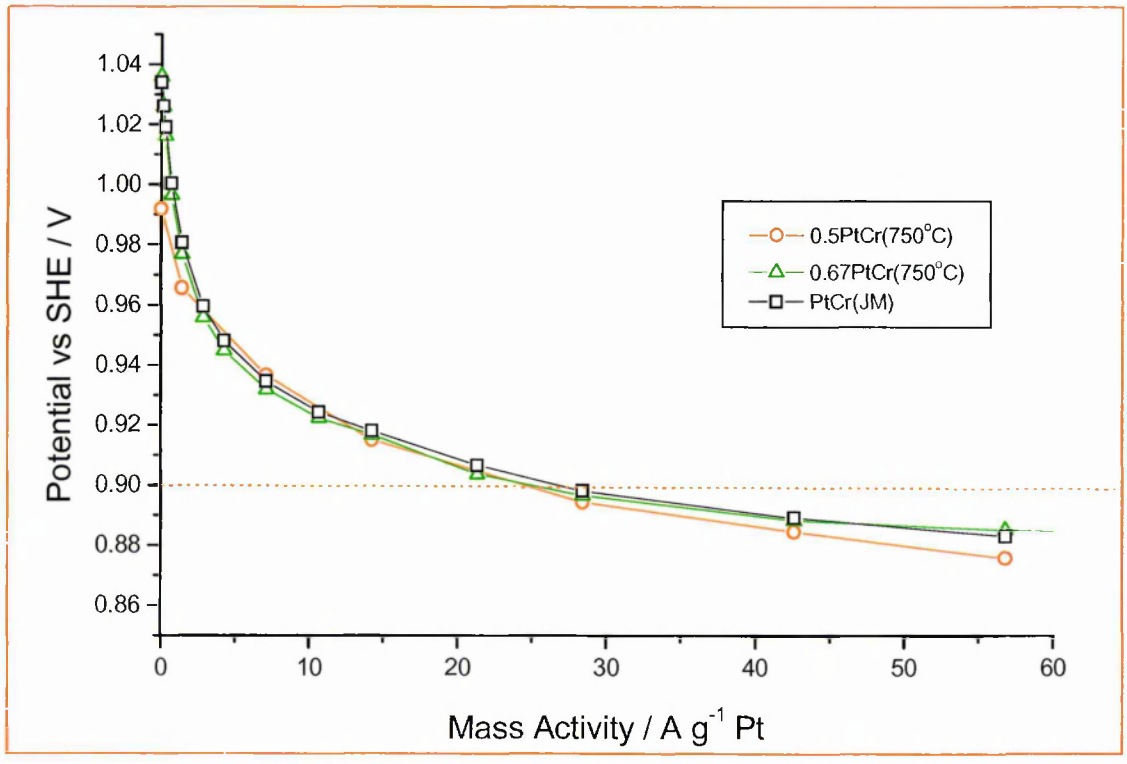

Figure 6.21 Mass activity for the ORR on 0.5PtCr/C(750°C), 0.67PtCr/C(750°C) and PtCr(JM) electrocatalysts

6.4 Conclusion

The electrocatalytic activity for the ORR on PtCr/C electrocatalysts was studied for different compositions of Pt/Cr and heat-treatment temperatures. The 0.67PtCr/C electrocatalyst, whose atom ratio of Pt/Cr nearly equals 3:1, has the highest electrocatalytic activity for ORR when it was treated at 750 °C after SOMC preparation. This catalyst matches the activity of the commercial catalyst, but has superior particle size and sintering resistance.

6.4 References

1. V.M. Jalan and E.J. Taylor, J. Electrochem. Soc., 1983. **130**: p. 2299.
2. J.T. Glass, G.L. Cathen and G.E. Stoner, J. Electrochem. Soc., 1987. **134**: p. 58.
3. M.T. Paffet, G.J. Beery and S. Gottesfeld, J. Electrochem. Soc., 1998. **135**: p. 1431.
4. A.J. Appleby, Energy, 1986. **11**: p. 13.
5. M. Min, J. Cho, K. Cho and H. Kim, Electrochim. Acta, 2000. **45**: p. 4211.
6. S. Mukerjee and S. Srinivasan, J. Electroanal. Chem., 1993. **201**: p. 357.
7. F.J. Luczak and D.A. Landsman, US Patent 4, 880 711, 1989.
8. T. Toda, H. Igarashi, H. Uchida and M. Watanabe, J. Electrochem. Soc., 1999. **146**: p. 3750.
9. B.C. Beard and P.N. Ross Jr., J. Electrochem. Soc., 1990. **137**: p. 3368.
10. A.J. Bard and L.R. Faulkner, Electrochemical Methods, John Wiley, 1980.
11. T.R. Ralph and M.P. Hogarth, Platinum Metal Review, 2002. **46**: p. 3.
12. J. Jiang and A. Kucernak, Electrochem. Solid-State Lett., 2000. **3**: p. 559.
13. J.T. Hwang and J.S. Chung, Electrochim. Acta, 1993. **38**: p. 2715.